

TESTING CPT AND ANTIGRAVITY WITH TRAPPED
ANTIHYDROGEN AT ALPHA

ANDREA CAPRA

A DISSERTATION SUBMITTED TO
THE FACULTY OF GRADUATE STUDIES
IN PARTIAL FULFILMENT OF THE REQUIREMENTS
FOR THE DEGREE OF

DOCTOR OF PHILOSOPHY

GRADUATE PROGRAM IN PHYSICS AND ASTRONOMY
YORK UNIVERSITY
TORONTO, ONTARIO
NOVEMBER 2015

©ANDREA CAPRA, 2015

Abstract

High precision antihydrogen experiments allow tests of fundamental theoretical descriptions of nature. These experiments are performed with the ALPHA apparatus, where ultra-low energy antihydrogen is produced and confined in a magnetic trap. Antihydrogen spectroscopy is of primary interest for precision tests of CPT invariance - one of the most important symmetries of the Standard Model. In particular, the 1S-2S transition frequency in hydrogen is the most precisely known quantity in Physics thus measuring the same quantity with antihydrogen provides the most stringent comparison between matter and antimatter. Antimatter gravity is an open experimental question that deserves to be directly addressed in order to test the foundation of the General Theory of Relativity. Methods to produce, trap, detect and identify antihydrogen are presented in this work, alongside the first high precision measurement of an antihydrogen property, i.e., the electric neutrality of an antiatom. This measurement also constitutes a three-fold improvement to the measured value of the positron charge. The focus is then shifted to the proposed experiment to measure the antihydrogen gravitational acceleration, with particular attention to the antihydrogen detector.

Acknowledgements

My supervisor, SM, for his patience and the long and illuminating discussions that we had in his office (or in the corridor). The whole ALPHA collaboration which gave me something interesting to do, in particular, WB and NM for their help in making me understand how things work. The ALPHA-Canada group for the support, in particular MF and AO. I am particular grateful to TF and JMK. A special thanks goes to PP for the unique opportunity he gave me. JF, AZ and AL allowed me to visit a new place. Mille grazie a SS per gli stimoli che mi ha dato. Questa tesi non sarebbe stata possibile senza la preparazione che mi ha fornito lavorare con AF. Un ringraziamento va a OC per avermi spinto ad intraprendere nuove avventure. Un riconoscimento va anche a MB per essermi amico anche sulle lunghe distanze (spaziotemporali, s'intende). CA welcomed me in Canada and GP helped me to finish many pitchers. RH for having me get started. I miei genitori PC and RC, senza il loro sostegno non sarei arrivato fin qui. AG pour tout le reste.

by any means I may arouse in the interiors of Plane and Solid Humanity a spirit of rebellion against the Conceit which would limit our Dimensions to Two or Three or any number short of Infinity.

E. A. Abbott, *Flatland*, Sec. 19

Table of Contents

Abstract	ii
Acknowledgements	iii
Table of Contents	v
Abbreviations	ix
1 Introduction	1
1.1 Discrete Symmetries in Particle Physics	2
1.1.1 CPT Invariance	3
1.1.2 CPT Tests	6
1.2 Equivalence Principle and General Relativity	9
1.2.1 Weak Equivalence Principle	10
1.2.2 WEP tests	13
1.3 Why Antihydrogen Experiments?	14
1.4 Gravitational Experiments and Neutral Antimatter	16
2 Antihydrogen at ALPHA	19
2.1 Penning Trap	21
2.2 The Catching Trap	24
2.3 Magnetic Trapping of Neutral Atoms	31
2.4 The Atom Trap	36

2.5	Outline of an Experiment	42
3	The Silicon Vertex Detector	44
3.1	Design and Features	45
3.2	Data Acquisition System	48
4	Simulation and Reconstruction	54
4.1	Virtual Monte Carlo and Geant3	54
4.1.1	Geometric Model	55
4.1.2	Primary Generator	57
4.1.3	Simulation Output	58
4.2	Tracking	59
4.2.1	Pattern Recognition	60
4.2.2	Track Reconstruction	64
4.2.3	Track Pruning	65
4.3	Vertexing	68
4.4	Note on Reconstruction Performance	71
4.5	Simulation Results	73
5	Limit on the Electric Charge of \bar{H}	76
5.1	Description of the Measurement	77
5.2	SVD Characterization	80
5.3	Annihilation Data	84
5.4	Simulation and Sensitivity	87
5.5	Long Term SVD Drift	89
5.5.1	Method	90
5.5.2	Results	93
5.6	Survey of Systematic Errors	96

5.7	Result and Discussion	101
6	ALPHA-2 Commissioning	103
6.1	SVD Commissioning	104
6.1.1	Relative Alignment of the Hybrids	107
6.1.2	Efficiency per Hybrid	110
6.2	Background Rejection	112
6.2.1	Discriminating Variables	113
6.2.2	Cuts Placement	116
6.2.3	Results	119
6.3	Standard Analysis of Trapped Antihydrogen	122
6.3.1	Analysis	122
6.3.2	Conclusions	126
6.4	Multi-Variate Analysis of Trapped Antihydrogen	127
6.4.1	Training of the Classifier	129
6.4.2	Analysis of Quench Data	135
6.4.3	Results of Quench Data	136
6.4.4	Analysis and Results of Monte Carlo Data	137
6.4.5	Analysis and Results of Hold Data	139
6.4.6	Conclusions	142
7	Measurement of \bar{H} Gravity	143
7.1	ALPHA-g	144
7.1.1	Magnet System	145
7.1.2	Gravity Measurements	146
7.1.3	Atom Interferometry	147
7.1.4	Antihydrogen Cooling	149
7.1.5	Antihydrogen Detection	151

7.2	A Radial TPC for \bar{H} Detection	153
7.2.1	Simulation	156
7.2.2	Tracking	164
7.2.3	Vertexing	170
7.2.4	Results	172
7.2.5	Conclusion	177
8	Conclusion	179
A	Helix Equations	181
B	Positron Spin in Magnetic Field	184

Abbreviations

AD	Antiproton Decelerator
CERN	European Organization for Nuclear Research
ALPHA	A Laser PHysics Apparatus
\bar{p}	antiproton
\bar{H}	antihydrogen
e^+	positron
γ	photon
π^\pm, π^0	charged and neutral pions, i.e., the lightest mesons
μ^\pm	muons, charged particles similar to electrons/positrons but heavier
SM	Standard Model
QFT	Quantum Field Theory
GR	General Relativity
SVD	Silicon Vertex Detector
MC	Monte Carlo simulation
DAQ	Data AcQuisition system
TPC	Time Projection Chamber

1 Introduction

Antihydrogen is the bound state of a positron, the antimatter counterpart of the electron, and an antiproton, the antiparticle of the proton, whereas hydrogen is an atom composed of an electron and a proton. The existence of the positron was postulated in the late 20's [1] and it was subsequently found in cosmic radiation in 1932 [2]. Since then, many other natural sources of positrons have been identified, such as potassium, sodium or magnesium salts, containing unstable isotopes of those elements. The existence of the antiproton was confirmed much later [3], in 1955, by means of a particle accelerator in Berkeley, USA. To date, the only way to obtain antiprotons is to produce them in particle accelerators. This is the main reason why experiments on antiatoms came about only in recent years as there is a lack of atomic antimatter in the visible Universe. The Big Bang Theory, that is, the most advanced theory of the origin of the Universe, predicts that, at least initially, equal amounts of matter and antimatter were created. Yet the balance seems at present to be overwhelmingly in favour of matter. This imbalance is known as *baryon-antibaryon asymmetry*.

Performing experiments on antihydrogen is challenging since its components are produced at high energy (e.g., antiprotons in particle accelerators), whereas their recombination must occur at extremely low energy to favour antiatom formation. Once an antihydrogen atom is formed, its motion must be confined either in a trap or in a slow beam; in both cases the kinetic energy of the newly born antiatom must be much lower than the production energy of its constituents, in jargon, it has to be *cold*.

Experiments with antiparticles have achieved remarkably precise results. Nevertheless, atomic antimatter, i.e., atoms made of antiparticles, is a relatively new line of inquiry for the reason mentioned above. Testing the most fundamental theories describing the physical world in the atomic realm is the next logical step to undertake.

Such fundamental theories are based on symmetry principles, which are ultimately deduced from empirical evidence; whether these symmetry principles are violated is therefore an experimental question that demands high precision measurements.

After explaining the symmetries underlying Particle Physics in Sec. 1.1 and Gravitational Physics in Sec. 1.2, this chapter deals with the motivation in Sec. 1.3 as to why the comparison between matter and antimatter is such an important line of experimental inquiry. A brief discussion of the relevance in the present context of the measurement of the antihydrogen electric charge is given in Sec. 1.4.

1.1 Discrete Symmetries in Particle Physics

The *Standard Model* (SM) accommodates six quarks and six leptons which, together with their antiparticles, constitute the three generations of elementary particles so far discovered. The Standard Model is a Quantum Field Theory (QFT), which is the only known way of combining Quantum Mechanics and Special Theory of Relativity in order to describe three of the four fundamental interactions: electromagnetic, weak and strong. The fourth interaction, gravity, is not described by a quantum theory. The *General Theory of Relativity* (GR) is instead a classical theory and gravity arises as curvature of spacetime caused by the presence of mass-energy.

Both GR and QFT embed *Lorentz Invariance*, that is, the statement that

the equations of the theory are invariant under rotations and boosts - *Lorentz Transformations*. Lorentz Invariance is the backbone of Special Relativity and it is actually the conjugation of Lorentz Invariance with Quantum Mechanics that allowed the prediction of the existence of antiparticles. One of the consequences of Lorentz invariance in QFT is the *CPT invariance theorem*, whose proof requires few other technical hypotheses. An overview of this symmetry is given in Sec. 1.1.1. This theorem became popular when violations of parity reflection [4], P, charge conjugation [5], C, their combination [6], CP, and time reversal [7], T, were discovered in the weak interaction of elementary particles. The CPT invariance tests are described in Sec. 1.1.2, where a review of the *Standard Model Extension* (SME) is provided as a helpful framework to compare the outcome of various experiments searching for CPT violation signals.

1.1.1 CPT Invariance

A transformation is a *symmetry transformation* of a QFT if it leaves the Lagrangian density \mathcal{L} of the theory *invariant* up to a 4-divergence, since the action is given by

$$S = \int \mathcal{L} d^4x \rightarrow \int (\mathcal{L} + \partial_\mu J^\mu) d^4x = S, \quad (1.1)$$

where d^4x is the measure over the spacetime. Thus, the equations of motion, following from the variational method, remain unchanged.

A Lagrangian density in QFT is constructed to be a “Lorentz-scalar”, i.e., invariant under the proper orthochronous Lorentz group, that is, the above-mentioned Lorentz invariance. Therefore, \mathcal{L} need not be invariant under parity reflection P, that sends (t, \mathbf{x}) to $(t, -\mathbf{x})$, and time reversal T, that sends (t, \mathbf{x}) to $(-t, \mathbf{x})$, belonging to the improper and non-orthochronous Lorentz group, respectively. In addition to these spacetime transformations, there is another transformation C, charge conjugation, that sends particle to antiparticle, i.e., it changes the sign of

every internal quantum number, such as the electric charge, the magnetic dipole moment, the lepton number, etc..

The Quantum Electro-Dynamics (QED) Lagrangian that describes the interactions of fermions, e.g., electrons and positrons, with the electromagnetic field, e.g., the electromagnetic field of a proton or an antiproton, is given by

$$\mathcal{L}_{\text{QED}} = \bar{\psi} (\imath\partial_\mu - eA_\mu) \gamma^\mu \psi - m\bar{\psi}\psi - \frac{1}{4}F^{\mu\nu}F_{\mu\nu}, \quad (1.2)$$

where $\mu = 0, 1, 2, 3$ is the spacetime coordinates index, ψ and $\bar{\psi} = \gamma^0\psi^\dagger$ are the fermion fields, A_μ is the electromagnetic potential 4-vector, e is the electron charge, m is the mass of the fermion, $F_{\mu\nu} = \partial_\mu A_\nu - \partial_\nu A_\mu$ is the electromagnetic field tensor and the γ^μ matrices obey the usual Dirac algebra. The relevance of the QED in the present work is clear since it is the fundamental theory describing the bound state of a positron and an antiproton¹.

The Lagrangian Eq. (1.2) is invariant under C, P and T separately, as it is built from Lorentz vectors V^μ and scalars S only. The transformation properties of the scalar part are trivial since

$$\mathcal{O}S\mathcal{O}^{-1} = S,$$

where \mathcal{O} is an operator representing C, P or T and the only scalar in Eq. (1.2) is $\bar{\psi}\psi$. The transformation of a Lorentz vector is as follows:

$$\mathcal{O}V^\mu\mathcal{O}^{-1} = \begin{cases} -V^0 \\ V^i \quad \text{for } i = 1, 2, 3 \end{cases}$$

if \mathcal{O} is P or T and

$$CV^\mu C^{-1} = -V^\mu.$$

¹To be strictly accurate, one should take into account the complete SM. However, it is irrelevant for the purpose of the present discussion.

The 4-vectors in Eq. (1.2) are $i\partial_\mu$, $\bar{\psi}\gamma^\mu\psi$ and A_μ and they always appear in pairs so that the minus signs cancel out every time ², leaving \mathcal{L}_{QED} invariant. However, a Lagrangian density with terms bearing the V-A structure, i.e., containing terms that are the difference of a Lorentz vector and a pseudo-vector, are not invariant under P or C separately. This is the behaviour of the weak interaction that is also known to violate the product transformation CP, at least in the quark sector due to the presence of a complex term in the CKM matrix (see, for example, [8]).

It is clear from the previous discussion that the QED Lagrangian is invariant under the product CPT, i.e., CPT is a symmetry of QED, that is intimately connected to the fundamental Lorentz invariance and locality of the theory, since the action S is obtained from the spacetime integral of the Lagrangian density given by Eq. (1.1). Indeed, there is a proof that a CPT violating theory implies Lorentz violation [9].

It turns out that there is also a very general proof of CPT invariance [10] for any QFT constructed from spin zero, one-half and one fields with local interactions, if the usual connection between spin and statistics is valid (i.e., fermion fields anticommute, for a proof see [11]) and the products are normally ordered (i.e., Wick product, see, for example, [12]). Given the close relation between CPT invariance and the basics of a QFT, the next section focuses on tests of this fundamental symmetry.

²The transformation properties of the electromagnetic tensor $F^{\mu\nu}$ can be inferred from the ones of ∂_μ and A_μ . In particular, whenever a minus appear in the transformation of $F_{\mu\nu}$, the contraction with the contravariant tensor $F^{\mu\nu}$ eliminates it.

1.1.2 CPT Tests

Various experiments at different energy scales have probed and/or are probing several matter-antimatter systems in order to search for signals of CPT violation. Typical searches involve measuring a fundamental property of a particle and of an antiparticle, like the electric charge or the mass, or the lifetime for unstable systems. For example, in low-energy experiments, the proton-antiproton charge-to-mass ratio has been measured by the BASE collaboration and found to differ from one by less than a part in 10^{12} [13]. In high-energy experiments, the ALICE collaboration recently reported a limit on the mass difference between light nuclei and antinuclei of the order of $10^{-3}-10^{-4}$ GeV/c² [14]. However, the most accurate determination of the CPT invariance is due to a re-analysis of the data of the KTeV experiment at Fermilab, where the mass difference between K_0 and \bar{K}_0 is found to be less than 4.8×10^{-19} GeV/c² [15].

In order to provide quantitative bounds on CPT invariance, a theoretical framework has been developed by Kostelecký *et al.* that incorporates *spontaneous CPT and Lorentz symmetry breaking*, while maintaining the usual gauge invariance and renormalizability [16, 17]. The Extension of the minimal Standard Model, called SME, amounts to a parametrization of the Lorentz and CPT symmetry violations and is considered as an *effective field theory*, underlying a complete fundamental theory that includes gravity, valid at the Planck mass scale $m_P \approx 10^{19}$ GeV/c².

As an example of SME, the Dirac equation for the free hydrogen atom, modified to include Lorentz violating terms, is given by [18]

$$\left(i\gamma^\mu D_\mu - m_e - a_\mu^e \gamma^\mu - b_\mu^e \gamma^5 \gamma^\mu - \frac{1}{2} H_{\mu\nu}^e \sigma^{\mu\nu} + ic_{\mu\nu}^e \gamma^\mu D_\nu + id_{\mu\nu}^e \gamma^5 \gamma^\mu D_\nu \right) \psi = 0, \quad (1.3)$$

where $iD_\mu = i\partial_\mu + eA_\mu$, $\sigma^{\mu\nu} = i[\gamma^\mu, \gamma^\nu]/2$, m_e is the electron mass and ψ is the

electron field. The electromagnetic vector potential is given by the proton Coulomb potential $A_\mu = (-e/4\pi r, 0, 0, 0)$. The five coefficients appearing in Eq. (1.3) break the Lorentz invariance: a_μ^e and b_μ^e are “CPT-odd”, i.e., they violate CPT, while $H_{\mu\nu}^e$, $c_{\mu\nu}^e$ and $d_{\mu\nu}^e$ are “CPT-even”, i.e., they conserve CPT. The corresponding Dirac equation for the free antihydrogen atom is obtained by changing the sign of the two CPT-odd terms and of the electric charge.

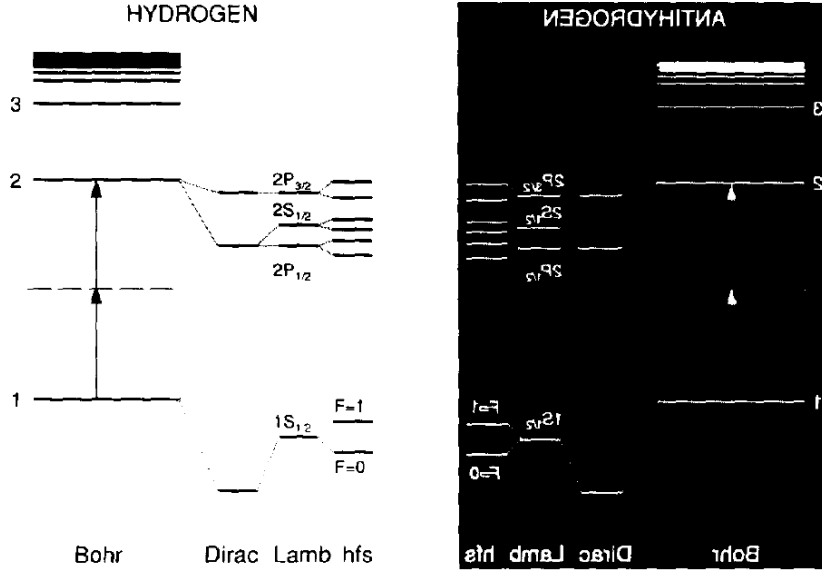


Figure 1.1: Energy levels of hydrogen and antihydrogen, taken from [19]. “Dirac” are the corrections to the levels due to the electron/positron spin. The “Lamb shift” is the correction to the S-states due to the quantum vacuum fluctuation. “hfs” is the hyperfine splitting due to the interaction between the total electron/positron angular momentum with the proton/antiproton spin. The arrows indicate the two-photon 1S-2S transition.

Within the SME and by using perturbation theory, it is possible to calculate the expected frequency shifts for the hydrogen and the antihydrogen spectral lines, including the most promising 1S-2S transition [19] (see Fig. 1.1), whose attainable resolution is order of 10^{-18} . However, at the leading order in pertur-

bation theory, there is an identical energy shift for both the 1S and the 2S levels, so that no observable signal can be measured. Nevertheless, for magnetically confined hydrogen and antihydrogen, the hyperfine Zeeman splitting is dependent on the principal quantum number, therefore CPT violating signals can be measured for selected transitions between Zeeman states of the two levels. In addition, microwave spectroscopy of the hydrogen/antihydrogen ground state gives access to several SME coefficients.

All the operators appearing in Eq. (1.3) are of mass dimension equal or less than four and, as such, they are considered in the framework of the so-called minimal SME. Spectral shifts of hydrogen and antihydrogen can arise from operators of higher dimension in the *non-minimal SME*. An unsuppressed signal of CPT violation is finally present at the leading order in the frequency shift of the 1S-2S transition in magnetically trapped antihydrogen [20]

$$\delta\nu_{1S-2S} = \frac{3}{\sqrt{4\pi 4}}(\alpha m_r)^2 \sum_{w=e^+, \bar{p}} (c_2^w + a_2^w) + \frac{67}{\sqrt{4\pi 16}}(\alpha m_r)^4 \sum_{w=e^+, \bar{p}} (c_4^w + a_4^w), \quad (1.4)$$

where α is the fine structure constant and $m_r = m_{e^+}m_{\bar{p}}/(m_{e^+} + m_{\bar{p}})$ is the reduced mass of the antihydrogen system. The a_k^w (CPT-odd) and c_k^w (CPT-even) coefficients control the Lorentz violation and correspond to isotropic and non-relativistic physical effects [21]. Moreover, additional CPT-odd terms are present in the frequency shifts of the transitions between Zeeman sublevels of the 1S state of hydrogen and antihydrogen, enriching the search for CPT violations.

Complete and updated tables of the most recent measurements of the minimal and non-minimal SME coefficients in various sectors (electron, proton, neutrino, etc.) can be found in [22].

1.2 Equivalence Principle and General Relativity

The successful attempt to describe simultaneously classical electrodynamics and gravitation lead to the formulation of GR. In GR, Lorentz invariance, mentioned in the previous section, is part of Einstein's Equivalence Principle (EEP) - the fundamental assumption that makes gravity a property of spacetime.

The EEP can be broken down into the following three distinct statements:

Weak Equivalence Principle (WEP) or *Universality of Free Fall* (UFF) states that the acceleration of a freely falling body is independent of its internal structure and composition. The freely falling state implies that the body has to be small enough to not be affected by tidal forces, in addition to be free from any other interaction, like the electromagnetic one.

Local Lorentz Invariance (LLI) is the assumption that Lorentz Invariance applies to an infinitesimal region of spacetime at every point.

Local Position Invariance (LPI) requires that the results of any non-gravitational experiment be independent of where and when it is performed. This implies that the various physical constants do have “constant” values.

A *metric* is a function that is used to calculate distances between points and describes the properties of spacetime [23]. If the EEP is valid, then gravity is the effect of curved spacetime and the only viable theories of gravity are “metric”, which assume that [24]:

- Spacetime is endowed with a symmetric metric.
- The trajectories of freely falling bodies are geodesics of that metric. In their local reference frame, they appear to move along locally straight lines.

- The non-gravitational laws of Physics in local Lorentz frames are compatible with the Special Theory of Relativity. The established non-gravitational laws that fulfill this requirement are classical electrodynamics (governed by Maxwell’s equations) and the Standard Model.

Since the EEP is the foundation of GR, GR is a metric theory. Two main consequences can be drawn from the validity of EEP and the metric formulation of gravity. Firstly, the metric is a property of spacetime, rather than a field over the spacetime, because every field (lepton, quark, electromagnetic, etc.) couples in the same way to gravity. This “universal coupling” allows one, for example, to measure the proper time between two events, independently of the clock used. Secondly, every equation that obeys Special Relativity, formulated in terms of the Minkowski metric and partial derivatives, can be “translated” in curved spacetime by replacing the flat metric with the metric that is the solution of the Einstein equation given the distribution of mass-energy and the ordinary partial derivative with the covariant one.

The WEP is the main subject of the next section and some experimental evidence of its validity is presented in Sec. 1.2.2. The LLI can be studied within the SME framework, described in the previous section (see Sec. 1.1.2). The LPI can be tested by measuring the gravitational redshift, for example, by using atom interferometry [25] and will not be discussed any further.

1.2.1 Weak Equivalence Principle

For clarity’s sake, the following discussion of the WEP involves explicitly a system composed of an atom subjected to the Earth’s gravitational field.

The WEP states that the *gravitational mass* m_G of an atom is equal to its *inertial mass* m_I

$$m_I = m_G. \tag{1.5}$$

The distinction occurs when one considers, on the one hand, *Newton's gravitational law*,

$$|\mathbf{F}_G| = \frac{GM}{r^2} m_G, \quad (1.6)$$

where $G = 6.674 \times 10^{-11} \text{ m}^3 \text{ kg}^{-1} \text{ s}^{-2}$ is the gravitational constant, $M = 5.97 \times 10^{24} \text{ kg}$ is the Earth mass and r is the distance between the centre of the Earth and the atom while, on the other hand, there is *Newton's second law* of mechanics,

$$|\mathbf{F}| = m_I a, \quad (1.7)$$

where a is the acceleration of the atom. The gravitational mass m_G is the “charge” of the gravitational interaction and the inertial mass m_I is the “resistance” that the atom would oppose to its motion. If the various forms of energy of the atom, such as the rest mass of its constituents, the binding energy, etc., contribute differently to m_I with respect to m_G , the WEP is violated.

An equivalent formulation of the WEP is the Universality of the Free Fall that states that the acceleration a of an atom, under the sole influence of gravity, is independent of its gravitational mass m_G . The equivalence of WEP and UFF can be proved by equating Eqs. (1.6) and (1.7)

$$m_I a = \frac{GM}{R^2} m_G, \quad (1.8)$$

and solving for a

$$a = \frac{GM}{R^2} \frac{m_G}{m_I} = \frac{m_G}{m_I} g, \quad (1.9)$$

where $R = 6371 \text{ km}$ is the mean Earth radius and

$$g = \frac{GM}{R^2} \approx 9.81 \frac{\text{m}}{\text{s}^2}. \quad (1.10)$$

Therefore, the acceleration due to gravity is

$$a = g, \quad (1.11)$$

independent of the gravitational mass, if and only if WEP, Eq. (1.5), holds.

If one considers antiatoms instead, one may wonder whether the WEP is violated for antimatter, i.e., is

$$\bar{m}_I \stackrel{?}{=} \bar{m}_G, \quad (1.12)$$

where \bar{m}_G and \bar{m}_I are, respectively, the gravitational mass and the inertial mass of an antiatom. A detailed discussion of antimatter gravity is presented in [26].

If CPT invariance holds, then

$$\bar{m}_I = m_I \quad (1.13)$$

and combining together Eqs. (1.5), (1.12) and (1.13) gives

$$m_G \stackrel{\text{WEP}}{=} m_I \stackrel{\text{CPT}}{=} \bar{m}_I \stackrel{\text{WEP?}}{=} \bar{m}_G. \quad (1.14)$$

It is worth noting here that CPT invariance does not imply the WEP or vice-versa, as shown in Eq. (1.14), where the chain of equalities can be interrupted by CPT violation without affecting the last equality or inequality. Moreover, CPT invariance does not inform whether $m_G \stackrel{?}{=} \bar{m}_G$, so that Eq. (1.14) cannot be read as proof of WEP for antimatter, for two reasons. Firstly, the CPT theorem is proved in a flat spacetime for a local quantum theory and gravity does not have a quantum formulation and implies a curved spacetime. Secondly, if the CPT theorem is valid in curved spacetime, then it predicts that an antiatom would fall towards an “anti-Earth” with the same acceleration as an atom towards Earth: it does not say anything about an antiatom towards Earth.

Despite the previous statement, the SME allows a departure from the WEP by including Lorentz and CPT violating terms in definition of the inertial and gravitational masses of composite bodies, such as atoms [27]. Notably in the cited work, the *Isotropic Parachute Model* (IPM) predicts that antimatter would freely fall with an acceleration smaller than g .

1.2.2 WEP tests

The torsion balance experiment at the University of Washington (Eöt-Wash) has achieved remarkable results directly testing WEP, by comparing the acceleration of two bodies of different composition. The device is composed of two different test objects attached to a rigid rod that is suspended in vacuum by a fibre, and is extremely sensitive to a differential acceleration Δa of the two bodies orthogonal to the fibre [28]. The most recent limit on Δa is $< 10^{-15} \text{ m/s}^2$ [29]. This result shows that the gravitational accelerations of two matter objects are independent of their composition at the 10^{-15} level.

The Lunar Laser Ranging (LLR) tests of the WEP have the audacity of comparing the free fall accelerations of the Earth and Moon towards the Sun. LLR determines the time of flight of a laser beam from an observatory on the Earth to a retro-reflector on the Moon, placed by the Apollo missions, and back. Since the lunar orbit can be calculated with GR, the Earth-Moon distance can be expressed as a function of the ratios of the gravitational to inertial masses of the Earth and of the Moon. The time of flight gives a precise measurement of such a distance, i.e., “ranging”, and the limit to the difference of the two ratios is $< 10^{-13}$ [30].

Atom interferometry (for a review of the topic see [31] and Sec. 7.1.3) has aggressively entered the landscape of precision tests of GR [32]. For example, the validity of the WEP is discussed in [33], based on recent results with atomic fountains. Given the relatively small size that an interferometer can achieve, a proposal to test WEP with these devices on board of satellites have been put forward.

In spite of the large number and the high precision of the WEP tests on matter, there is still a need for experiments with antiatoms. Nevertheless, several authors

have argued that the WEP tests mentioned above [34, 35] and spectroscopic experiments [36] suffice to solve the question of the antimatter gravity.

Supporting the idea that an $\bar{\text{H}}$ gravity experiment is unnecessary, a measurement of the antiproton cyclotron frequency subjected to the gravitational redshift has been reported in [37] as WEP tests. However, as mentioned at the end of Sec. 1.2, it is actually a test of LPI.

In addition, a re-analysis of the CP-LEAR data of $\text{K}_0\text{-}\bar{\text{K}}_0$ interference [38] does not demonstrate the WEP for neutral kaons, because it only shows that gravity, and the other bosonic fields considered in the cited paper, couple with nearly identical strength to both mesons and not that the gravitational interaction of antimatter is the same as for baryonic matter. These results constitute instead an indirect test of the WEP, since they imply that gravity couples with nearly identical strength to quarks and antiquarks, and one can be easily persuaded that an antiproton obeys the WEP as the proton does based on the quark model. In any case, the neutral kaon experiment does not disentangle WEP and CPT tests.

There are strong arguments against antigravity [26], i.e., matter and antimatter actually repelling one another, such as the one presented in [39]. Nonetheless, several authors have reported to various degrees of clarity (for instance, Chardin [40], Hajdukovic [41] and Villata [42]) that there is a place for antigravity in the current theoretical picture. There is no doubt that even if antimatter gravitates as expected, any direct evidence will be a milestone in experimental Physics.

1.3 Why Antihydrogen Experiments?

Antihydrogen ($\bar{\text{H}}$) was first produced in 1996 at the CERN Low Energy Antiproton Ring (LEAR) in the scattering of antiprotons ($\bar{\text{p}}$) from a thin target [43]. However, its kinetic energy was too high to perform high-precision CPT tests, let

alone WEP tests. Since then many efforts have been made at CERN to produce *ultra-low energy* \bar{H} [44]. The reasons to pursue such an endeavour are discussed in the following.

As mentioned in Sec. 1.1, GR and SM are incompatible and future experiments will inevitably lead to the modification of one of them, if not both. Testing these theories using \bar{H} is the kind of crucial experiment that is needed. For example, GR does not exhaust the possibilities of metric theories of gravity, whereas the notion of curved spacetime, that follows from the EEP, is a very elegant and general one. Therefore, testing the EEP is not an academic exercise but rather it sets the foundation of the modern conception of gravity. Gravitational tests on antimatter are compelling in order to prove the validity of the WEP in the realm of atomic antimatter. Moreover, \bar{H} experiments provide tests of Lorentz Invariance - the second pillar of the EEP - as discussed in Sec. 1.1.2.

The SM, despite its remarkable success (e.g., the high-precision electroweak tests [45], the evolution of the strong coupling constant [46] and the Higgs boson couplings measurements [47, 48]), is not free from defects, not the least of which is the naturalness problem and the unexplained existence of dark matter. Moreover, it fails to include gravity. A theory that describes all the four fundamental interactions (and also that takes into account dark matter) is highly desirable. In searching for Physics beyond the Standard Model, the most elementary question to ask is whether the foundations of the current accepted theory are solid. Of particular interest is searching for signals of violation of CPT symmetry and the related Lorentz Invariance. Many theories have been proposed, e.g., string theories, that include breaking of the Lorentz and CPT symmetries to some extent. Such effects are suppressed by the Planck mass $M_P \approx 10^{19}$ GeV scale and are hence hardly attainable in collider physics. However, if one wishes to consider experiments where extremely low energy protons and antiprotons are

involved, the sensitivity to CPT violating effects can be expressed by $m_p^2 c^2 / M_P \approx 10^{-20}$ GeV, where $m_p \approx 1$ GeV is the proton/antiproton mass: although small, the sensitivity in frequency units is ≈ 20 kHz and is within reach of those high precision experiments [49].

It is legitimate to wonder whether high-precision experiments with matter, e.g., hydrogen, are enough to set stringent limits on Lorentz and CPT violating effects. The answer is not “yes”, as one might intuitively expect. There is a non-negligible chance that some effect may only arise by comparing matter to antimatter systems, a possibility that can be deduced, for instance, by using the SME, where some coefficients are CPT violating, whereas experiments with matter are sensitive only to combinations of CPT-even and CPT-odd terms [50].

In addition to the incontrovertible fact that $\bar{\text{H}}$ is the only antiatomic system within the reach of the current technological means, hydrogen is the best known physical system, both theoretically [51] and experimentally [52]. High-precision spectroscopy on this atom has achieved a relative uncertainty of less than one part per trillion [53]. Therefore, experiments on $\bar{\text{H}}$ have been sought for years since they permit the most precise direct comparison between matter and antimatter. This gives the opportunity to attempt to tackle the problem of the baryon-antibaryon asymmetry - the overwhelming imbalance in the visible Universe of the amount of matter with respect to antimatter. CPT and/or Lorentz violation and/or a gravitational anomaly might be viable explanations to it and, therefore, worth testing.

1.4 Gravitational Experiments and Neutral Antimatter

Testing the WEP with charged antiparticles and particles turns out to be a very difficult task [54]. Indeed, the historical experiments at the end of the

60's, performed by Witteborn and Fairbank [55, 56], never produced convincing results for electrons, nor reached the stage of measuring the free fall acceleration of positrons. However, they broke ground for the idea of measuring the antimatter gravity. In the 90's, another experiment to measure the antiproton free fall acceleration, encouraged by new availability of low-energy antiproton sources, was also proposed but never performed [57, 58].

\bar{H} is a suitable candidate for a gravity experiment because it has zero electric charge. Positronium, i.e., the bound state of an electron and a positron with an extremely short lifetime of 142 ns, is another interesting candidate, but is not entirely made of antimatter, even if an experiment with muonic hydrogen has been proposed [59]. The antineutron is an excellent system to test, but the technological challenge is beyond solution at present. This begs the question, “How electrically neutral is \bar{H} really?”.

Naturally, the \bar{H} electric charge is given by the sum of the electric charges of its constituents. Therefore, for \bar{H} to be neutral, the charge of the e^+ and the \bar{p} must be exactly opposite. This raises the fundamental question as to how well we know that matter is neutral and to what degree of accuracy the charge of the electron is measured to be equal in strength and opposite in sign to that of the proton. Of course, protons and antiprotons are not elementary particles and the final answer can be referred to the quark model. Measuring the \bar{H} electric charge not only represents a CPT test, when a similar measurement is performed on hydrogen, but tests another important aspect of the SM, as explained in the following.

The SM is a chiral theory, i.e., distinguishes between “right-handed” and “left-handed” fermions, because the weak interaction violates parity. The presence in the theory of axial currents coupling to a pair of gauge vector bosons in the so-called “triangle diagrams” produces inconsistencies in the calculation of the

one-loop correction to the three-gauge boson vertex. These inconsistencies arise since the divergence of the axial current is zero in the classical picture, while it acquires a non-zero value in QFT, i.e., it is a *quantum anomaly*. It can be shown that gauge invariance is guaranteed only if these anomalous contributions cancel out. The cancellation occurs by summing together all the possible triangle diagrams for all the known fermions, as shown with great care in [60], resulting in a zero net contribution to the loop correction because quarks and leptons appear within one *generation* in equal number and their colour and weak charges add up to zero. One of the consequences of this fundamental structure is that the sum of the electric charges of the valence quarks in the proton with the charge of the electron gives zero. The same reasoning can be applied to neutrons and \bar{H} . Therefore, the \bar{H} electric charge is intimately connected with the structure of the SM and so it is fundamentally important that it be measured experimentally.

2 Production and Trapping of $\bar{\text{H}}$ at ALPHA

Several experiments, all located at the Antiproton Decelerator (AD) at CERN, have been working, since the early 2000s, on the production and on the study of $\bar{\text{H}}$ [61]. These experiments are ATHENA, ATRAP, ASACUSA, ALPHA, AEGIS and GBAR.

While ATHENA [62] is concluded and GBAR [63] has been approved to be built, ATRAP [64], ALPHA and AEGIS [65] are currently making remarkable progress in this line of research. The Physics program of ASACUSA is not limited to $\bar{\text{H}}$ [66] but also includes the study of “antiprotonic helium” [67]. ATRAP has also performed an important measurement of the $\bar{\text{p}}$ magnetic moment [68].

The present work focuses on the ALPHA experiment that, as the other experiments, receives from the AD a beam of slow $\bar{\text{p}}$. All the experiments had to develop techniques to trap and cool e^+ and $\bar{\text{p}}$, and make them recombine to produce the simplest antiatom, the $\bar{\text{H}}$ atom. ASACUSA and AEGIS shape the formed $\bar{\text{H}}$ in a beam, while ATRAP and ALPHA employ trapped $\bar{\text{H}}$. The main goal of ATRAP, ASACUSA and ALPHA is to perform high-precision $\bar{\text{H}}$ spectroscopy, while AEGIS is focused on the measurement of its gravitational acceleration.

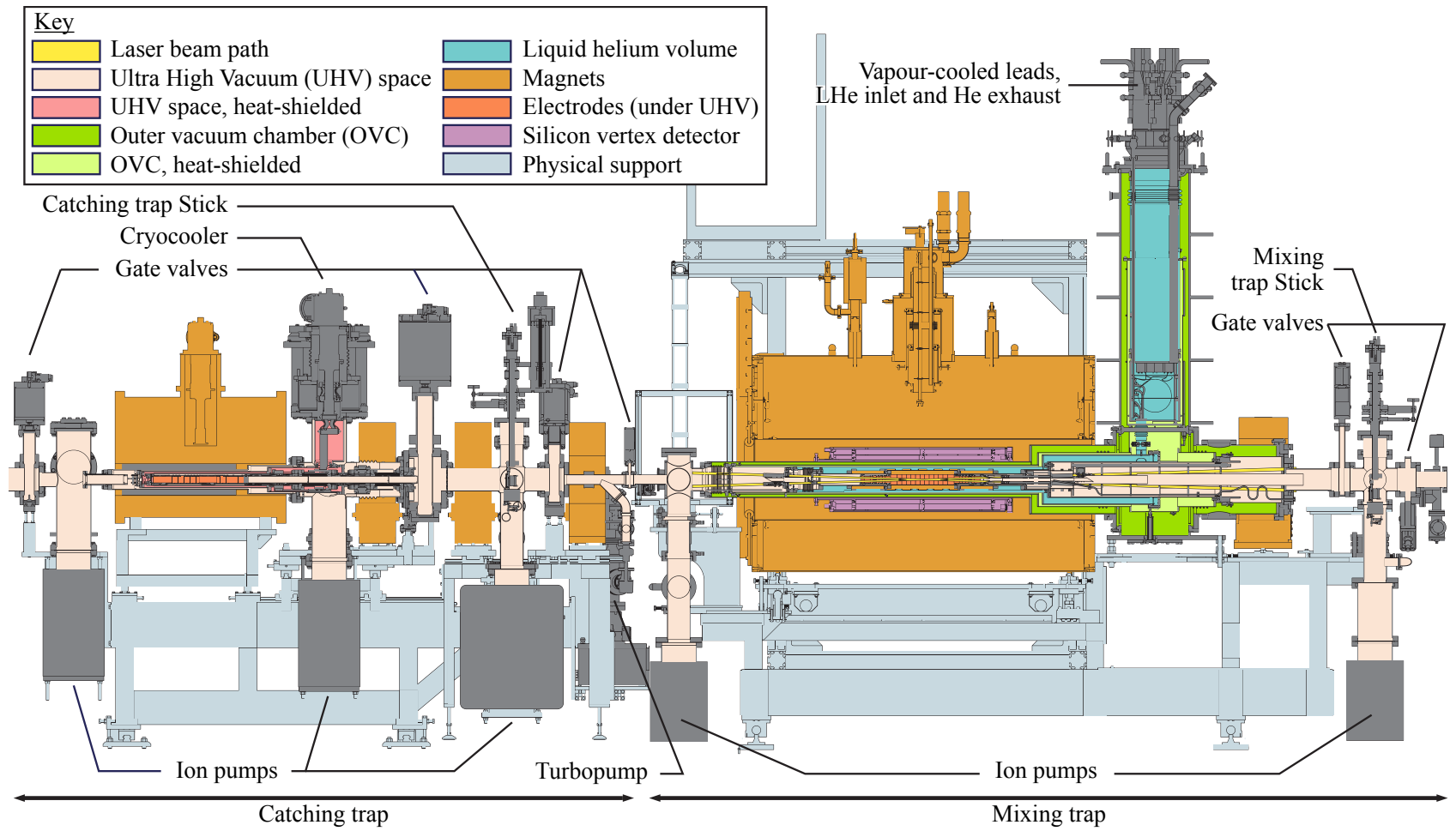


Figure 2.1: Side view of the ALPHA-2 apparatus. Credits: ALPHA

This chapter is devoted to the methodology used by ALPHA to produce, confine and, eventually, perform high-precision measurements on $\bar{\text{H}}$. At the end of 2011, the so-called ALPHA-1 apparatus [69] was de-commissioned, after the successful campaign of trapping cold $\bar{\text{H}}$ [70] and the first spectroscopy experiment [71]. In 2012, an improved version of the apparatus, dubbed ALPHA-2, was built and started taking data in 2014. The present chapter focuses on the ALPHA-2 hardware, while the methods and the techniques to manipulate the $\bar{\text{p}}$, e^+ and e^- , and to produce and trap $\bar{\text{H}}$ are similar to the ones adopted in the original apparatus. In Sec. 2.1 the physics of charged particles and antiparticles manipulation is presented. The description of the device used to capture and cool the $\bar{\text{p}}$ is given in Sec. 2.2. The confinement of neutral atoms in a magnetic trap is described in Sec. 2.3. The device where $\bar{\text{H}}$ production and confinement takes place is presented in Sec.2.4. The outline of a typical experiment in ALPHA, regardless whether the ALPHA-1 or ALPHA-2 apparatus is involved, is shown in Sec. 2.5

2.1 Penning Trap

The device that allows ALPHA to manipulate antiparticles, e^+ and $\bar{\text{p}}$, as well as electrons, is a *Penning trap*. This device holds *charged* particles in vacuum and constrains their motion by combining electric and magnetic fields. The main goal of the Penning trap is to separate antiparticles from ordinary matter, in order to avoid annihilation between the two. A less obvious goal is thermal isolation for achieving ultimate low temperatures that are well suited for production and trapping of $\bar{\text{H}}$.

A Penning trap is designed to confine the motion of charged particles in a crossed static electric field $\mathbf{E} = -\nabla\varphi$ and a solenoidal magnetic field $\mathbf{B} = (0, 0, B)$. The scalar potential φ displays an interesting form when it is rotationally sym-

metric around the z -axis, which gives the quadratic formula

$$\varphi(r, z) = \frac{V_0}{d^2} \left(z^2 - \frac{r^2}{2} \right), \quad (2.1)$$

where d is the trap dimension. The equipotential surfaces of φ are hyperboloids of revolution, therefore one can manufacture conducting surfaces, or *electrodes*, with these shapes, place them at distance d apart and apply between them the static voltage V_0 , creating an ideal Penning trap (see Fig. 2.2).

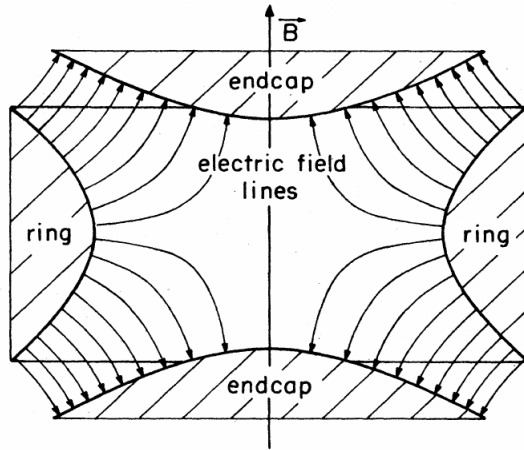


Figure 2.2: Sketch of the Penning trap electric and magnetic field lines. The “rings” and the “end-caps” are hyperboloid electrodes. Taken from [72].

It is worth noting at this point the use of Earnshaw’s theorem [73, 74]: it is not possible to create a minimum of the electrostatic potential in free space. This can be inferred from the difference in sign between r and z in Eq. (2.1), where φ has a minimum along one direction and a maximum along the other. In order to create a trap, a magnetic field \mathbf{B} must be added to confine the particle’s motion, in this case, in the x - y plane.

The equation of motion of a particle of charge q and mass m in the ideal Penning trap,

$$m\ddot{\mathbf{r}} = q(-\nabla\varphi + \dot{\mathbf{r}} \times \mathbf{B}), \quad (2.2)$$

where \mathbf{r} is the position of the particle, can be solved analytically. The motion in the z direction is determined by the electrostatic force, and is a simple harmonic oscillator with angular frequency

$$\omega_z = \sqrt{\frac{2qV_0}{md^2}}. \quad (2.3)$$

The motion in the x - y plane is characterized by the cyclotron frequency

$$\omega_c = \frac{|qB|}{m} \quad (2.4)$$

and is due to the confining magnetic force and the repulsive electrostatic one. The motion of a charged particle can be described as the superposition of three independent oscillations: the simple harmonic motion parallel to \mathbf{B} , with frequency ω_z given by Eq. (2.3), the cyclotron motion in the x - y plane, with modified cyclotron frequency given by

$$\omega'_c = \frac{1}{2}(\omega_c + \sqrt{\omega_c^2 - \omega_z^2}), \quad (2.5)$$

and the magnetron motion, with magnetron frequency given by

$$\omega_m = \frac{1}{2}(\omega_c - \sqrt{\omega_c^2 - \omega_z^2}), \quad (2.6)$$

due to the cross-product of the perpendicular \mathbf{E} and \mathbf{B} fields [75]. A schematic view of the orbits in this ideal configuration is shown in Fig. 2.3.

There exists a strict hierarchy among the frequencies [72], given by Eqs. (2.3), (2.5) and (2.6):

$$\omega'_c \gg \omega_z \gg \omega_m. \quad (2.7)$$

Since, from Eqs. (2.5) and (2.6), $\omega_c = \omega'_c + \omega_m$, Eq. (2.7) shows that the modified cyclotron frequency is approximately the same as the cyclotron frequency $\omega'_c \simeq \omega_c$.

The magnetron motion has a larger radius compared to the others and is much slower. Adding the axial oscillation to the magnetron motion produces

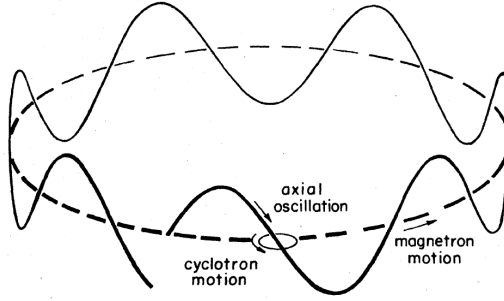


Figure 2.3: The solid lines offer a sketch of the orbit of a charged particle in an ideal Penning trap. Taken from [72].

the so-called *guiding-centre motion*, shown in Fig. 2.3 by the solid line. The complete description of the motion a charged particle in the ideal Penning trap is given by the rapid and small amplitude cyclotron motion around this moving guiding-centre.

One of the disadvantages of the hyperboloid electrodes is that they enclose the trapping region, hindering particles loading and monitoring. Whereas the electric potential of Eq. (2.1) allows analytical calculation, there is no other special advantage in that. The ALPHA traps replace the hyperboloid electrodes with cylindrical ones to form a *Penning-Malmberg trap*. This configuration is very versatile as many electrodes can be stacked together, forming a long trap that allows access for particles on both ends of the cylinder and the introduction of diagnostic instrumentation. A charged particles undergoes the same motion described previously, albeit with different frequencies.

2.2 The Catching Trap

Having outlined how a Penning trap works, it is easy to describe the ALPHA *catching trap* (CT), which is no more than a Penning trap (specifically a Penning-

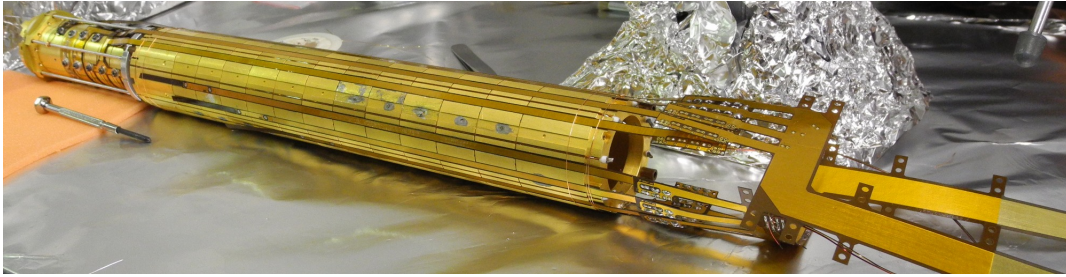


Figure 2.4: Electrodes assembly for ALPHA Atom Trap. The single cylindrical electrodes are clearly visible, along with the electrical connection providing the voltages.

Malmberg trap) designed to capture, cool and, eventually, accumulate, the \bar{p} delivered, every 100 s or so, by the *Antiproton Decelerator* (AD) with a momentum of 5.3 MeV/c. While a description of the AD operation is beyond the scope of the present work, it is interesting to list in Fig. 2.5 the process that the \bar{p} undergo before being sent to ALPHA. The AD provides about 3×10^7 \bar{p} to each experiment in bunches ~ 200 ns long.

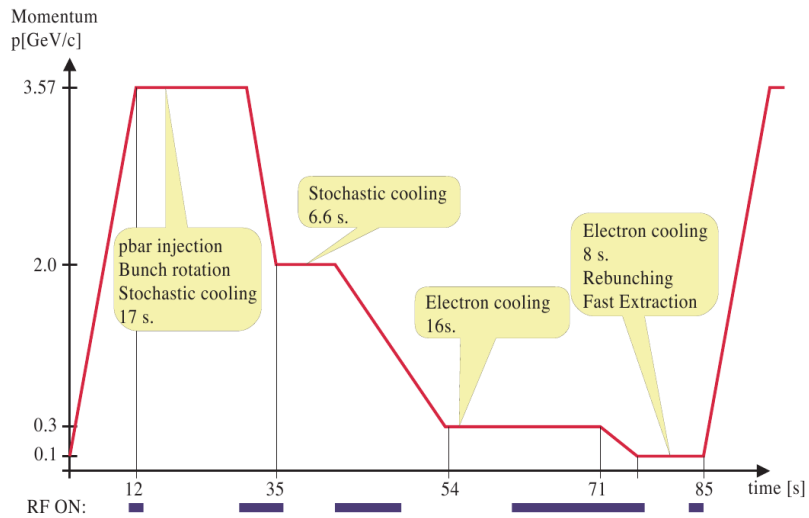


Figure 2.5: AD cycle. Taken from [61].

The description of a \bar{p} CT is given in [76], and the ALPHA CT shares many features of that original device. The magnet of the ALPHA CT is a small superconducting solenoid that can produce a magnetic field of strength up to 5 T. Nevertheless, the routine operations of the CT use $B = 3$ T. A view of the Penning trap electrodes is shown in Fig. 2.6, together with some other features of the CT, explained in the following. The CT environment is cooled to cryogenic temperatures using a helium gas compressor. The vacuum pumps can reduce the pressure to as low as 10^{-11} mbar. The CT can stack several \bar{p} bunches and can be operated independently of the rest of the ALPHA apparatus, acting as an \bar{p} accumulator.

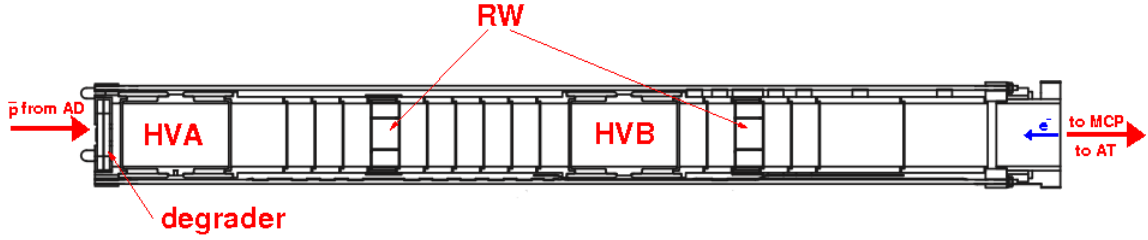


Figure 2.6: Drawing of the CT electrodes and a number of features described in the text.

The \bar{p} delivered by AD have too high an energy to allow the formation of \bar{H} , or to perform any manipulation at all. They are therefore further slowed down through a series of thin foils of different materials, called the *degrader*. The first of them is a “tunable degrader”, made of $26 \mu\text{m}$ of aluminum, whose thickness can be changed to yield the highest fraction of cold \bar{p} (see Fig. 2.7). The second foil made of $10 \mu\text{m}$ of aluminum serves as a “radiation shield” to block the thermal radiation coming, e.g., from the joint between the AD beam line and the ALPHA apparatus. The third foil is a “vacuum window” made of beryllium, $50 \mu\text{m}$ thick, that prevents vacuum contamination on either side, i.e., pressure increase in ALPHA with respect to the AD, or vice-versa. The last foil is used as

a “Faraday Cup”, and is made of 165 μm of beryllium. This foil is instrumented to give off a signal that is proportional to the charge collected on it. Since the charge of the \bar{p} is known, their number can be calculated.

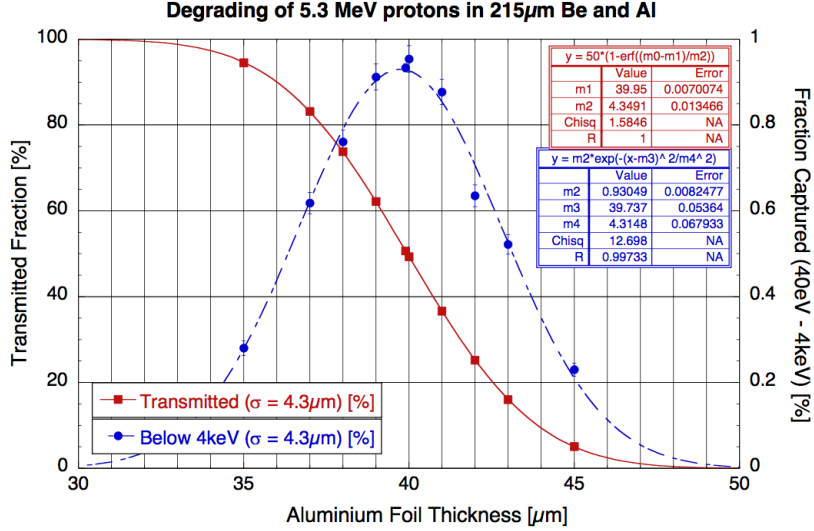


Figure 2.7: Measured \bar{p} catching efficiency as function of the aluminum degrader thickness (the beryllium thickness is fixed to 215 μm). The underlying assumption here is that the catching efficiency peaks around an optimal value of the aluminum degrader thickness, and decreases on both sides following a Gaussian distribution of $\sigma = 4.5 \mu\text{m}$.

When the \bar{p} annihilate on the degrader, according to the reaction

$$\bar{p} + N \rightarrow n'\pi^+ + n''\pi^- + m\pi^0, \quad (2.8)$$

where N is a nucleon, the π^\pm are detected by plastic scintillators placed in the vicinity of the CT. There are two pairs on both sides of the apparatus. The light is collected by four magnetically shielded photomultiplier tubes (PMTs), biased to give the optimal amplification of the electric signal. Each PMT signal is processed by a NIM standard discriminator, and each pair is put in coincidence,

“logical AND”, to reduce the electronic noise. The signal of the pair is further put in a “logical OR” coincidence, which is fed to a VME scaler module to record the counts (see Sec. 3.2). The efficiency of the “OR” is calculated with a Monte Carlo simulation, and it is estimated to be $\approx 20\%$, with a systematic error, of the order of 7%, due to the fact that their position is not fixed relative to the degrader. These detectors are extremely useful to measure the quality of the AD beam, as well as, the *electron cooling* efficiency.

Before the AD ejects the \bar{p} to the ALPHA CT, the region of the trap between the electrodes, labelled “HVA” and “HVB” in Fig. 2.6, is loaded with e^- . It is well-known that electrons in a magnetic field emit radiation, in this case *cyclotron radiation*, due to the fast motion in the x - y plane, described in the previous section. The time that this motion takes to reach thermal equilibrium with the environment is given by [72]

$$\tau = \frac{3\pi\epsilon_0 c^3 m^3}{e^4 B^2}, \quad (2.9)$$

where ϵ_0 is the vacuum permeability, c is the speed of light, m is the mass of the particle emitting cyclotron radiation and e is the elementary charge. In the $B = 3\text{ T}$ field of the CT, the e^- cool in $\lesssim 3\text{ s}$, whereas the \bar{p} in $\sim 1.8 \times 10^9\text{ s}$. Therefore, the \bar{p} are trapped together with the e^- , and are indirectly cooled through Coulomb collisions with them. The efficiency of the *electron cooling* depends on e^- density as well as the degree of overlap between the e^- plasma and the captured \bar{p} .

The role of the electrodes labelled HVA and HVB (high-voltage “A” and “B”) in Fig. 2.6 is very important in the context of \bar{p} catching. After the CT has been loaded with e^- , the HVB is biased at about 5 kV, that is the CT is “transparent” to \bar{p} with energy higher than 5 keV. A few hundred nanoseconds after the AD has ejected the beam, that is the \bar{p} bunch length, HVA is raised to 5 kV as well, allowing the \bar{p} to sympathetically cool with the e^- . After a variable time,

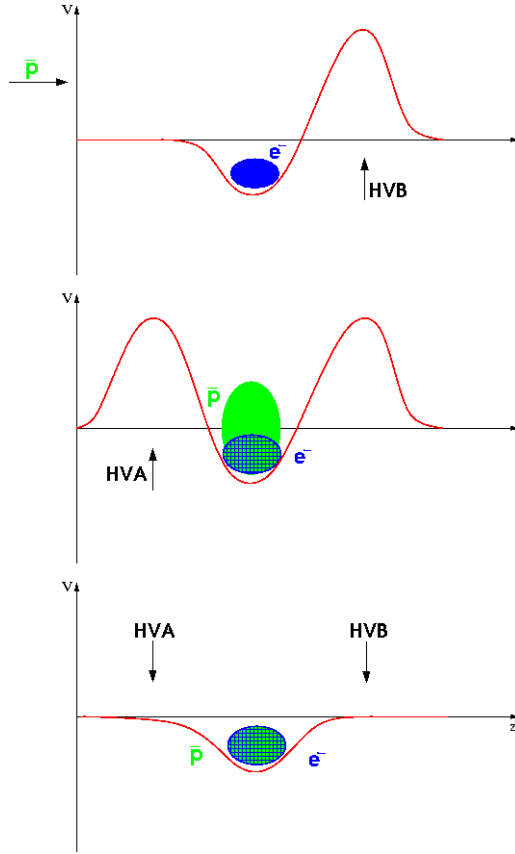


Figure 2.8: Schematic view of the potential wells to catch and cool the \bar{p} . The three phases correspond to (top) pre-loading the e^- and raising HVB, (middle) raising HVA and electron cooling of \bar{p} , and (top) lowering HVA and HVB to let the hot \bar{p} escape.

determined experimentally, of the order of several tens of seconds, the HVA and HVB are morphed to a shallower well, letting the \bar{p} that have not been cooled to escape and annihilate with the trap wall, the so-called “hot dump” (see Fig. 2.8). Once again the role of the scintillators is to monitor the number of \bar{p} and infer the cooling efficiency, knowing how many \bar{p} have been delivered by the AD.

Having a small size \bar{p} plasma eases the transfer to the Atom Trap (see Sec. 2.4). Therefore a technique called *rotating wall (RW)* is used to compress the \bar{p} . One

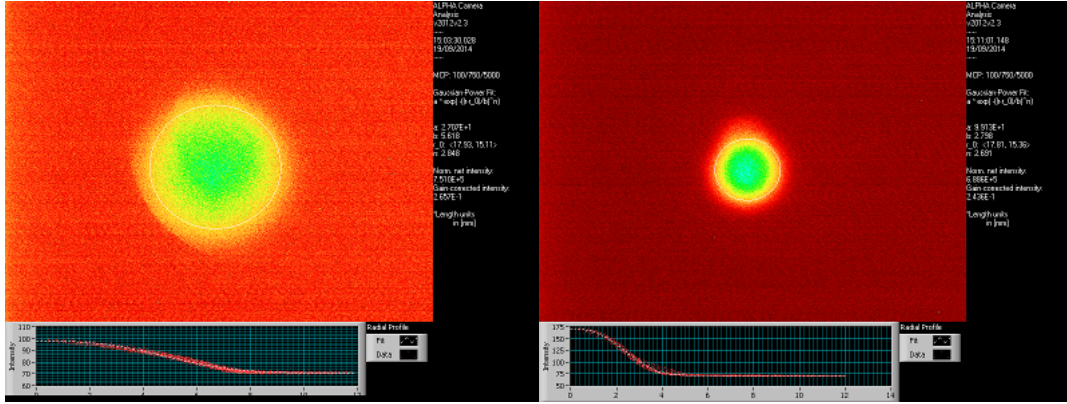


Figure 2.9: Left: MCP image of \bar{p} - e^- plasma after rotating wall, with voltage amplitude 1 V. Right: the voltage amplitude is increased to 4 V, showing more compression. The density is higher at the centre of the circle (green), and decreases gradually to zero (yellow to red). Also shown is the radial profile fitted to a bi-dimensional Gaussian function. What the MCP is actually showing is a planar projection of the \bar{p} - e^- cloud.

of the azimuthally segmented electrodes, labelled “RW” in Fig. 2.6, applies a sinusoidal voltage to the plasma, whence the waveform of each segment is phase shifted with respect to the adjacent one. This causes the plasma to change rotation rate (a torque is applied) and increase its density, by decreasing the radius [77]. The applied torque also introduces a large amount of heat that the e^- quickly lose by cyclotron radiation. Since pure \bar{p} plasmas do not shrink in size upon application of the rotating wall, possibly due to the small density, compression is achieved with the help of the e^- plasma, and the mixed plasma system is observed to equilibrate such that \bar{p} radial distribution follows that of the e^- . The latter also provides the necessary re-cooling.

While the e^- are necessary to cool and compress the \bar{p} , they might be detrimental for \bar{H} formation. Therefore the e^- are removed from the plasma before transfer by applying short pulses (e^- -kick), of the order of 100 ns, to an electrode

that constitutes one side of the potential well that confines the $e^- - \bar{p}$ plasma (see Fig. 2.8). The \bar{p} , by virtue of their higher mass, are only slightly perturbed by these pulses, while the e^- escape the confinement. To get rid of all the e^- , more than one pulse is required, whose amplitude is determined experimentally to produce \bar{p} as cold as possible. After each e^- -kick, the $e^- - \bar{p}$ plasma is compressed with RW, a technique that is called “Kick And Re-compress”, or KAR.

The scintillators are not the sole diagnostic device present in the ALPHA CT. A “vertical vacuum manipulator”, called the *CT stick*, is placed at the far end of the CT and it allows the alignment of different instruments with the electrode stack. The most relevant for the CT are a micro-channel plate (MCP) with a phosphor screen (see Fig. 2.9) for diagnostic purposes [78], an electron source filament, that provides e^- produced by thermionic emission, needed for \bar{p} cooling, and a “pass-through” cylinder to allow \bar{p} transfer to the Atom Trap.

2.3 Magnetic Trapping of Neutral Atoms

The potential energy of an \bar{H} atom in a magnetic field \mathbf{B} is

$$U = -\boldsymbol{\mu}_{\bar{H}} \cdot \mathbf{B}, \quad (2.10)$$

where $\boldsymbol{\mu}_{\bar{H}}$ is the atomic magnetic dipole moment. In an inhomogeneous magnetic field $\mathbf{B} = \mathbf{B}(x, y, z)$, it experiences the force

$$\mathbf{F}_M = -\nabla U = \nabla(\boldsymbol{\mu}_{\bar{H}} \cdot \mathbf{B}). \quad (2.11)$$

Eq. (2.11) can be naively interpreted as the need for a magnetic field maximum to generate a minimum in the potential, namely a *trap*. However Maxwell’s equations forbid local maxima [79] and magnetic trapping can only be achieved by constructing a magnetic field minimum. Eq. (2.11) also shows that the angle between the field and the dipole moment is crucial to the trapping force, hence the

orientation of the magnetic moment with respect to the field must be preserved as the atom moves in the trap [80]. This requires the magnetic moment to follow *adiabatically* the magnetic field direction, leaving the \bar{H} internal energy unchanged.

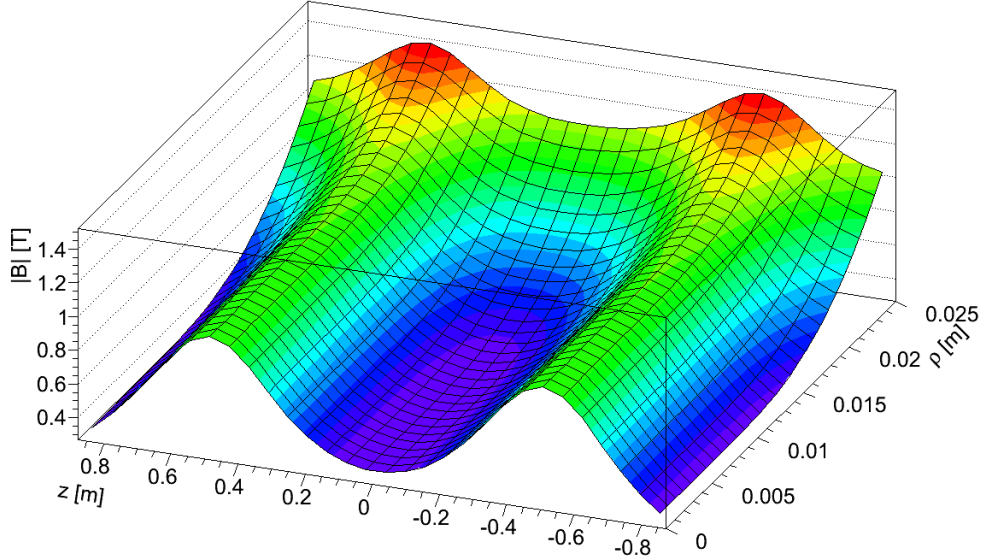


Figure 2.10: Envelope of a confining magnetic field for neutral particles (magnetic trap), with the features of the one used in ALPHA.

Since the magnetic moment does not depend *explicitly* on spatial coordinates (but only on internal quantum numbers), the argument of the gradient operator is

$$\boldsymbol{\mu}_{\bar{H}} \cdot \mathbf{B} = \mu_{\bar{H}} B \cos(\widehat{\boldsymbol{\mu}_{\bar{H}} \mathbf{B}}) = \tilde{\mu}_{\bar{H}} B, \quad (2.12)$$

where $\tilde{\mu}_{\bar{H}}$ refers to the projection of the \bar{H} magnetic moment onto the magnetic field direction and $B = B(x, y, z)$ is the magnitude of the magnetic field. Combining Eqs. (2.11) and (2.12) gives the following expression for the trapping force

[81]:

$$\mathbf{F}_M = \tilde{\mu}_{\bar{H}} \nabla B. \quad (2.13)$$

Force Eq. (2.13) can confine \bar{H} near the minimum of the potential Eq. (2.10), if $\boldsymbol{\mu}_{\bar{H}}$ points in the direction opposite to that of the magnetic field \mathbf{B} , namely if $\tilde{\mu}_{\bar{H}} < 0$. These (anti)atoms are called *low-field seekers*.

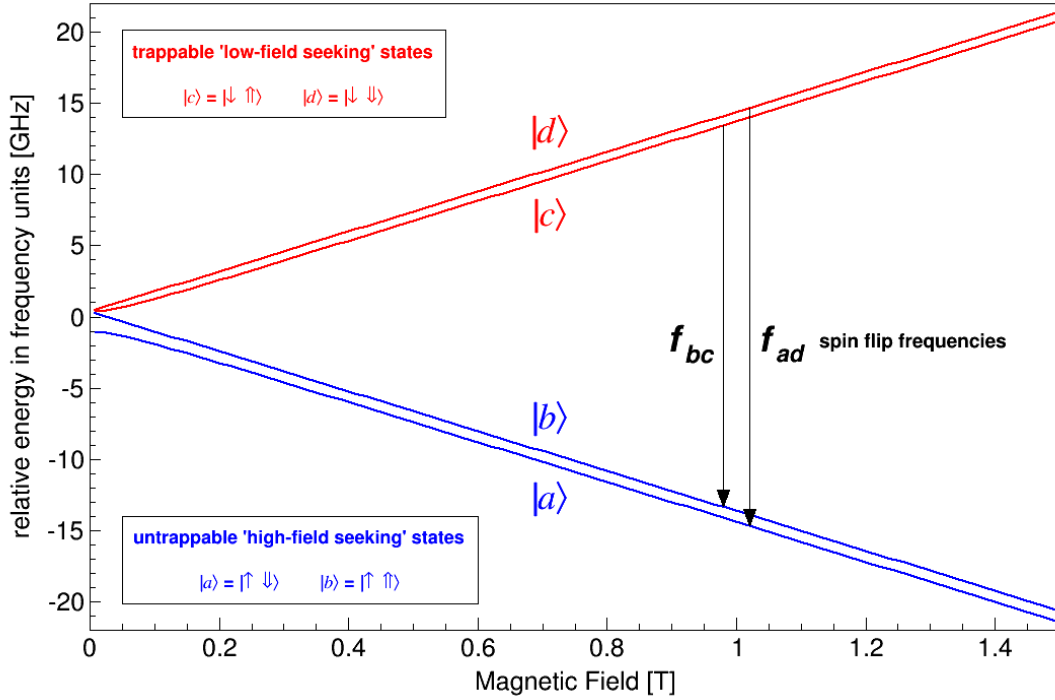


Figure 2.11: Breit-Rabi diagram for ground-state \bar{H} shows the magnetic field strength dependence of the hyperfine Zeeman sublevels. The insets show the spin assignments for the four states.

The magnetic dipole moment is given by

$$\boldsymbol{\mu}_{\bar{H}} = \mu_B (g_L \mathbf{L} + g_s \mathbf{S}) + \mu_N g_P \mathbf{I}, \quad (2.14)$$

where μ_B and μ_N are the Bohr and the nuclear magneton, respectively, $g_{L,s,P}$ are

the gyromagnetic ratios, and \mathbf{L} , \mathbf{S} and \mathbf{I} are the e^+ orbital angular momentum, e^+ spin and \bar{p} spin, respectively. It is worth commenting on the signs in Eq. (2.14) since it assumes that the e^+ magnetic moment and the spin are parallel, such that the $\bar{\text{H}}$ hyperfine states (see the inset in Fig. 2.11) have the correct energy shifts [82] as opposed to the magnetic quantum numbers of ordinary hydrogen [83]. In particular the state $|d\rangle$ can be defined as the one with the largest Zeeman shift: for H $|d\rangle = |F = 1; m_F = 1\rangle$ while for $\bar{\text{H}}$ $|d\rangle = |F = 1; m_F = -1\rangle$.

Since $\mu_N/\mu_B \approx 5 \times 10^{-4}$, $L = 0$ for the $\bar{\text{H}}$ ground-state, and $g_s \simeq 2$, Eq. (2.14) simplifies to

$$\tilde{\mu}_{\bar{\text{H}}} = \pm \mu_B, \quad (2.15)$$

where the projections $\pm \frac{1}{2}$ of \mathbf{S} onto \mathbf{B} are taken into account. The magnitude of magnetic moment of $\bar{\text{H}}$ is therefore $\mu_B \approx 5.788 \times 10^{-11} \text{ MeV T}^{-1}$. The positive sign indicates non-trappable high-field seekers, while the negative sign corresponds to the trappable low-field seekers (see Fig. 2.11).

In regions of the trap where B is small (or zero), the separation between the trappable and non-trappable state is small, hence there is considerable probability that $\bar{\text{H}}$ undergoes a *Majorana transition* (or spin-flip) and is ejected from the trap [84]. Such a situation can occur when $\bar{\text{H}}$ passes too fast into these critical regions and its magnetic moment cannot adiabatically follow the rapidly changing magnetic field direction, resulting in a change of the mutual orientation of the atom magnetic moment and the magnetic field. In order to assure that the interaction between $\bar{\text{H}}$ and the magnetic field is adiabatic, the following condition must be met

$$\frac{d\theta}{dt} \ll \omega_L, \quad (2.16)$$

where $\theta = \widehat{\boldsymbol{\mu}_{\bar{\text{H}}}\mathbf{B}}$ and $\omega_L = \mu B/\hbar$ is the Larmor frequency. The dynamics of a

magnetic dipole in a magnetic field is given by the torque equation

$$\boldsymbol{\tau} = \boldsymbol{\mu}_{\bar{H}} \times \mathbf{B}, \quad (2.17)$$

hence the spin evolution is governed by (see Eq. B.4 in App. B)

$$\frac{d\mathbf{S}}{dt} = \boldsymbol{\tau}. \quad (2.18)$$

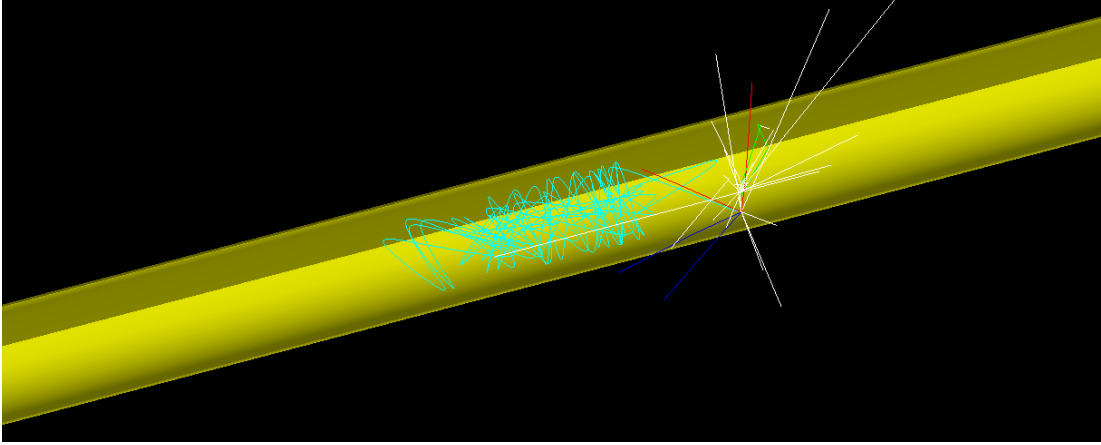


Figure 2.12: Simulated trajectory of \bar{H} in the magnetic field of Fig. 2.10 (light blue line). This is an example of low-field seeker, since it is trapped as long as the magnetic field is on. The coloured lines at the end of the trajectory are the annihilation products. The yellow tube represents the electrodes stack.

The ALPHA “neutral atom trap”, or “minimum-B trap” is designed to circumvent the issue of the Majorana transition, with the introduction of a magnetic field offset, i.e., $|\mathbf{B}| \neq 0$, given by the solenoidal magnetic field for charged particle confinement. The axial confinement is created with two cylindrical coils, on either side of the trapping region. The radial confinement is due to a multipole field, that, in general, is weaker than the axial one. Such a magnetic trap arrangement is called an *Ioffe-Pritchard trap* [85].

Magnetic trapping is effective for *cold* $\bar{\text{H}}$ only, since the typical depth of such a trap is of the order of

$$\frac{\mu_B}{k_B} \approx 0.67 \frac{\text{K}}{\text{T}}. \quad (2.19)$$

In ALPHA, the radial trap depth is

$$\sqrt{B_w^2 + B_z^2} - B_z \approx 0.8 \text{ T}, \quad (2.20)$$

where B_w is the magnetic field strength at the electrodes radius and $B_z = 1 \text{ T}$ is the solenoidal field for charged particle confinement. Hence, from Eqs. (2.19) and (2.20), only $\bar{\text{H}}$ with kinetic energy $\lesssim 0.56 \text{ K}$, or $\lesssim 0.05 \text{ meV}$, can be trapped.

2.4 The Atom Trap

The Atom Trap, or AT, labelled as “mixing trap” in Fig. 2.1, is actually composed of two adjacent Penning traps, sharing the same magnetic field, in ultra-high vacuum conditions at cryogenic temperatures. The solenoidal magnetic field for charged particle confinement is generated by a large superconducting solenoid, manufactured by Oxford Instruments, that produces a highly uniform 1 T field.

The first Penning trap is the so-called “re-catching trap”, or RCT, where the $\bar{\text{p}}$ are re-cooled and re-compressed after the transfer from the CT. The second trap is the actual mixing trap where the $\bar{\text{p}}$ recombine with the e^+ to form $\bar{\text{H}}$. The electrodes in the mixing region are heavily filtered to avoid introducing electronic noise, that produces undesirable heat. Such electrodes are located around the minimum of the magnetic field gradient generated by the superposition of a set of superconducting magnets, as shown in Fig. 2.13. The *mirror coils* provide the axial confinement by locally increasing the solenoidal magnetic field, while an *octupole* winding generates the radial gradient of magnetic field. The choice of the octupole magnet, as opposed to a simpler quadrupolar arrangement, as was

the case for the original Ioffe-Pritchard trap, is dictated by its properties near the Penning trap axis, where the octupolar field perturbs less the confinement of charged particles [86].

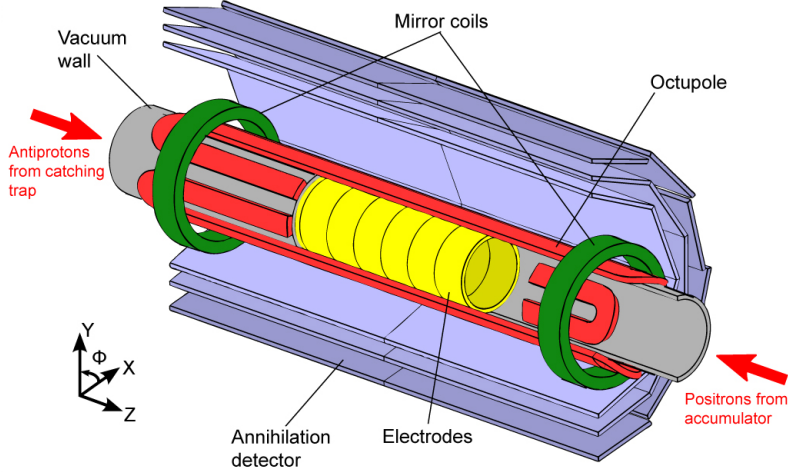


Figure 2.13: Schematic view of the central part of ALPHA-1. ALPHA-2 differs in the number of mirror coils. Taken from [69].

The AT is endowed with a similar “stick” as the CT, with an electron source filament, MCP and pass-thru cylinder to allow the passage of the e^+ . During the transfer of the \bar{p} from the CT to the RCT heating and expansion of the plasma inevitably occurs, therefore, additional electron cooling is required. Since the \bar{H} production rate increases with the density of its constituents [87], the RW technique is used once again to obtain a denser \bar{p} cloud, which, as discussed in Sec. 2.2, needs the presence of e^- . An additional motivation to compress the \bar{p} cloud is the presence of the octupole field, which perturbs the symmetry of the Penning trap, causing \bar{p} radial loss [88]. Since the octupole influence falls quickly near the trap axis, a smaller \bar{p} plasma reduces the chance to lose particles [89]. Finally, one has to also consider that an \bar{H} formed near the trap axis is closer to the minimum of the magnetic field, increasing its probability to be confined. The

e^- are removed again, following the KAR technique described in Sec. 2.2.

In order to achieve the lowest temperature, the \bar{p} are further cooled by means of a technique, well known in “ultra-cold matter physics”: *evaporative cooling*, or EVC. The voltage on one side of the \bar{p} confining well is linearly decreased in time, causing the hottest ones to escape the trap. The \bar{p} left in the well rearrange their energy, producing a plasma with lower temperature. Typical \bar{p} temperatures before evaporative cooling is of order 200 K, while after cooling it can be as low as ~ 10 K [90]. The \bar{p} manipulation are monitored at every stage by two pairs of scintillator detectors, identical to the ones used in the CT.

The other ingredient to produce \bar{H} is a cold e^+ plasma [91]. The e^+ in ALPHA are produced by a ^{22}Na radioactive source, which is β^+ emitter. The energy of the β^+ decay particles is, of course, too high for manipulation and \bar{H} production. The device used to cool and store the e^+ is a *Surko-type accumulator* (see Fig. 2.14). The e^+ emitted by the radioactive source have an energy of the order of ~ 1 MeV, which is decreased to ~ 1 eV, upon re-emission from a thin layer of material, called the *moderator*, made of solid neon at 7 K. After moderation, the e^+ are transferred to a Penning-Malmberg trap, where their energy is further reduced by inelastic collisions with nitrogen gas molecules [92]. Prior to the final transfer to the AT, the nitrogen gas is pumped out until the pressure is sufficiently low to avoid contamination of the ultra-high vacuum in the mixing region. The ALPHA e^+ accumulator delivers about 8×10^7 e^+ every 200 s.

The chance to produce \bar{H} depends crucially on the e^+ plasma temperature [93]. Evaporative cooling is used on the e^+ , once they are in the mixing trap. The e^+ are then held in a well at the centre of the mixing region, as shown in Fig. 2.15, and the \bar{p} in an adjacent well. The \bar{p} are injected, or mixed, into the e^+ plasma by means of the *autoresonance* technique [94], which has the advantage, over other mixing schemes, to impart as little as possible longitudinal kinetic

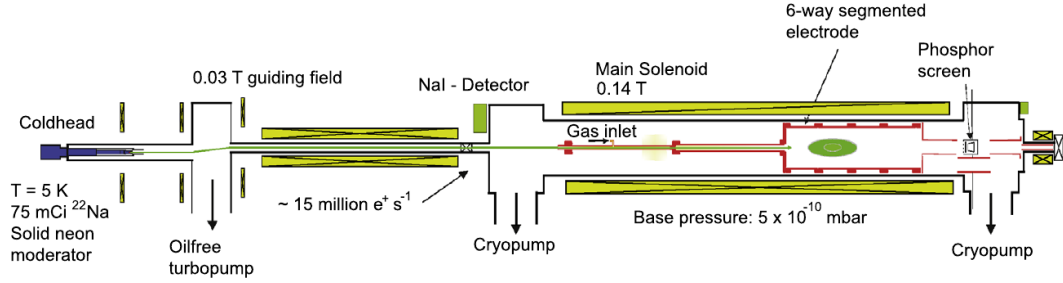


Figure 2.14: Schematic view of the ALPHA e^+ accumulator. Taken from [69].

energy, with small changes in the transverse one [95].

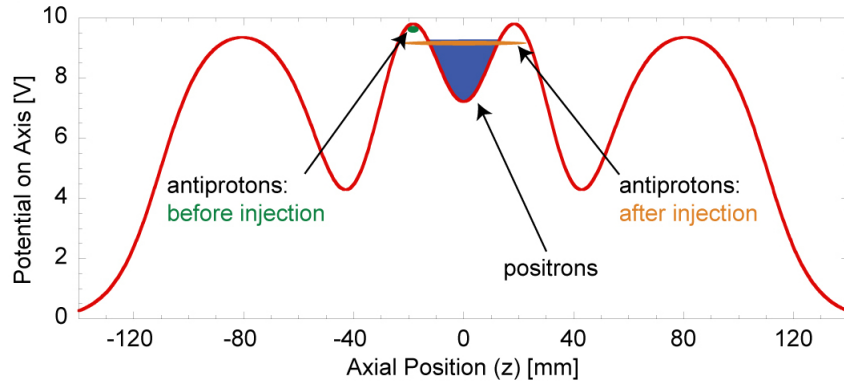
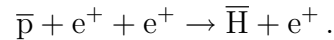


Figure 2.15: On-axis potential during mixing. Taken from [69].

Once the \bar{p} are mixed with the e^+ plasma, they quickly equilibrate with it [96], and they can recombine to form \bar{H} atoms. Most of the newly formed antiatoms are weakly bound and therefore ionize immediately, or have a too high kinetic energy to be trapped. Moreover, trapping \bar{H} requires that the octupole magnet and the mirror coils are energized during the mixing procedure, which might cause \bar{p} losses [97]. The most likely process that leads to \bar{H} is the *three-body recombination* [98]



The octupole is wound around a support that is mounted on the ultra-high

vacuum chamber, where the antiparticles are stored and \bar{H} is produced. The five mirror coils in ALPHA-2 (two in ALPHA-1) are wound around the octupole support, as shown in Fig. 2.16. Together, the windings are immersed in a liquid helium bath at 4 K, which keeps the magnets in the superconducting state, but also maintains a temperature between 6 and 10 K in the mixing region. The design of the “minimum-B trap” is detailed in [99].

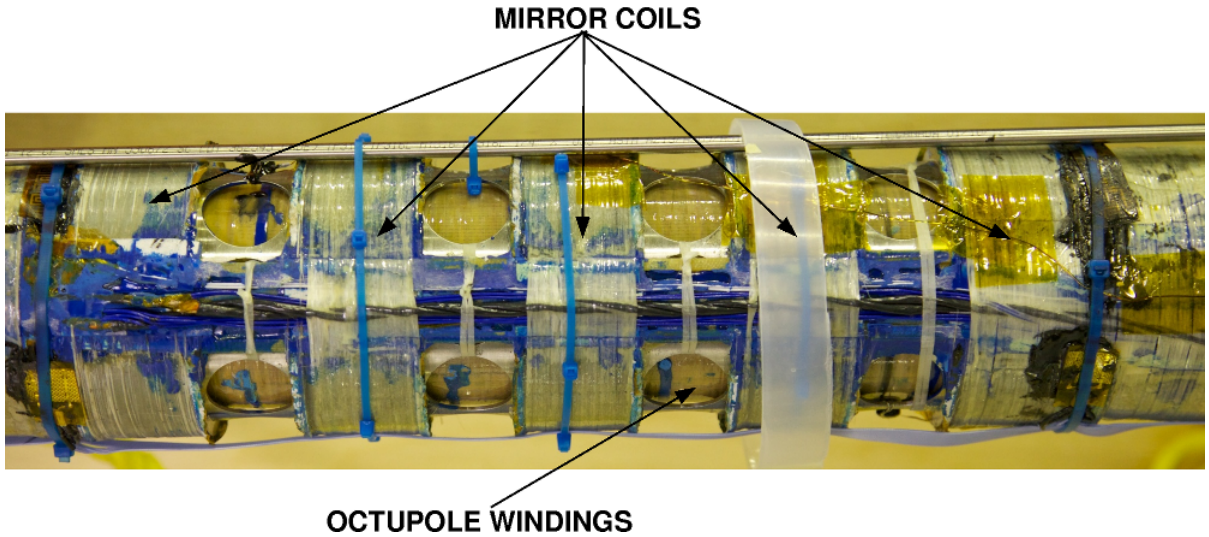


Figure 2.16: Superconducting magnets moments before being installed in the ALPHA cryostat. These magnets are manufactured by Brookhaven National Laboratory, on a support that is mounted on the ultra-high vacuum chamber, where \bar{H} is produced.

After the mixing, which usually lasts ~ 1 s, the antiparticles that have not recombined are removed from the trap. First, the e^+ are dumped towards the “AT stick”, where their temperature is measured. Afterwards, a series of strong “clearing” electric pulses is used to eject the \bar{p} .

When the magnetic trap is turned off, \bar{H} escapes radially and undergoes the

annihilation process

$$\bar{\text{H}} + A \rightarrow n_+ \pi^+ + n_- \pi^- + m \pi^0 + 2\gamma, \quad (2.21)$$

where A is an atom of the electrodes stack (the “trap wall”), the π^\pm and π^0 are produced in the $\bar{\text{p}}$ annihilation, n_+ , n_- and m are their multiplicities, and the γ are due to the e^+ annihilation. It is worth noting that Eq. (2.4) is not the only $\bar{\text{p}}$ annihilation mode, but it is definitely the most probable [100].

In order to release the trapped $\bar{\text{H}}$ [70] as quickly as possible the superconducting magnets are *quenched*. This process requires the transition to the normal conducting state and is accompanied by the release of a large amount of energy. This potentially dangerous situation is overcome by a specially designed circuit, called the *quench protection system*, that is water-cooled.

The device used to detect the π^\pm of Eq. (2.21) is a position-sensitive silicon detector and is described at length in Sec. 3.1. The methodology employed to determine the $\bar{\text{H}}$ annihilation position from the reconstruction of the π^\pm trajectories is detailed in Sec. 4.2 and 4.3.

$\bar{\text{H}}$ annihilation is indistinguishable from a “bare” $\bar{\text{p}}$ annihilation. The latter might be due to “mirror-trapped” $\bar{\text{p}}$ [101] that are released at the same time as the true $\bar{\text{H}}$, representing a serious source of irreducible background in the silicon detector. Fortunately, it is possible to let such $\bar{\text{p}}$ annihilate in a specific region of the apparatus by using electric fields. Such a *quench with power*, or QWP, is useful not only to distinguish the $\bar{\text{p}}$ annihilation, but it plays a central role in the first high precision measurement on $\bar{\text{H}}$ ever performed, and is described in Sec. 5.1 and following.

The other source of background in the silicon detector is cosmic rays, and the analysis of this issue is discussed at length in Sec. 6.2.

The time between the $\bar{\text{H}}$ formation and the magnet shutdown can be prolonged as desired [102]. During this time spectroscopy can be performed. ALPHA-2

is endowed with an ultra-violet laser enhancement cavity to perform *two photon spectroscopy* of the 1S-2S transition, like with ordinary hydrogen [53]. The ALPHA-2 apparatus has also a dedicated access for a *Lyman- α* laser to measure the 1S-2P transition line [103], and to apply a laser cooling method to $\bar{\text{H}}$ [104]. In addition to laser spectroscopy, high precision measurement of the hyperfine transition, from “low-field seeker” to “high-field seeker”, the so-called e^+ *spin flip* (see Fig. 2.11), is made possible by the direct injection of microwaves into the $\bar{\text{H}}$ trap, through a series of waveguides connected to a powerful radio-frequency amplifier.

2.5 Outline of an Experiment

The operation of the ALPHA apparatus is coordinated by the *sequencer*, a system of digital inputs and outputs controlled by a Field Programmable Gate Array (FPGA) controller. The sequencer is organized into three independent controllers, one for the CT, one for the re-catching trap (RCT) and one for the AT and the e^+ accumulator (ATM).

Each experiment is performed by loading in the sequencer the appropriate list of time-ordered operations that are prepared with the aid of a custom graphical user interface (GUI). The most typical of such operations is the application of voltages to the electrodes of the Penning traps. Each operation is represented as a change of state of the sequencer and is signalled to the equipment by digital triggers. Since the synchronization among the different controllers, with the AD and with external devices, is essential to successfully perform an experiment, the sequencer can be programmed to “wait” an indefinitely long time to receive a trigger to perform an operation.

The operations, arranged by the controller, of a typical experiment in ALPHA

is shown in Tab. 2.1, with a rough timing of the main events.

CT	RCT	ATM
Load e^- Catch \bar{p} from AD Cool \bar{p} for ~ 80 s Hot dump RW and e^- -kick for ~ 55 s Transfer \bar{p} to RCT	Load e^- Re-catch \bar{p} from CT Cool \bar{p} for ~ 30 s Hot dump RW and e^- -kick for ~ 70 s Transfer \bar{p} to ATM	Load e^+ from accumulator Cool e^+ for ~ 30 s RW e^+ for ~ 60 s \bar{p} EVC Neutral atom trap ON e^+ EVC Mixing 1 s e^+ dump \bar{p} clearing pulses <i>Hold \bar{H} for Physics</i> Prepare QWP Quench

Table 2.1: Outline of an experiment. The abbreviations are explained in the text.

3 The Silicon Vertex Detector

The detection of \bar{H} in ALPHA is accomplished through a technology commonly used in High-Energy Physics experiments. The device used in ALPHA is a Silicon Vertex Detector, or SVD. It allows one to reconstruct the trajectories, or *tracks*, of the \bar{H} annihilation products, mainly π^\pm . Nevertheless, the analysis software (described in Sec. 4.3) allows one to reconstruct the \bar{H} annihilation point, called the *vertex*.

The SVD is a powerful imaging device in the sense that it provides a “photograph” of the instant when the \bar{H} annihilation occurred. This information is essential as a diagnostic tool in the development of the techniques to produce and confine \bar{H} (see Sec. 2.5). It is also informative on the \bar{H} dynamics in the trap while it is confined [105]. Above all, the SVD is employed as measurement tool in the spectroscopy experiments [71], in the gravity tests [106] and in the charge (neutrality) determination [107]. Central to its capability of performing meaningful physics measurements is its background rejection power (see Sec. 6.2). The main source of background events, as opposed to signal events due to \bar{H} annihilation, are cosmic rays, typically muons, μ^\pm , which are byproducts of high energy collisions in the upper atmosphere.

The design characteristics and the assembly features are described in Sec. 3.1. The SVD read-out and its electronics are reviewed in Sec. 3.2.

3.1 Design and Features

The ALPHA-1 SVD is composed of 60 modules, called *hybrids*, since each one is made of two silicon sensors (see Fig. 3.1). The hybrids are arranged symmetrically in three layers, in two opposite halves, centred around the “neutral atom trap”. The inner layer consists of 8 hybrids, the middle layer of 10 and the outer layer of 12, as shown in Fig. 3.2. The SVD is spatially constrained by the beam pipe (outer diameter of 14 cm), where the neutral atom trap is inserted, and the external solenoid magnet (inner diameter of 26 cm), which is part of the charged particle trap.

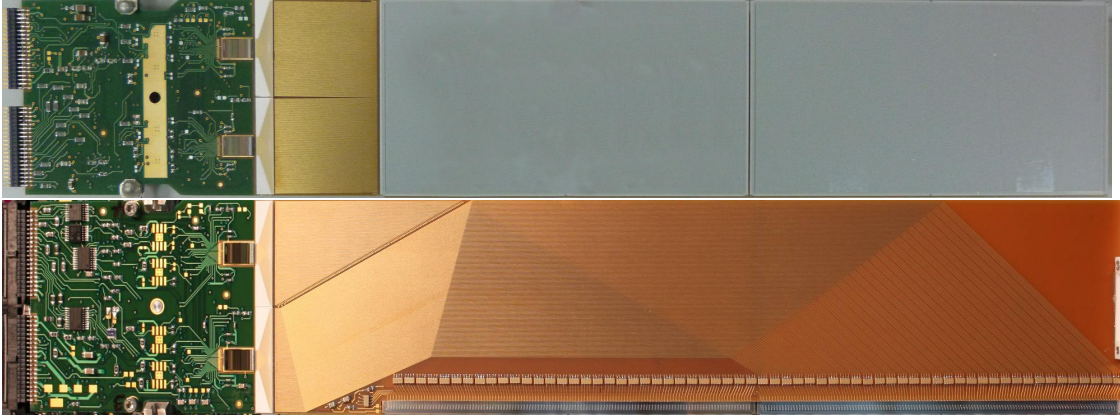


Figure 3.1: ALPHA SVD hybrid. Front view (top): the silicon sensors are connected to the ASICs (Application Specific Integrated Circuits) through bond wires, which are the path of the p-strips signals (see text). Rear view (bottom): n-strips connected to the ASICs. In both views the PCB (Printed Circuit Board) and the four VA1TA ASICs mounted on it are clearly visible. Credits: JTMK.

For the ALPHA-2 SVD the number of hybrids was increased to 72. The inner layer consists of 10 hybrids, the middle layer of 12 and the outer layer of 14. Each layer is staggered, as shown in Fig. 3.2, improving the solid angle coverage with respect to the ALPHA-1 design [108]. The SVD in ALPHA-2 had to meet new

spatial requirements, with the outer diameter of the beam pipe at 16 cm, and the inner diameter of the bore of the external solenoid at 35 cm (see Sec. 2.4).

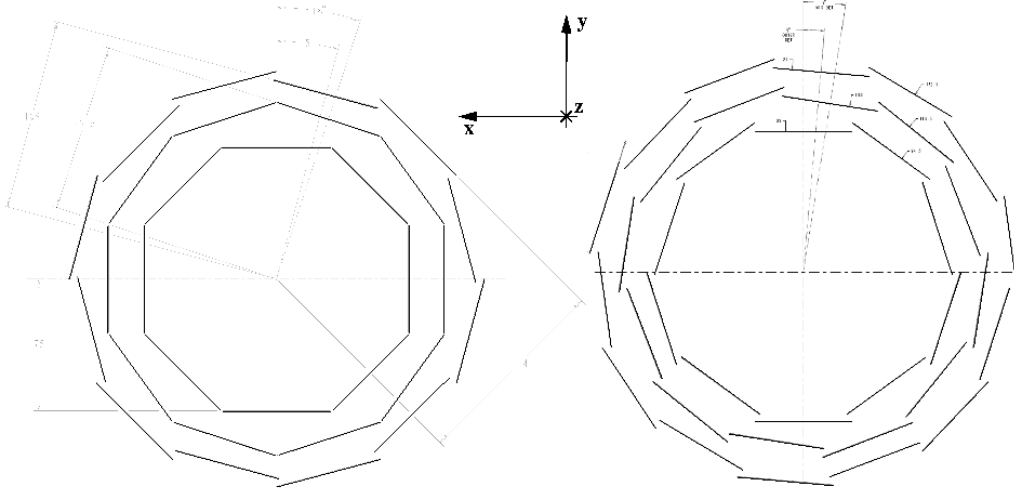


Figure 3.2: Drawings (end-view) provided by the Liverpool Semiconductor Detector Centre of the ALPHA-1 (left) and the ALPHA-2 (right) SVDs.

The detector is operated at atmospheric pressure in a dry and cooled environment. The cooling is provided by two Vortex Tubes [109] supplied with filtered, dry air, pressurized at about 4 bar. The SVD produces about 50 W when powered, but the cooling system allows one to run it continuously at about 14° C and relative humidity around 12%.

The SVD support structure is designed to minimize the amount of necessary scattering material, since the π^\pm are already travelling through the cryostat before impinging on the hybrids. The structure is made of aluminum alloy and the inner drum, onto which the hybrids support is mounted, is machined down to 0.4 mm thickness. In addition to the support structure, the only other passive components between the SVD layers are the 1.6 mm thick printed circuit boards, or PCBs, onto which the silicon sensors are fixed.

Each silicon sensor is a *double-sided microstrip* detector, where the p-strips

Layer	ALPHA-1 radius [cm]	ALPHA-2 radius [cm]
Inner	7.50	8.90
		9.45
Middle	9.55	10.80
		11.35
Outer	10.80	12.70
	11.40	13.25

Table 3.1: SVD layer radii.

run parallel to the length of the module and the n-strips are orthogonal to them, as shown in Fig. 3.3. The sensors are built from $300\ \mu\text{m}$ thick³ “6 inch wafers” and the strips are composed of p+ and n+ implants on the two sides of the n-bulk [110]. The electrons drift to the n+ doped strips and the charges collected are then induced by AC coupling, using an external 1 nF capacitor, to the charge preamplifier of the Application Specific Integrated Circuit (ASIC), through thin copper wires and microvias. The p+ doped strips are instead DC coupled to the ASIC’s charge preamplifiers.

The hybrids were assembled at the Liverpool Semiconductor Centre, where the silicon sensors were mounted on the PCBs, bonded together (along the p-strips) and to the ASICs. Each hybrid required 1144 ultrasonic wire bonds. Moreover, each one of them was visual inspected and individually electrically tested to ensure strict high quality.

The p-strips are routed through the shortest path possible to the ASIC’s charge preamplifiers. The n-strips are routed on the back of the hybrid, as shown in the bottom diagram of Fig. 3.3, causing higher noise levels on this side.

Each sensor has 128 n-strips and 256 p-strips for a total active area of $5.8 \times 11.2\text{cm}^2$. Each hybrid has four ASICs connected to 128 strips each. ASIC 1 and 2 handle the 256 n-strips, while ASIC 3 and 4 the 256 p-strips. An hybrid

³A Minimum Ionizing Particle (MIP) generates 24 000 electron-hole pairs in $300\ \mu\text{m}$ silicon.

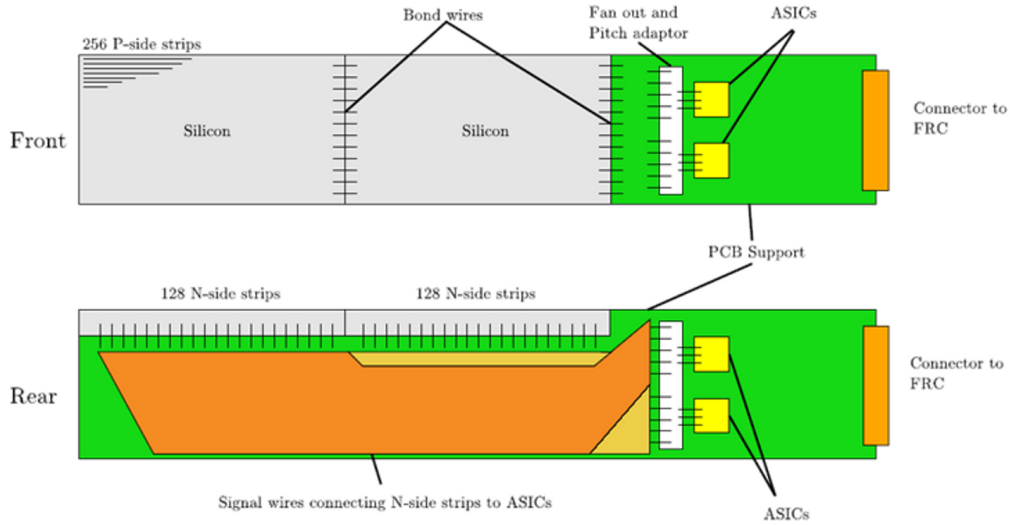


Figure 3.3: Schematic view of a hybrid.

has a total of 512 channels. Therefore the whole SVD in ALPHA-2 has 36 864 channels.

The strip pitch, that is, the distance between adjacent strip centres, is a very important parameter in the design of the microstrip sensor. In order to avoid under-specification or over-specification of the pitch, Monte Carlo simulations were employed. The n-strip pitch is $875 \mu\text{m}$ whereas the p-strip one is $227 \mu\text{m}$. The decisive factor in the simulation (and in the final choice) is the amount of scattering material that the π^\pm have to travel through before reaching the SVD.

The signal to noise ratio for the two sides of the silicon is typically 15 and 33 on the n and p sides, respectively, [111].

3.2 Data Acquisition System

The ASICs mounted on the hybrids are *VA1TA* readout chips [112] and they are made of two parts. The TA part provides the trigger signal, while the VA part takes care of the analog readout. A schematic view of one channel of the chip

is shown in Fig. 3.4, where the two parts have different colours. As mentioned in the previous section, each chip handles 128 strips and there is one common preamplifier to both parts. The parameters of the VA1TA chip can be controlled through a 680 bit long shift register.

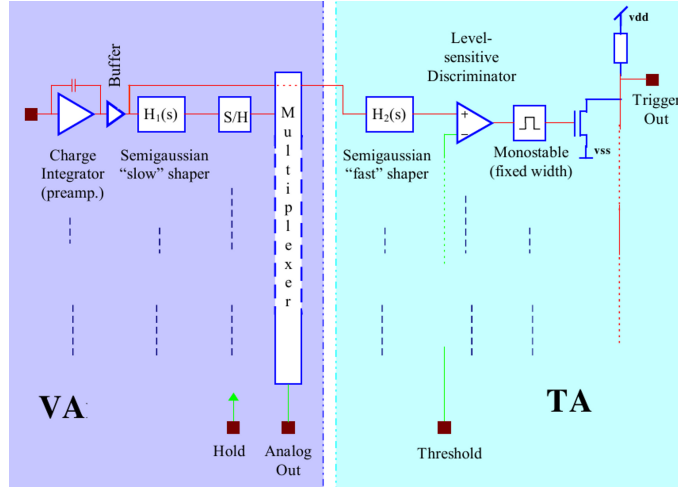


Figure 3.4: Schematic of one of the 128 channels of a VA1TA chip [112]. For a description of the various components, see the text.

Each ASIC produces one trigger signal and one analog output, that is, each hybrid has a total of eight outputs. In order to do so, the 128 digital signals from the TA part are logically put in coincidence (logical OR), forming the so-called *TA signal*. The signals of the VA part are multiplexed, where the analog output of the strips is sampled and held until it is read out, producing the so-called *VA signal*.

The fast pulse shaper of the TA part has a time constant of ≈ 75 ns and, when the pulse height exceeds a predefined threshold (the *TA threshold*) on the level-discriminator, a monostable oscillator is engaged, giving a fixed-width trigger pulse. ASICs 3 and 4 are the only ones used for the trigger signals, since the p-side has a better noise performance. The triggering is organized per layer and the

trigger signals are fed into two *Timing and Trigger Control*, or TTC, units [113]. The TTCs are special-purpose VME modules, based on Field Programmable Gate Array (FPGA), that are programmed to compute the TA signals multiplicity per layer and to supervise the readout of the VA signals. The control bits register of the VA1TA chips are also provided by the TTC modules.

The TTC communicates with SVD hybrids via the *Front-end Repeater Cards*, or FRCs. The FRCs take care of powering the ASICs and of the communications between the VA1TA chips and the rest of the data acquisition system (DAQ). The 20 FRCs are placed near to SVD and are connected to the hybrids with two “ribbon cables”, one cable for the TA signals and the other for the VA signals. Up to four hybrids can be connected to a single FRC.

The slow pulse shaper of the VA part has a time constant of $\approx 1 \mu\text{s}$ and it is followed by the “sample and hold” component of the VA circuit that keeps the signal multiplexed, until the full detector readout is triggered. The 288 VA signals, after amplification through the FRCs, are then read out in parallel into eight *VF48* digitizers [114]. Each VF48 is a 10-bit analog-to-digital converter (ADC) VME module with 48 channels. The TTCs provide the hold signal and the multiplexer clock to the ASICs and the sampling clock to the VF48s.

A trigger configuration routinely used in experiments with the ALPHA-2 apparatus is the so-called “2-1-1”, where each number indicates the multiplicity per layer, starting from the innermost one. While events of this type are good candidates to trigger the readout of the analog levels of the strips, the digitization might take longer than the time between successive triggerable events. This situation is common during the “mixing phase” of the experiment (see Sec. 2.5). In order to avoid disturbing the digitization in progress, the multiplicity trigger is combined with a *busy* signal broadcasted by the VF48s, when they are processing a triggered event, to the IO32 [115]. The IO32 is a general-purpose VME

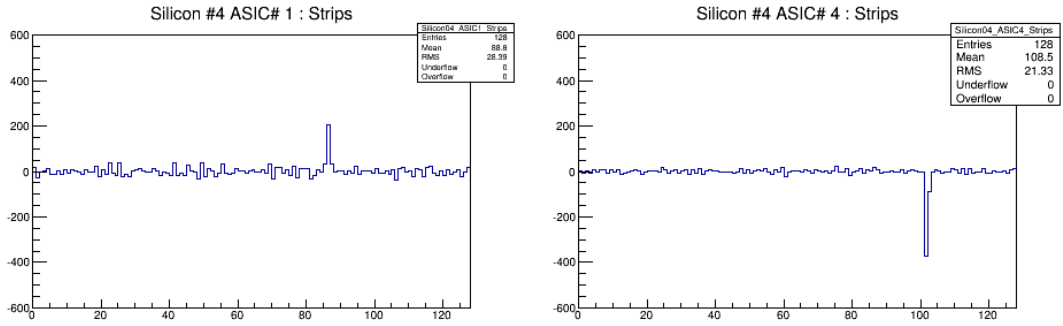


Figure 3.5: Analog readout of ASIC 1 (n-strips) and ASIC 4 (p-strips) of hybrid 4 during a run. The horizontal axis represents the strip number (from 0 to 127), while the vertical one is the ADC value. The spikes indicate that a group of strips have been hit by a charged particle.

FPGA board that receives as inputs the multiplicity triggers from the TTCs and the busy signals from the VF48s and takes the final decision whether to trigger the full readout of the VA signals. This *readout trigger*, or RO trigger, is then fed back into the TTCs that, as mentioned several times, supervise the analog readout of the strips by sending the hold signals to the VA1TA chips. The IO32 board also provides a common reference clock for the TTCs and VF48s.

The control and the communication among the VME modules is taken by a GE Fanuc V7805 VME controller [116], which is a single-board processor unit where the data acquisition frontend program runs and is connected through Gigabit Ethernet to the ALPHA Linux cluster for storage and processing. The VME controller starts and stops the data acquisition, reads out and records the digitized data, the trigger information and counts of the multi-channel scaler SIS3820⁴. The SVD readout system is part of the MIDAS [118] data acquisition

⁴The two “SIS modules” [117], named after the manufacturer, have 32 inputs each and provide accurate timing, through a 10 MHz atomic clock signal from CERN. Whenever a sequence is running (see Sec. 2.5), any change of state in the sequencer is recorded in the SIS by incrementing the counts in a specific channel. The SVD triggers and the scintillators counts

system, which is also the system used to acquire data from other instrumentation in the ALPHA experiment.

While, in principle, the maximum readout rate is limited by the multiplexer clock, with little overhead from the communications, the bottle neck of the DAQ is the speed to which the data can be transferred and written to the MIDAS shared-memory buffer. This limitation currently set the maximum readout rate to ~ 500 Hz.

are recorded, too. By aligning the timestamps of the counts due to the instrumentation with the ones given by the atomic clock, accurate timing of all the interesting events in the ALPHA apparatus is accomplished.

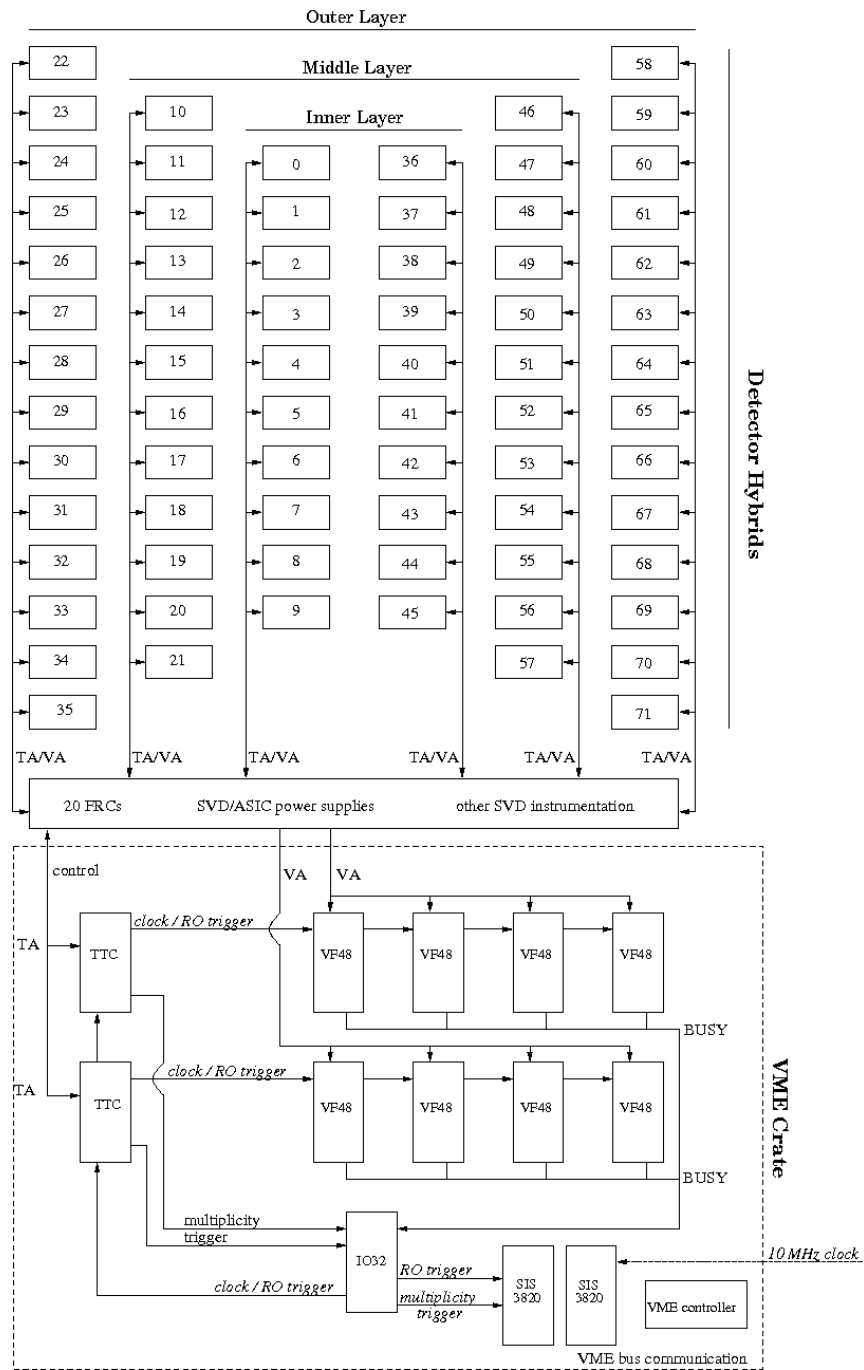


Figure 3.6: Schematic overview of the DAQ. While all the relevant connections are shown, this diagram is a simplified version of the system. For an explanation of the modules and the connections, see the text.

4 Simulation and Reconstruction Software

The reconstruction procedure aims to determine as accurately as possible the location (called the *vertex*) of the \bar{H} annihilation. The goal of the Monte Carlo simulation, or MC, of the SVD is to establish the vertex reconstruction efficiency and resolution, as well as to develop, test and improve the reconstruction software itself.

Both the MC simulation and the reconstruction software are based on ROOT [119]. At the end of this chapter the vertexing efficiency and resolution will be given as an overall performance parametrization of the reconstruction for the ALPHA SVD.

4.1 Virtual Monte Carlo and Geant3

The *Virtual Monte Carlo* [120], or VMC, package in ROOT offers the opportunity to choose among three “transport engines”: Geant3 [121], Geant4 [122, 123] and Fluka. The VMC acts as an interface to the *concrete Monte Carlo* instance. For historical reasons, the choice of the concrete Monte Carlo instance is Geant3.

The main class that manages the simulation is `TAlphaMCApplication`. It takes care of initializing the geometric model, instantiating the primary particle generator and retrieving information from the particles stepping through the materials. Also, it creates the output ROOT file, containing several `TTree` objects where the relevant features of the simulated events are stored, such as the position of the generated \bar{H} annihilation and the strips *hit* in the SVD by the annihilation

products.

The simulation is run via a ROOT macro that at run-time loads the relevant libraries and selects the transport engines and other user-defined settings, such as the number of events to be generated.

For clarity’s sake, the coordinate system used has its origin at the centre of the SVD which, in principle, should coincide with the centre of the neutral atom trap. The z axis coincides with the central axis of the trap and its direction is the one of \bar{p} as they are extracted from the AD, i.e., the CT lies at negative z , while the e^+ accumulator is at positive z . By assuming that the vertical axis is y pointing up, towards the ceiling, the right-hand rule pinpoints the x axis. As mentioned in Sec. 3.1, the SVD is organized into two opposite halves, for which a simple naming scheme is in place: the one that lies at negative z is called the “upstream end” and the one at positive z is called the “downstream end”.

4.1.1 Geometric Model

The definition of the volumes in the simulation of the ALPHA apparatus is performed by the `TAlphaDetectorConstruction` class, which parses three XML files. XML is *mark-up language*, like HTML; in this case the tags define the geometric properties of a solid, such as the size and the rotation with respect to a coordinate system, and the physical properties of such a volume, like density and radiation length. The detector and the cryostat geometry are coded in different files.

Both the ALPHA-1 and ALPHA-2 geometries are implemented, where the most relevant features of the cryostat, the Penning trap and the neutral atom trap are faithfully represented. Fig. 4.1 shows some views of the ALPHA-2 apparatus.

The VMC allows one to define complicated magnetic fields by using “maps”, i.e., a file that contains the value of the magnetic field \mathbf{B} at every point (x, y, z)

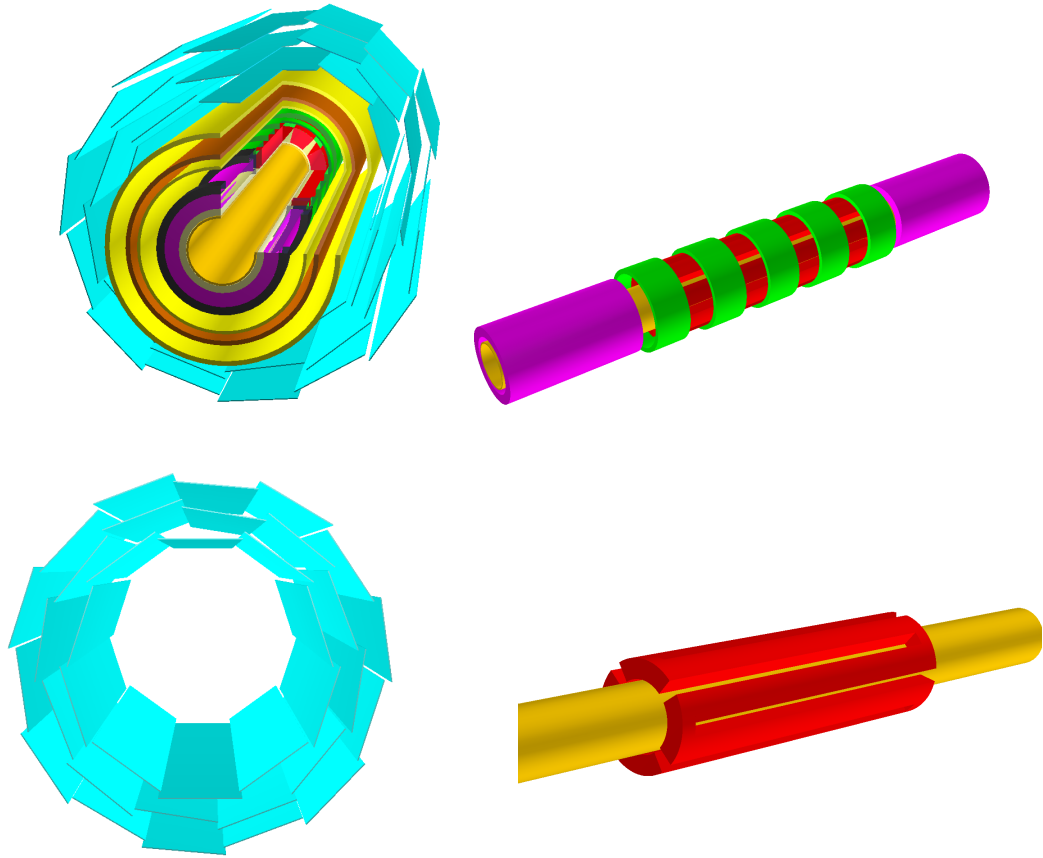


Figure 4.1: Three views of the simulated ALPHA apparatus where all relevant components (described in Sec. 2.4) are shown. The SVD hybrids are represented as cyan boxes. These images are generated through the OpenGL interface of ROOT. In the top left corner, the cut view of the apparatus shows the stacking of the various chambers and magnets. The top right corner shows the main part of the apparatus, namely the superconducting magnets that form the neutral trap (mirror coils in green and octupole in red), the capture solenoids (pink) and the electrodes in yellow. The bottom left picture shows the SVD and the arrangement of the hybrids. The bottom right picture gives emphasis to the octupole structure (red) and its “winding” around the electrodes (yellow).

along a predefined grid. The map is read at run-time and the value of \mathbf{B} is used to compute the trajectory of the particles.

4.1.2 Primary Generator

An $\bar{\text{H}}$ annihilation event is simulated by directly creating the annihilation products on the electrodes, since they are the innermost volume in the apparatus. The underlying physical reaction that is parameterized in `TAlphaPrimaryGenerator` is



where p is a proton of the electrodes, which are gold-plated. The values of n and m , as well as their probabilities, are taken from [100] and shown in Fig. 4.2.

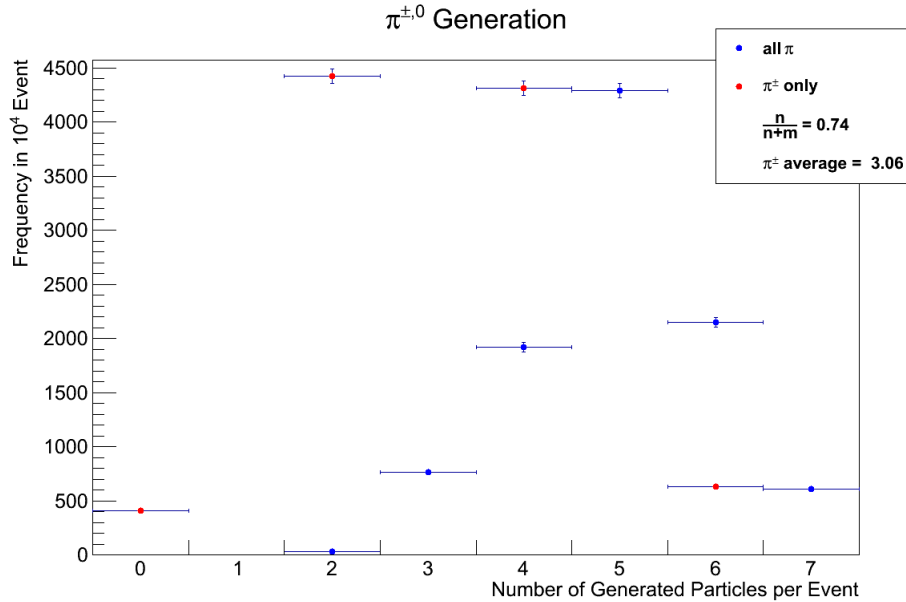


Figure 4.2: Distribution of primary π^{\pm} and π^0 . n and m are defined in Eq. (4.1).

This generator assumes that $\bar{\text{H}}$ annihilation occurs at rest, hence the total available energy to the π^{\pm} and π^0 mesons is twice the rest mass of the p , or

≈ 1.9 GeV. The momenta distributions of the annihilation products are determined by the `TGenPhaseSpace` class [124], provided by ROOT.

When the vacuum condition of the experiment are good, the \bar{H} annihilation takes place on the inner surface of the gold-plated electrodes, symmetrically in the azimuthal coordinate and limited in z by the axial extension of the neutral trap. Therefore, for the MC purpose, the π^\pm and π^0 mesons are uniformly generated on a circle of radius $R_w = 2.2275$ cm, the inner radius of the electrode. The z position is instead picked randomly from a Gaussian distribution, in order to simulate the shape and extension of the plasma. The triplet

$$\begin{aligned}x_{\text{MC}} &= R_w \cos \xi \\y_{\text{MC}} &= R_w \sin \xi \\z_{\text{MC}} &= \zeta,\end{aligned}$$

where ξ is distributed uniformly in $(0, 2\pi]$ and ζ is distributed as Gaussian centred around $z = 0$ and with standard deviation 2.5 cm, is called the *MC vertex*.

4.1.3 Simulation Output

The most important method of `TAlphaMCApplication` is the `Stepping` method, which creates a `TAlphaMCDigi` instantiation for each particle interaction with the detector. Such interactions are converted, or *digitized*, in the information of which strip is hit in each ASIC (see Sec. 3.1) in each detector module; this is the output of the Monte Carlo simulation. The reconstruction software starts from the knowledge of the strips hits in each detector hybrid module.

The flavour and the charge of the particles produced by Geant3 are shown in Fig. 4.3, together with their frequencies with respect to the number of π^+ mesons.

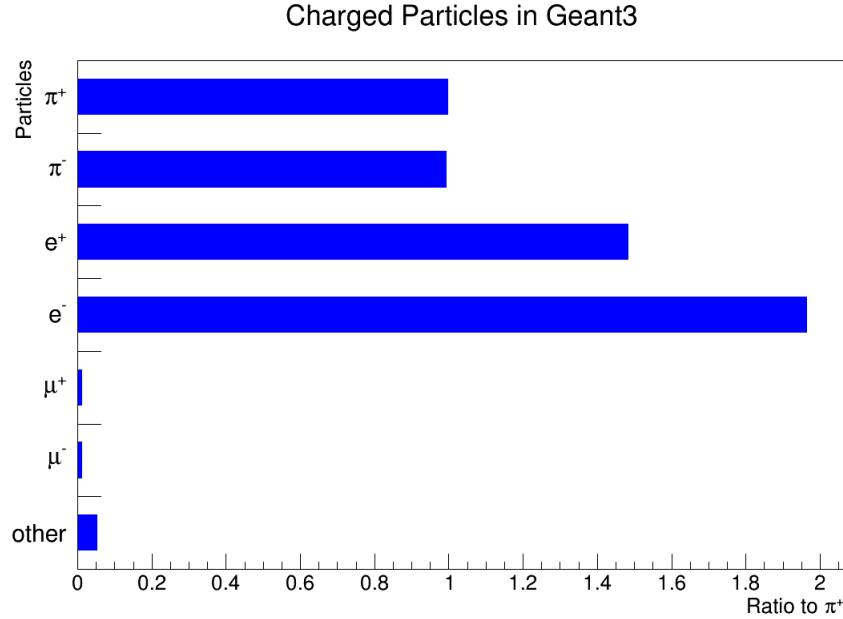


Figure 4.3: Monte Carlo distribution of charged particles produced by Geant3. Each bin content is normalized to the number of π^+ mesons. The μ^\pm are the decay products of π^\pm mesons. The e^\pm are likely the result of pair-production of the two photons generated in the π^0 meson decay, whose lifetime is of the order of 10^{-17} s.

4.2 Tracking

The fundamental class of the ALPHA reconstruction software is `TAlphaEvent`. The main method of this class is `RecEvent`, which performs sequentially all the operations needed to reconstruct the vertex from the strips hit per hybrid of the SVD.

The first operation is to *cluster* adjacent strips, which amounts to calculating a weighted average of the strips that fired, where the weight is given by the charge collected (or ADC value, see Sec. 3.2) in that channel. Since the n-strips provide the z and the p-strips the y coordinates (in the local reference of the hybrid)

of the point where the radiation impinges on the SVD, the n- and p-clusters, built of the respective types of strips, provide more accurate positions of z and y , respectively.

A SVD hit is represented by a `TAlphaEventHit` and is defined by the intersection of a n-cluster with a p-cluster. In this way, the position of the hit is known in the local reference frame of the hybrid and a trivial rotation returns it in the global reference frame of the SVD. The error on the hit position is calculated from a uniform distribution over the strip pitch:

$$\sigma_n^2 = \frac{\text{pitch}^2}{12} = 6.38 \times 10^{-4} \text{ cm}^2$$

$$\sigma_p^2 = \frac{\text{pitch}^2}{12} = 4.29 \times 10^{-5} \text{ cm}^2.$$

Since π^\pm mesons are associated with the $\bar{\text{H}}$ annihilation, the following studies focus on the recognition and on the reconstruction of the tracks that are most likely due to those particles.

4.2.1 Pattern Recognition

The cluster and hit reconstruction is performed by `TAlphaEventSil` class. The `GatherHits` method of `TAlphaEvent` loops over all the constructed `TAlphaEventSil` objects to create an array of hits that are processed to build tracks. A track is represented by a `TAlphaEventTrack` and is defined by *three hits, one per layer* of the SVD. The selection of the three hits, or *pattern recognition*, is based on a series of cuts on discriminating variables, calculated for all the possible combinations of three hits belonging to different layers. The cardinality C of all the possible combinations is

$$C = \prod_{i=1}^3 N_i,$$

where N_i is the number of hits in the layer, indicated by $i = 1, 2, 3$ for “inner”, “middle” and “outer”. The following discriminating variables are employed:

- separation in ϕ : $|\phi_1 - \phi_2| + |\phi_2 - \phi_3|$,
- displacement along z : $|z_1 - z_2|$ and $|z_2 - z_3|$,
- correlation (see description below).

Here the subscript 1, 2, 3 indicates again the layer. The cuts are placed by using the Monte Carlo simulation to study the underlying distribution of the variables for π^\pm mesons, that are known to be produced by the \bar{H} annihilation. Such distributions are shown in Figs. 4.4, 4.5.

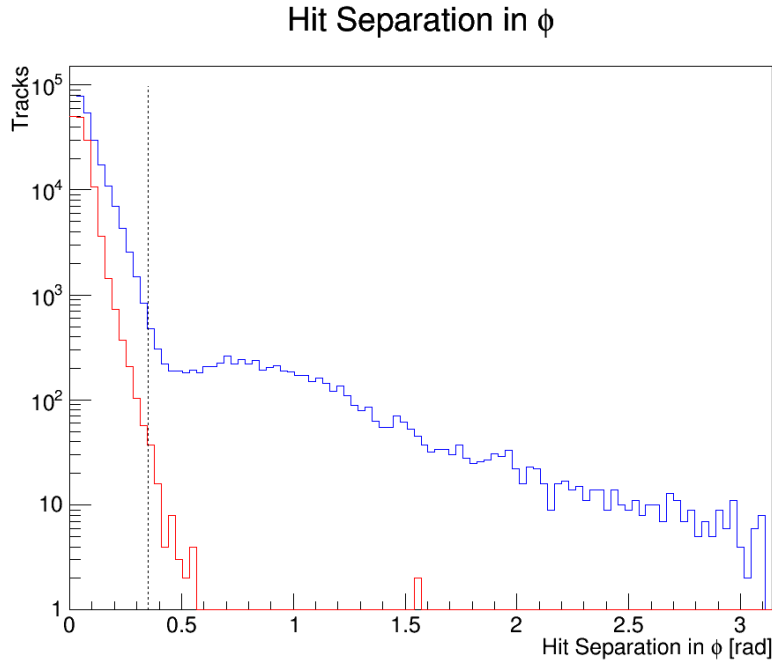


Figure 4.4: Distribution of the hit separation in ϕ . Blue: all MC tracks. Red: π^\pm MC tracks. The dashed line represents the cut.

After careful analysis of these distribution, the cuts that accept the largest number of tracks due to π^\pm mesons are:

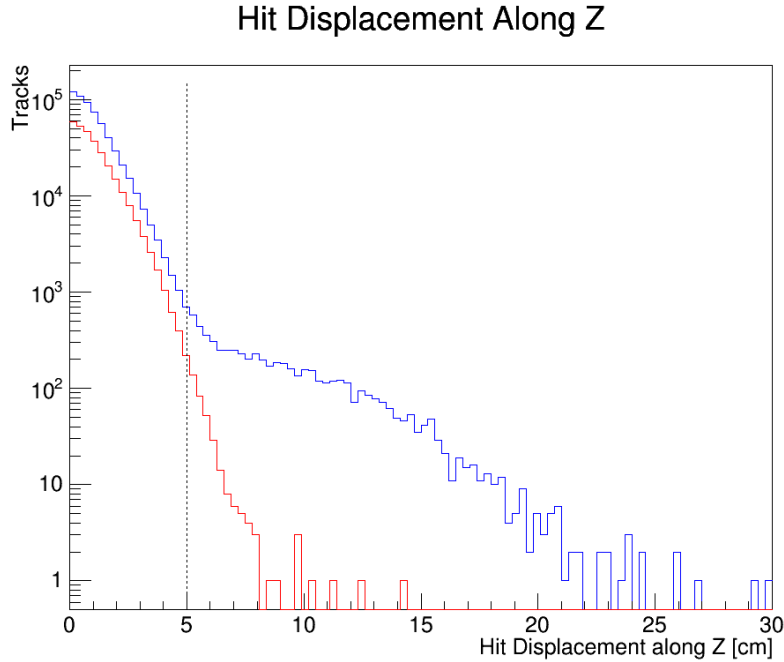


Figure 4.5: Distribution of the hit displacement along z . Blue: all MC tracks. Red: π^\pm MC tracks. The dashed line represents the cut.

- separation in $\phi < 0.35 \text{ rad} \approx 20^\circ$,
- displacement along $z < 5 \text{ cm}$.

Groups of hits selected in this way are examined using the Principal Component Analysis (PCA) [125]. This procedure reduces the dimensionality of the problem at hand by finding the appropriate rotation in the pattern space, such that the eigenvectors, corresponding to the largest eigenvalues of the covariance matrix of the measurements, represent the most significant features of the problem. In the present case, the parameter space is constituted by the three Cartesian coordinates of the three hits. By limiting the analysis to the largest eigenvalues, and their associated eigenvectors, the error due to this reduction in dimensionality is minimized.

This pattern recognition task has dimensionality of three, therefore there are only three eigenvalues. The largest of them, which is ≤ 1 since the covariance matrix is normalized, is used as *position correlation coefficient* and ensures that noise and *ghost hits*⁵ are eliminated. The distribution of the correlation coefficients is again plotted for π^\pm tracks and all the tracks, as shown in Fig. 4.6.

Only hits that are highly correlated in space are retained. The optimal cut on the correlation is found by examining Fig. 4.6

- correlation > 0.95 .

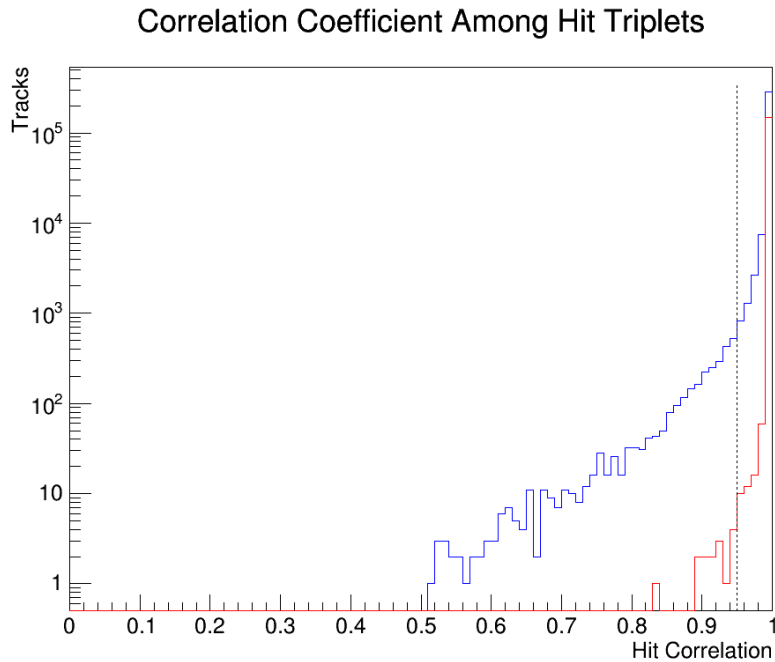


Figure 4.6: Distribution of correlation coefficient among hits. Blue: all MC tracks. Red: π^\pm MC tracks. The dashed line represents the cut.

The combinations of hits satisfying all these criteria are called track candidates. There are more track candidates than the actual number of charged

⁵Ghost hits occur when a single hybrid has more than one cluster on either its p-side or n-side. Their intersections result in four hits, only two of which are real.

particle tracks, since the former can share hits. This issue is resolved once the groups of hits are modelled with an *helix*, as described in the next section.

4.2.2 Track Reconstruction

Since the manipulation of \bar{p} and e^+ requires the presence of a solenoidal magnetic field (see Sec. 2.2), the mathematical description of the path of a track candidate is an *helix*, where the energy losses are neglected. For each `TAlphaEventTrack` candidate a `TAlphaEventHelix` is built in the `RecTrackCandidates` method of `TAlphaEvent`.

The canonical helix description consists of five parameters $(R_c, D, \phi_0, z_0, \lambda)$, where R_c is the radius of curvature, D is the signed distance of closest approach to the axis, ϕ_0 is the azimuthal angle at the point of closest approach to the axis, z_0 is the z coordinate of the distance of closest approach of the track to the axis and $\lambda = \cot \theta$, θ being the polar angle measured from the positive z axis.

The helix formula Eq. (A.1), given in App. A, can be split into the radial and axial parts. The former is governed by $\mathbf{v} \times \mathbf{B}$ and the latter is unaffected by the magnetic field.

The radial part is determined by using only the $x - y$ information of the hits. Since in this projection the particle follows a circular trajectory in the $x - y$ plane and the SVD is limited to three layers (hence three points), the radial parameters of the helix (R_c, D, ϕ_0) can be calculated exactly by using simple linear algebra.

The axial part undergoes a fitting procedure using the χ^2 method. Eq. (A.5) is minimized with the `TMinuit` fitter in `ROOT`.

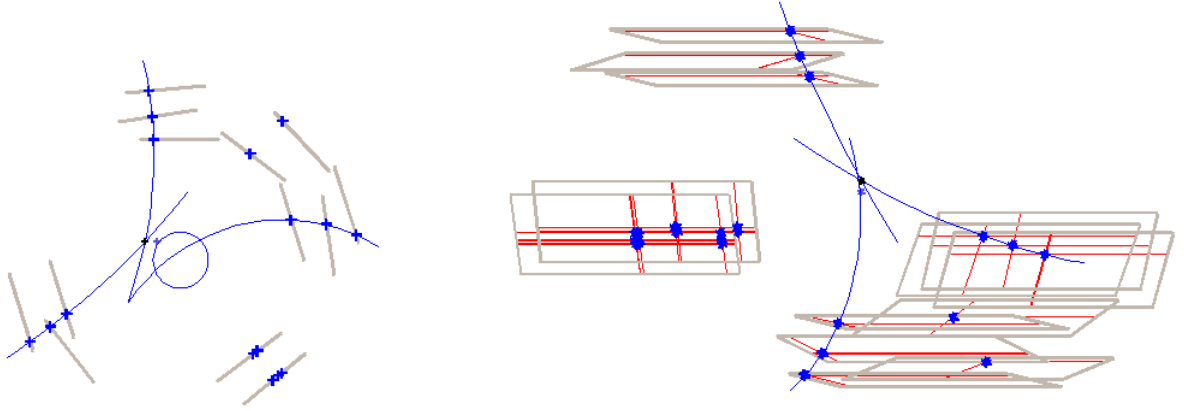


Figure 4.7: Reconstruction of a (Monte Carlo) event. Left: Front view of the reconstructed event. Right: Side view of the same event. The grey boxes represent the hybrids with hits (see Sec. 3.1). Hits are identified by blue crosses. The red lines depict the strips that gave a signal. The blue lines are the reconstructed helices (see Sec. 4.2.2 and Sec. 4.2.3). The black is the reconstructed vertex (see Sec. 4.3). The light blue cross is the position of the MC vertex (see Sec. 4.1.2).

4.2.3 Track Pruning

Not all the reconstructed helices are physical tracks resulting from the \bar{H} annihilation (e.g. e^-e^+ pairs created by high energy photons from the π^0 meson decay). Indeed, only the helices that originate close to the ultra-high vacuum space (the trap region) are likely due to π^\pm and carry the most information about the \bar{H} annihilation point. Moreover, only those tracks with $\chi^2 < \chi_{\max}^2$ are kept since they give the best fit, by definition, to the helix model. For the rest of the present discussion, the χ^2 refers necessarily to the axial fit, since the radial projection of the helix is known analytically. The method `PruneTracks` of `TAlphaEvent` is tasked with eliminating such unwanted tracks, in addition to removing the ones that are duplicated, i.e., are built from the same hits.

The limits on the χ^2 and the distance of closest approach to the trap, or DCA,

$D_w = D - R_w$, where $R_w = 2.2275$ cm is the trap radius, are once again tuned with the help of the MC. Fig. 4.8 shows the distribution of χ^2 for π^\pm and for the all the reconstructed tracks and Fig. 4.9 the one of D_w .

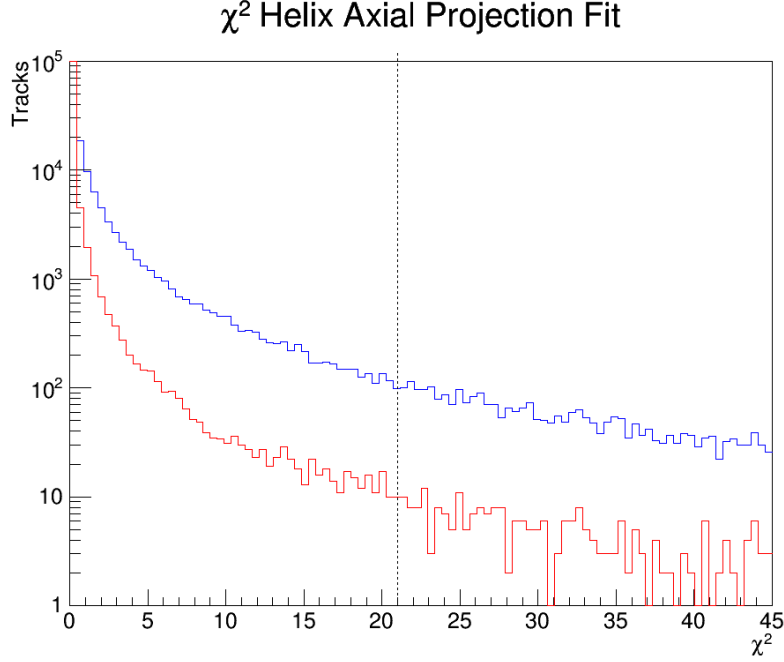


Figure 4.8: Distribution of χ^2 of the helix axial fit. Blue: all MC tracks. Red: π^\pm MC tracks. The dashed line represents the cut.

The helices are selected based on the χ^2 and the DCA as follows:

- $\chi^2 < 21$,
- $D_w < 7$ cm.

As mentioned in the previous section, there are helices that share one or more hits. When two helices are found to share a hit, the one with the largest radius of curvature R_c (the “stiffest”) is kept.

In addition to reconstructed helices sharing some hits, there are cases when a pair of helices shares the same silicon hybrid and have the same radius of curva-

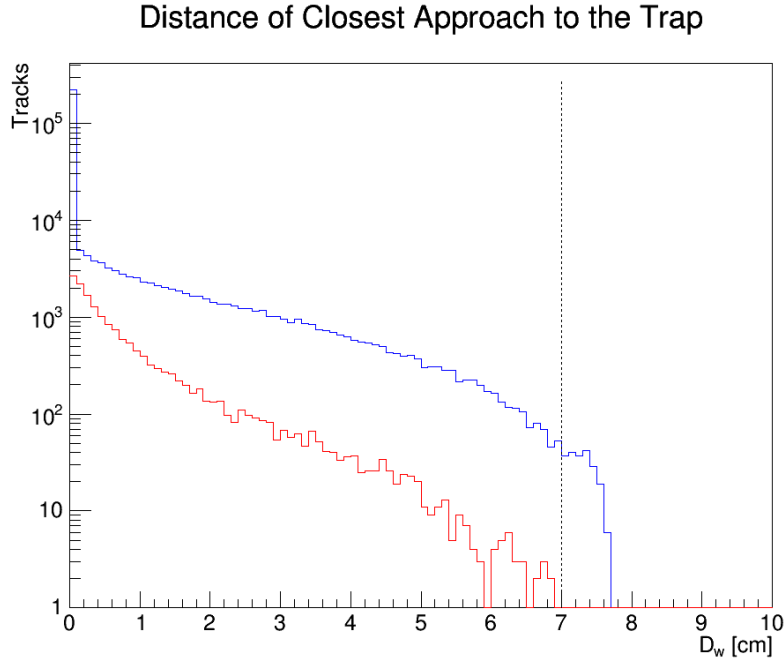


Figure 4.9: Distribution of the distance of closest approach to the trap. $D_w = D - R_w$, where $R_w = 2.2275$ cm is the trap radius. Blue: all MC tracks. Red: π^\pm MC tracks.

Tracking Cuts	
Hit Displacement along z	< 5 cm
Hit Separation in ϕ	< 0.35 rad
Hit Correlation (PCA)	> 0.95
χ^2	< 21
D_w	< 7 cm

Table 4.1: Summary of the cuts at tracking level.

ture. It has been found that about 8% of the reconstructed events were biased by the presence of such helices, dubbed *side tracks* because they are visualized on the top of one another when seen in the $x - y$ plane. It can be seen from Fig. 4.10

how the dark blue and light blue track stem for the same particle, hence double-counting it. Events containing such double-counted tracks do not pose an issue per se, rather, the vertex reconstruction accuracy is biased.

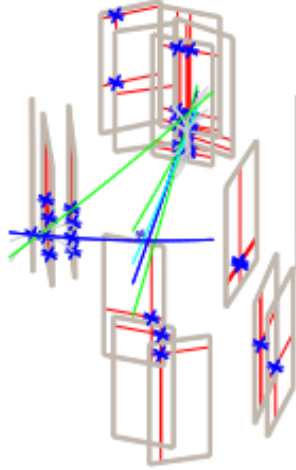


Figure 4.10: MC event display showing the presence of a side track. The helix coloured in cyan is a side track and is removed from the reconstructed event. The green helices are the ones failing the χ^2 cut.

The tracking efficiency evaluated on MC data, where it is known how many tracks intercept the SVD, gives

$$\frac{\text{Reconstructed Tracks}}{\text{MC Tracks}} = (95.20 \pm 0.04) \%$$

4.3 Vertexing

As mentioned in the introduction to Ch. 3, the determination of the \bar{H} annihilation position, or vertexing, is essential to the \bar{H} identification. In addition, the vertex position is meaningful in its own since it can be used to analyze the \bar{H}

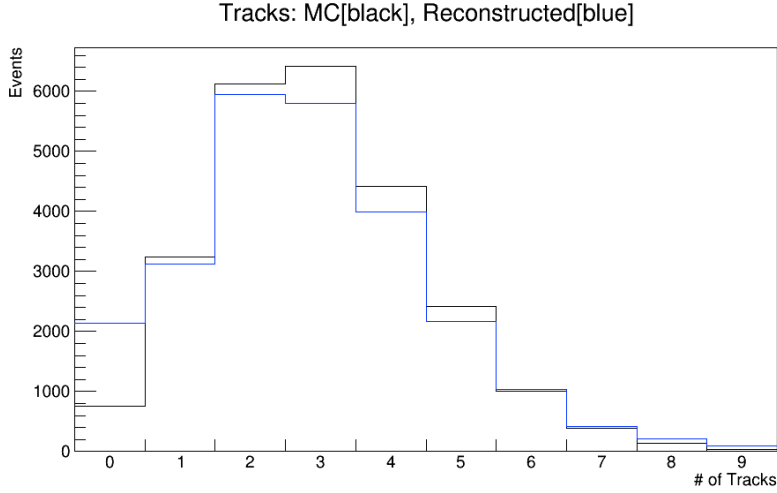


Figure 4.11: Distribution of numbers of simulated tracks (black) and reconstructed helices (blue) for 25 000 MC events.

dynamics in the trap and to perform physics measurements, as the one described in the next chapter.

The vertexing procedure is tasked to find the best estimate of the point $\mathbf{v} = (v_x, v_y, v_z)$, where all the helices intersect. This is the last step of the reconstruction as (v_x, v_y, v_z) is considered as the \bar{H} annihilation location. The central concept utilized in the `RecVertex` method of `TAlphaEvent` is the *distance of closest approach*: tracks do not necessarily intersect but it is possible to find the point where they pass closest to each other.

Vertexing can take place only if there are at least two reconstructed helices N . The `RecVertex` method of `TAlphaEventVertex` performs this check ($N \geq 2$) and all necessary steps to extrapolate the (v_x, v_y, v_z) of the \bar{H} annihilation. `RecVertex` performs all the minimizations with `TMinuit`.

The first step, performed by `RecVertex`, consists of minimizing the distance

squared between each pair of reconstructed helices

$$\min_{s, s' \in \mathbb{R}} \sum_i^3 [f_i(s) - f'_i(s')]^2, \quad (4.2)$$

where f, f' are the helix parametrization, given by Eq. (A.1) and s, s' are the arclength parameter given by Eq. (A.2). The midpoint lying on the segment joining the points $\mathbf{f}(\bar{s})$ and $\mathbf{f}'(\bar{s}')$, where \bar{s} and \bar{s}' are the arclength parameters found in Eq. (4.2), is the distance of closest approach

$$\mathbf{d} = \frac{\mathbf{f}(\bar{s}) + \mathbf{f}'(\bar{s}')}{2}. \quad (4.3)$$

Averaging Eq. (4.3) over all the pairs gives the vertex position

$$\mathbf{v} = \frac{1}{N_p} \sum_{k=1}^{N_p} \mathbf{d}_k, \quad (4.4)$$

where $N_p = \frac{N!}{2(N-2)!}$ is the number of pairs. When $N = 2$, the vertexing is terminated, the $\bar{\mathbf{H}}$ annihilation point is given by Eq. (4.4) and the quality of the calculation is expressed in terms of mean distance of closest approach of each helix to the vertex

$$\bar{\mathbf{d}}_i = |\mathbf{f}(\bar{s}) - \mathbf{v}|, \quad (4.5)$$

where \bar{s} is the result of the minimization

$$\min_{s \in \mathbb{R}} |\mathbf{f}(s) - \mathbf{v}|^2.$$

The average over all helices is the sought as a figure of merit:

$$\text{DCA} = \frac{1}{N} \sum_{i=1}^N |\mathbf{v} - \bar{\mathbf{d}}_i|. \quad (4.6)$$

When there are more than two reconstructed helices, the vertex is obtained from the minimization of Eq. (4.6) with respect to the tentative vertex

$$\min_{\tilde{\mathbf{v}} \in \mathbb{R}^3} \frac{1}{N} \sum_{i=1}^N |\tilde{\mathbf{v}} - \bar{\mathbf{d}}_i|,$$

where $\bar{\mathbf{d}}_i$ for $i = 1, \dots, N$ is given by Eq. (4.5), when $\mathbf{v} = \tilde{\mathbf{v}}$. In words, this step consists in the minimization of the mean of the distances between the tentative vertex and point of closest approach of each helix to a tentative vertex. Once the minimum is reached, the quality of the calculation of the vertex position \mathbf{v} is again measured by Eq. (4.6).

The presence of helices that do not extrapolate well to a common origin is detrimental to the vertexing accuracy, for example, tracks that are scattered through large angles or e^-e^+ pairs that are likely to be produced far from the annihilation point. The procedure to eliminate these tracks involves excluding one helix at a time and re-calculating the vertex position with the method described above. The routine calculates N new vertexes, with the corresponding DCAs that are ordered from the smallest to the largest. If the smallest of the newly calculated distances of closest approach DCA_0 is significantly improved,

$$\frac{\text{DCA} - \text{DCA}_0}{\text{DCA}} > 40\%, \quad (4.7)$$

the helix is eliminated, the new vertex is stored as new $\bar{\mathbf{H}}$ annihilation point, and DCA_0 takes the place of the formerly calculated DCA. The elimination procedure is continued until Eq. 4.7 is no longer valid or the number of remaining helices is equal to two.

The final position of the vertex, the helices used to achieve the results, and the vertex quality, the DCA, are stored in a `TAlphaEventVertex` object. The distribution of the DCAs for MC data is given in Fig. 4.12 and shows that the vast majority of the helices extrapolate very closely to the found vertex.

4.4 Note on Reconstruction Performance

The accuracy with which the vertex can be reconstructed is seriously limited by multiple scattering of the π^\pm in the cryostat. The main parameter that governs

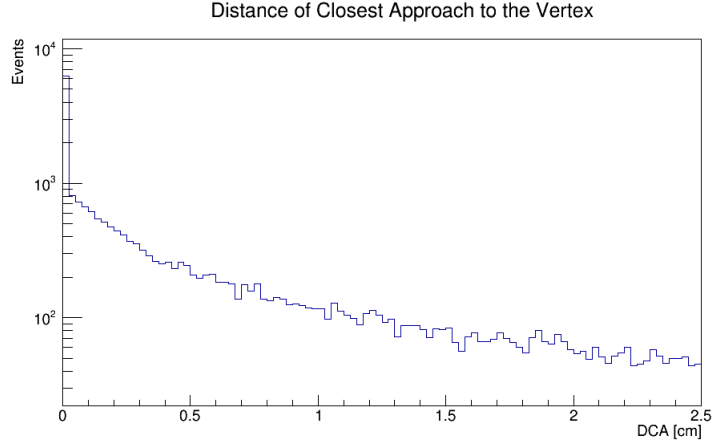


Figure 4.12: Distribution of DCAs for reconstructed vertexes in 25 000 simulated annihilations.

such a process is the radiation length of the material.

The radiation length is calculated as the average radiation length for the material stack in the cryostat:

$$X_R = d_T \left(\sum_n \frac{d_n}{X_{Rn}} \right)^{-1} \approx 3.21 \text{ cm}, \quad (4.8)$$

where d_T is the total thickness, d_n is the thickness of a single volume and X_{Rn} its radiation length. For a π^\pm meson with momentum magnitude $p \approx 250 \text{ MeV}$, the RMS of the distribution of scattering angle is [126]

$$\theta_0 = \frac{13.6 [\text{MeV}]}{\beta c p} \sqrt{\frac{x}{X_R}} \left[1 + 0.038 \ln \left(\frac{x}{X_R} \right) \right] \approx 5^\circ,$$

where βc is the velocity and $x \approx d_T$ is the path length of the π^\pm meson (this assumes that it goes through the octupole winding, which is not always the case). If a π^\pm meson travels radially through the apparatus to the SVD, the displacement with respect to the original path, hence from the true annihilation point, is $\approx 7 \text{ mm}$.

The substantial amount of scattering material (with high atomic number Z) provides also the ideal environment for the high energy photons (produced, e.g.,

in the instantaneous decay of the π^0 meson) to create e^-e^+ pairs. These particles are not immediately relatable to the \bar{H} annihilation hence, if used for reconstruction, degrade further the vertexing accuracy.

Another limitation of the SVD, as embedded in the ALPHA apparatus, is that the number of layers is limited to three, which amounts to the number of measurements that can be made of a track. Indeed, three is the minimum number of points required to determine the radial projection of an helix. A non-essential drawback is the impossibility to associate an error to the reconstructed momentum of the tracks, making any estimation meaningless. A more pressing issue is the possible inefficiencies of the SVD, in the sense that a hit that fails to be properly reconstructed causes the complete loss of the whole track. As mentioned in the beginning of Sec. 4.3, the minimum requirement to build a vertex is the presence of two tracks: if an event has only two reconstructable tracks but one is not found as a consequence of a missing hit, the vertexing efficiency is degraded.

The reason behind the limited number of SVD layers is the space requirement. The SVD fits inside the bore of the external solenoid and outside the outer vacuum chamber (see Sec. 2.4). The radial dimension of the external solenoid is constrained by budget.

4.5 Simulation Results

The accuracy and the efficiency is assessed on MC data and this section shows such results for the ALPHA-2 implementation of the reconstruction software. The results for ALPHA-1 are presented in [127].

The accuracy is measured as the distance between the MC vertex and the

reconstructed one. The distribution of the three quantities

$$\begin{aligned}
 r_{\text{MC}} - r_v \\
 \phi_{\text{MC}} - \phi_v \\
 z_{\text{MC}} - z_v,
 \end{aligned}
 \tag{4.9}$$

where $r_v = \sqrt{v_x^2 + v_y^2}$ and $\phi_v = \arctan(\frac{v_y}{v_x})$, for 25 000 simulated annihilations is plotted in Fig. 4.13.

The *vertex resolution* is determined through a 6-parameter fit to a bi-Gaussian

$$B(t; \mu_1, \mu_2, \sigma_1, \sigma_2) = A_1 e^{-\frac{(t-\mu_1)^2}{\sigma_1^2}} + A_2 e^{-\frac{(t-\mu_2)^2}{\sigma_2^2}},
 \tag{4.10}$$

where A_1 and A_2 are normalization constants, $\mu_1 \approx \mu_2 \approx 0$ are the means and $\sigma_1 < \sigma_2$ are the standard deviations. One meaningful quantity to quote as the vertex resolution is the smallest of the standard deviations, i.e., σ_1 . The resolutions calculated from Fig. 4.13 are presented in Tab. 4.2.

The vertexing efficiency is simply calculated as the ratio of the number of successfully reconstructed vertexes to the number of generated annihilations and is shown in the last row of Tab. 4.2.

Vertex resolution	
r	(0.893 ± 0.008) cm
ϕ	$(17.4 \pm 0.2)^\circ$
z	(0.521 ± 0.005) cm
Efficiency	
$(78.6 \pm 0.2)\%$	

Table 4.2: Vertexing resolution and efficiency.

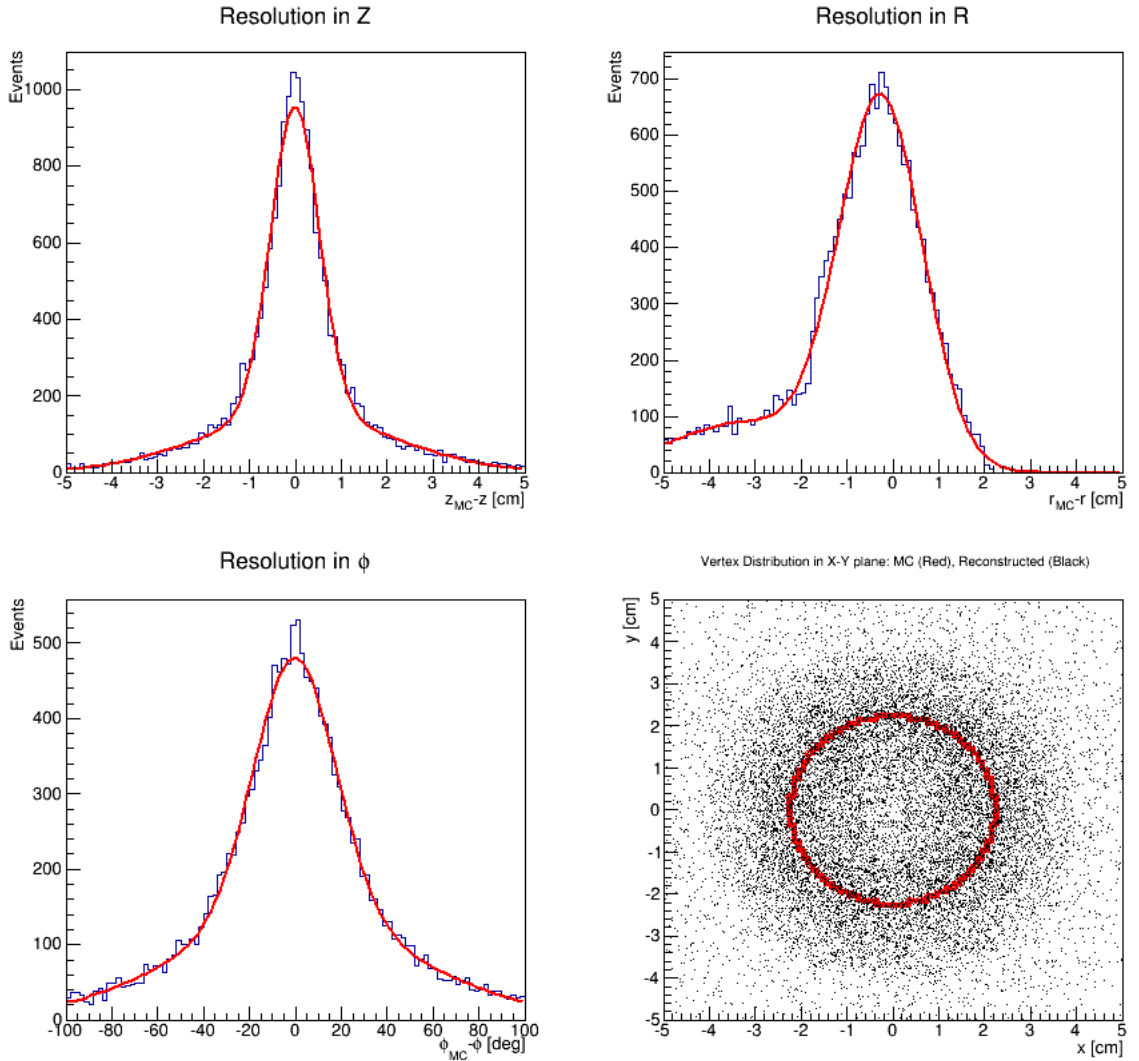


Figure 4.13: Distribution of the quantities shown in Eq. (4.9) for 25 000 generated annihilations. The data are shown as a blue line while the red line is the best-fitted bi-Gaussian, given in Eq. (4.10). The bottom right corner is a scatter plot of the MC vertexes (red dots) in the $x - y$ plane with the same projection for the reconstructed one (black dots).

5 Limit on the Electric Charge of Antihydrogen

In Sec. 2.4 the QWP, or “quench with power”, technique was mentioned in connection with discrimination of bare, or “unbound”, \bar{p} annihilation from \bar{H} annihilation. The background due to bare \bar{p} arises from the fact that the 511 keV γ from the e^+ annihilation are not detected and there is no clear signature that the detected \bar{p} was bound in \bar{H} . It was also mentioned in the same paragraph that this method turns out to be also useful to put an upper limit on the \bar{H} charge. This chapter deals exclusively with the determination of the \bar{H} charge in the ALPHA-1 apparatus. This is, to date, the only high-precision measurement of a fundamental property of \bar{H} . This measurement is reported in [107].

As discussed in Sec. 1.4, the \bar{H} neutrality is also central with respect to a measurement of its gravitational acceleration. It is argued, in the same section, that the neutrality of atoms and antiatoms is expected from the *quantum anomaly cancellation* [60]. From the limit on the \bar{H} charge, it is also possible to deduce a limit on the charge of the e^+ . In addition, whether the electric charge of hydrogen is measured, the current measurement represents a CPT test, too (see Sec. 1.1.2).

The details of the measurement are presented in Sec. 5.1. The calculations that connect the measured quantities with the \bar{H} charge are explained in Sec. 5.4. Given the rather trivial method used to achieve such a stringent limit of the \bar{H} charge and the fact that ALPHA was not originally designed to perform this measurement, the intensive campaign to spot any possible source of systematic

errors is described in Sec. 5.6. Among the main sources of systematic errors, a change in the SVD performance over the two years of data collection might have introduced a shift in the experimental data. The analysis of the SVD performance is detailed in Sec. 5.5. A summary of the procedure and the results is given in Sec. 5.7.

5.1 Description of the Measurement

The AR mixing (see Sec. 2.4) of e^+ and \bar{p} is followed by a series of clearing pulses, as shown in Tab. 2.1, of increasing intensity to remove \bar{p} from the minimum-B trap. This technique is adopted to ensure that no “mirror-trapped” \bar{p} are left in the trap, as discussed in [101]. If any \bar{p} is left in the trap, the bias fields, shown by the red and green lines in Fig. 5.1, cause these charged antiparticles to drift towards one end of the mixing region in a given time.

The electric field in the QWP is called *bias-right* E_R , if it sweeps the \bar{p} to right-hand side of the trap, i.e., $z > 0$, and *bias-left* E_L to left-hand side of the trap, i.e., $z < 0$.

The bias is applied when the \bar{H} is trapped in the magnetic trap. If \bar{H} has a charge Qe , where e is the elementary charge and Q is the *fractional charge*, then the electric fields employed in the QWP would have a measurable effect on trapped \bar{H} . The present measurement is the search for a deflection of a trapped \bar{H} in these fields due to its putative fractional charge Q .

The origin of this measurement can be understood if one considers that, on the one hand, the trap depth is estimated (at the end of Sec. 2.3) to be of 5×10^{-5} eV while, on the other hand, the average potential during the QWP can be read off from Fig. 5.1 to be $\Delta V \approx 50$ V. Since ALPHA has observed trapped \bar{H} [70], the electrostatic energy $Qe\Delta V$ due to the putative charge must be less

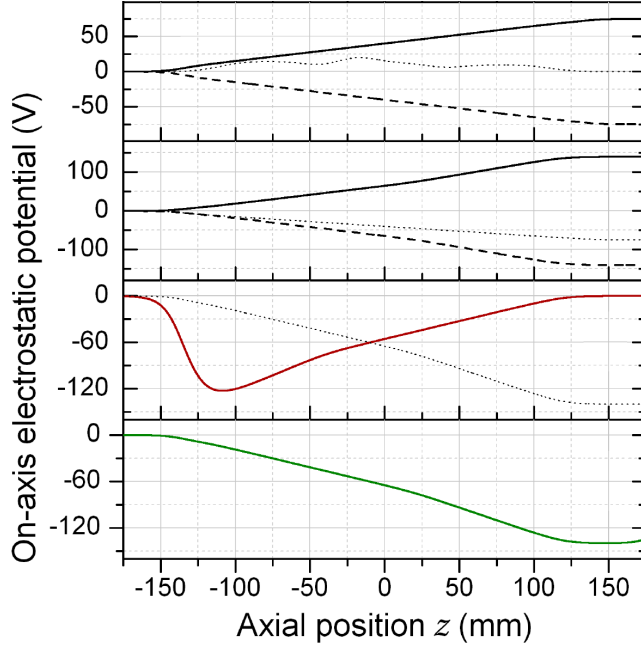


Figure 5.1: Black lines: clearing pulses of increasing strength to remove \bar{p} from the mixing region. The dotted, dashed and solid lines indicate the potential at three different time instant. Red line: QWP *bias-right*. Green line: QWP *bias-left*. Adapted from [128].

than the trap depth

$$Qe\Delta V < 5 \times 10^{-5} \text{ eV},$$

therefore

$$Q < 10^{-6}$$

for the potential difference given above. This heuristic calculation shows the power of this measurement, once the electric and magnetic fields in the trap are precisely known. For example, one can approximate the magnetic field near the minimum at $z = 0$ as

$$B(z) = B_0 + \beta z^2, \quad (5.1)$$

where $B_0 = 1 \text{ T}$ is the solenoidal field at $z = 0$ and $\beta = 1.6 \times 10^{-3} \text{ T/cm}^2$ is known

from measurements of the magnetic field near the trap centre [129]. The potential energy of $\bar{\text{H}}$ in this unidimensional model is therefore

$$U(z) = -\mu_B B(z) + QeEz, \quad (5.2)$$

where the magnetic part is described in details in Sec. 2.3 and E is the bias electric field. If $Q = 0$ the minimum of U occurs at $z = 0$; on the contrary, if $Q \neq 0$, the shift in the potential minimum is given by

$$\Delta z = \frac{QeE}{2\mu_B\beta}, \quad (5.3)$$

where Eq. (5.1) has been used. Such a shift in the potential minimum causes the centroid of the $\bar{\text{H}}$ annihilation distribution along z to shift as well. This is the deflection mentioned above. The bias right field E_R causes a shift $\Delta z = \langle z \rangle_R$ and the bias left E_L the shift $\Delta z = \langle z \rangle_L$. Putting these all together in Eq. (5.3), taking the difference and solving for Q gives

$$Q = \frac{2\mu_B\beta}{e(E_R - E_L)} (\langle z \rangle_R - \langle z \rangle_L). \quad (5.4)$$

The previous equation can be re-arranged by introducing the deflection parameter

$$\langle z \rangle_\Delta = \frac{\langle z \rangle_R - \langle z \rangle_L}{2}, \quad (5.5)$$

which has the advantage of canceling out any offset, constant in time, of the averages $\langle z \rangle_{L,R}$, introduced in the measured z of the antiatom annihilation position.

Indeed, Eq. (5.4) is re-written, by making it manifestly *linear* in the quantity $\langle z \rangle_\Delta$, which is experimentally accessible:

$$Q = \frac{4\mu_B\beta}{e(E_R - E_L)} \langle z \rangle_\Delta = s \langle z \rangle_\Delta. \quad (5.6)$$

s is a parameter, dubbed *sensitivity*, that depends only on constants and on the electric and magnetic fields present in the trap. In this example, the sensitivity

is $s = 3.7 \times 10^{-8} \text{ cm}^{-1}$, when the value of β given before is used in Eq. (5.6), together with an average value of the electric fields near the trap centre determined from Fig. 5.1. At the end of Sec. 5.3 the measured value of $\langle z \rangle_{\Delta}$ will be given, so that Q can be estimated with this simplified model. However, the determination of $\langle z \rangle_{\Delta}$ obviously depends on the SVD, and that involves a number of effects that have to be considered.

5.2 SVD Characterization

Since the SVD reconstruction characteristics of ALPHA-2, like vertex reconstruction resolution and efficiency (see Sec. 4.5), differ from the ones of ALPHA-1, the following briefly summarizes such results for the latter. In particular, the rejection of the background due to cosmic rays has not been discussed yet in the context of the new apparatus and it has been postponed to Sec. 6.2, since it represents a central topic for the present work. Nevertheless, it suffices to say that, for ALPHA, the cosmic rejection is performed on an event-by-event basis by looking at certain properties of the event.

The overwhelming majority of the events recorded by the SVD due to cosmic rays are reconstructed as two “stiff” tracks, i.e., with very large radius of curvature. They can be physically interpreted as a single track, composed of six hits, due to a high energy μ^{\pm} that travels across the apparatus, as shown on the right panel of Fig. 5.2. The topology of the cosmic event is remarkably different from an \bar{p} annihilation, shown in the left panel of Fig. 5.2. By virtue of this difference, it is possible to use a set of variables to discriminate cosmic rays from the true \bar{H} signal [130].

The cosmic rejection proceeds by dividing the events into two categories based on the number of reconstructed tracks N_{helices} . Events where $N_{\text{helices}} = 2$ have

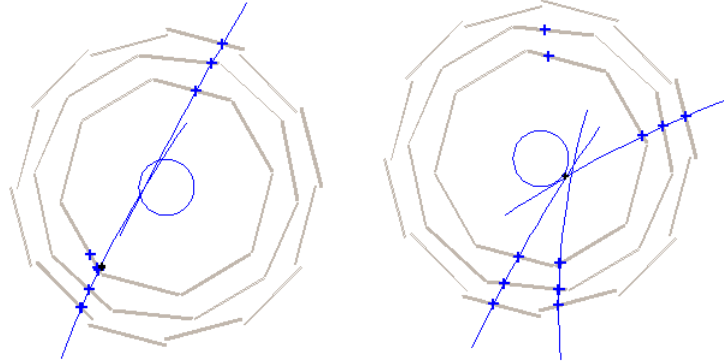


Figure 5.2: Left: Cosmic event reconstructed with the ALPHA-1 SVD. Right: \bar{p} annihilation.

higher probability of being a cosmic ray, requiring tighter cuts on the discriminating variables. Events that fall in the category $N_{\text{helices}} > 2$ are very unlikely to be due to cosmic rays.

The first of the discriminating variables is the radius of the reconstructed vertex. Ideally, all the reconstructed vertices should have a radius smaller or equal to the electrodes radius since that is where the \bar{H} (and the \bar{p}) are confined. In the presence of the effects described in Sec. 4.4, one can only expect to find the \bar{H} vertex close “enough” to the trapping region, where “enough” is the radial cut value.

The second discriminating variable measures the straightness of the reconstructed tracks using the six hits from every possible combination of two tracks. The six-hits-combination that results in the highest correlation coefficient (note that for cosmic rays there is only one possibility) is kept for calculating the squared residual, that is, the sum of the square of distances between each hit and the track. Intuitively, for cosmic rays the computed value is small, since the curvature is small, and for annihilation products it is large, where the relative magnitude of the two is the value of cut on the residual.

Cuts	$N_{\text{helices}} = 2$	$N_{\text{helices}} > 2$
Vertex Radius R_{cut} [cm]	4	4
Residual δ_{cut} [cm ²]	2	0.05

Table 5.1: Value of the cuts on the discriminating variables used in cosmic rejection in ALPHA-1.

The cuts on the radius and on the residuals in order to maximize the background rejection, while retaining as many true annihilations as possible, are described for ALPHA-1 in [130] and Tab. 5.1 reports those findings. Events in each category that satisfy the criteria $R < R_{\text{cut}}$ and $\delta > \delta_{\text{cut}}$ are called *passed-cuts*. The amount of background is estimated by operating the SVD with antiparticles in the apparatus and the cosmic rate is given by

$$\frac{\text{passed-cut events}}{\text{data collection time}} = (47 \pm 2) \text{ mHz}. \quad (5.7)$$

An important feature of the reconstruction in the present experiment is in the accuracy of the determination of the z (axial) position of the annihilation vertex. The axial resolution of the vertex clearly has an impact on the measurement of the shift Δz introduced in the previous section. The Monte Carlo simulation described in Sec. 4.1 in its ALPHA-1 incarnation is used to estimate the resolution. After applying the cuts of Tab. 5.1 on the reconstructed vertices, it produces the distribution in Fig. 5.3 of the difference of the reconstructed z position and the one of the generated vertex.

The axial vertex resolution is determined by fitting the distribution with the function given by Eq. (4.10). The resolution is estimated from the standard deviation of the narrower Gaussian to be (0.4 ± 0.2) cm.

The z dependence of the reconstruction efficiency is another input to the present measurement, as it informs whether the shift Δz is due to detection inefficiencies, rather than non-zero charge. For clarity's sake, one can think of a situation where $\Delta z > 0$ because a fraction of events in the region $z < 0$ have not

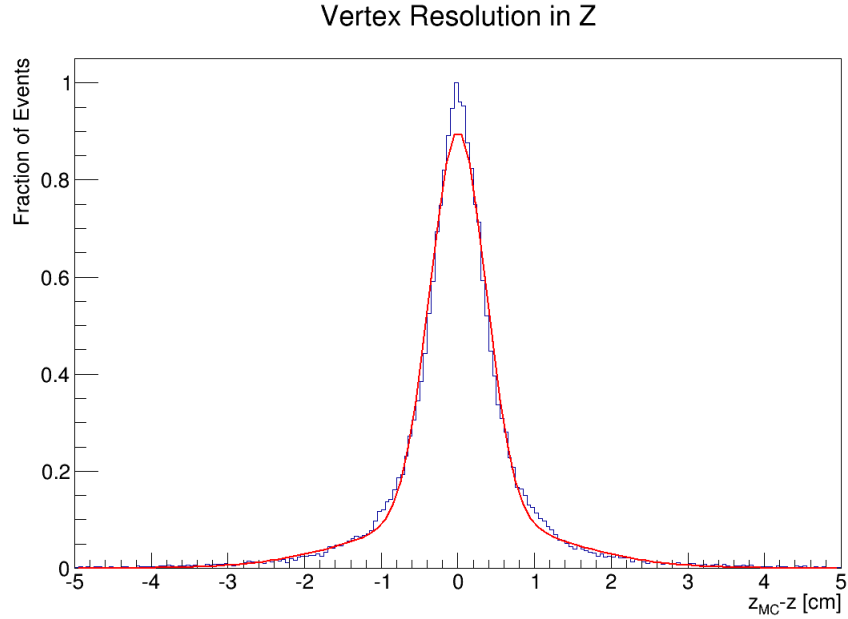


Figure 5.3: Vertex axial resolution after cosmic rejection is applied to Monte Carlo data.

been properly reconstructed. A simulation where the \bar{H} annihilations are uniformly generated along the trap axis z (but still on the electrodes' inner surface) is used to determine the number of reconstructed vertices per number of events generated in a 1 cm bin of the z axis. The resulting efficiency curve, after applying the cuts of Tab. 5.1, is shown in Fig. 5.4.

Ideally, the efficiency curve reaches its maximum symmetrically around the centre of the SVD, where the solid angle coverage of the (simulated) annihilation is maximum, and decreases rapidly towards zero, as fewer and fewer charged particles have the chance to intercept the active region. In ALPHA-1, the SVD hybrid number 10, in the middle layer in the upstream half, was not functioning, probably due to a faulty connection on the PCB. Since the simulation is designed to represent the real SVD, the resulting efficiency curve is asymmetric and skewed towards $z > 0$.

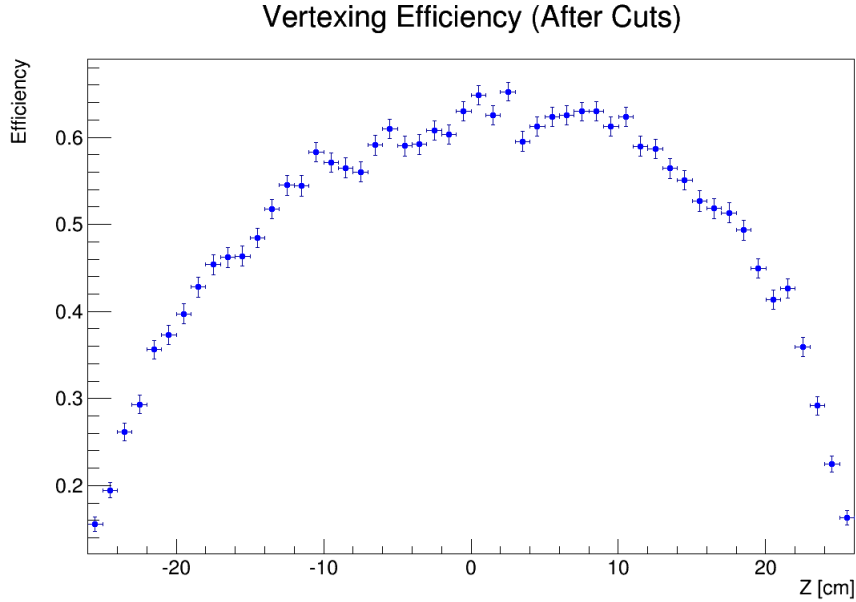


Figure 5.4: Vertexing efficiency dependence on the axial position of the generated vertex, after cosmic rejection is applied.

By using the default generator (see Sec. 4.1.2), the overall efficiency is computed as $(65.248 \pm 0.002)\%$, after the vertex cuts of Tab. 5.1 are taken into account.

5.3 Annihilation Data

The data for the present measurement were collected in the years 2010 and 2011. The reconstructed vertices have to meet a list of requirements in order to be considered \bar{H} annihilation and enter the dataset. The first of them is the cosmic rejection criteria of Tab. 5.1. Since ALPHA did not perform *ad-hoc* experiments to determine the \bar{H} charge, a selection of the experiments entering the dataset is needed. In the following, the experimental conditions met by the events entering the dataset and the additional cuts on the reconstructed vertices are enumerated.

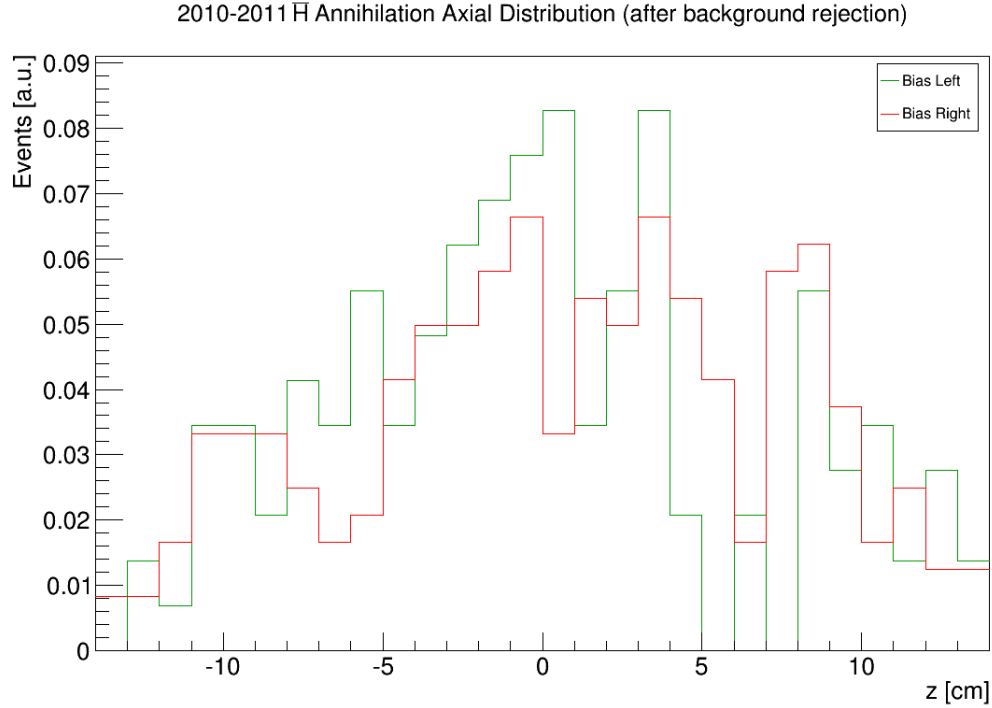


Figure 5.5: Distribution of the \bar{H} annihilation position along the trap axis z . The entries of these histograms meet the requirements described in the text (see also Tab 5.2).

The obvious requirement is that the \bar{H} trapping sequence (see Tab. 2.1) employs the QWP, in one of the two field configurations, bias left or bias right. This is not always the case, since the QWP technique was introduced in order to rule out the presence of mirror trapped \bar{p} at the time of the magnet shutdown. Moreover, the \bar{H} must have been confined for more than 400 ms, a time that is considered long enough to allow it to radiatively decay to the ground state [102, 131].

In order to reduce the background due to cosmic rays, additional cuts on the time and on the position of the reconstructed annihilation are adopted. Since the \bar{H} axial confinement is provided by the mirror coils, located at $z_{\text{mirror}} = \pm 13.6$ cm,

the vertices reconstructed at $|z| > 13.6$ cm are unlikely to be due to \bar{H} and thus are discarded.

The superconducting magnet shutdown has a known finite time constant. The magnetic confinement is less than 0.1% of the initial depth after $t_q = 30$ ms from the magnets shutdown trigger [96]. Therefore, only events detected within this 30 ms time window are accepted.

The contamination due to bare \bar{p} is the concern for which the QWP was introduced. This is because the photons from the e^+ annihilation are not detected in ALPHA. As mentioned before, the \bar{p} are forced to annihilate in one end of the mixing region in a given time window, determined by their kinetic energy and the shape of the electric potential. Indeed, the studies published in [101] conclude that they preferentially annihilate in the elliptical regions centred at $z_{\bar{p}} = \pm 13$ cm, with semi-axes 2 cm and 4 ms, respectively, and $t_{\bar{p}} = 5$ ms. Reconstructed vertices lying in these regions are not taken into account.

It has also been found that a fraction of the experiments originally included in the dataset display an intermittent SVD readout error, and, hence are excluded from the final count of selected events, presented in Tab. 5.2. This table aggregates the number of events classified as \bar{H} annihilation, organized by year and by QWP configuration. The average position along z of the vertices is also shown, as it enters the calculation of the deflection parameter $\langle z \rangle_{\Delta}$. The distribution of the vertex positions along z for the selected events for the two bias configurations is displayed in Fig. 5.5, from which the average $\langle z \rangle_{L,R}$ and their uncertainties are extracted.

The value of Eq. (5.5), calculated from the experimental data, is

$$\langle z \rangle_{\Delta} = (0.4 \pm 0.3) \text{ cm} \quad (5.8)$$

where the uncertainty is given by the propagation of the uncertainties on $\langle z \rangle_{L,R}$.

Field Configuration	Run 2010	Run 2011	Total $\bar{\text{H}}$	$\langle z \rangle_{L,R}$ [cm]
Bias Left	145	-	145	-0.02 ± 0.53
Bias Right	27	214	241	0.79 ± 0.42

Table 5.2: Summary of the events accepted as $\bar{\text{H}}$ annihilation. The average annihilation position $\langle z \rangle_{L,R}$ in the last column is calculated from the distributions shown in Fig. 5.5.

By using the approximated value of the sensitivity obtained at the end of Sec. 5.1 and the measured shift parameter Eq. (5.8), a crude estimation of the $\bar{\text{H}}$ fractional charge is $Q = (-1.5 \pm 1.3) \times 10^{-6}$.

5.4 Simulation and Sensitivity

Since the electric and magnetic fields present in the trap are considerably more complicated than the approximations given in Sec. 5.1, the measurement of the $\bar{\text{H}}$ charge requires numerical calculation of the $\bar{\text{H}}$ motion in the trap, performed with accurate modelling of all the known effects such as electric field timing and intensity, magnetic field inhomogeneities, and SVD imperfections.

The relation between the $\bar{\text{H}}$ charge Q and deflection parameter Eq. (5.5) is obtained from the numerical solution of the equation of motion of trapped $\bar{\text{H}}$, with the assumption that it has a non-zero electric charge Qe :

$$m\ddot{\mathbf{r}} = \mu_B \nabla B(\mathbf{r}, t) + Qe[\mathbf{E}(\mathbf{r}, t) + \dot{\mathbf{r}} \times \mathbf{B}(\mathbf{r}, t)] \quad (5.9)$$

where m is the $\bar{\text{H}}$ mass, \mathbf{r} is its centre-of-mass position, $\mathbf{B}(\mathbf{r}, t)$ is the trapping magnetic field and $\mathbf{E}(\mathbf{r}, t)$ is the electric field in the clearing pulses and the QWP. The spatial and time structure of \mathbf{E} and \mathbf{B} are precisely modelled [101].

The initial kinetic energy of the antiatoms is drawn from a Maxwell-Boltzmann distribution truncated at the trap depth. The initial position of $\bar{\text{H}}$ is considered to be uniformly distributed in an ellipsoid of 16 mm in length and 0.8 mm in radius

at the centre of the trap. The integration of Eq. (5.9) with these random initial conditions gives the tridimensional trajectory of an antiatom in the trap, i.e., a *full simulation* of the $\bar{\text{H}}$ dynamics in the trap. The simulation begins with the $\bar{\text{H}}$ propagation in the trap for about 1 s, followed by the clearing pulses, the QWP ramp after about 130 ms and the magnet shutdown after additional ~ 20 ms, for a total integration time of about 1.19 s. The time t and the axial position z at each integration step is recorded for each generated $\bar{\text{H}}$. The final value of (t_f, z_f) , i.e., annihilation time and location, for each particle constitutes the simulation output.

The solution of Eq. (5.9) for different values of the fractional charge Q , with the initial condition specified above, connects the deflection parameter $\langle z \rangle_{\Delta}$ with Q , as shown in Fig. 5.6. For each value of Q , the trajectories of 450 000 $\bar{\text{H}}$ atoms are calculated. The uncertainty on $\langle z \rangle_{L,R}$ is 0.1 mm and is too small to be seen in Fig. 5.6. Thus, by propagating in quadrature the uncertainties on the averages, the error on $\langle z \rangle_{\Delta}$ is 0.07 mm.

The sensitivity is calculated from Fig. 5.6 by fitting a straight line to the $(Q, \langle z \rangle_{\Delta})$ data and by taking the inverse of the slope:

$$s = \left(\frac{d\langle z \rangle_{\Delta}}{dQ} \right)^{-1} = (-3.31 \pm 0.04) \times 10^{-9} \text{ mm}^{-1}. \quad (5.10)$$

The linear model follows from Eq. 5.6 but the goodness of the model can be seen directly from Fig. 5.6. The best-fit line is constrained to pass through the origin on the physical expectation that for $Q = 0$ the deflection is zero.

The simulation takes into account the SVD effects by including its z resolution and its efficiency as a function of z . The SVD efficiency curve, shown in Fig. 5.4, is normalized to one and, for each annihilation location z_f , a random number in $[0, 1]$ is picked from a uniform distribution. An antiatom is discarded if the random number is greater than the value of the efficiency at z_f . The SVD resolution is

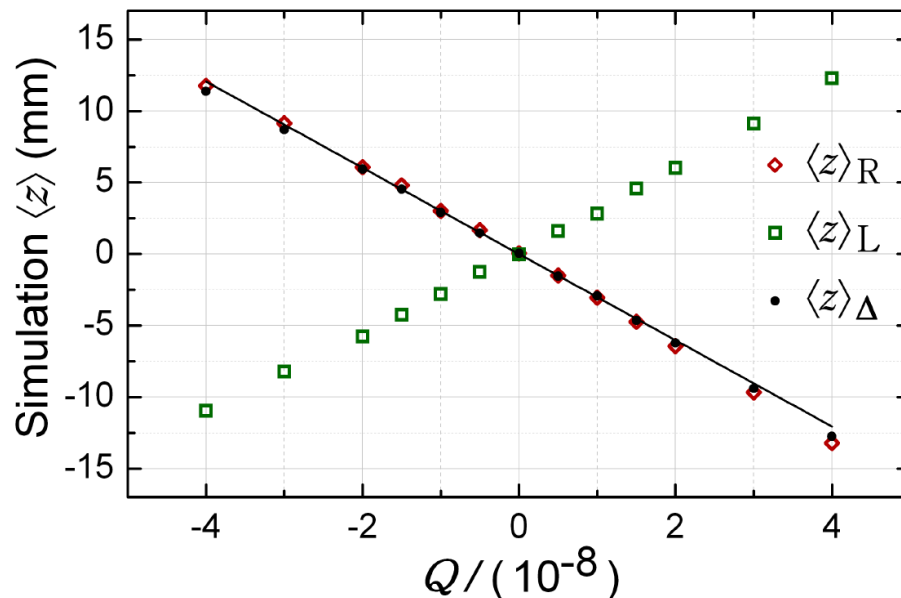


Figure 5.6: Results of the systematic study of effect of the \bar{H} charge Q on the deflection parameter $\langle z \rangle_{\Delta}$ (black dots). The resulting shift calculated with the two configurations of the bias voltages, *left* and *right*, are also shown as green boxes and red diamonds, respectively. The overlaid black line is the result of the best-fit. Taken from [128].

taken into account, instead, by smearing the annihilation location z_f with the addition of a random number drawn from the distribution in Fig. 5.3.

5.5 Long Term SVD Drift

The modules of the SVD are arranged in two halves around $z = 0$, covering the upstream and the downstream end of the neutral atom trap, as discussed in Secs. 3.1 and 4.1. The trapping experiments carried out with the two bias field configurations were not interspersed but, on the contrary, the bias-left configuration corresponds roughly to the 2010 data collection run and the bias-right to the 2011 (as can be seen from Tab. 5.2). Hence, a change over time of the detection

efficiency in one end of the detector with respect to the other may introduce a systematic shift in $\langle z \rangle_{\Delta}$, without necessarily implying non-zero Q .

The goal of the following analysis is to assess whether there is a change in the detector behaviour of one end with respect to the other from 2010 to 2011. The evaluation of such stability over the two years of operation crucially contributes to the calculation of the systematic uncertainty on the upper bound to the \bar{H} charge.

5.5.1 Method

In order to make the present analysis independent of the particular experimental conditions of the \bar{H} synthesis and trapping, cosmic rays are exploited under the assumption that there is a constant flux of cosmic rays across the SVD, which is surely justified given its dimension.

The cosmic runs considered in the present study span from May 2010 to December 2011. The only inclusion criteria is the maximum coverage of the period under consideration, taking into account runs from different days. In case of multiple runs for a single day, the longest is chosen.

The central quantity in the present study is the single hybrid *occupancy*, that is, the number of *hits per hybrid* in each run, normalized to the total number of hits occurring in that particular run (see Fig. 5.7). The definition of this quantity automatically rules out the seasonal (and, perhaps, daily) variation of the cosmic flux reaching the detector, since the normalization is relative to the specific circumstances under which the data were taken (length of the run, weather condition, temperature of the hybrids, etc.). The occupancy embodies the performance of the SVD and is directly related to its long-term behaviour, as it connects hardware-level information, such as strip clusters, to reconstructed quantities, such as charged particles tracks.

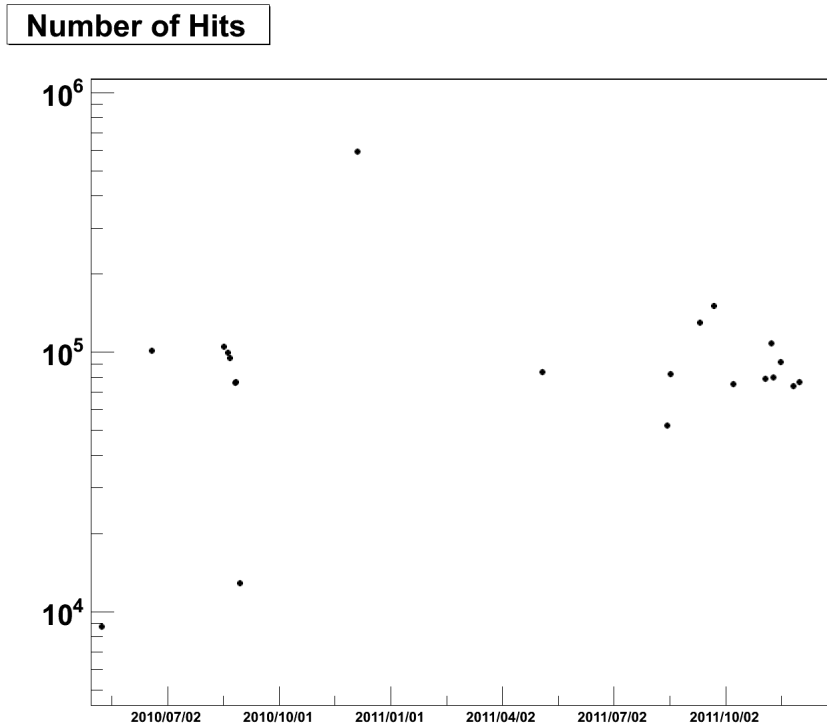


Figure 5.7: Total number of hits in the reconstructed helix per run under consideration. The errors bars are too small to be clearly seen.

The cosmic data are fed into the standard ALPHA analysis tools which search for sets of three hits that fit to the helix model. Only hits belonging to an helix participate in the calculation of the occupancy. This constraint makes the occupancy an ideal quantity for comparison against \bar{H} trapping data, given that it represents the last stage in the reconstruction procedure before the determination of the \bar{H} annihilation vertex (the latter is clearly meaningless for cosmic rays).

Once all the occupancies per hybrid per run, spanning the whole period of time under study, are acquired (see Fig. 5.8), the calculation of the occupancy variation in time is carried out. This requires finding the average occupancy per hybrid in 2010 and 2011 separately, by fitting a constant line, or level of occupancy

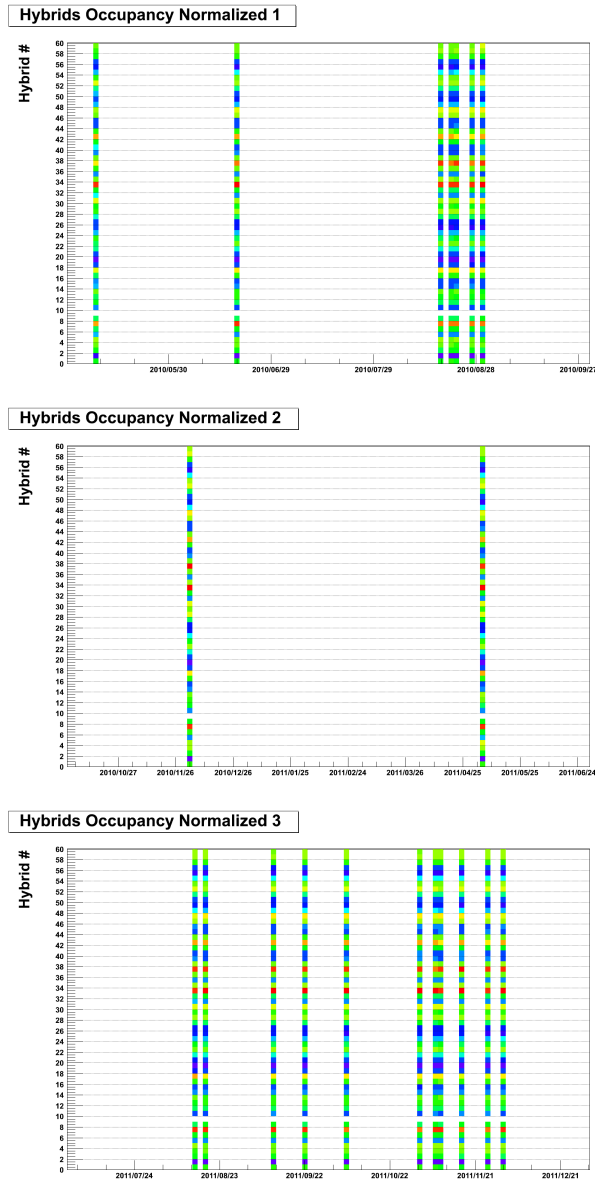


Figure 5.8: Normalized Occupancy (defined in the text): the x -axis is run date, the y -axis the hybrid number, and the colour code indicates the occupancy level, where red is high and violet is low. Run date in 1) 1 May 2010 - 1 October 2010, 2) 1 October 2010 - 1 July 2011, 3) 1 July 2011 - 31 December 2011.

q_i in that year $i = 2010, 2011$, to the normalized occupancies per hybrid. At this point, an asymmetry parameter per hybrid is computed from q_{2010} and q_{2011} :

$$a_h = \frac{q_{2010} - q_{2011}}{(q_{2010} + q_{2011})/2}, \quad (5.11)$$

where $h = 1, \dots, 60$ (see Fig. 5.10). In other words, the difference in occupancy level between the two years divided by the mean occupancy level is used to assess the stability of a detector module, i.e., whether it shows an anomalous or asymmetric behaviour in time.

The uncertainty on the q_i s is given by the error on the best-fit σ_i . The uncertainty on a_h is obtained by propagating the error on the q_i s:

$$\begin{aligned} \sigma^2[a_h] &= \left(\frac{\partial a_h}{\partial q_{2010}} \right)^2 \sigma_{2010}^2 + \left(\frac{\partial a_h}{\partial q_{2011}} \right)^2 \sigma_{2011}^2 \\ &= \frac{16}{(q_{2010} + q_{2011})^4} (q_{2011}^2 \sigma_{2010}^2 + q_{2010}^2 \sigma_{2011}^2). \end{aligned} \quad (5.12)$$

Lastly, the average asymmetry is calculated for the upstream and downstream end of the detector separately by fitting a constant line, or magnitude of asymmetry in that end, to the asymmetry per hybrid. These two values quantify the detector stability; if they are compatible, it is possible to claim that the two sides of the detector do not show an asymmetric behaviour. Eventually, if they are compatible with “zero”, it is possible to state that the detector behaviour is stable over the period of time under consideration. The uncertainty on these quantities is given by the error of the best-fit.

5.5.2 Results

Visual inspection of Fig. 5.8 indicates that no remarkable anomalies are present from one run to another, in the sense that the pattern of occupancies per run does not change significantly over the whole period under study.

Reduced Chi-Square (2010-2011)

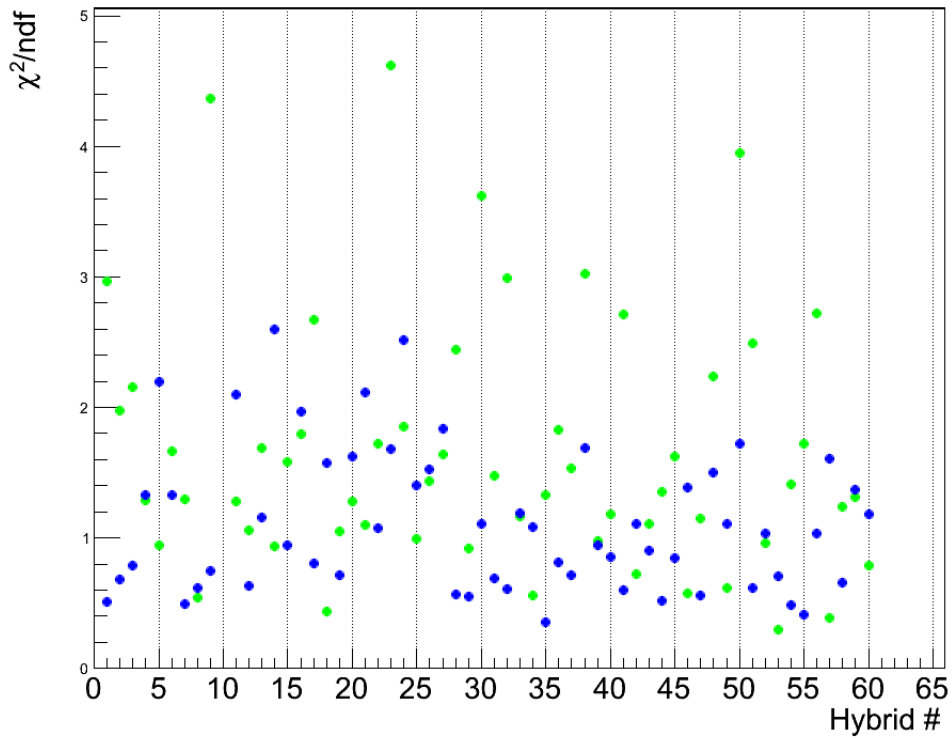


Figure 5.9: χ^2 of best-fit to average occupancy. Green Dots: 2010 data. Blue Dots: 2011 data.

The quantitative estimation of the change in occupancy is shown in Fig. 5.10, which displays the change in occupancy per hybrid over the period of time under consideration. The goodness of the assumed model of constant occupancy in the year under consideration is shown in Fig. 5.9, where the reduced χ^2 of the best-fitted occupancy level is given per hybrid. Few reduced χ^2 are larger than three and all of them are relative to 2010 data which are less sparse than the 2011 one.

From Fig. 5.10 two points, corresponding to modules 2 and 20, seem to have an anomalous behaviour, but this is easily understood when it is recalled that module 10 was malfunctioning, i.e., disconnected. The latter, being in the middle layer

between modules 2 and 20, reduces significantly the number of helices that could pass across the other two modules, resulting in a built-in occupancy deficiency. Of course, this situation does not pose any problem at all, as long as it does not change over time.

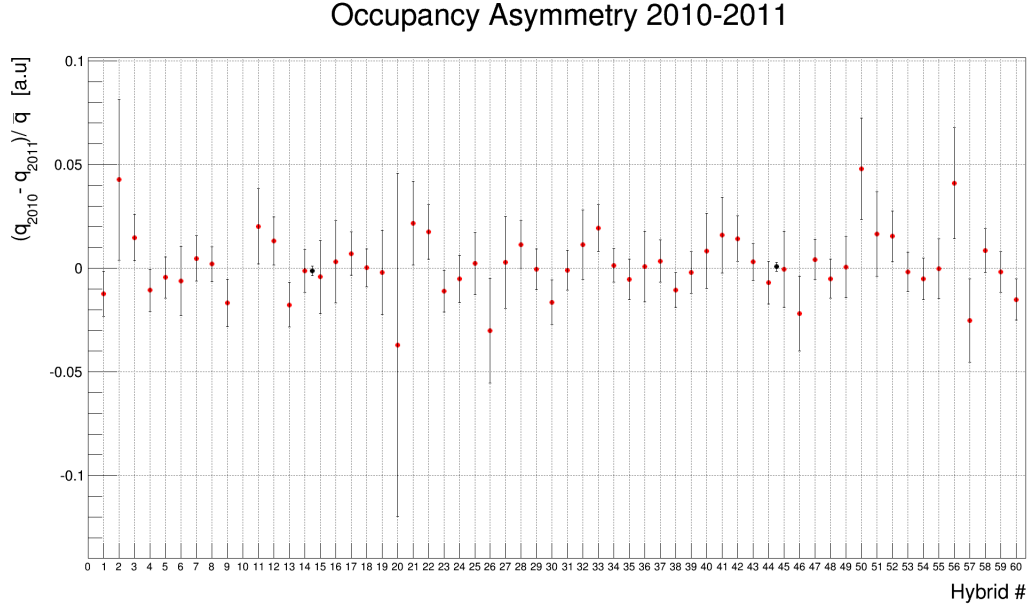


Figure 5.10: Red dots: occupancy change per hybrid given by Eq. (5.11). Black Dots: occupancy asymmetry per detector end.

The average change in occupancy per detector end (black dots in Fig. 5.10) are

$$\text{Upstream end } (z < 0) : (0.2 \pm 0.2)\% , \quad (5.13)$$

$$\text{Downstream end } (z > 0) : (-0.2 \pm 0.2)\% . \quad (5.14)$$

Both are consistent with no change in occupancy over time at the 0.2% level and compatible with each other at 0.4%.

5.6 Survey of Systematic Errors

A number of sources can contribute to a drift over time of $\langle z \rangle_\Delta$ (e.g., the subject of the previous section) and to a change in the sensitivity s with respect to its nominal value Eq. (5.10) (e.g., an inaccurate knowledge of the current in the mirror coils). These effects are taken into account in the calculation of the systematic error of Q . The investigation of the various errors proceeded by comparing simulations with and without the proposed sources.

The absolute offset of the average \bar{H} annihilation location, which affects $\langle z \rangle_\Delta$, is indicated by ζ and it is assumed to have occurred discontinuously between the 2010 and the 2011 data collection run. In other words, the drift over time of $\langle z \rangle_\Delta$ is understood as a “sudden” change of the experimental conditions from one year of data collection to the other. Therefore, ζ affects only the fraction of antiatoms in the bias-right dataset $N_{2011}/N_R = 214/241 = 0.89$, where N_{2011} and N_R are read off from the third and the fourth column, respectively, of the second row in Tab. 5.2. The error on the average annihilation position $\langle z \rangle_R$ is then

$$\delta \langle z \rangle_R = \frac{N_{2011}}{N_R} \zeta,$$

which is propagated in quadrature to $\langle z \rangle_\Delta$, yielding

$$\delta \langle z \rangle_\Delta = \frac{1}{2} \frac{N_{2011}}{N_R} \zeta. \quad (5.15)$$

The change in sensitivity affects both field configurations and is quantified by its relative change ϵ with respect to the nominal value s_0 , given by Eq. (5.10):

$$\epsilon = (s/s_0 - 1) \quad . \quad (5.16)$$

The error on Q due to a change in sensitivity is therefore given by

$$\delta Q_s = s_0 \epsilon \langle z \rangle_\Delta \quad (5.17)$$

and the one due to a drift in the average annihilation location is

$$\delta Q_z = s_0 \delta \langle z \rangle_\Delta . \quad (5.18)$$

By summing in quadrature Eqs. (5.17) and (5.18), one obtains the uncertainty induced on Q by the proposed sources of systematic error

$$\delta Q = \sqrt{\delta Q_s^2 + \delta Q_z^2} . \quad (5.19)$$

Four sources of systematic effects have been identified in the simulation. The code used to produce Fig. 5.6 is benchmarked against the one used in [101] that employs a different numerical solver and a more accurate magnetic field model that includes the electric field induced by ramping the magnetic field. The error due to an inaccurate model of the electric field is studied with a simulation that uses a somewhat degraded \mathbf{E} . The nominal simulation assumes that all the antiatoms are in the $|d\rangle$ state (see Fig. 2.11): inclusion of the $|c\rangle$ state has a limited impact on the sensitivity. The magnitude of these errors is shown in the first block of Tab. 5.3. Finally, the \bar{H} propagation is extended to 10s, to be compared to the ~ 1.19 s of the nominal calculation, without displaying any significant effect on the sensitivity or on the deflection.

Inaccurate measurement of the mirror coil currents introduces uncertainties on the magnetic trap shape, in particular a differential drift of the current in the two magnets would cause a shift in the magnetic field minimum, thus an offset of the average \bar{H} annihilation position and of the deflection parameter. In addition, a common mode drift also causes an error on the evaluation of s , as well as on $\langle z \rangle_\Delta$, albeit of a smaller magnitude with respect to the differential drift. The continuous monitoring of these currents set the maximum drift to $\pm 1\%$. Inclusion of the maximum allowed tilt of the solenoidal field with respect to the trap axis affects s and $\langle z \rangle_\Delta$ only marginally. Drift of the octupole current of the same

magnitude as the mirror currents, since they are monitored by the same device, is also taken into account. While the magnetic environment in ALPHA is under strict control, it is possible that an unknown and unidentified source of magnetic field was placed near the experiment in 2011, but was not there in 2010: this totally hypothetical field affects s and $\langle z \rangle_{\Delta}$. The magnitude of these errors and their impact on the measurement is reported in the second block of Tab. 5.3.

The initial conditions used in the simulation certainly play a role in the final answer. The $\bar{\text{H}}$ formation occurs in the volume occupied by the e^+ plasma as the $\bar{\text{p}}$ are injected into it. A calculation is performed with the antiatoms generated in a region three times larger in radius and two times longer, yielding a small contribution to the error on the sensitivity and on the deflection. The deviation from the truncated Maxwellian distribution of energies, observed for trapped $\bar{\text{H}}$ [96], is also investigated by using a uniform and a “linear” distribution that accept, respectively, more low-energy and more high-energy trapped $\bar{\text{H}}$. The effect on s is, by far, the greatest. Finally, anisotropic initial conditions are explored, where the energy distribution among the axial and radial degrees of freedom differs from that predicted by the equipartition theorem. The results of these investigations are presented in the third block of Tab. 5.3.

The SVD position with respect to the electrodes is not known a priori and is measured by using $\bar{\text{p}}$ annihilation in poor vacuum conditions. The offset between the trap centre and the SVD is not relevant since the calculation of the deflection parameter leads to the cancellation of such a difference. However, the displacement changed between 2010 and 2011 by a small amount contributing to $\delta \langle z \rangle_{\Delta}$. In addition, the Penning trap centre might be offset with respect to the magnetic trap centre, but mechanical constraints make it constant in time, thus irrelevant.

The SVD vertexing efficiency curve (introduced towards the end of Sec. 5.2)

Systematic error source	ϵ [$\times 10^{-9}$ mm $^{-1}$]	$\delta \langle z \rangle_{\Delta}$ [mm]	δQ [$\times 10^{-8}$]
Simulation benchmarking	± 0.01	± 0.09	± 0.03
Degraded $\mathbf{E}(\mathbf{r}, t)$	± 0.01	± 0.10	± 0.03
$ c\rangle$ state inclusion	± 0.01	-	± 0.01
$\pm 1\%$ differential mirror drift	-	± 0.13	± 0.05
$\pm 1\%$ common mode mirror drift	± 0.01	± 0.02	± 0.02
2 mrad solenoid tilt	± 0.01	± 0.07	± 0.03
$\pm 1\%$ error octupole current	-	± 0.01	± 0.01
External magnet	-	± 0.06	± 0.02
$3\times$ radius, $2\times$ length	± 0.01	± 0.07	± 0.03
Initial energy distribution	± 0.22	± 0.04	± 0.31
Anisotropic initial distribution	± 0.08	± 0.17	± 0.12
SVD w.r.t. trap centre	-	± 0.17	± 0.06
<i>SVD efficiency</i>	± 0.03	± 0.02	± 0.04
<i>Long term SVD drift</i>	-	± 0.04	± 0.01
<i>Cosmic background</i>	-	± 0.25	± 0.08
\bar{p} contamination	-	± 0.13	± 0.04
Overall error in quadrature			± 0.4

Table 5.3: Sources of systematic errors. ϵ in the second column is calculated using Eq. (5.16) and $\delta \langle z \rangle_{\Delta}$ in the third one from Eq. (5.15). The systematic error on Q for the proposed source is given by using Eqs. (5.17) and (5.18) in Eq. (5.19). The entries in italics are the subject of the present chapter.

plays an important role in the simulation. A different curve, obtained with an earlier version of the reconstruction software and shown in Fig. 5.11, is used to study a possible deviation from the values displayed in Fig. 5.4, affecting the sensitivity and the measured deflection.

The study of the long term SVD drift (see Sec. 5.5) is incorporated using the efficiency curve once again. Following the working hypothesis that a change in efficiency occurred abruptly between 2010 and 2011, the efficiency curve for the latter year is modified according to the prescriptions of Eq. (5.13), that is, the efficiency is uniformly decreased by 0.2% for $z > 0$ and uniformly increased by the same amount for $z < 0$. The simulation with the new curve produces the error on $\delta \langle z \rangle_{\Delta}$ given by the last entry of the fourth block of Tab. 5.3.

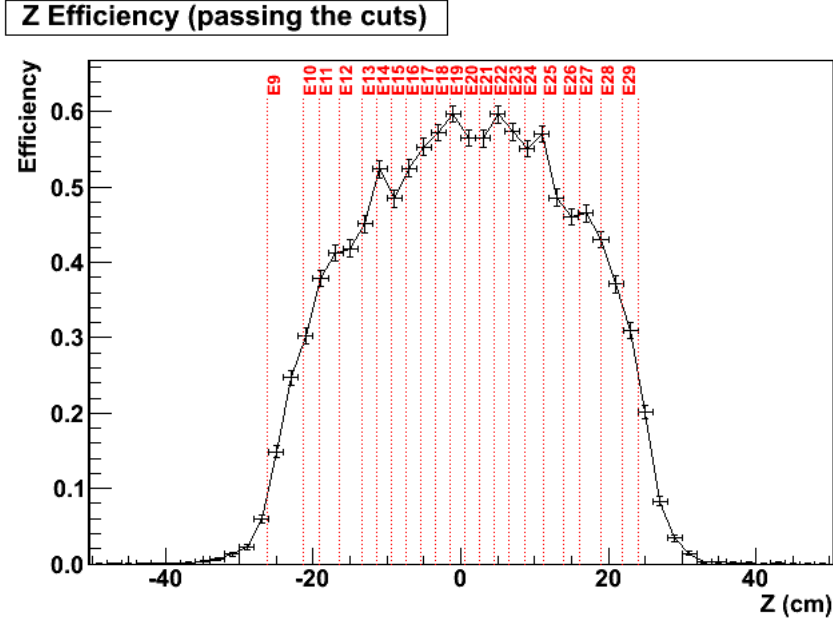


Figure 5.11: Vertexing efficiency as function of z , after cosmic rejection, obtained with an older version of the reconstruction software. The red lines indicate the position of the electrodes.

Cosmic rays impinge on the SVD uniformly along z and the expected number of background events B in $N_{\text{run}} = 506$ trapping experiments is

$$B = N_{\text{run}} \times t_q \times \rho \approx 1, \quad (5.20)$$

where $t_q = 30$ ms is the observation time window (see Sec. 5.3) and the cosmic rate ρ is given by Eq. (5.7). However, the structure of the efficiency curve skews the distribution of cosmic rays along z , shifting the average annihilation location if background events are accepted. While this error is not time dependent and might have affected equally the bias-right and bias-left data, it is included as worst-case-scenario in $\delta \langle z \rangle_{\Delta}$.

Lastly, the contamination due to bare \bar{p} is taken into account. Although experimental evidence rules out that any bare \bar{p} is left in the trap, under the pessimistic

scenario where the nine $\bar{\text{H}}$ candidates, excluded from the measurement for lying inside the elliptical cuts region, are all actually due to $\bar{\text{p}}$, the contamination in the acceptance region causes an error in the average annihilation location. Such an error is treated on the same footing as the one due to cosmic ray contamination. The last block of Tab. 5.3 shows the determination of these errors.

It is worth remembering at this point that a trapped $\bar{\text{H}}$ is held long enough that it has decayed to its ground state, whose electric polarizability is very small [132], being at second-order in perturbation theory. Therefore, the Stark force has a negligible effect on the measurement, given the magnitude of the electric fields involved (see Fig. 5.1).

5.7 Result and Discussion

The data selection, described in Sec. 5.3, including the cosmic rejection procedure of Sec. 5.2 as well as the numerical calculations of Sec. 5.4, was performed before analyzing the annihilation data. The result of the data analysis is presented in Fig. 5.5 and in Tab. 5.2.

By using the measured deflection of Eq. (5.8) and the simulation result of Eq. (5.10), the fractional charge of $\bar{\text{H}}$ from Eq. 5.6 is $Q = -1.3 \times 10^{-8}$, which translates into the following limit

$$|Q| < (1.3 \pm 1.1 \pm 0.4) \times 10^{-8}, \quad (5.21)$$

where the first error is the statistical error due essentially to $\langle z \rangle_{\Delta}$, since the uncertainty on s has a negligible contribution, and the second error is the overall systematic error on Q from the last row of Tab. 5.3.

This limit is a million-fold improvement over the previous experimental result obtained with an energetic $\bar{\text{H}}$ beam [133]. The best limit on the neutrality of ordinary atoms and molecules, such as He, H₂ and SF₆, is $10^{-21}e$, due, of course,

to the availability of large quantities of those species [134], while less than 1000 antiatoms have been trapped to date (and then only one at any one time). The accuracy of the present measurement, Eq. (5.21), is limited by statistics and currently is the first high precision one on antimatter. This result also represents a test of CPT invariance, provided that the hydrogen (fractional) charge is measured.

The \bar{H} charge is assumed to be the sum of the charges of the \bar{p} and of the e^+ , $Qe = q_{\bar{p}} + q_{e^+}$. The latter expression can be re-arranged to give the e^+ charge anomaly

$$\frac{q_{e^+} - e}{e} = Q - \frac{q_{\bar{p}} + e}{e}, \quad (5.22)$$

where the \bar{p} anomalous charge is $|(q_{\bar{p}} + e)/e| < 7 \times 10^{-10}$ [126]. Therefore, a limit on the e^+ charge anomaly can be inferred from Eqs. (5.21) and (5.22):

$$\left| \frac{q_{e^+} - e}{e} \right| \approx |Q| < (1.3 \pm 1.1 \pm 0.4) \times 10^{-8}, \quad (5.23)$$

which represents a three-fold improvement of the previously measured value, reported in [126]. In addition, Eq. (5.23) is a test of CPT invariance in the lepton sector.

The ALPHA collaboration has planned to use a novel approach to place a more stringent bound on the \bar{H} charge. The technique, called *stochastic acceleration* and described in [135], employs a series of randomly oscillating electric fields to walk the antiatoms out of the trap, if they are charged. The advantage of this technique is that the experimental sensitivity depends strongly on the number of acceleration cycles, which can be made arbitrarily large by exploiting the long \bar{H} confinement time. The data collected in 2014 are part of the analysis presented in the next chapter.

6 ALPHA-2 Commissioning

In 2014 the upgraded ALPHA apparatus started taking data and the new SVD commenced its operations. The goal of ALPHA was to re-establish the $\bar{\text{H}}$ trapping procedure and to test the new spectroscopy tools: the UV laser (wavelength of 243 nm) system for the two-photon spectroscopy of the 1S-2S transition, the μW injector for the positron-spin-flip measurement and, eventually, the Ly- α laser (Lyman-alpha with a wavelength of 122 nm) system for spectroscopy of the 1S-2P transition and laser cooling.

The SVD is employed in the detection of $\bar{\text{H}}$, or lack thereof in the case of the so-called *disappearance* measurement, where the antiatoms are ejected from the trap upon interaction with the radiation. Therefore, the SVD requires careful testing that is performed, mainly, with cosmic rays and, secondly, with hot $\bar{\text{H}}$ during the $\bar{\text{p}}\text{-e}^+$ mixing phase. Functionality of all the SVD channels can be tested at once by using cosmic rays and comparison with their known physical features gives assurance of data quality (see Sec. 6.1). In addition, performance stability is guaranteed by comparing the analysis of cosmic data taken on different days.

Operating the SVD without antiparticles in the traps is useful not only for its commissioning, but also to devise a procedure to discriminate background events, i.e., rays cosmic, from signal events, i.e., $\bar{\text{H}}$ annihilations. Studying the properties of the events in a cosmic sample and in a hot $\bar{\text{H}}$ sample (typically produced in the “mixing” phase of the experiment) allows one to identify the signature of true annihilations. The discrimination of the $\bar{\text{H}}$ annihilation from the background is

obtained by means of two different procedures:

- “cut” analysis and
- Multi-Variate Analysis, or MVA.

The former is discussed in Sec. 6.2 and the latter in Sec. 6.4. Both analyses are used in the present work to determine the trapping rate of selected experiments, as described in Secs. 6.3 and 6.4.2, respectively. The cut analysis is used to establish the trapping capabilities of the upgraded apparatus (ALPHA-2), while the MVA is adopted in a new and more accurate determination of the \bar{H} electric charge, that will be published in a forthcoming paper. However, the MVA is extremely powerful in extracting small signals from a large background. This is the case of spectroscopy in ALPHA, where the small number of available antiatoms is balanced by the longer exposure time to laser and/or microwave radiation. The analysis presented here represents a useful test-bench for this technique.

6.1 SVD Commissioning

The performance of the SVD is evaluated with cosmic rays. The procedure employs “low-level” reconstruction information, e.g., strips fired, assuming that all the silicon modules and the VA1TA chips (see Sec. 3.2) are properly biased. Once all the hits are reconstructed from the strips clusters, the Principal Component Analysis (PCA) is applied to study events due to cosmic rays.

As mentioned in Sec. 4.2.1, the PCA selects the most significant features of a set of measurements by looking at the largest eigenvalue, and the corresponding eigenvector, of the covariance matrix. This method is particularly suited for cosmic rays that can be modelled by straight lines. When one of these high energy particles travels through the SVD, it is very likely that it creates three

hits, one per layer, at its entering point and three more, again one per layer, on the opposite side, for a total of six hits, as shown in Fig. 6.1. These measurements of the cosmic track are fed into the PCA. When the largest eigenvalue of the covariance matrix of the hit positions, i.e., “the correlation”, is very close to unity, it is certain that a track due to a high energy μ^\pm has been found. The cosmic track is given by

$$\mathbf{l}(t) = \begin{cases} u_x t + x_0 \\ u_y t + y_0 \\ u_z t + z_0, \end{cases} \quad (6.1)$$

where t is a real parameter, $\mathbf{u} = (u_x, u_y, u_z)$ is its slope, such that $|\mathbf{u}| = 1$, and (x_0, y_0, z_0) is a point on the track given by the average hits positions. The slope is indeed the covariance matrix eigenvector corresponding to the largest eigenvalue.

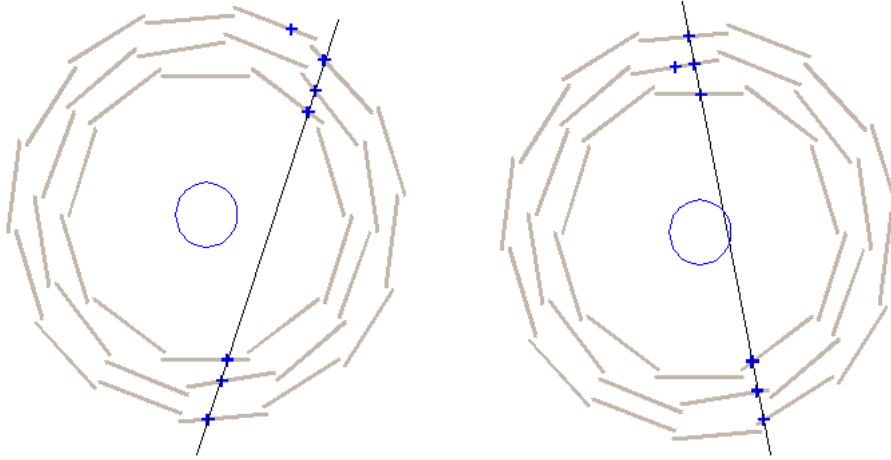


Figure 6.1: Front view of cosmic tracks (black line) reconstructed with the PCA from groups of six collinear hits (blue crosses).

The distribution of the time elapsed between two events reconstructed with the method described above must follow a negative exponential function, if successful reconstruction of a cosmic ray is achieved. Fig. 6.2 shows the expected

behaviour and the cosmic rate Γ from the best-fit to the function

$$\exp(-\Gamma\Delta t + A) \tag{6.2}$$

is equal, within the statistical error, to its more conventional form as the number of reconstructed vertices over the data collection time.

Time Interval Between Cosmic Rays

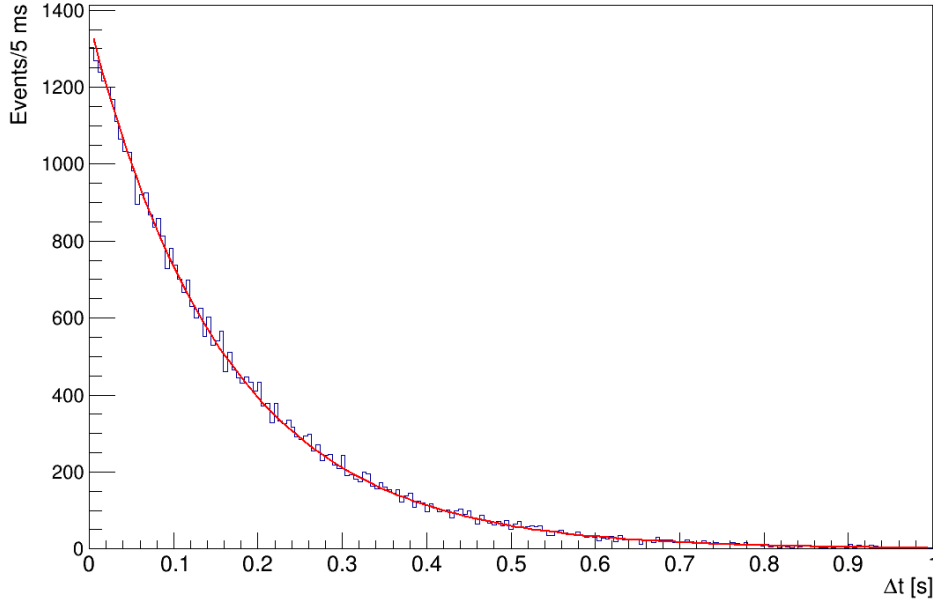


Figure 6.2: Time interval between cosmic events Δt (blue line) and best fit to negative exponential function (red line) given by Eq. (6.2).

Cosmic Sample	
Total Run Time	28 991 s [~ 8 h]
Number of Reconstructed Vertices	178 516
Vertices for $N_{\text{helices}} = 2$	168 916 [95%]
Vertices for $N_{\text{helices}} > 2$	9 600 [5%]
Rate	(6.22 ± 0.03) Hz

Table 6.1: Main characteristics of the cosmic data sample used for SVD commissioning.

6.1.1 Relative Alignment of the Hybrids

The first utilization of the above procedure is to evaluate the relative alignment of the hybrids with respect to each other. For each hit in the cosmic track calculated above, a new track is found with the same method, using the other five hits. Then, the distance between the excluded hit and the intersection of the new track with the plane identified by the hybrid of the excluded hit yields a measurement of the relative alignment of the hybrid under consideration with respect to the other five.

The position of an hybrid is uniquely determined by the coordinates of its centre (x_c, y_c, z_c) and the azimuthal angle ϕ . The hybrid therefore lies in the plane described by its normal vector $(\cos \phi, \sin \phi, 0)$ and its centre and given by the following formula

$$(x - x_c) \cos(\phi) + (y - y_c) \sin(\phi) = 0, \quad (6.3)$$

where (x, y) is a point on the hybrid. The axial coordinate of centre is $z_c = \pm 11.5$ cm, where the $-$ sign indicates the upstream end and the $+$ sign the downstream one. The intersection point (x_I, y_I, z_I) of the new five-hit track with the plane of the hybrid is given by

$$\begin{aligned} x_I &= u_x \frac{(x_c - x_0) \cos \phi + (y_c - y_0) \sin \phi}{u_x \cos \phi + u_y \sin \phi} + x_0 \\ y_I &= u_y \frac{(x_c - x_0) \cos \phi + (y_c - y_0) \sin \phi}{u_x \cos \phi + u_y \sin \phi} + y_0 \\ z_I &= u_z \frac{(x_c - x_0) \cos \phi + (y_c - y_0) \sin \phi}{u_x \cos \phi + u_y \sin \phi} + z_0, \end{aligned} \quad (6.4)$$

where the analytic expression of the track Eq. (6.1) is obviously still valid. Since the hybrid alignment will be expressed for the p- and n-side separately, the coordinates of the intersection point are rotated into local coordinates system of the

hybrid (x_L, y_L, z_L) by means of the following transformation:

$$\begin{aligned}
x_L &= (x_I - x_c) \cos \phi + (y_I - y_c) \sin \phi \\
y_L &= (y_I - y_c) \cos \phi - (x_I - x_c) \sin \phi \\
z_L &= z_I.
\end{aligned} \tag{6.5}$$

The distance between the actual hit position, in the local reference frame of the hybrid, (p, n) and the intersection point gives the alignment between the hybrid containing the hit. The distance is broken up into the p-strip component, that is, the y direction in the local reference frame of the hybrid, and the n-strip direction, that is, the z direction, yielding the residual per strip per hybrid:

$$\begin{aligned}
\delta_y &= p - y_L, \\
\delta_z &= n - z_L.
\end{aligned} \tag{6.6}$$

In order to grasp the general trend of the alignment, the residuals δ_y and δ_z are averaged over the totality of the p-strips and the n-strips, respectively, of the hybrid and over all N events collected:

$$\begin{aligned}
\langle \delta_y \rangle_m &= \frac{1}{N} \sum \frac{1}{256} \sum^{256} \delta_y, \\
\langle \delta_z \rangle_m &= \frac{1}{N} \sum \frac{1}{256} \sum^{256} \delta_z,
\end{aligned} \tag{6.7}$$

where $m = 0, \dots, 71$ is the hybrid number. The results are plotted in Fig. 6.3, where the error bars are given by the standard deviations

$$\begin{aligned}
s_y &= \sqrt{\langle (\delta_y - \langle \delta_y \rangle_m)^2 \rangle}, \\
s_z &= \sqrt{\langle (\delta_z - \langle \delta_z \rangle_m)^2 \rangle}.
\end{aligned} \tag{6.8}$$

The overall trend in Fig. 6.3 shows a good relative alignment within $200 \mu\text{m}$ for the p-strips and $100 \mu\text{m}$ for the n-strips.

Whether the SVD is rotated with respect to its axis, that is, the z axis, can be assessed by looking at the angle α between the cosmic track and the vertical,

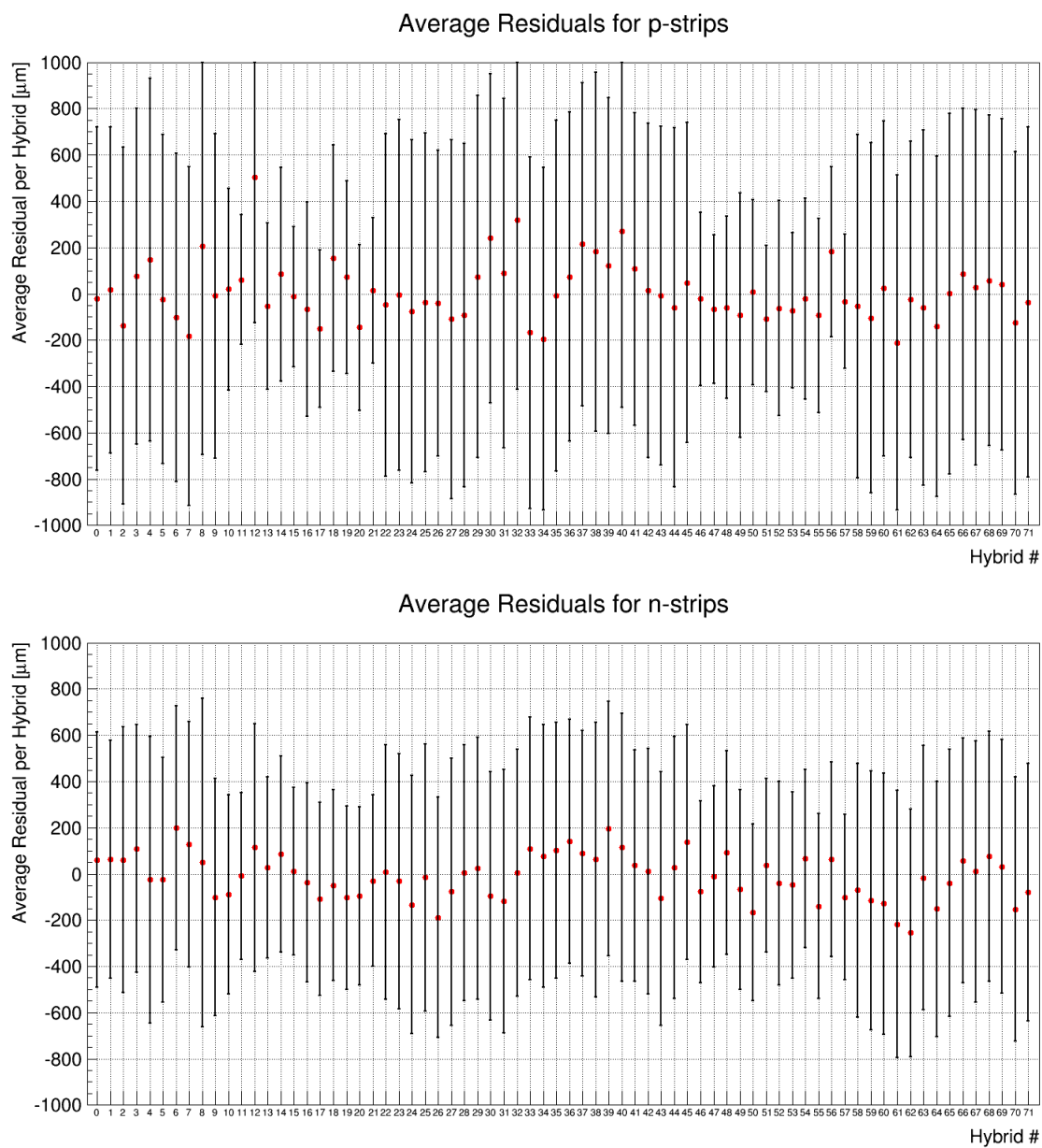


Figure 6.3: Relative alignment of the hybrids given by the residual per strip, Eq. (6.7). The error bars are calculated with Eq. (6.8).

for which $\alpha = 0$. This follows from the known distribution “cosine squared” of the direction of the cosmic rays, thus is suitable for testing the SVD features.

The distribution obtained by calculating the angle between the y axis and the cosmic tracks is shown in Fig. 6.4, together with the best-fit function

$$A \cos^2(w\alpha + \alpha_0). \quad (6.9)$$

The role of w is to assess whether there is any anomaly in the distribution. The result of the fit shows that $w \approx 1$, as expected, and $\alpha_0 = (17.8 \pm 0.1)$ mrad, giving a good indication that there is not a significant rotation of the SVD with respect to its axis.

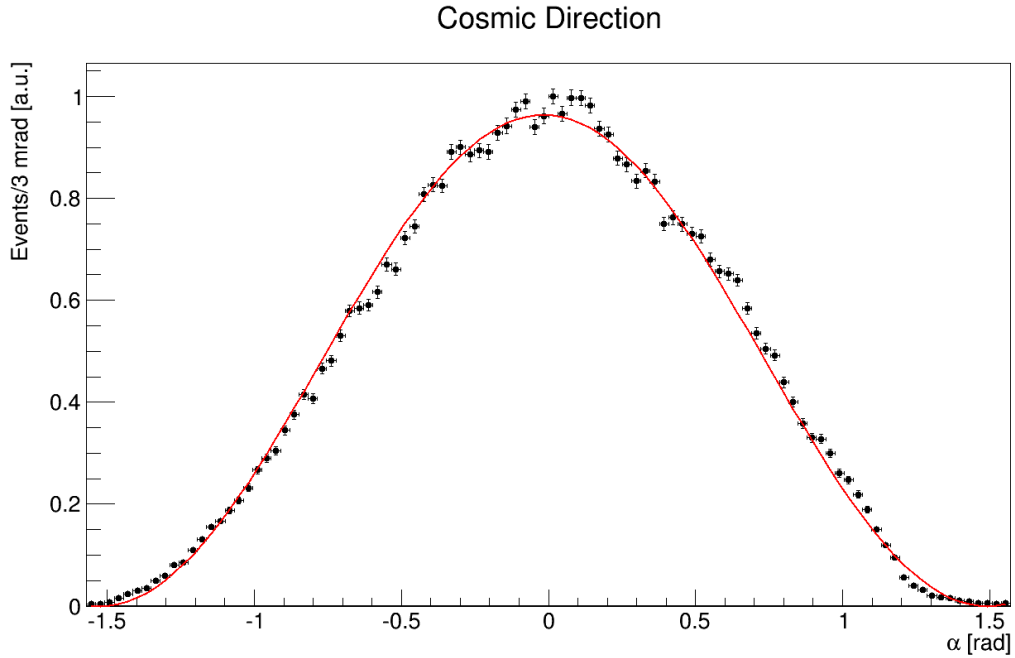


Figure 6.4: Distribution of the angle between the cosmic track Eq. (6.1) and the vertical (black dots) and best-fit (red line) to Eq. (6.9).

6.1.2 Efficiency per Hybrid

The strip efficiency per hybrid is evaluated by taking the ratio of the number of strips in a hybrid that contains a hit to the number that should have been hit by

a cosmic ray.

A straight line Eq. (6.1) is calculated with the PCA from the combination of five hits that yields the highest correlation and its intersection with the hybrids is found from Eq. (6.4). For each hybrid, the intersection, i.e., the expected hit, is transformed to the local coordinate system of the hybrid and is separated into its p and n contributions. Their number in all the collected events is called I^p and I^n , respectively.

If an intersection is found on the hybrid, the actual p- and n-strip clusters (if any) are also recorded. Their number is labelled H^p and H^n , respectively. The strips efficiency per hybrid is therefore the ratio

$$\epsilon_m^{p,n} = \frac{H^{p,n}}{I^{p,n}}, \quad (6.10)$$

where $m = 0, \dots, 71$ is the hybrid number. The results are shown in Fig. 6.5, where the error bars are given by

$$\delta\epsilon_m^{p,n} = \sqrt{\frac{\epsilon_m^{p,n}(1 - \epsilon_m^{p,n})}{I^{p,n} - 1}}. \quad (6.11)$$

The p-strips are slightly more efficient than the n-strips, as it can be expected from the different noise level for the two (the bonding wires of the n-strips are longer and thus noisier, see Sec. 3.1). However, Fig. 6.5 shows that the overall efficiency is very high. For the p-strips it is always greater than 96% and for the n side it is greater than 95%, i.e., both averages are close to one. This result is very important in the light of the fact that the SVD is limited to three layers because, as mentioned in Sec. 4.4, losing a hit due to a strip inefficiency might cause the loss of a whole track that, for events with low multiplicity, means failing to reconstruct the vertex.

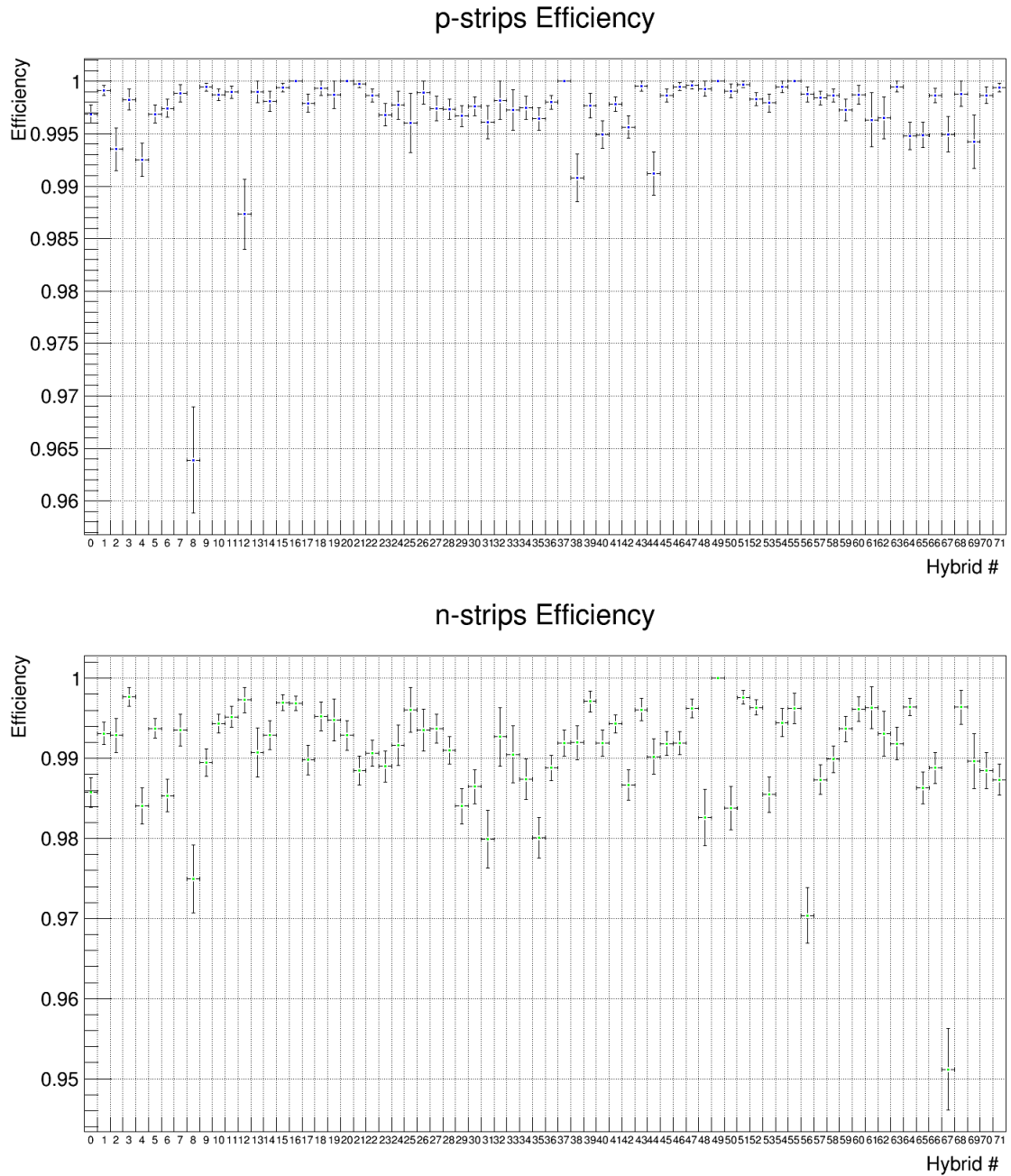


Figure 6.5: Strips efficiency

6.2 Background Rejection

The goal of the following analysis is to determine whether an event recorded by the SVD is compatible with the background or is “true signal”, i.e., \bar{H} annihilation

lation. The discrimination occurs by applying *cuts on selected variables*, which characterize the event under consideration.

A sample representing the signal and a sample representing the background are used to determine the optimal cut values. The so-called *signal sample* or *mixing sample* is constituted by events recorded by the SVD during the mixing phase of the experiment, where hot (hence un-trappable) \bar{H} are produced (see Tab. 6.2). The advantage of using “mixing data” lies in the high number of events available in a short period of time, that happens in every experiment cycle. More importantly, knowledge of the mixing data does not bias any other analysis conducted on trapped \bar{H} . The signal sample contains a contamination due to cosmic rays of $\sim 1\%$. The cosmic sample, as mentioned several times in this chapter, is collected by operating the SVD without antiparticles in the trap.

Mixing Sample	
Total Run Time	129 s
Number of Reconstructed Vertexes	58 265
Vertexes for $N_{\text{helices}} = 2$	17 054 [29%]
Vertexes for $N_{\text{helices}} > 2$	41 211 [71%]

Table 6.2: Main characteristics of the mixing data sample used for the determination of the optimal cuts for background rejection.

6.2.1 Discriminating Variables

For each event that has a reconstructed vertex, the discriminating variables are:

- the number of reconstructed tracks N_{helices} ,
- the radial position of the vertex R ,
- the residual squared δ (defined below).

As discussed in Sec. 5.2, the vast majority of cosmic rays appear in the SVD as two helices (also see Tab. 6.1), with a very large radii of curvature (since in reality they are two halves of a single track). Therefore, events with $N_{\text{helices}} = 2$ and with $N_{\text{helices}} > 2$ are treated separately, as they represent two physically distinct categories.

The radial position of the reconstructed vertex, R , of an \bar{H} annihilation cannot be greater than the electrodes inner radius. However, due to the finite resolution of the SVD and other physical effects, like the multiple scattering of the annihilation products, the distribution of the reconstructed vertices has a finite width centred around the electrodes inner radius. The radius of the vertex of a cosmic event can, in principle, take any value, since there is no physical meaning associated with it. Only vertices close enough to the trap are likely due to \bar{H} annihilation. The distribution of the radius of reconstructed vertices for \bar{H} annihilation and cosmic rays is shown in Fig. 6.6.

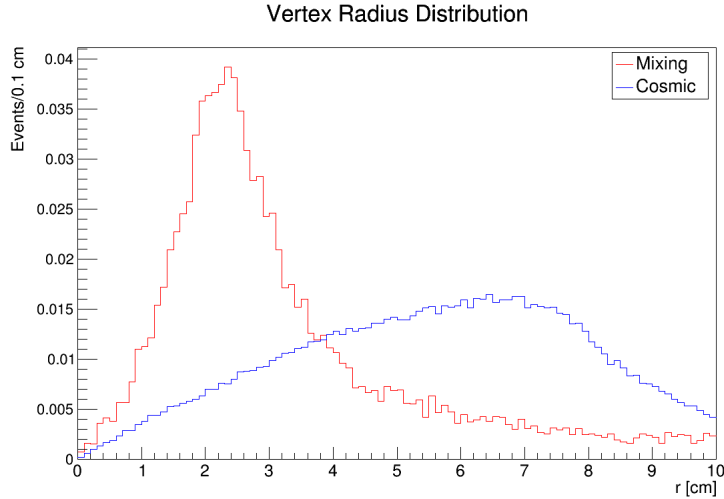


Figure 6.6: Distribution of the radius of the reconstructed vertex for cosmic and mixing data.

A typical π^\pm due to \bar{H} annihilation has a momentum of ≈ 300 MeV, thus the radius of curvature of its trajectory in the 1 T solenoidal field is ≈ 1 m. The momentum of the typical cosmic ray is much higher: for a μ^\pm of 1 GeV the radius of curvature is ≈ 3 m. That is, cosmic trajectories look much straighter than annihilation products by virtue of their higher momentum. As mentioned in Sec. 5.2, the straightness of the reconstructed tracks is determined by taking six hits belonging to a pair of tracks (recall that a track is defined by exactly three hits, one per each layer of the SVD) and applying the PCA, described in Sec. 4.2.1, to them. The correlation coefficient that results from this procedure is very close to one for cosmic tracks, as shown in Fig. 6.7.

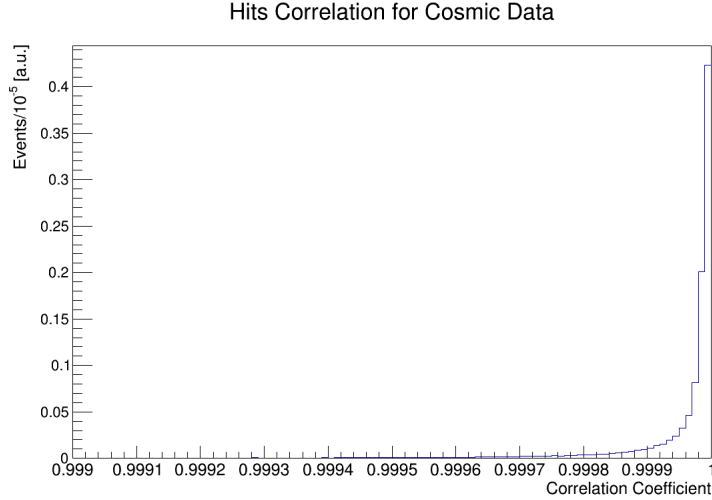


Figure 6.7: Correlation among hits, due to cosmic rays, used in the calculation of the squared residual Eq. (6.12).

At this point the role of the two distinct categories, $N_{\text{helices}} = 2$ and $N_{\text{helices}} > 2$, should be clear, since there is no ambiguity on which pair of helices to use to determine the correlation coefficient for events in the $N_{\text{helices}} = 2$ category. For events for which $N_{\text{helices}} > 2$, the ambiguity is solved by iterating the PCA on every possible combination of two helices and keeping only the pair with the highest

correlation coefficient. By labelling the coordinates of the six hits (x_h, y_h, z_h) , for $h = 1 \dots 6$, and by using the equation of the straight line found by the PCA and given by Eq. (6.1), the squared residual is

$$\delta = \sum_{h=1}^6 (l_x(\tilde{t}_h) - x_h)^2 + (l_y(\tilde{t}_h) - y_h)^2 + (l_z(\tilde{t}_h) - z_h)^2, \quad (6.12)$$

where

$$\tilde{t}_h = \frac{u_x(x_0 - x_h) + u_y(y_0 - y_h) + u_z(z_0 - z_h)}{|\mathbf{u}|^2}. \quad (6.13)$$

The residual is large for π^\pm and small for cosmic rays, as shown in Fig. 6.8.

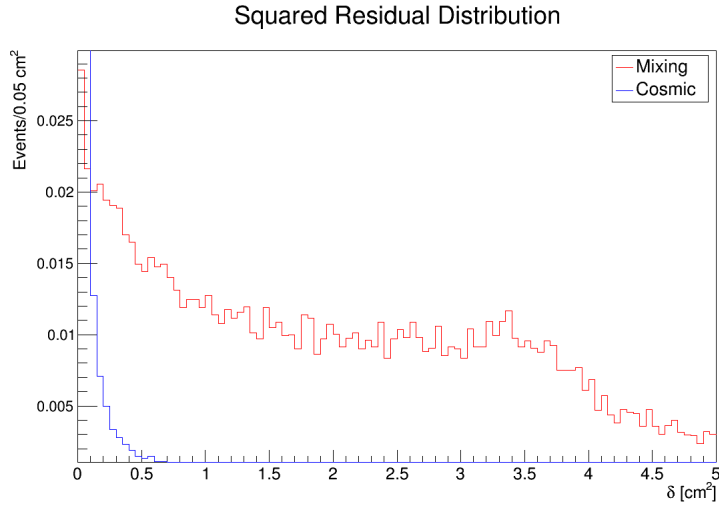


Figure 6.8: Distribution of the squared residual Eq. (6.12) for cosmic and mixing data. The content of the first bin of the distribution of the cosmic ray is off scale.

In the present analysis, events without a reconstructed vertex are not considered.

6.2.2 Cuts Placement

The number of observed events s is, by hypothesis, due solely to background, namely, produced by any mechanism other than $\bar{\text{H}}\text{H}$ annihilation and, given Fig. 6.2,

the background is distributed like a Poissonian with mean b

$$P(s; b) = \frac{b^s e^{-b}}{s!}. \quad (6.14)$$

The number of observed events in the signal sample s and the number of cosmic events in the background sample b are functions of the cut values R_{cut} and δ_{cut} :

$$s = s(R_{\text{cut}}, \delta_{\text{cut}}, N_{\text{helices}}) \quad (6.15)$$

$$b = b(R_{\text{cut}}, \delta_{\text{cut}}, N_{\text{helices}}). \quad (6.16)$$

The dependence on N_{helices} is “removed” in the following formulas, in the sense that the cuts are studied independently for the two categories of events: the ones with $N_{\text{helices}} = 2$ and the ones with $N_{\text{helices}} > 2$. In the present derivation, all the formulae refer to a particular category only and the variable N_{helices} is omitted.

The significance of observing s events, i.e., the p-value, called α here, is calculated for each set of cuts. The optimal set of cuts is obtained by minimizing α , i.e., the probability of making an error of the first kind, that becomes a function of the cuts. The p-value for a fixed set of cuts is

$$\alpha = \alpha(\bar{s}, \bar{b}) = \sum_{n=\bar{s}}^{\infty} \frac{\bar{b}^n e^{-\bar{b}}}{n!}, \quad (6.17)$$

where \bar{s} is the number of *passed-cuts* events, \bar{b} is the number of expected background events and the Poisson probability distribution function $P(n; \bar{b})$ is given by Eq. (6.14) with $n = s$.

The expected background is given by

$$\bar{b} = \frac{T_{\text{sig}}}{T_{\text{bkg}}} b(R_{\text{cut}}, \delta_{\text{cut}}), \quad (6.18)$$

where T_{sig} is the total signal collection time, T_{bkg} is the total background collection time and $b(R_{\text{cut}}, \delta_{\text{cut}})$ is obtained from Eq. (6.16) by parsing the background

dataset and counting how many events satisfy the particular cuts R_{cut} and δ_{cut} . The role of the ratio $T_{\text{sig}}/T_{\text{bkg}}$ is to normalize the number of background events to the one expected in a single experiment.

The number of *passed-cuts* events is given by

$$\bar{s} = \frac{n_0}{s_{\text{scale}}} s(R_{\text{cut}}, \delta_{\text{cut}}), \quad (6.19)$$

where $n_0 \in [10, 120]$ is the *guessed* number of passed-cuts events and s_{scale} is the value assumed by Eq. (6.15) with a default set of cuts that, for convenience's sake, are the ones employed in ALPHA-1 (see Tab. 5.1). The role of the ratio n_0/s_{scale} is to normalize the number of passed-cuts events to that expected in a single experiment. The value of $s(R_{\text{cut}}, \delta_{\text{cut}})$ is calculated from Eq. (6.15) by parsing the signal dataset and counting how many events satisfy the particular cuts R_{cut} and δ_{cut} .

Given Eqs. (6.18) and (6.19) the dependence of α on R_{cut} and δ_{cut} is evident.

The guessed number of passed-cuts events n_0 assumes $k = 111$ different values and embodies the principle that the number of true $\bar{\text{H}}$ annihilation is unknown, and must remain so, until the experimenter looks at the actual data of the measurement of interest. A mean p-value for a particular set of cuts is thus taken as log-average of the k values assumed by Eq. (6.17):

$$\bar{\alpha}(R_{\text{cut}}, \delta_{\text{cut}}) = \exp \left(\frac{1}{k} \sum_{n_0=10}^{120} \ln \alpha(\bar{s}, \bar{b}) \right). \quad (6.20)$$

The significance of each set of cuts is determined as

$$\sigma(R_{\text{cut}}, \delta_{\text{cut}}) = \sqrt{2} \operatorname{erfc}^{-1}(2\bar{\alpha}), \quad (6.21)$$

where $\operatorname{erfc}^{-1}(x)$ is the inverse of the complementary error function

$$\operatorname{erfc}(x) = \frac{2}{\sqrt{\pi}} \int_x^{\infty} dt e^{-t^2}. \quad (6.22)$$

The calculation of σ in Eq. 6.21 is repeated for every pair $(R_{\text{cut}}, \delta_{\text{cut}})$, spanning the range of interest in discrete small steps, as shown in Fig. 6.9 for $N_{\text{helices}} = 2$ and in Fig. 6.10 for $N_{\text{helices}} > 2$.

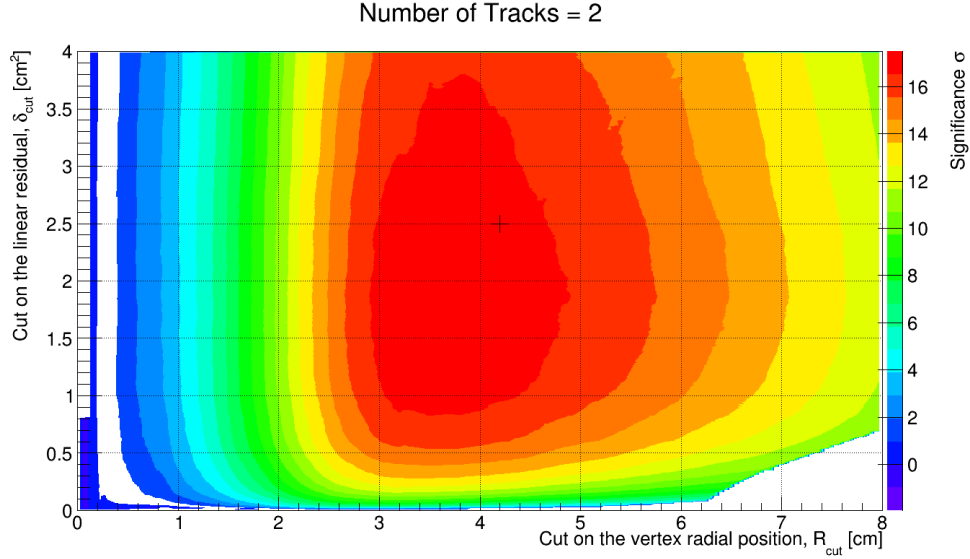


Figure 6.9: Significance σ , given by Eq. (6.21), as a function of the cuts R_{cut} and δ_{cut} for $N_{\text{helices}} = 2$ events. The position of the cross indicates the chosen optimal cuts.

6.2.3 Results

The optimal cuts are found by locating the maxima along the z -axis (colours) in Figs. 6.9 and 6.10 and by reading off the x and y values. The final choice is made by taking into account the fraction of background events rejected against the fraction of events accepted in the mixing sample. In addition, the residual cut for the $N_{\text{helices}} > 2$ category is chosen by keeping in mind that only a small fraction of the background sample falls into this category, as can be seen from Fig. 6.11.

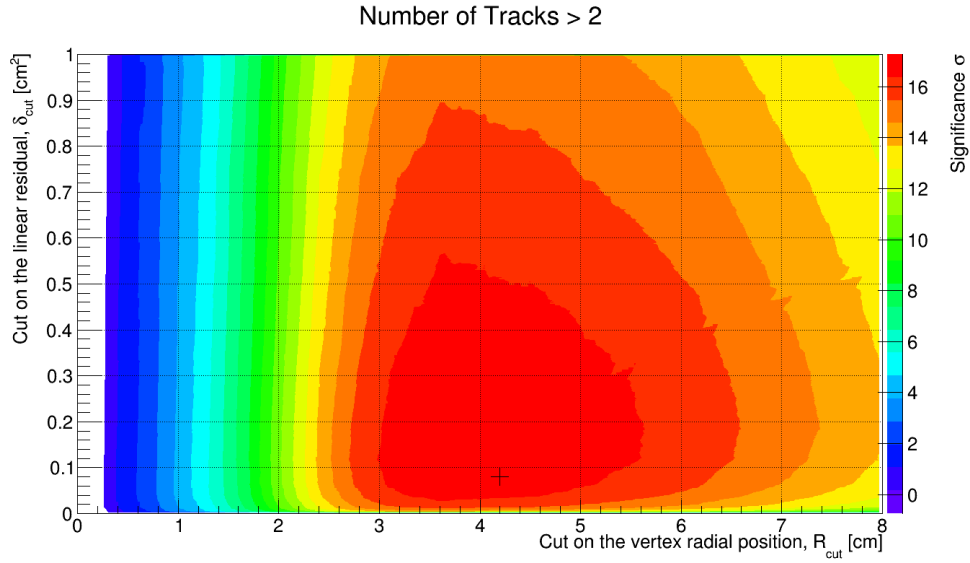


Figure 6.10: Significance σ , given by Eq. (6.21), as a function of the cuts R_{cut} and δ_{cut} for $N_{\text{helices}} > 2$ events. The position of the cross indicates the chosen optimal cuts.

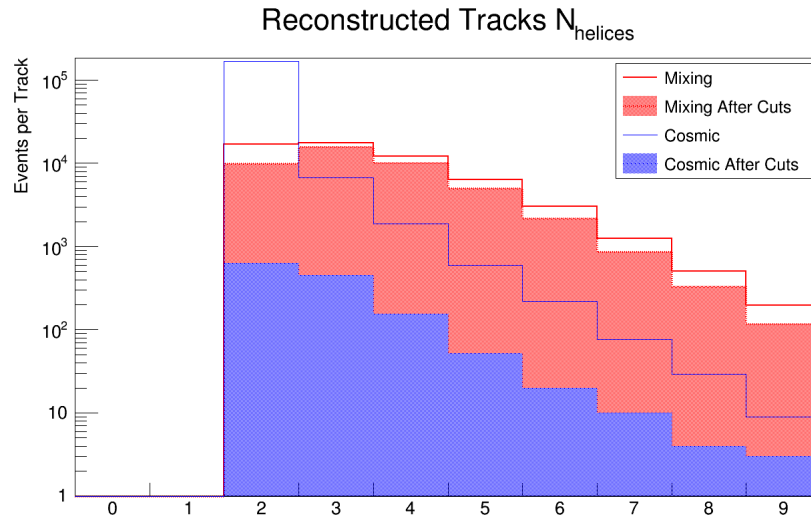


Figure 6.11: Distributions of the number of reconstructed tracks in the mixing and cosmic samples before and after using the cuts of Tab. 6.3.

The cuts deemed optimal are listed in Tab. 6.3. With this set of cuts, $(99.26 \pm 0.02)\%$ of the vertices in the background sample are rejected, while $(75.9 \pm 0.1)\%$ of the vertices in the signal sample are accepted.

	$N_{\text{helices}} = 2$	$N_{\text{helices}} > 2$
Vertex Radius R_{cut} [cm]	4.20	4.20
Squared Residual δ_{cut} [cm ²]	2.50	0.08

Table 6.3: Value of the cuts on the discriminating variables used in cosmic rejection in ALPHA-2.

The cosmic rate is calculated from the background sample with the cuts listed in Tab. 6.3:

$$\frac{\text{passed-cut events}}{\text{background collection time}} = (46 \pm 1) \text{ mHz}. \quad (6.23)$$

The effect of the cuts on the distributions of the vertex radius and the squared residual is shown in Fig. 6.12 and in Fig. 6.13, respectively. The blue-shaded distribution is the irreducible background that corresponds to the rate Eq. (6.23). However, the cosmic rejection can be further improved by studying the time and axial vertex position distributions.

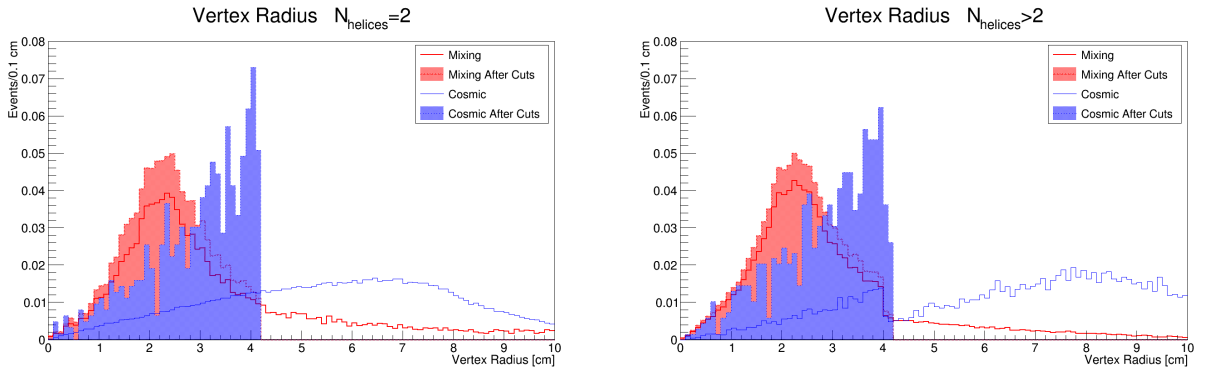


Figure 6.12: Distributions of the vertex radius for mixing and cosmic data before and after the cuts given in Tab. 6.3. Each distribution is normalized to its integral.

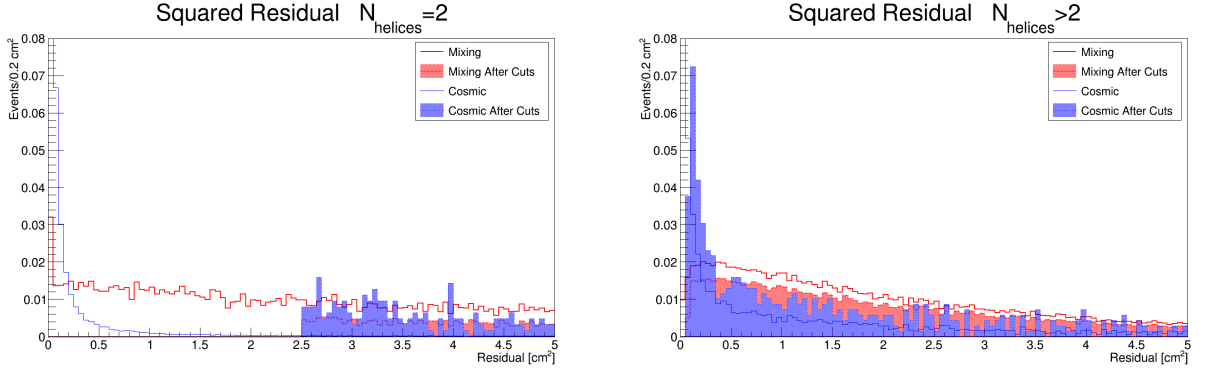


Figure 6.13: Distribution of the squared residual Eq. (6.12) for mixing and cosmic data before and after the cuts given in Tab. 6.3. Each distribution is normalized to its integral.

6.3 Standard Analysis of Trapped Antihydrogen

The previous analysis is applied in this section to the study of 104 experiments of $\bar{\text{H}}$ trapping to prove that the new ALPHA-2 apparatus works at least as well as ALPHA-1. A single experiment was outlined in Tab. 2.1, where each phase is optimized to eventually yield the largest number of trapped antiatoms. This brief section deals with the analysis of the events detected by the SVD when the magnetic trap is shut down, i.e., the so-called “quench”.

6.3.1 Analysis

In these experimental series, the antiatoms are confined for ≈ 400 ms and then released by quickly shutting down the superconducting magnets. In about $t_q = 30$ ms the inhomogeneous magnetic field that confines $\bar{\text{H}}$ is 0.01 % of its initial value, therefore only antiatoms detected within this time window are taken into account.

The number of reconstructed vertices in $104 \times 30 \text{ ms} = 3.12 \text{ s}$ is 128.

The expected number of cosmic events, from Eq. (6.23), is

$$3.12 \text{ s} \times 46 \text{ mHz} = 0.144 \pm 0.003 \ll 1.$$

After applying the cuts in Tab. 6.3, 86 ± 9 passed-cuts events are found and their distribution in the trapping attempts is shown in Fig. 6.14.

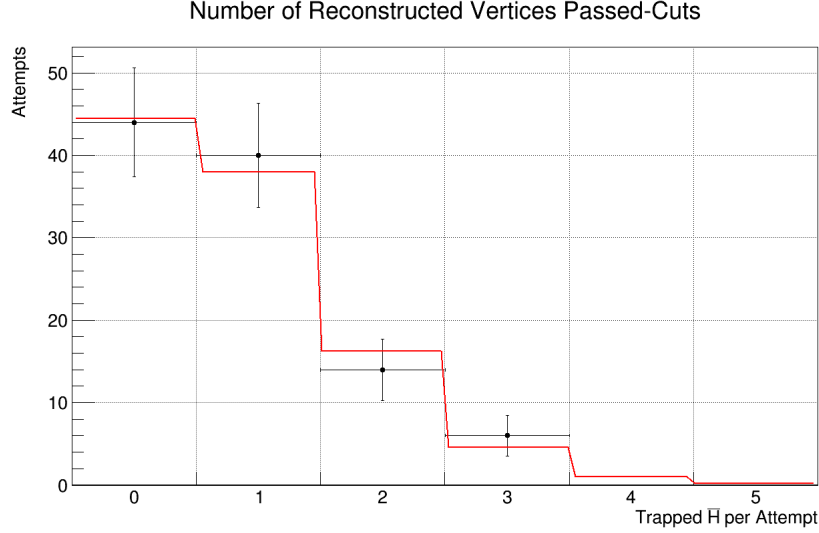


Figure 6.14: Distribution of passed-cuts \bar{H} (black dots) in 104 trapping attempts, for a total observation time of 3.12 s. The best-fit with Eq. (6.24) is overlaid (red line).

Since the trapping experiments are independent, the distribution in Fig. 6.14 is Poissonian and the fit to the probability distribution function

$$\frac{\mu^n e^{-\mu}}{n!}, \quad (6.24)$$

where n is the number of \bar{H} trapped in each attempt, gives the best estimation of the mean $\mu = 0.9 \pm 0.1$.

The radial and the axial position of the vertices that passed the selection are shown in Fig. 6.15. The radial distribution is peaked around the trap radius

2.275 cm. One event in the z distribution is found beyond the physical position of the mirror coils, i.e., outside the trap, and therefore it can be excluded, yielding 85 ± 9 trapped $\bar{\text{H}}$.

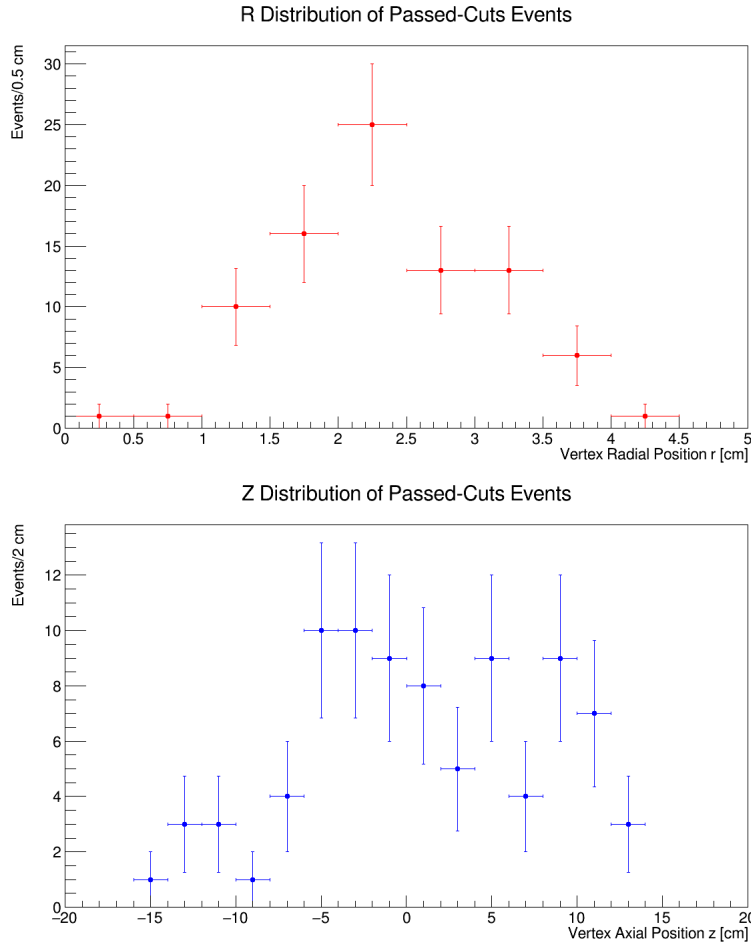


Figure 6.15: Distributions of the radial (top) and axial (bottom) position of the passed-cuts vertices.

The time distribution of the events is shown in Fig. 6.16 along with its cumulative distribution and the ones calculated from thermal energy distribution at the temperatures indicated. By observing the cumulative distribution, one can estimate that the temperature of the trapped $\bar{\text{H}}$ is between 50 and 100 mK.

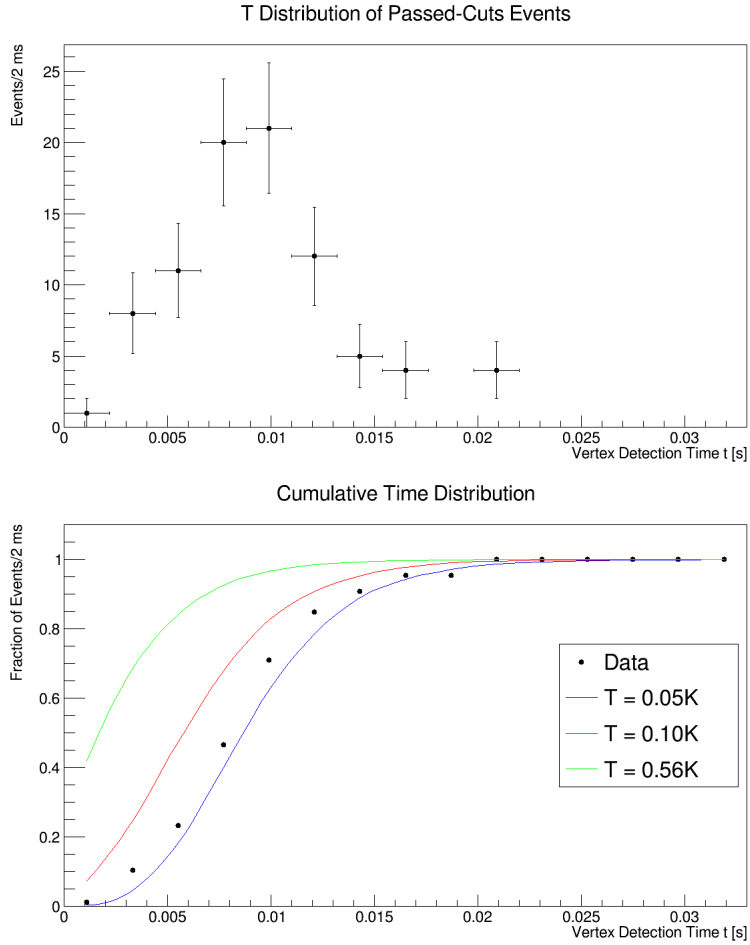


Figure 6.16: Top: Distribution of passed-cuts events as function of time from the magnet shutdown. Bottom: Cumulative of the time distributions of the passed-cut events, along with the ones estimated from thermal distribution of energies at the temperatures indicated in the inset. The green curve $T = 0.56$ K corresponds to the trap depth, estimated at the end of Sec. 2.3.

The cumulative of the time distribution at different temperatures (shown by the solid coloured lines in Fig. 6.16) are calculated by assuming that the trapping magnetic field, and hence the magnetic potential energy U , given by Eq. (2.10),

decreases in time t according to

$$B(t) = B_0 \exp(-\beta t) , \quad (6.25)$$

where B_0 is given by Eq. (2.20) and $\beta^{-1} \approx 4$ ms. By drawing 10 000 energy values U for each temperature $T = 0.56, 0.1, 0.05$ K from the Maxwell-Boltzmann energy distribution

$$f(U) = 2 \left(\frac{U}{\pi} \right)^{\frac{1}{2}} (k_B T)^{-\frac{3}{2}} \exp \left(-\frac{U}{k_B T} \right) ,$$

where $k_B = 0.086$ meV/K is the Boltzmann constant, the annihilation time is found by inverting Eq. (6.25), upon multiplication by the Bohr's magneton. The annihilation time $t = U(t)^{-1}$ then populates different histograms, whose cumulative distributions are shown in Fig. 6.16.

6.3.2 Conclusions

While the analysis of the mirror-trapped \bar{p} is neglected in the present discussion, the clearing pulses after the mixing phase are still employed and, as concluded in [101], they are sufficient to remove unbound \bar{p} from the trap.

The SVD is shown in Sec. 6.1 to perform according to design. The cosmic rejection procedure, described in Sec. 6.2, gives a powerful way to discriminate between background and \bar{H} annihilation events, allowing to study to the properties of the latter.

The present analysis shows that the ALPHA-2 apparatus has improved trapping capabilities with respect to ALPHA-1 and that the new apparatus is ready to perform high-precision measurements on trapped \bar{H} .

The next section presents an alternative and more powerful technique to extract the SVD signals due to \bar{H} from the cosmic background.

6.4 Multi-Variate Analysis of Trapped Antihydrogen

In this section a different approach to the analysis of the $\bar{\text{H}}$ candidates detected by the SVD is adopted. The present analysis targets twenty experiments conducted to improve the determination of the upper limit to the $\bar{\text{H}}$ electric charge. They are constituted by ten trials where a stochastic time-varying electric field is applied to trapped $\bar{\text{H}}$, interleaved with ten other trials where the potentials are zeroed, while $\bar{\text{H}}$ is confined for the same amount of time. The technique goes under the name of *stochastic acceleration* and is described in [135]. Since the experiment under consideration is a “counting experiment”, where the comparison of the number of $\bar{\text{H}}$ detected after the magnet shutdown in the stochastic acceleration and the null trials is used to establish whether the electric potentials had an effect on trapped $\bar{\text{H}}$, a Multi-Variate Analysis, or MVA, is applied to the study of the “quench data” for the twenty experimental runs.

The standard procedure to determine whether an event is an $\bar{\text{H}}$ candidate makes use of the radius of the vertex, hence a fully reconstructed event is always necessary. On the contrary, the MVA classification includes, but is not limited to, the vertex position. Given the nature of the experiment under consideration, the actual location of the $\bar{\text{H}}$ annihilation is irrelevant, while the MVA can still safely identify an $\bar{\text{H}}$ candidate.

The MVA, as used in this analysis, is a pattern recognition algorithm⁶ whose goal is to classify events, mixed in a data sample, to different categories, i.e., signal and background. The events are characterized by a set of variables and a classifier uses them to assign to each event a label that is consistent with either category. The MVA chosen for the present study assigns a *continuous* value between 0 and 1 to an event, where a low score means that the event is compatible with the

⁶The PCA, described in Sec. 4.2 and extensively used in Sec. 6.1 is another example of pattern recognition algorithm.

background.

The MVA classifier used here is the *Bootstrap Aggregating Decision Trees*, or Bagging DTs [136], and its implementation is found in the statistical analysis package SPR, described in [137]. A *decision tree* is a classifier structured like a tree, where the input data are recursively split into rectangular regions, or *nodes*. At each iteration, the split that optimizes the separation between signal and background in the node is retained and is further split into finer nodes, until a stopping condition is reached that makes that node “terminal”, or a *leaf*. The optimal separation between signal and background is assessed by means of a figure of merit: the present analysis makes extensive use of the *Punzi significance* [138]. A leaf is reached when it is impossible to find a split that improves the figure of merit and/or the minimal number of events per node is attained.

A single decision tree has not enough predictive power to yield a good separation of signal from background. The classification capability is enhanced by growing an ensemble of trees, using a randomness element to generate a forest [139]. A popular method to create a *random forest* is by employing a *bagging algorithm*, which trains new classifiers on bootstrap replicas of the input data. A bootstrap replica is obtained by sampling with replacement the training dataset until the size of the original set is reached. Upon completion of the training, an event is classified according to the majority of votes of the trained classifiers.

The classifier is optimized and validated on independent samples, while a third, test, sample is used to assess its performance. The classifier has three important parameters: the number of bootstrap copies, the maximum number of features (variables) sampled in each tree⁷ and the minimal number of events in a leaf (training stopping criterion).

The optimization, validation and test samples are mixing data (see Tab. 6.2)

⁷This parameter is available thanks to the random forest approach.

for signal representation and dedicated cosmic runs (see Tab. 6.1) for the background part. The choice of the classifier configuration is made by establishing its rejection power on the test sample, hence independently of the real data. This procedure allows the performance of a *blind analysis on the quench data*, in other words the outcome of the analysis is not biased by training the classifier on the actual data sample.

In the following, the term *MVA-selected event*, unless noted otherwise, will denote the events that passed the classifier selection. Moreover, the term Random Forest, or RF, appearing in several histograms, is used as a shorthand for the voting result of the classifiers.

6.4.1 Training of the Classifier

The classification is achieved based on the following nine discriminating variables, chosen after careful comparison between their distributions in the mixing and cosmic samples:

1. number of hits N_{hit} ,
2. number of reconstructed tracks N_{helices} ,
3. number of reconstructed tracks used in vertexing $\tilde{N}_{\text{helices}}$,
4. squared residual δ ,
5. ϕ component of generalized sphericity tensor eigenvector Σ_{ϕ} ,
6. z component of generalized sphericity tensor eigenvector Σ_z ,
7. combination of two largest generalized sphericity tensor eigenvalues $\sqrt{\lambda_1^2 + \lambda_2^2}$,
8. ϕ component of the reconstructed vertex,

9. r component of the reconstructed vertex.

The difference between the second and third variable is explained in Sec. 4.3. However, it is clear that $N_{\text{helices}} \geq \tilde{N}_{\text{helices}}$. If a vertex is reconstructed, then $\tilde{N}_{\text{helices}} \geq 2$, otherwise $\tilde{N}_{\text{helices}} = 0$ and N_{helices} can be different from zero.

The generalized sphericity tensor is calculated from all the reconstructed tracks, thus not necessarily entering the determination of the vertex position, and is given by

$$S_{ab} = \frac{1}{\tilde{N}_{\text{helices}}} \sum_{i=1}^{\tilde{N}_{\text{helices}}} \frac{p_a^i p_b^i}{|\mathbf{p}_i|^2}, \quad (6.26)$$

where \mathbf{p}_i is the momentum of the i^{th} reconstructed track (see Eq. (A.6)) and $a, b = x, y, z$. The eigenvalues λ_j of S with $j = 1, 2, 3$ are such that $\lambda_1 \geq \lambda_2 \geq \lambda_3$. The eigenvector, whose components Σ_ϕ and Σ_z are used as the fifth and sixth discriminating variables, corresponds to the eigenvalue λ_1 .

Several configurations of the classifier are trained on mixing and cosmic samples, characterized in Tabs. 6.1 and 6.2. The ones giving the highest and most stable significance are evaluated on a test sample, where the estimated background rate (MVA-selected events per second in the cosmic sample) and signal acceptance (MVA-selected events over total population in the mixing sample) are calculated. It is worth stressing here that the MVA-selected events do not necessarily have a reconstructed vertex.

In order to normalize the training sample to the expected amount of data in the experiment, the background sample is weighted proportionally to the ratio of the observation time to the background collection time. The signal sample is also weighted to normalize the calculated significance to the expected one.

The performance of the Bagging DTs that has been deemed the best is shown in Tab. 6.4.

Classifier Configuration		
Bootstrap Decision Trees		300
Sampled Features		4
Minimum Number of Events in Leaf		4
Classifier Performance		
Optimal Classifier Cut RF_{cut}		0.54
Punzi Significance	$S/(1.5 + \sqrt{B})$	2.23
Background Rate (cosmic test sample)	M/T	242 mHz (2% error)
Signal Acceptance (mixing test sample)	M/E	0.823 ± 0.002
Vertex Rate (cosmic test sample)	M_V/T	153 mHz (2% error)
Vertices Accepted (mixing test sample)	M_V/E_V	0.931 ± 0.002

Table 6.4: Configuration and performance of the best classifier. The optimal value on the classifier cut is obtained by maximizing the Punzi significance, described in [138]: S and B are the number of expected signal and background events, respectively. M : MVA-selected events. T : total run time. E : total number of events. M_V : MVA-selected vertices. E_V : total number of reconstructed vertices. P_V : passed-cuts vertices.

On one hand, the estimated background rate is higher than with the “standard pass-cut analysis” since the classifier is optimized for very short observation times. On the other hand, the signal acceptance is much higher than the standard procedure. However, the background rate is likely to be overestimated since it is calculated on a dataset recorded with a looser trigger than the one used for quench data. The cosmic runs in 2014 have been acquired with the so-called “cosmic trigger”, which requires at least one hit per each layer. While this trigger configuration is ideal for testing the SVD with cosmic rays, it is different from the one used in the trapping experiments throughout the 2014 data take, where the requirement is of at least two hits in the inner layer and at least one in each middle and outer layer. Since the cosmic trigger represents a subset of the tighter trigger for the mixing (and trapping) data, the classifier is still informed on the characteristics of the comics events.

The classifier output, i.e., the result of the random forest voting, for the test sample of the mixing and the cosmic data is shown in Fig. 6.17. The bump present in both the mixing and cosmic data (for a discussion of its origin, see Sec. 6.4.4) in the middle of the acceptance region (and magnified by the logarithmic scale of the y axis) reduces the background rejection capability, and yet the Punzi significance optimization is successful.

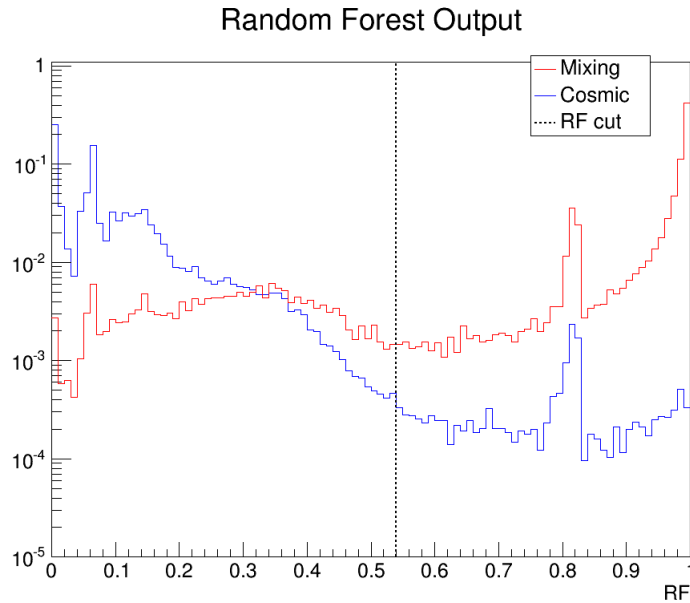


Figure 6.17: Classifier output for test sample of the mixing and the cosmic data. The dashed line indicates the cut on the classifier output that maximizes the Punzi figure of merit: events falling on the right hand side on this line $RF > RF_{\text{cut}}$ are compatible with the “signal” category.

The effect of the MVA selection on distributions of the number of hits, of the number of tracks and of the vertex radial and axial position is presented in Figs. 6.18, 6.19, 6.20 and 6.21, respectively. In particular, it is of interest whether the MVA selection distorts the original distribution of the mixing test sample (shown by the red line on the left of the plots) and whether the distributions

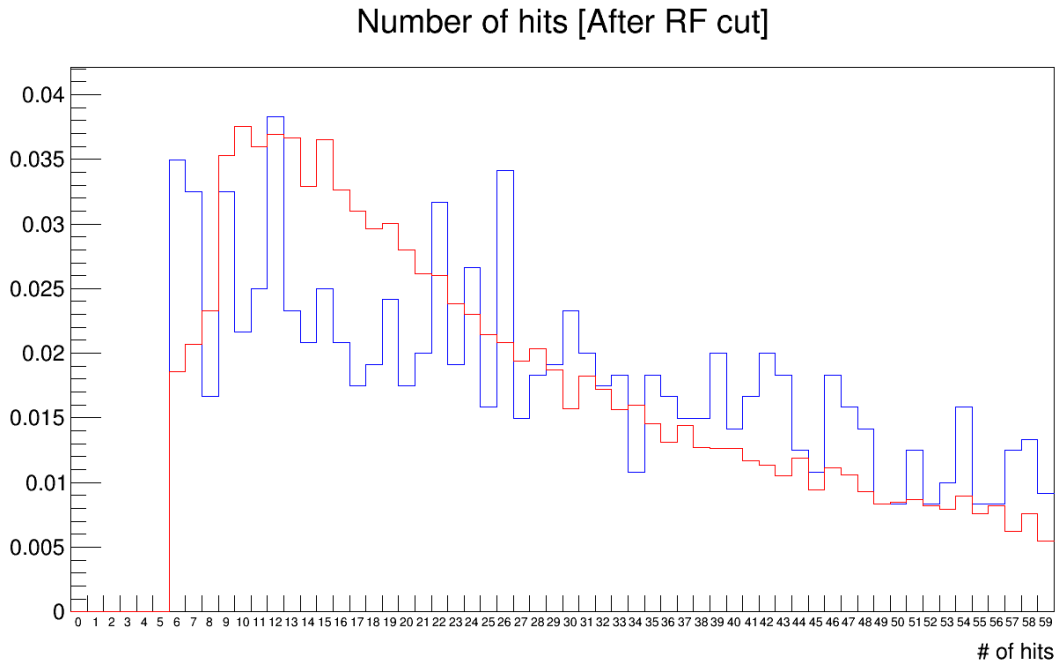
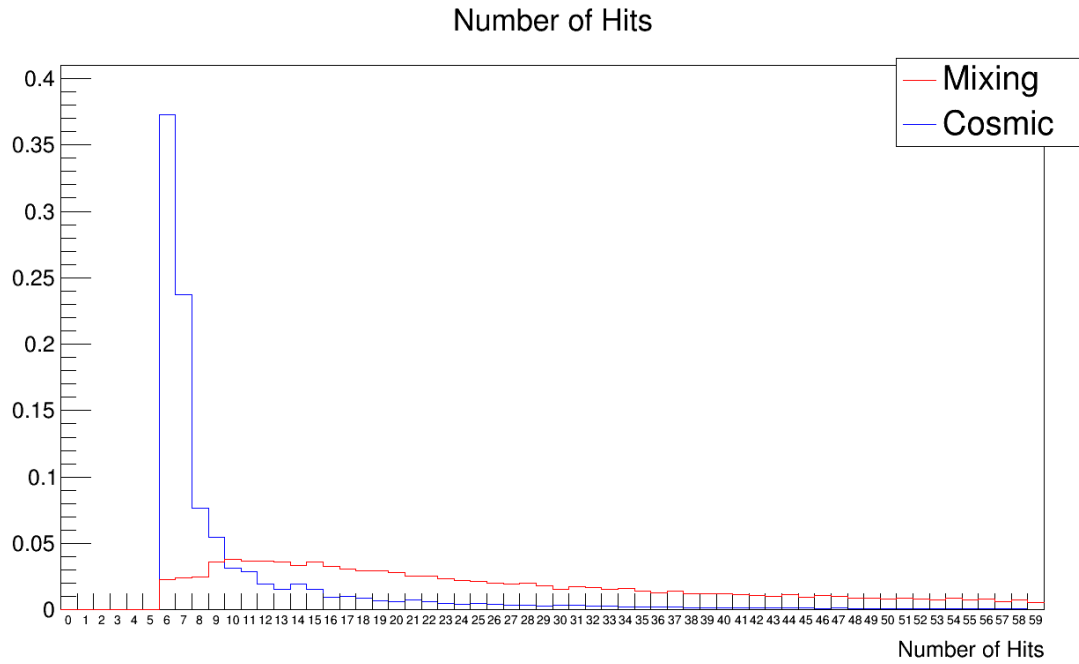


Figure 6.18: Distributions of the number of reconstructed hits before (top) and after (bottom) classifier selection on the cosmic and mixing test samples.

of the cosmic test sample are indistinguishable, up to a normalization factor, from the mixing data. By observing the distributions it is clear that the above conditions are met.

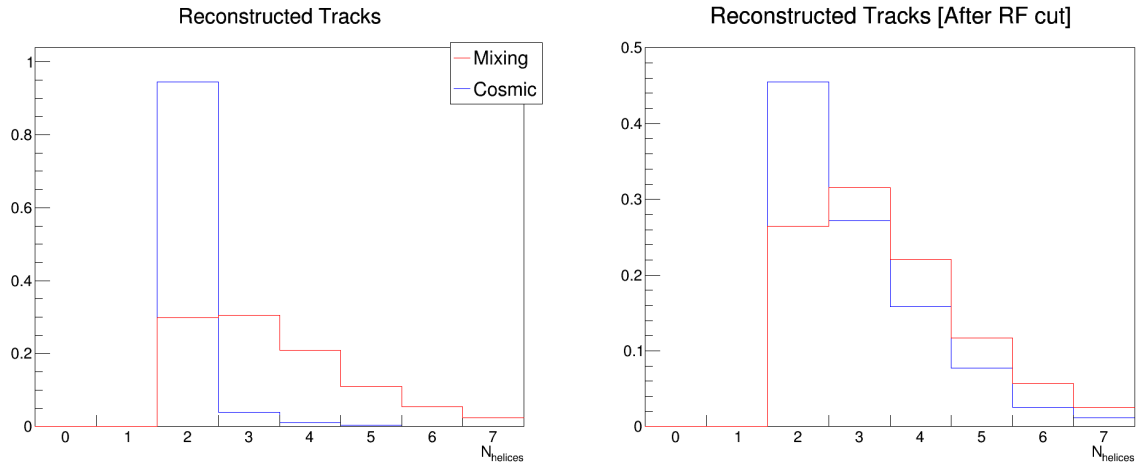


Figure 6.19: Distributions of the number of reconstructed tracks before (left) and after (right) classifier selection on the cosmic and mixing test samples.

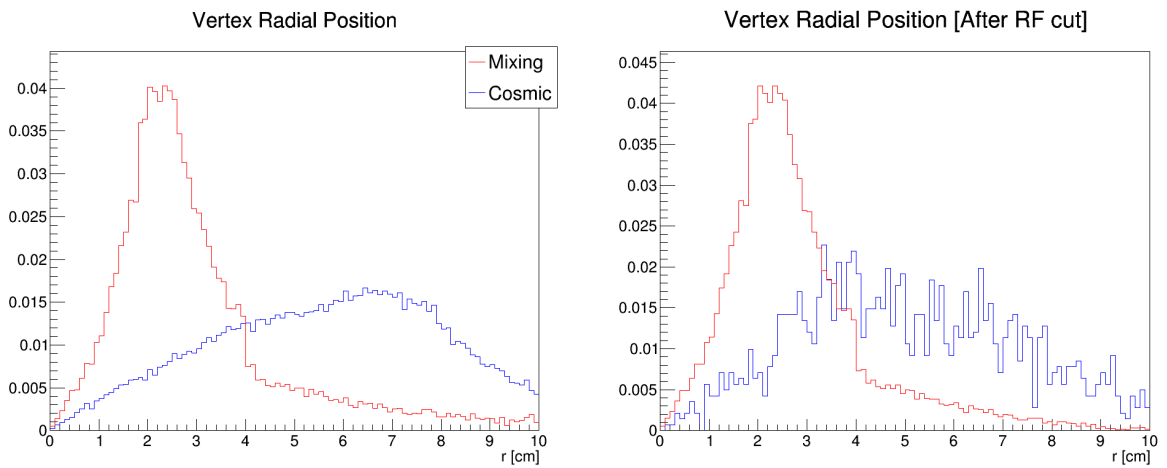


Figure 6.20: Distribution of the radial vertex position before (left) and after (right) classifier selection on the cosmic and mixing test samples.

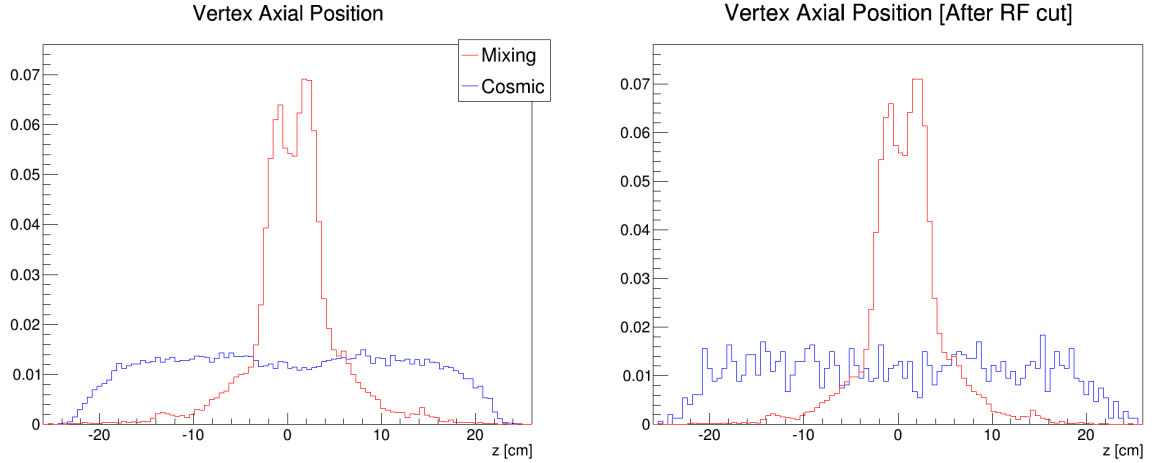


Figure 6.21: Distributions of the axial vertex position before (left) and after (right) classifier selection on the cosmic and mixing test samples.

6.4.2 Analysis of Quench Data

The trained classifier is here applied to the quench data of both trial series. An additional cut on the time of the event is used to ensure that the candidate is within the observation window $t_q = 30$ ms, dictated by properties of the magnet system, as mentioned at beginning of Sec. 6.3.1. The expected number of cosmic events in a single trial series is calculated from the relevant row in Tab. 6.4:

$$t_q \times 10 \times 242 \text{ mHz} = 0.072 \pm 0.001 \ll 1. \quad (6.27)$$

The classifier output, after the additional time cut, is shown in Fig. 6.22 for both series. Events appearing on the right side of the black dashed line are deemed \bar{H} .

It is worth stressing at this point that the results of the present analysis are obtained once the performance of the trained classifier is assessed on an independent dataset (test sample). The final decision on whether an event is classified as \bar{H} or background is therefore taken by the analysis program, without

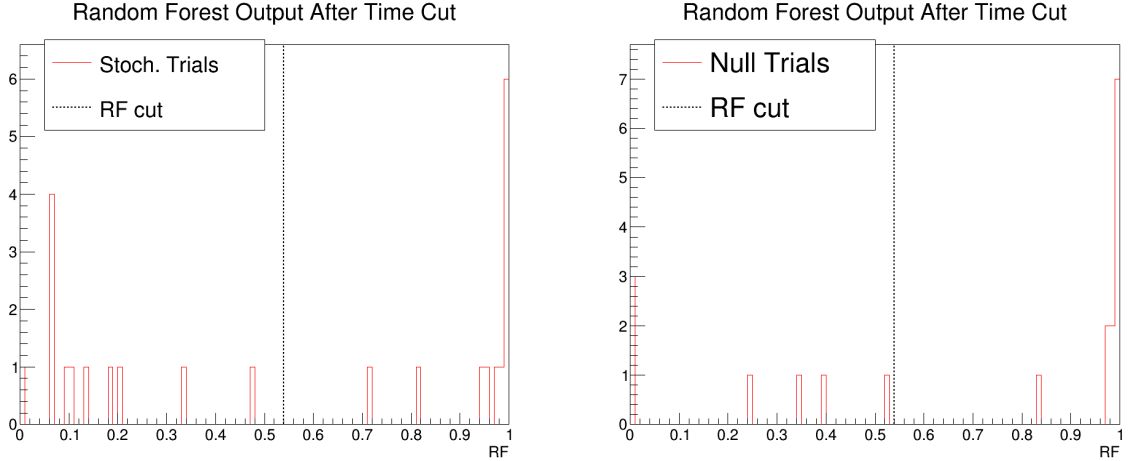


Figure 6.22: Classifier output for stochastic acceleration (left) and null (right) trials. The cut $t < t_q$ is also applied. The events on the right of the dashed line are accepted as \bar{H} annihilation.

prior knowledge of the possible outcome.

6.4.3 Results of Quench Data

The results of the MVA are summarized in Tab. 6.5. The table shows that the number of MVA-selected events in the quench data is independent of the application of the stochastic acceleration.

Trials	MVA-selected	Significance	Mean	Vertices
Stochastic Acceleration	12 ± 4	2.42	1.2 ± 0.4	11 ± 3
Null	12 ± 4	2.90	1.4 ± 0.4	12 ± 4

Table 6.5: Summary table of the quench data for stochastic acceleration experiment. The second column, “MVA-selected”, refers to classifier cut and time cut. Significance is the Punzi Significance. The fourth column shows the expected mean and error obtained with a Poisson fit (see Fig. 6.23) and the last column gives the number of vertices that survived the classifier cut and time cut.

The distributions of the events in the attempts for both trials is shown in

Fig. 6.23, together with the underlying Poisson probability function Eq. (6.24).

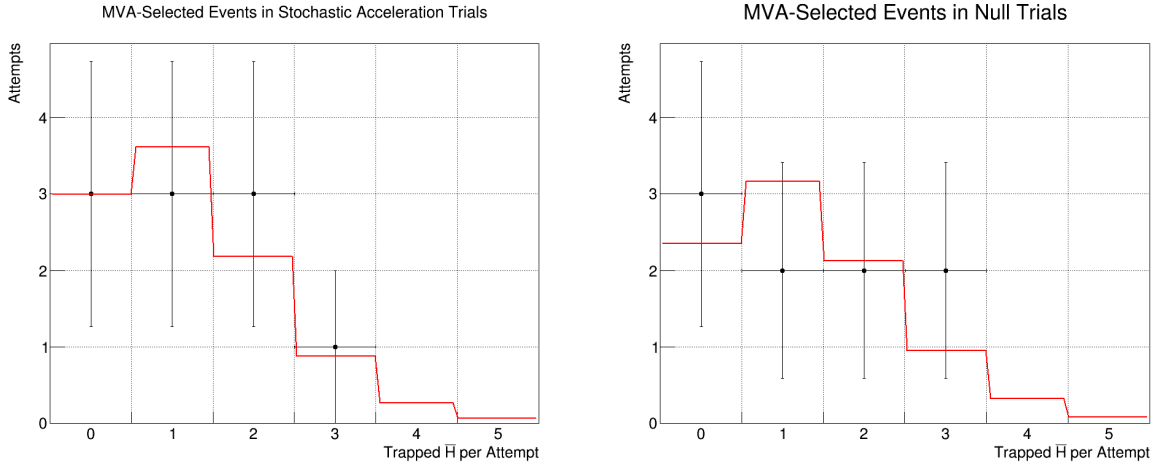


Figure 6.23: Distribution of the number of MVA-selected \bar{H} with the time cut in the stochastic acceleration (left) and null (right) trials. A fit with the Poisson distribution Eq. (6.24) is overlaid (red line), whose best-fit parameters are given in the fourth column of Tab. 6.5.

The event in the stochastic acceleration trials that passed the MVA selection (and satisfied the time cut) but does not have a vertex is shown in Fig. 6.24. While the classifier is very robust, one may wonder if this event is, instead, a misclassified cosmic shower (definitely not a single muon travelling through the apparatus, due to the visible lack of a straight track). The high classifier score, 0.81, would point in the direction of “invisible” \bar{p} annihilation mode, where only π^0 mesons are produced: these particles decay instantly into two photons which create e^+e^- pairs detected by the SVD.

6.4.4 Analysis and Results of Monte Carlo Data

The simulation of 100 000 \bar{H} annihilations with the ALPHA VMC (see Sec. 4.1) has been used to test the performance of the chosen classifier. Once the number

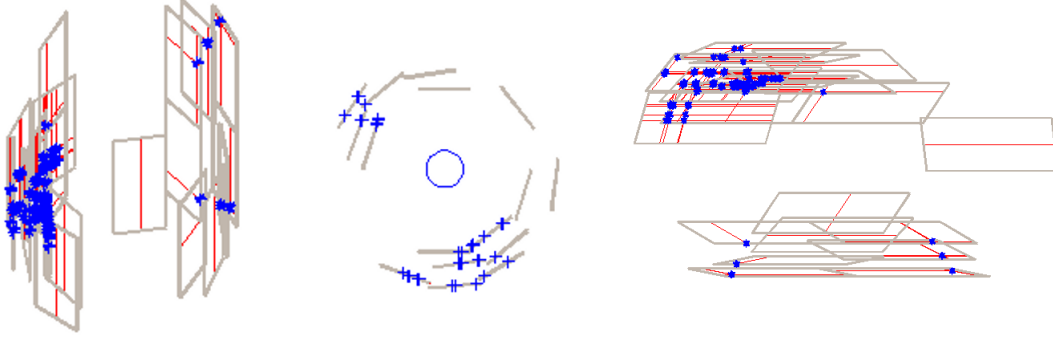


Figure 6.24: Possible \bar{H} annihilation into π^0 mesons seen from the top, front and side view of the SVD, respectively. The number and the distribution of the hits in SVD indicate that at least one γ , produced in the π^0 meson decay, converted into a e^+e^- pair.

of events is trimmed to 95094, due to the simulation of the “2-1-1” trigger of ALPHA-2, the signal acceptance is

$$\frac{\text{MVA-selected}}{\text{Total Number of MC Events}} = 0.811 \pm 0.001,$$

which is in agreement with what was found with mixing data. Also the number of accepted vertices gives good agreement

$$\frac{\text{MVA-selected vertices}}{\text{Total Number of Reconstructed vertices}} = 0.917 \pm 0.001.$$

The classifier output is shown in Fig. 6.25. The performance of the classifier evaluated on MC data is in agreement with the one found in Sec. 6.4.1.

The bump in the middle of the acceptance region, $\text{RF} > 0.54$, present also in the mixing and cosmic data, is due to the omission of the vertex requirement, as can be seen in Fig. 6.26, where the classifier output on all three datasets for events with a reconstructed vertex is shown. On the one hand, ignoring the presence of a reconstructed vertex comes at a price of a bump in the classifier output, displayed

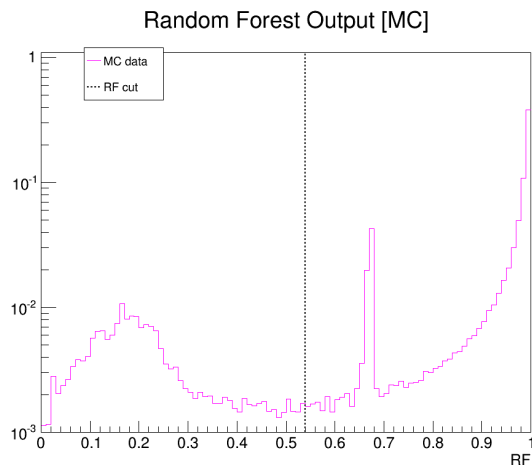


Figure 6.25: Classifier output, configured for the quench phase, for MC data.

in Figs. 6.17 and 6.25, that increases the background rate (see Tab. 6.4). On the other hand, taking into account the vertex, when is not essential to the accuracy of the measurement, e.g., like in the counting experiment discussed in the present section, reduces the signal acceptance. The choice made for the current setup is the former by relying upon the discrimination power offered by the MVA, as the expected number of background events is very low, as shown by Eq. (6.27).

6.4.5 Analysis and Results of Hold Data

An additional analysis has been performed on the “hold phase” of the experiment (see Tab. 2.1). $\bar{\text{H}}$ is confined in the minimum-B trap for about two minutes in every single experiment, and the stochastic acceleration is applied or not, during the null trials. The goal of this analysis is to decide whether the trapping conditions for both trials were the same, in other words, whether there is loss of trapped antiatoms that would lead to different (and incompatible) results in the quench phase. This analysis does not enter directly into the determination of the charge, but it is a validation of the trials dataset.

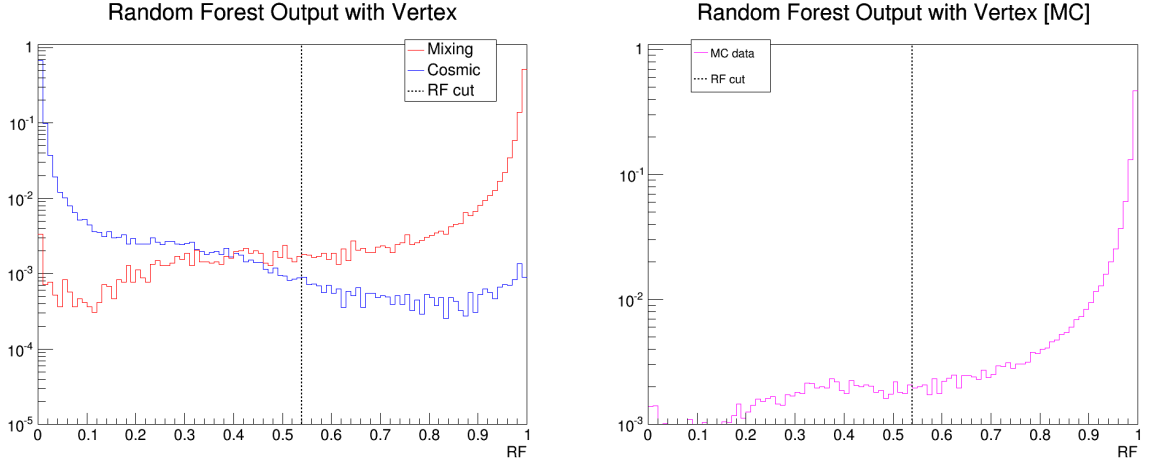


Figure 6.26: Classifier output, configured for the quench phase, for mixing, cosmic and MC data with reconstructed vertex.

Of course, this has required a new training of the classifier, since the observation time is much longer. The advantage of the MVA over the standard pass-cut analysis is clear here: by re-training the classifier with the proper parameters, the background rate can be significantly reduced. The expected background rate on the best performing classifier is

$$R = 6 \text{ mHz} \quad (11\% \text{ error}) \quad (6.28)$$

and the signal acceptance is

$$0.470 \pm 0.003,$$

while the fraction of accepted vertices is

$$0.577 \pm 0.004.$$

The Punzi Significance of the chosen classifier is 3.7. The reduction in background is dramatic, by a factor of 40, and it goes with a reduction in signal by only a factor of two.

The number of \bar{H} candidates in each series, shown in the second column of Tab. 6.6, is less than 2σ apart, making the two results compatible with a p-value of 0.166. They are also compatible with the estimated background.

Trials	MVA-selected	z cut
Stochastic Acceleration	6 ± 2	5 ± 2
Null	11 ± 3	6 ± 2
Expected Cosmics $R \times T$	7 ± 1	5 ± 1

Table 6.6: Summary table for stochastic acceleration and null trials during the holding phase. The second column refers to classifier cut. The third column shows the number of events that survive the additional cut on the vertex axial position. The last row shows the expected background rate where R is given by Eq. (6.28), in the second column, and by Eq. (6.29), in the second column, while $T \approx 1150$ s is the observation time.

If the vertex requirement is restored and, additionally, a cut on its z position is applied, the background rate is further reduced. The cut on the z position of the vertex is placed at ± 13 cm, which is roughly the position of the most external mirror coils, and is introduced to adhere to the obvious physical constraint that \bar{H} annihilation during the confinement cannot be detected outside the boundaries of the trapping field. The new background rate of the test sample is

$$R = 4 \text{ mHz} \quad (16\% \text{ error}), \quad (6.29)$$

while the signal acceptance is 0.461 ± 0.003 .

The results of the application of the classifier with the “ z cut” to the series stochastic acceleration and null trials are shown in the third column of Tab. 6.6. Also, this case proves that the events passing the selection are compatible with each other (they are 0.35σ apart, resulting in a p-value of 0.72) and with the background.

6.4.6 Conclusions

This section presented an overview of the Multi-Variate Analysis statistical pattern recognition method applied to the ALPHA experiment. The Bagging Decision Tree algorithm is used to separate \bar{H} annihilation signals from the cosmic background.

Two datasets, representing a sample of the signal and of the background events, respectively, are first split into three parts, and then used for optimization, validation and testing of the chosen classifier. It is worth noting that, since the training dataset is independent of the experimental data, this is an example of a “blind analysis”. The optimal classifier is finally applied to the experimental data, an operation sometimes called “un-blinding”. The experimental goal is to improve the upper bound on the \bar{H} electric charge by means of the stochastic acceleration technique. The analysis is also applied to Monte Carlo data in order to cross-check the classifier performance.

The classifier is also trained to look at the “hold phase” of the twenty experiments, when the stochastic accelerating electric potentials, interleaved with null potentials, are applied to trapped \bar{H} , in order to ensure that the trapping conditions remain unchanged from one trial to another.

The results presented in this section, together with SVD data quality tests performed by the author, are part of a forthcoming ALPHA paper.

7 An Apparatus to Measure the Gravitational Interaction of Antihydrogen

The measurement of the $\bar{\text{H}}$ gravitational acceleration has drawn a lot of attention in the past twenty years, given its implications in Cosmology and in other fundamental Physics theories, as discussed in Sec. 1.2.1. Many authors have proposed experiments on $\bar{\text{H}}$ gravity as a viable alternative to using charged antiparticles since, to date, there is not a single direct measurement involving antimatter. The ALPHA collaboration embarked on this quest by proposing a novel apparatus, dubbed ALPHA-g, whose design is currently underway and is to be built alongside ALPHA-2.

The first section provides an overview of the proposed apparatus, that includes a magnets system in Sec. 7.1.1, the antiatom interferometer in Sec. 7.1.3 and the particle detectors in Sec. 7.1.5, and of the experimental techniques, such as the measurement procedures in Sec. 7.1.2 and the $\bar{\text{H}}$ cooling schemes in Sec. 7.1.4. The second section is dedicated to the design, the simulation (in Sec. 7.2.1) and the analysis (in Secs. 7.2.2 and 7.2.3) of the $\bar{\text{H}}$ annihilation detector. The results of the simulation are presented in Sec. 7.2.4. A summary of the current status of the detector design and a discussion on the further steps of its finalization are given in Sec. 7.2.5.

7.1 ALPHA-g

The ALPHA-g apparatus is *vertical*, i.e., its axis is parallel to the Earth's gravitational field, with the \bar{p} and the e^+ injected into the Penning trap from the bottom end. The apparatus is divided into two regions, at different heights, with different functions. The lower part, called the trapping or mixing region, is similar to the ALPHA-2 mixing region (see Sec. 2.4), where an electrode stack, together with a solenoid magnet, are used for \bar{p} and e^+ manipulation, leading to \bar{H} formation. The upper part, called the analysis or measurement region, is where the actual determination of the \bar{H} gravitational acceleration takes place.

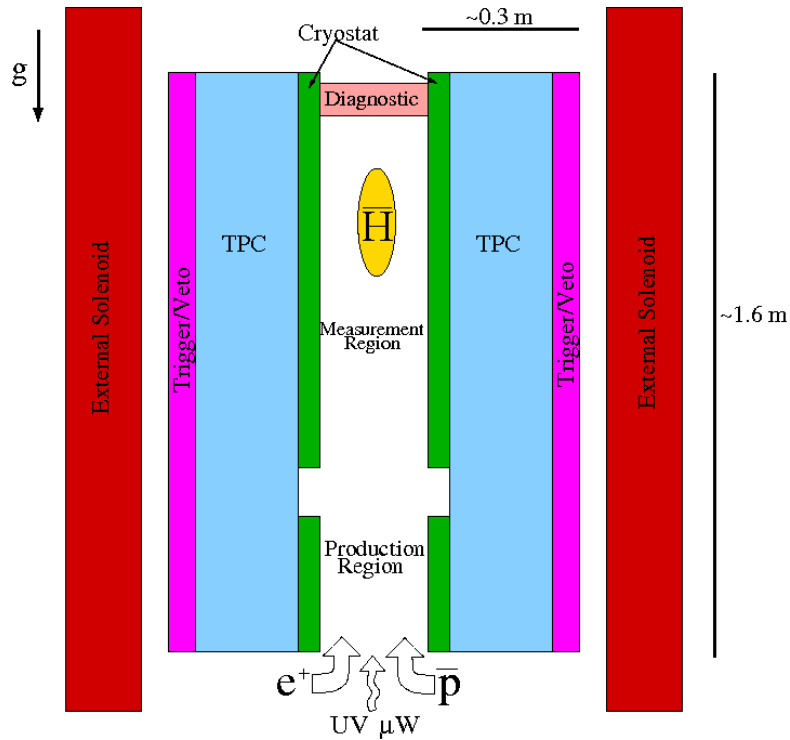


Figure 7.1: Sketch of the future ALPHA-g apparatus, where only the components relevant to the present discussion are shown. The annihilation detector (TPC) and the cosmic veto are discussed in the present chapter.

In addition to antiparticles, the bottom end is the preferred access point for laser and microwave radiation: the former is involved in the gravity measurement and the latter is part of a dedicated experiment to probe the $\bar{\text{H}}$ ground state hyperfine transitions with high precision. The top end is instrumented with diagnostic tools, such as a multi-channel plate (or MCP) detector, and the electron emitter filament (e^- -gun).

7.1.1 Magnet System

The magnet system plays a crucial role in the design; $\bar{\text{H}}$ has to be trapped first in the mixing region, as it is done in ALPHA-2 with an Ioffe-Pritchard trap (see Secs. 2.3 and 2.4), then transferred, with minimal losses, to the analysis region. The $\bar{\text{H}}$ trapping in the mixing region is accomplished in the axial direction with the mirror coils, spaced as much as in ALPHA-2, and in the radial direction with a long octupole magnet, whose winding extends to the analysis region, providing the necessarily radial confinement there, too. In the analysis region, the axial confinement is achieved by two mirror coils at each end of the region, separated by a distance of the order of one metre.

The number of coils in this experiment is likely to be larger than in ALPHA-2. However, some of them are not required to produce intense magnetic fields, i.e., they are low-current, the reason being that they are not used for trapping but rather to implement an $\bar{\text{H}}$ cooling scheme. Another coil, operated at very low current, is to be placed in the analysis region to perform the gravity measurement.

In this challenging magnetic environment, the presence of stray magnetic fields could mimic gravity and wash out the effect of the Earth's gravitational field. Indeed, the gravitational potential energy $U_g = mg\Delta z$, for a body of mass

$m = m_p \approx 938 \text{ MeV}$ and at height $\Delta z = 1 \text{ m}$, is

$$U_g \approx 0.1 \mu\text{eV}, \quad (7.1)$$

where $g = 9.81 \text{ m/s}^2$ and corresponds to a magnetic field

$$B = \frac{mg\Delta z}{\mu_B} \approx 18 \text{ G},$$

where μ_B is the Bohr’s magneton. Therefore, magnetometry and precise control over the magnet’s current are important aspects of the design as well. In addition, some of the coils mentioned above, particularly in the analysis region, have to be non-superconducting in order to reduce the residual fields due to persistent currents [140]. For the same reason, the number of octupole windings in the analysis region might be reduced with respect to the mixing region.

7.1.2 Gravity Measurements

The gravitational measurement is approached in successive phases, where each stage attains higher precision than the previous one. The first stage aims to rule out “anti-gravity” by determining the sign of $K = \frac{\overline{m}_G}{\overline{m}_I}$, where \overline{m}_G and \overline{m}_I are the $\overline{\text{H}}$ gravitational and inertial mass, respectively (see Sec. 1.2.1). This so-called “up-down measurement” provides the definitive and direct answer to whether antimatter “falls up”. While slowly ramping down the mirrors coils (either in the analysis region or even in the trapping region) with the octupole energized, the data analysis technique described in [106] yields the sought for measurement.

The second stage intends to perform a 1% measurement by using a magnetic field gradient, generated by the low-current coil, to compensate for the effect of gravity. As with the sign measurement, the octupole is energized all the time, while the mirror coils are slowly turned off. By knowing the strength of the magnetic field gradient and the “reverse cumulative average” of the $\overline{\text{H}}$

annihilation position, as described in [106], a limit on K is uniquely determined. However, detailed calculations of the $\bar{\text{H}}$ dynamics in complex magnetic fields under the influence of gravity, such as the one presented in [141], are necessary for a precision measurement. Systematic effects in both the first and the second phases are investigated with the magnet (coil) used to create the axial (gravity-compensating) gradient by, for instance, over-balancing the gravitational force.

The third stage aims to perform a high-precision measurement by means of atom interferometry [31]. In recent years, gravity measurements based on the quantum nature of the atoms [142] have achieved remarkable precision [143] and their popularity for testing the foundation of Relativity [32, 144–146] and measuring the fine structure constant [147], the gravitational acceleration [148] and Newton’s Gravitational constant [149] is growing. The proposed technique is described in [150], while other schemes with different $\bar{\text{H}}$ transitions are currently under consideration.

7.1.3 Atom Interferometry

The basic principle of atom interferometry is very simple. Classical interferometry employs a beam splitter, e.g., a glass slide, to split a laser beam into the two arms of the interferometer and a mirror to recombine them, producing the typical interference fringe pattern. By interchanging the roles of the light and the matter, an atom-wave can be split into the two arms of the interferometer by creating a superposition of states in momentum space upon interaction with laser light that carries the momentum $\hbar\mathbf{k} = \hbar(\mathbf{k}_1 - \mathbf{k}_2)$, where \mathbf{k}_1 and \mathbf{k}_2 are the wavevectors of the counter-propagating laser beams. The role of the mirror is played again by the light pulse that, this time, reverses the population of the states. A third interaction, identical to the first, is used to detect the population modulation, which presents itself with the characteristic fringe pattern. Since the atom-wave

split occurs in momentum space, the atom trajectories become spatially separated and they travel through the interferometer along different path with different momenta.

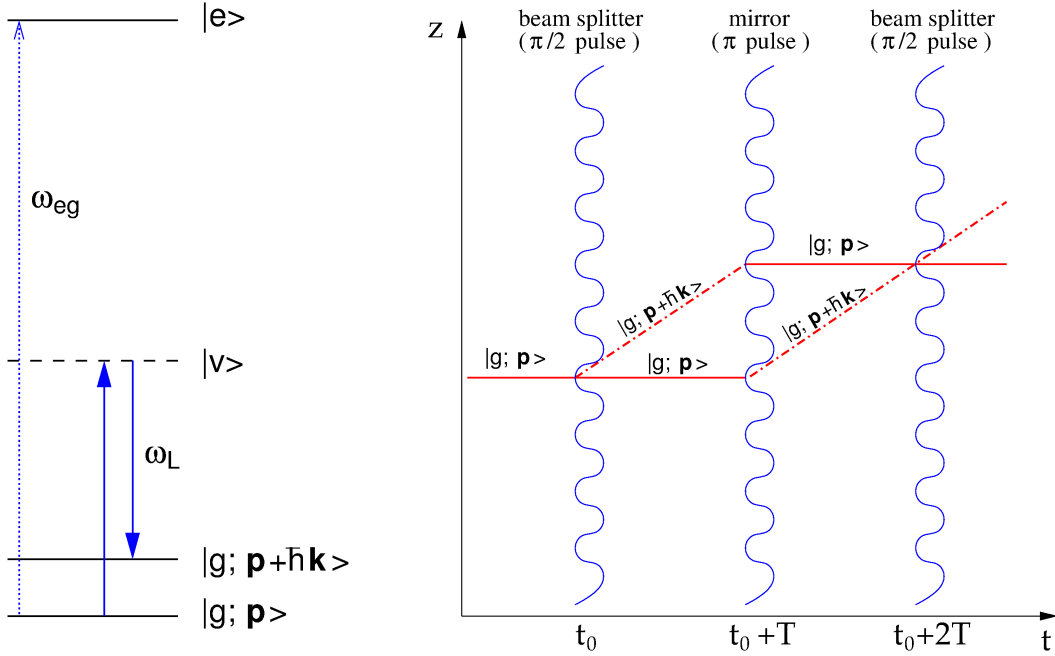


Figure 7.2: Schematic view of a Mach-Zehnder atom interferometry. Left: Bragg transition driven by a far-detuned laser (solid blue arrows). The atom with momentum \mathbf{p} , initially in the ground state $|g; \mathbf{p}\rangle$, is driven to the state $|g; \mathbf{p} + \hbar\mathbf{k}\rangle$, via the virtual state $|v\rangle$, by means of a laser with wavevector \mathbf{k} and frequency $\omega_L = c/|\mathbf{k}| \ll \omega_{eg}$, where ω_{eg} is the transition frequency of the ground state to the excited state $|e\rangle$ (dashed light blue arrow). Right: Sample path of an atom through the interferometer, without gravity. A “ $\pi/2$ pulse” is defined as the laser pulse duration that achieves superposition of states and a “ π pulse” as the laser pulse duration that achieves population inversion. In presence of gravity the path follows the characteristic parabolic trajectory between successive pulses.

Atom interferometry is a powerful tool for gravitational sensing because an

atom is a near perfect realization of a free-falling inertial reference frame. In the presence of gravity, the atoms' trajectory in a vertical interferometer, or *atomic fountain*, follow the characteristic parabolic trajectory. The atoms in the upper arm experience a different gravitational potential with respect to the lower arm, therefore the atom-wave accumulates a phase [143]

$$\varphi_g = kgT^2, \quad (7.2)$$

where T is the time elapsed between successive pulses. Detection of the interference fringe pattern permits the measurement of φ_g , hence the determination of g from the known laser wavevector k and laser pulse delay T .

7.1.4 Antihydrogen Cooling

A cooling mechanism for $\bar{\text{H}}$ is an essential prerequisite to antiatom interferometry and it would be beneficial to the second experimental phase, too, since the gravitational potential energy, given by Eq. (7.1), corresponds to a temperature

$$T_g = \frac{U_g}{k_B} \approx 1.2 \text{ mK},$$

where k_B is the Boltzmann constant. This is much lower than the typical values in, e.g., ALPHA-2. A proposal to reduce the $\bar{\text{H}}$ temperature to 20 mK by means of *laser cooling* has been put forward [104], provided that a Lyman- α laser source is available [103]. The traditional way to achieve the lowest temperature with hydrogen is by means of evaporative cooling [151], a technique that is completely unfeasible for $\bar{\text{H}}$ given its scarcity. The full development of ALPHA-g therefore requires in the near future to obtain laser cooling of (anti)hydrogen.

However, another cooling mechanism can be employed, namely *adiabatic expansion cooling*. The abundance of mirror coils (e.g., five in ALPHA-2) is needed exactly in order to reduce the $\bar{\text{H}}$ temperature by trapping it in a short axial well

and then lowering one end of the trap while energizing the adjacent coil. If this transition is slow compared to the coupling time between the radial and axial motional degrees of freedom, i.e., adiabatic, a three-dimensional cooling of the \bar{H} is accomplished.

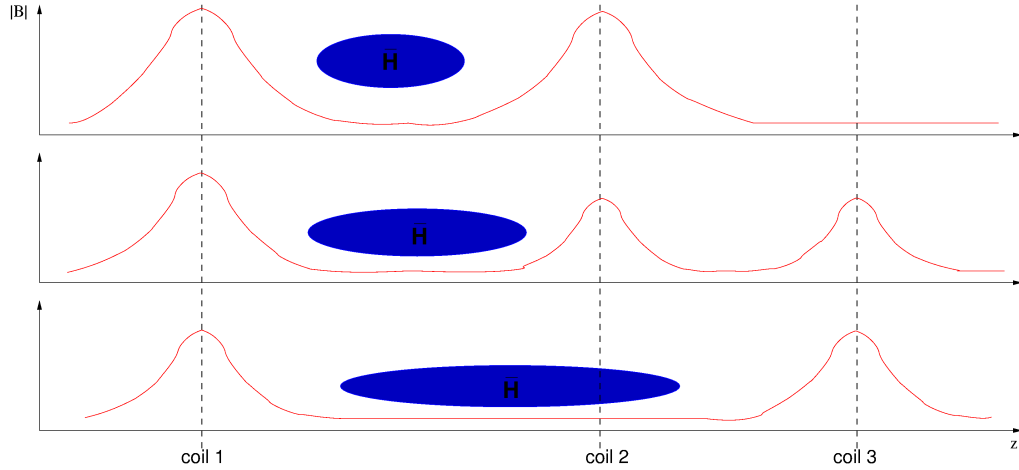


Figure 7.3: Sketch of the adiabatic expansion cooling. The magnetic field on axis, which is proportional to the potential energy, is controlled by the currents in the coils 1, 2 and 3. In the first stage (top), the \bar{H} is trapped in a magnetic field gradient. In the second stage (middle), the current of coil 2 is slowly ramped down, while coil 3 is energized. At the same time, the current in coil 1 is also reduced. In the final stage, the current in coil 2 is zero, while coils 1 and 3 are operated at lower current than the initial value of coil 1 in the first stage. The \bar{H} occupies a larger portion of the trap, while its temperature is effectively lower. By repeating this process several times, preliminary simulations show that a temperature of 20 mK is possible.

This technique also makes it possible to move the \bar{H} cloud to the analysis region, creating the *antiatomic fountain*. The standard technique for the atomic fountain requires that a vertical velocity be imparted to the atoms through a laser pulse, in a process that is the reverse of laser cooling. Since this method

is expensive in terms of atom losses, it is not applicable to $\bar{\text{H}}$. Instead, the initial vertical propulsion of the antiatoms is provided by adding a “kink” in the magnetic field envelope between, e.g., coil 1 and 2 in Fig. 7.3.

7.1.5 Antihydrogen Detection

Having summarized the main design features of the future ALPHA-g apparatus, now the focus of the following sections is on the $\bar{\text{H}}$ detection. Once again, identification of $\bar{\text{H}}$ annihilation and its location is a valuable tool to monitor the experiment and to achieve meaningful physics results. This includes the discrimination between $\bar{\text{H}}$ annihilation and cosmic rays.

Particle tracking in the ALPHA environment is challenging: the distance between the annihilation point and the first measurement of the annihilation products is of the order of several centimetres and the abundance of material with high density causes a degradation of the tracking performance due to multiple scattering (see Sec. 4.4). These factors are enhanced in ALPHA-g due to the presence of more coils. This means more dense material and possibly a larger distance between the tracking detector and the trap. Although a semiconductor detector is widely recognized to make an excellent tracking device, the ALPHA experiment is not the place where a double-sided silicon strip detector is optimal for several reasons.

- The number of detector layers is limited to three, which can cause the loss of a whole track if any strip inefficiency is present, as discussed in Sec. 4.4. Moreover, the particles’ momentum is poorly reconstructed.
- The strip pitch (see Sec. 3.1) is much larger than what is feasible with the current state of semiconductor technology, because the accuracy with which a particle trajectory can be reconstructed is limited by multiple scattering

along the path between the trap and the detector. In other words, there is a limit to the resolution that is not due to the detector resolution.

- The length of the active region of a detector module is limited to a few tens of centimetres by the electric coupling between the strips and the ASICs, whereas the length over which it is necessary to reconstruct the \bar{H} annihilation position is much larger in ALPHA-g than in ALPHA-2, namely, over the mixing region as well as the measurement region.

The cost and the time to manufacture a silicon detector are therefore not worthwhile. A gaseous tracking detector is thus an optimal solution, where relatively inexpensive gas replaces the solid-state active material for π^\pm detection. In addition, a gas detector allows many more than three samples of a particle track in its active region.

The choice of tracking detector for ALPHA-g is a *Time Projection Chamber*, or TPC, which retains the best features of the wire chamber technology, while simplifying the manufacture process at the cost of a more complicated readout. The rest of the present chapter deals with the design of such a detector for \bar{H} annihilation vertex reconstruction in ALPHA-g.

A *scintillator bars detector* is used in combination with the TPC to assist in the rejection of cosmic rays. A “cosmic veto” system that quickly gives an indication as to whether an event is due to a cosmic ray is highly desirable, since it allows more accurate event-by-event classification by adding further information to the \bar{H} annihilation reconstruction. Example variables include the hit multiplicity and the time delay between hits: the former is low for cosmic rays compared to \bar{H} annihilation while the latter is large. Such a system can also provide triggering to the TPC (i.e., setting the initial time for the event readout). Both applications - cosmic veto and triggering - require fast response photomultipliers

(possibly silicon photomultipliers) and good timing frontend electronics.

7.2 A Radial TPC for Antihydrogen Detection

A TPC is a gaseous tracking detector that provides multiple samples of the trajectory of a charge particle within its active volume. Three spatial coordinates are determined simultaneously for each point on the trajectory. When a charged particle interacts with the gas, electrons and ions are produced by ionization. The electric field constantly present in the active region sweeps the primary ionization, i.e., the electrons, towards high potential regions. If this feeble current is properly amplified, an analog signal that is proportional to the amount of ionization produced by the charged particle, hence to its energy deposition, is obtained.

The TPC design under consideration is an atypical barrel detector, where the electric field is radial:

$$\mathbf{E}(r) = \frac{V}{\ln \frac{b}{a}} \hat{\mathbf{r}}, \quad (7.3)$$

where r is the radial coordinate, $\hat{\mathbf{r}}$ is a unit vector in the radial direction, a and b are the inner and outer radius, respectively, of the TPC and the typical bias voltage is $V = 10$ kV. Here, the z axis is vertical pointing up. The ionization produced by the charged particles is therefore collected at the outer radius of the detector. More standard designs have the electric field parallel to the magnetic field, however the TPC in ALPHA-g is relatively long. This would imply very long drift times in a non-trivial magnetic field environment that might cause serious degradation of the accuracy with which a point on the particle track is determined. Another consideration that lead to this design is the tight spatial constraints, such as the need for plasma diagnostics and an e^- -gun at the top end of the apparatus and the injection of antiparticles and laser from the bottom.

While the electric field \mathbf{E} accelerates the electrons towards the outer wall, frequent collisions with the gas atoms causes the electrons to scatter in a random direction. The overall effect is that the primary ionization drifts with constant *drift velocity* [152]

$$\mathbf{v}_d = \mu_e \mathbf{E}, \quad (7.4)$$

where μ_e is a property of gas, called electron mobility, that is proportional to the average time τ between collisions.

The ionization is collected on the TPC outer wall, which is azimuthally (ϕ coordinate) and axially (z coordinate) segmented. Each segment is called a *pad*, so that the origin in space of each ionization along the charge particle trajectory is determined by the knowledge of which pad is *hit* by the drifting electrons. In order to uniquely determine the *space-point* along the charged particle trajectory, the radial coordinate r must be inferred from the ionization drift time t_d , i.e., r is determined from the “time projection”:

$$r = |\mathbf{v}_d| t_d. \quad (7.5)$$

The measurement of t_d is obtained by means of a digital clock in the readout chain, as the time elapsed between the trigger and hit on the pad. As mentioned before, the charge arriving at the pad is small and, without proper amplification, is undetectable. Thus, a series of anode wires are placed in front of the pads and biased to 3.5 kV, creating a large localized electric field that achieves charge multiplication.

In the presence of a magnetic field \mathbf{B} , as with the Penning trap, the electrons are subjected to the Lorentz force. If the electric field and the magnetic field are orthogonal, the drift is curved according to the Lorentz force and the angle α between the drift velocity and the electric field, called Lorentz angle, is given by

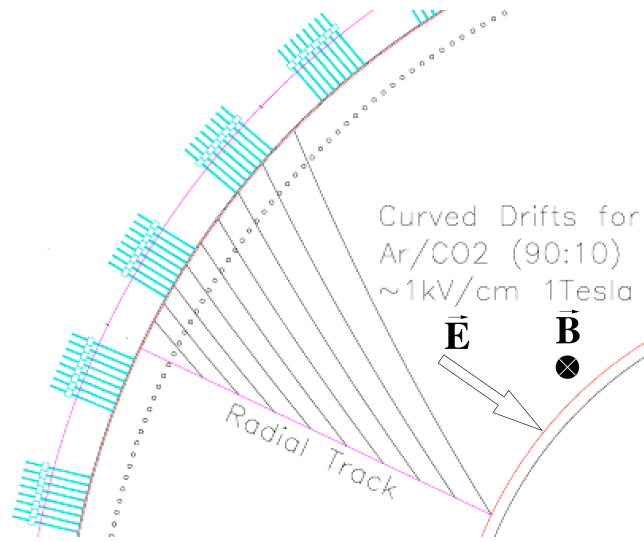


Figure 7.4: TPC concept developed at TRIUMF by the Detector Group. The direction of the electric and magnetic fields are shown for clarity.

the relation [152]

$$\tan \alpha = \omega \tau, \quad (7.6)$$

where $\omega = e |\mathbf{B}| / m$ is the electron Larmor frequency. In the ALPHA-g TPC the ϕ coordinate of the hit must thus be corrected for α .

It is important to choose a gas that has a low electron capture probability, otherwise the electrons are re-absorbed before reaching the collection point. Noble gases fit the purpose and a typical choice is argon. However, small quantities of polyatomic gases, such as CH_4 , CF_4 or CO_2 , are added to increase the drift velocity [126], a property that is particularly useful if the expected Lorentz angle is large. In ALPHA-g, the most likely choice for the drift gas is a mixture of 90% Ar and 10% CO_2 .

7.2.1 Simulation

The Geant4 [122, 123] simulation of the TPC for ALPHA-g was initially used to study the accuracy with which the \bar{H} annihilation vertex is reconstructed as a function of the radius of the drift region, i.e., the active volume where the annihilation products can ionize the gas and the ionization products drift to readout pads. Additional simulations were performed to study the behaviour with different pad sizes and timing resolution, which determine the hit accuracy. Since it became clear that the best configuration corresponds to a drift radius of $R_{\text{TPC}} = 10$ cm and a pad size of 4 mm in both the azimuthal and axial directions, the following description refers specifically to this case. Moreover, it was necessary to establish the TPC performance by developing a reconstruction algorithm, that required fixing the aforementioned TPC parameters in order to tune the various tracking and vertexing parameters.

The MC simulation described in the present section is still general and can be changed to another configuration, while the parameters and the results of the tracking in Sec. 7.2.2 and the vertexing in Sec. 7.2.3 depend on the particular choice of that configuration.

A word about the time resolution in the simulation is appropriate. In the absence of a faithful simulation of the readout, including the electron multiplication at the anode wires, the present code has to take into account the minimum separation in time between two hits, i.e., the minimum time for which two drifting electrons are distinguishable. This characteristic determines the accuracy with which the radial position of the space-points is reconstructed. In Sec. 7.2.2 and in Sec. 7.2.3, such a readout time resolution is assumed to be 10 ns, for the reason mentioned above. During the development of the simulation, other values (20, 25, 50 ns) were tested, resulting in the qualitative conclusion that up to 25 ns,

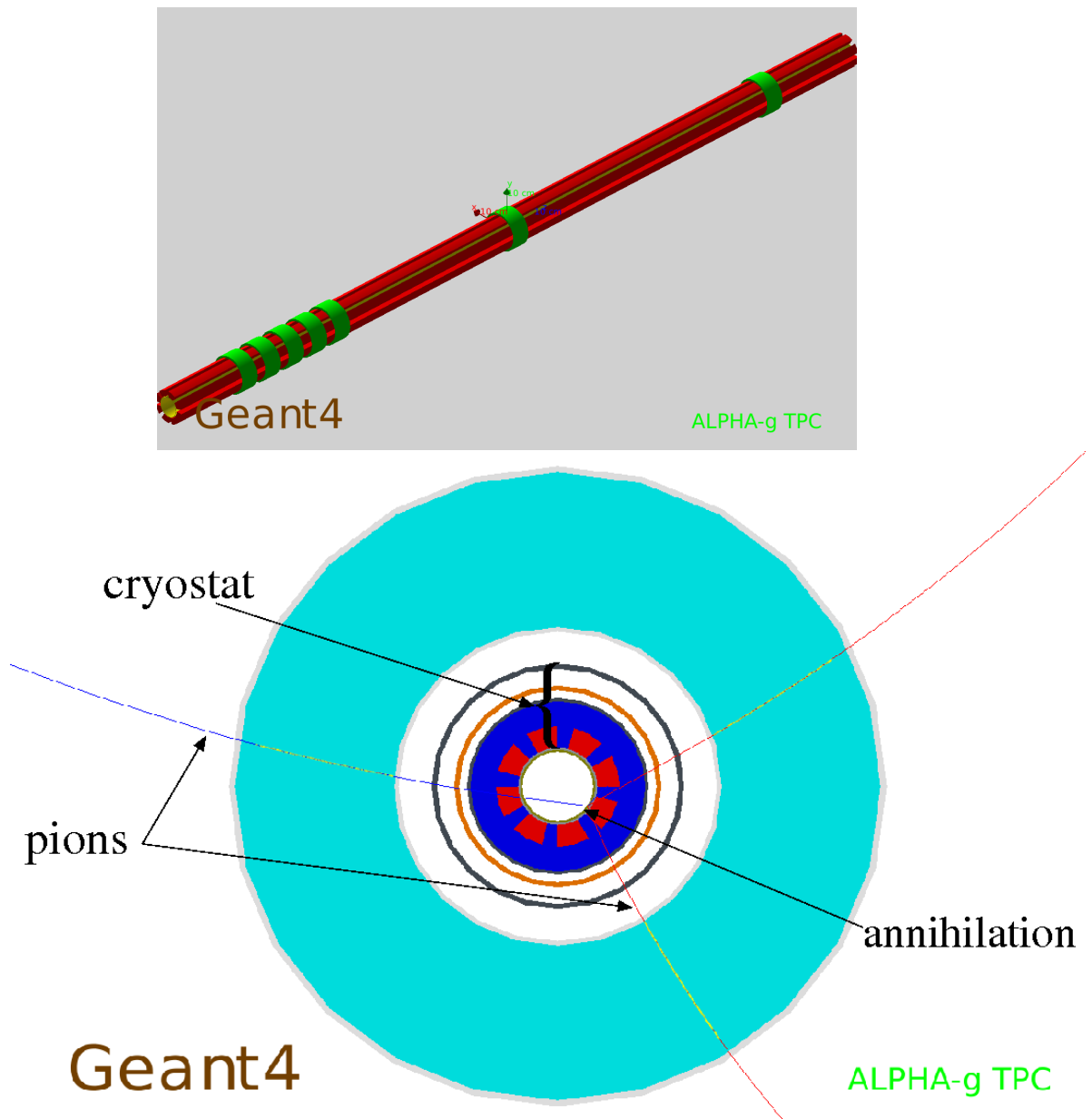


Figure 7.5: Graphic rendering of the geometrical model of ALPHA-g constructed with Geant4. On the top, the octupole (red) and the mirror coils (green) are shown. On the bottom, the cross-sectional view of the apparatus is displayed along with three π^\pm tracks.

the TPC reconstruction performance remains unchanged. With 50 ns “bunching time”, the number of reconstructed space-points along the tracks is significantly reduced, so that the overall reconstruction accuracy is slightly decreased.

Finally, it is worth stressing that the MC simulation presented here is detailed enough for the purpose of evaluating the reconstruction routines, but it is not complete, in the sense that the geometric model for ALPHA-g is more a prototype rather than the actual device and the physics of gas ionization and electron drift in an electromagnetic field is not fully implemented.

7.2.1.1 Detector Model

The volumes represented in the MC simulation correspond to the ALPHA-2 design and they are ordered in Tab. 7.1 by increasing inner radius.

The inner wall of the TPC, made of polycarbonate, is at a radius of $a = 10$ cm and it is $a_t = 3$ mm thick. The drift region extends over the radius R_{TPC} and contains a gas mixture of 90% Ar and 10% CO₂. The outer wall of the TPC at $b = a + a_t + R_{\text{TPC}} = 10.3 \text{ cm} + R_{\text{TPC}}$ is included in the MC but is irrelevant for the current purpose.

Name	Radius [cm]	Material
Electrodes	2.2275	Al
Ultra-High-Vacuum (UHV) chamber	2.3775	stainless steel
Octupole Magnet	2.5025	Cu-Nb-Ti
Seven mirror coils	3.9025	Cu-Nb-Ti
Outer-Vacuum Chamber (OVC) inner wall	5.5	stainless steel
Liquid He space	between UHV and OVC	
Heat shield	6.2	Cu
OVC outer wall	7.6	stainless steel

Table 7.1: Material budget in ALPHA-g MC. For the time being it is the same as in ALPHA-2. The radius is the inner one.

The present simulation includes a 1 T solenoidal field, along the z axis, while

no attempts have been made to introduce the detailed magnetic field of ALPHA-g, since, among other reasons, it has not yet been clearly defined. Once again this simplification is good enough for the purpose of the current simulation.

7.2.1.2 Charged Pion Generation

The \bar{H} annihilation is simulated as the process

$$\bar{H} + p + e^- \rightarrow n\pi^\pm + m\pi^0 + 2\gamma, \quad (7.7)$$

where n and m are distributed as shown in Fig. 4.2.

The Geant4 simulation begins with the generation of \bar{H} annihilation uniformly on the trap wall, i.e., on a circumference of radius $R_w = 22.275$ mm. Axially, i.e., along the z axis, the annihilations are distributed uniformly over a length of 2 cm centred around $z = 50$ cm.

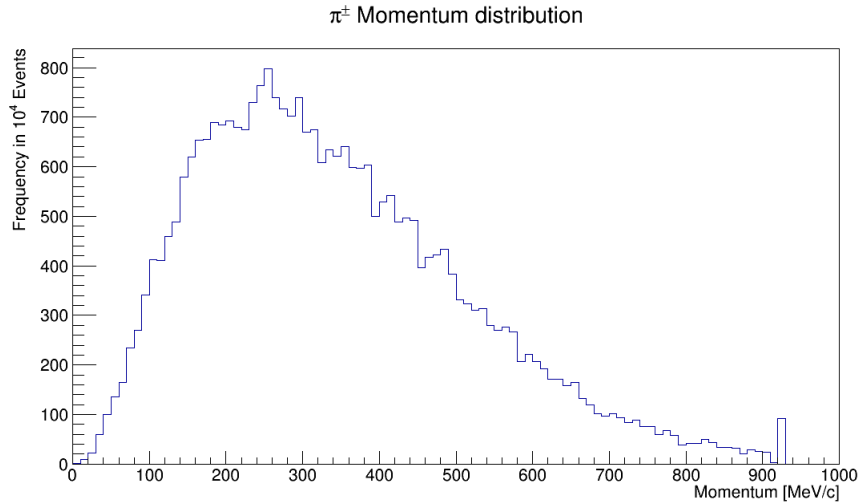


Figure 7.6: π^\pm momentum distribution as generated by MC.

The \bar{H} annihilation is assumed to occur at rest so that the total energy available for the annihilation products is twice the mass of the proton ≈ 1.9 GeV. The annihilation kinematics is taken care of by the class `SecondaryProducer`.

After the generation of the primary π^\pm , π^0 mesons and photons, these annihilation products are propagated into the apparatus according to the Geant4 standard electromagnetic physics list. The multiplicity and the frequency of particles reaching the detector is shown in Fig. 7.7.

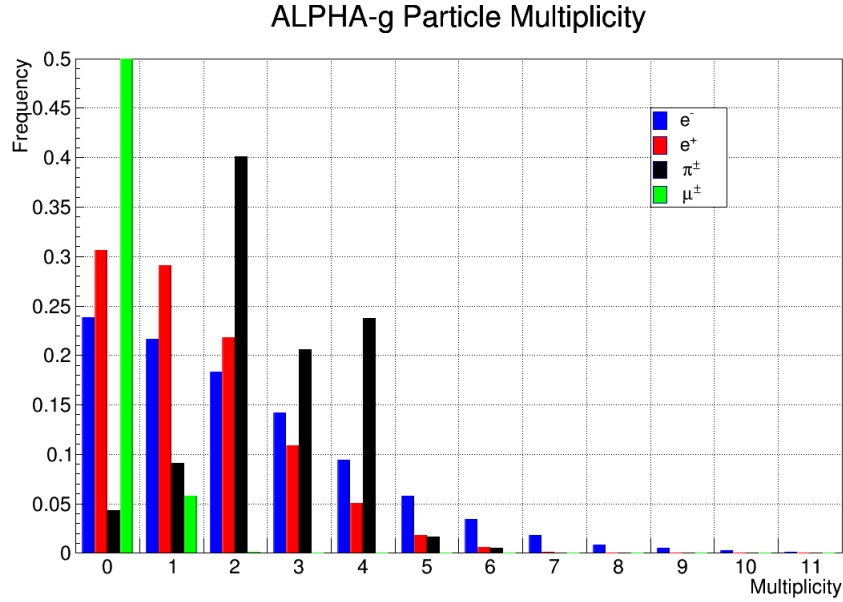


Figure 7.7: Particle multiplicity per event reaching the detector, for instance two π^\pm arrive in the TPC in 40% of the events. Note the μ^\pm fraction in channel 0 is off scale.

7.2.1.3 Ionization Signal Generation

The gas ionization due to the passage of π^\pm (and other particles, see Fig. 7.7) in the drift chamber is simulated with the *PhotoAbsorption Ionization*, or PAI, model that “describes the ionization energy loss of a relativistic charged particle in matter” [153].

The drift region is endowed with a specific production cut, or range cut-off, that is defined as a threshold below which no secondary particle will be generated.

Such a cut-in-range is converted into an energy threshold for the current gas mixture by Geant4. The obtained threshold in kinetic energy cannot be below a fixed lower limit.

For the current simulation the range cut-off is 0.1mm and the low energy limit is set to 26.7 eV, which is the weighted average of the ionization potential of Ar and CO₂. The amount of primary ionization obtained with this configuration is shown in Fig. 7.8.

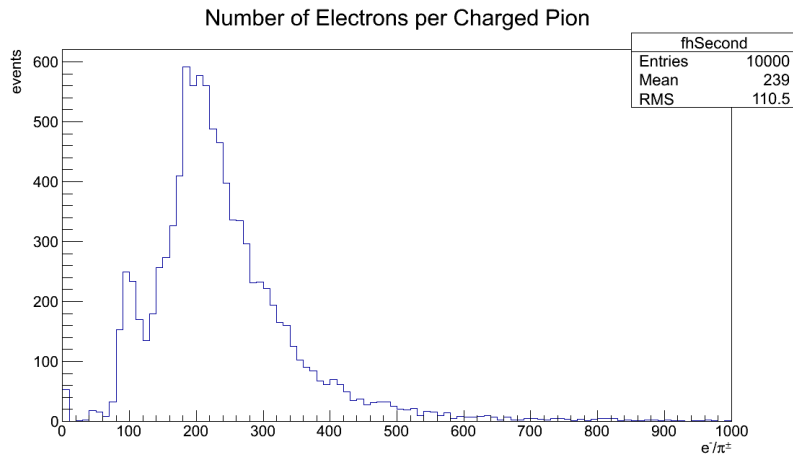


Figure 7.8: Primary electron yield per π^\pm in a 10 cm drift region.

While not all the features of this histogram are well-understood, the average amount of primary ionization matches the expected value. For the purpose of evaluating the TPC performance this suffices to extent that a more accurate simulation is required in the near future, perhaps by combining Geant4 with another simulation framework for drift chambers.

7.2.1.4 Hit Generation

The position and the time of the primary ionization is recorded and digitized by a proper class `TDigi` embedded in the Geant4 simulation. Such objects are

created from the MC information $(r_{\text{MC}}, \phi_{\text{MC}}, z_{\text{MC}}, t_{\text{MC}})$ and Garfield⁸ data. The end-point of the electron trajectory $(\tilde{r}, \tilde{\phi}, \tilde{z}, \tilde{t})$, where the charge is collected, is given by

$$\begin{aligned}\tilde{r} &= b = 10 \text{ cm} + R_{\text{TPC}} \\ \tilde{\phi} &= \phi_{\text{MC}} + \alpha \\ \tilde{z} &= z_{\text{MC}} \\ \tilde{t} &= t_{\text{MC}} + t_d,\end{aligned}$$

where α is the *Lorentz angle*, which is the angle between the drift-velocity and the electric field, and t_d is the drift time. Both quantities depend on r_{MC} and are calculated based on Garfield data using an object `TElectronDrift` [155] and plotted in Fig. 7.9.

While the gas filled volume extends from $a + a_t = 10.3 \text{ cm}$ to $b = 10.3 \text{ cm} + R_{\text{TPC}}$, the *fiducial radius* of the TPC is smaller due to the presence of the anode wires for ionization amplification. For the case of $R_{\text{TPC}} = 10 \text{ cm}$, the fiducial radius, namely the distance along which the ionization can be effectively collected, is $a + a_t + R_{\text{fiducial}} = 19.2 \text{ cm}$.

The conversion between $(\tilde{r}, \tilde{\phi}, \tilde{z}, \tilde{t})$ and readout channel number is accomplished by a simple arithmetic calculation, once the pad sizes in z and ϕ , p_z and p_ϕ , respectively, and the “bunching time” p_t are known. Each readout channel is identified by two non-negative integer numbers, c_z and c_ϕ , and a non-negative integer time bin, c_t , indicating the z and ϕ position and the arrival time of the electrons.

Algorithmically, this reads

⁸Garfield is a computer program for the detailed simulation of two- and three-dimensional drift chambers [154].

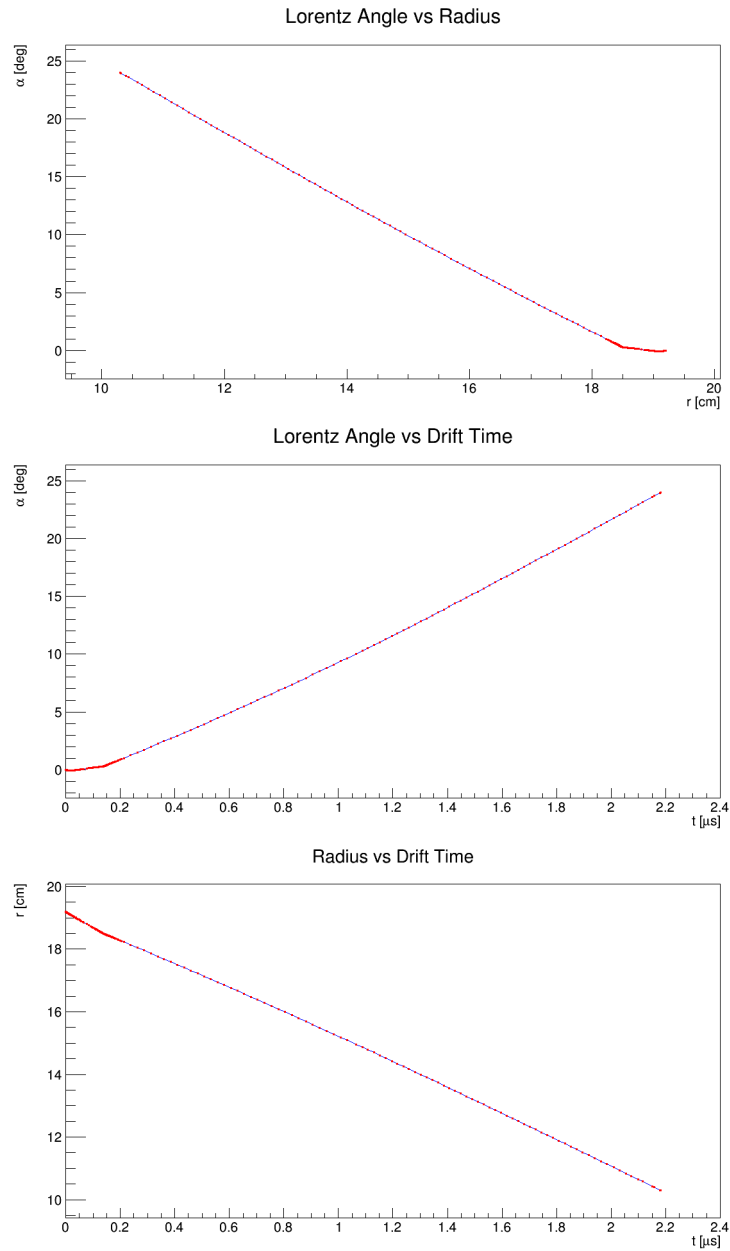


Figure 7.9: Lorentz angle α , drift time and hit radius for configuration under consideration. The data used to produce these plots are obtained with Garfield in [155].

$$\tilde{c}_i = \frac{\tilde{i}}{p_i} \rightarrow c_i = \begin{cases} \lfloor \tilde{c}_i \rfloor + o_i & \text{if } \tilde{c}_i - \lfloor \tilde{c}_i \rfloor < 0.5 \\ \lceil \tilde{c}_i \rceil + o_i & \text{otherwise} \end{cases} \quad i = z, \phi, t,$$

where o_i is the offset needed to make the channel number non-negative for any values of ϕ and z , and $\lfloor \dots \rfloor$ and $\lceil \dots \rceil$ denote, respectively, the largest integer less than the argument (*floor* function) and the smallest integer greater than the argument (*ceiling* function). Note that ϕ is multiplied by $b = 10.3 \text{ cm} + R_{\text{TPC}}$ prior to the calculation of the channel number.

The digitization routine saves the triplets (c_z, c_ϕ, c_t) to a ROOT file ordered by increasing c_t for each event, ready for the reconstruction.

7.2.2 Tracking

With the MC data at hand now is the time to turn to the reconstruction routines and evaluate the performance of the algorithm.

7.2.2.1 Track Identification

The position of the j^{th} hit in the channel (c_z, c_ϕ, c_t) is given by

$$\begin{aligned} x_{1j} &= r_j \cos \phi_j \\ x_{2j} &= r_j \sin \phi_j \\ x_{3j} &= z_j, \end{aligned} \tag{7.8}$$

where

$$\begin{aligned} \phi_j &= \frac{(c_\phi - o_\phi) p_\phi}{b} - \alpha \\ z_j &= (c_z - o_z) p_z \end{aligned}$$

and r_j and α are functions of c_t , namely the drift time. They are obtained from a *look-up table* generated using Garfield data [155]. The look-up table is described in the analysis code by the class `TLookUpTable` that performs the inverse operation of `TElectronDrift` (see Fig. 7.9). The advantage of using `TLookUpTable` comes from the capability of calculating the first derivative of r_j with respect to c_t that is used in the expression of the error associated with the hit position.

The error of the radial position of the hit is then given by

$$\sigma_r^2 = \left(\frac{\partial r}{\partial t} \right)^2 \sigma_t^2,$$

where

$$\sigma_t = \frac{p_t}{\sqrt{12}}.$$

The final expression of the errors associated with the hit position is

$$\begin{aligned} \sigma_{1j}^2 &= \left(\frac{\partial x_{1j}}{\partial r_j} \right)^2 \sigma_r^2 + \left(\frac{\partial x_{1j}}{\partial \phi_j} \right)^2 \sigma_\phi^2 = \frac{x_{1j}^2}{r_j^2} \sigma_r^2 + x_{2j}^2 \sigma_\phi^2 \\ \sigma_{2j}^2 &= \left(\frac{\partial x_{2j}}{\partial r_j} \right)^2 \sigma_r^2 + \left(\frac{\partial x_{2j}}{\partial \phi_j} \right)^2 \sigma_\phi^2 = \frac{x_{2j}^2}{r_j^2} \sigma_r^2 + x_{1j}^2 \sigma_\phi^2 \\ \sigma_{3j}^2 &= \sigma_z^2, \end{aligned} \tag{7.9}$$

where

$$\begin{aligned} \sigma_\phi &= \frac{p_\phi}{\sqrt{12}} \\ \sigma_z &= \frac{p_z}{\sqrt{12}}. \end{aligned}$$

A set of hits belonging to a single track form a specific pattern that must be identified in order to use such a set in an algorithm that calculates the track parameters. A so-called *pattern recognition* algorithm takes as input the whole sets of hits per event and produces as output distinct sets of hits, each forming a different track.

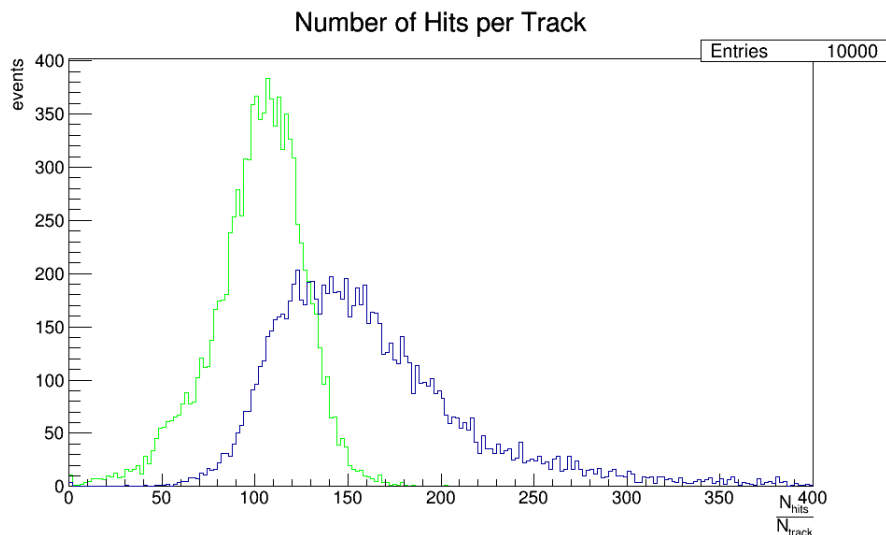


Figure 7.10: Number of hits per track found with pattern recognition routine (green) and with MC information (blue).

In the present analysis, the pattern is identified by searching nearby hits within a sphere of fixed radius, starting from hits at the largest possible radius, i.e., from increasing c_t . The radius of the sphere is a cut-off value on the allowed distance between hits. The procedure is outlined in Fig. 7.11. The default value for the cut, obtained through MC studies, is 11.5 mm.

7.2.2.2 Track Model

With the presence of a uniform magnetic field, the trajectory of the π^\pm can be modelled by an helix, whose *canonical* form $(c, \phi_0, D, \lambda, z_0)$ is given in App. A.

The Least Squares fitting of Eq. (A.1) to the points Eq. (7.8) is performed by minimizing the radial part independently from the axial part, using the `TMinuit` package provided by the ROOT framework.

Two different minimization are performed for the radial part, each using the χ^2 expression given by Eq. (A.4), with a different sign of ϵ . The one that results

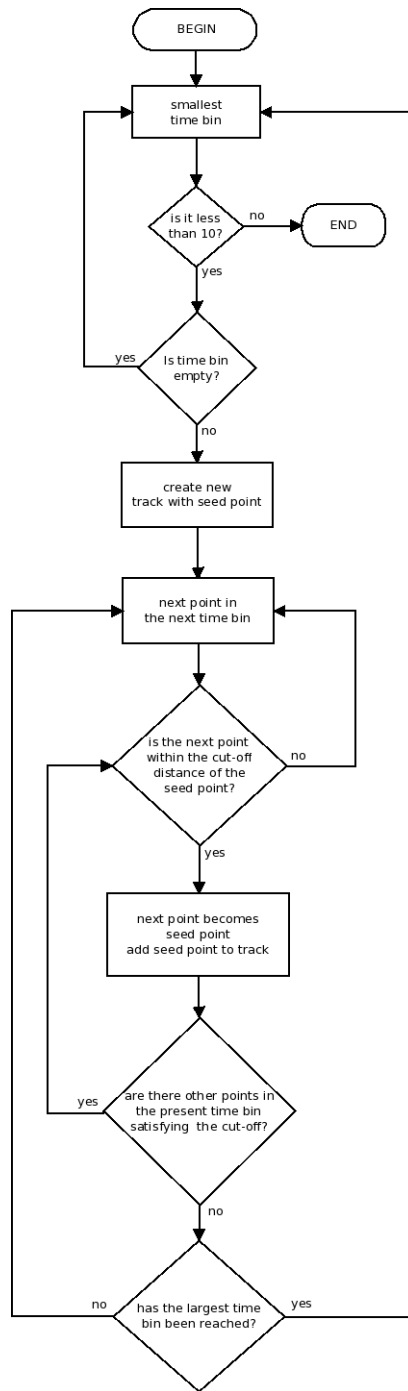


Figure 7.11: Flowchart describing the pattern recognition algorithm.

in the smallest χ_r^2 fixes the radial parameters (c, ϕ_0, D) and the sign of ϵ .

The axial parameters (λ, z_0) are determined by the minimization of the χ^2 given by Eq. (A.5).

The initial values for ($c, \phi_0, D, \lambda, z_0$) are calculated from the first and the last hits, assuming that a straight line passes through these two points.

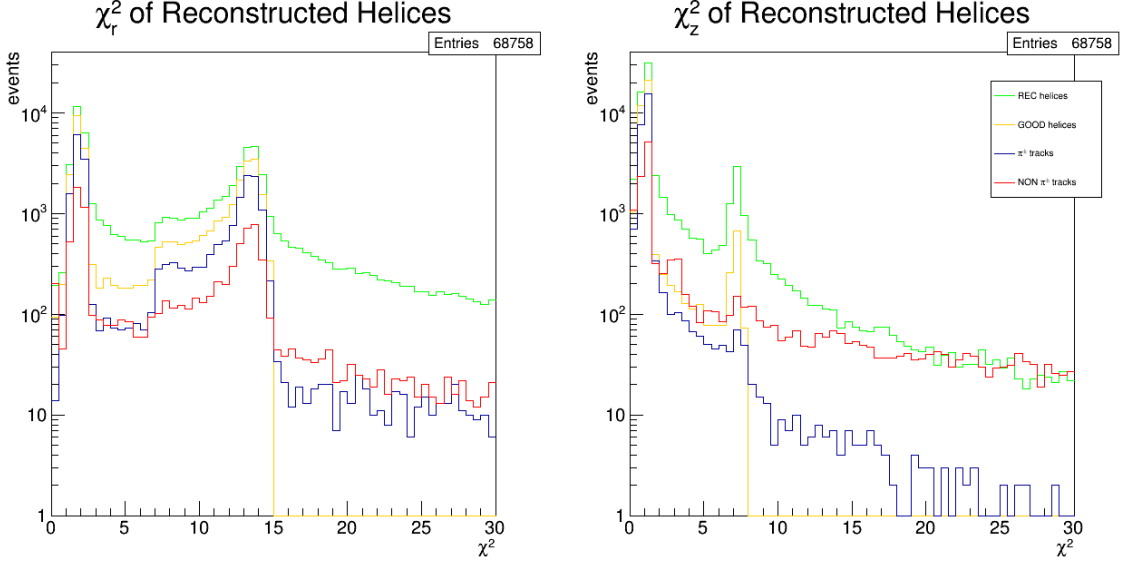


Figure 7.12: Distribution of $\chi_{r,z}^2$ for reconstructed helices using the present algorithm, good helices satisfying the cuts in Tab. 7.2, π^\pm tracks and non- π^\pm tracks from MC information combined with the helix reconstruction.

7.2.2.3 Helix rejection

Since not all the reconstructed tracks are due to π^\pm and, most important, not all of them point back to the \bar{H} annihilation vertex (e.g., low-energy electrons from photon conversion), it is convenient to remove such helices by placing a cut-off on the normalized $\chi_{r,z}^2$ (see Fig 7.12), i.e., divided by the number of degrees of freedom, and on other helix parameters, such as the signed impact parameter D .

Helices satisfying the default cuts, listed in Tab. 7.2, are dubbed *good helices*.

Tracking Cuts	
χ_r^2	< 15
χ_z^2	< 8
$ D $	< 40 mm

Table 7.2: Default helix selection cuts for ALPHA-g.

The effect of the cuts on the reconstructed helices is shown in Fig. 7.13, along with the relevant distribution for the helices reconstructed with the MC information.

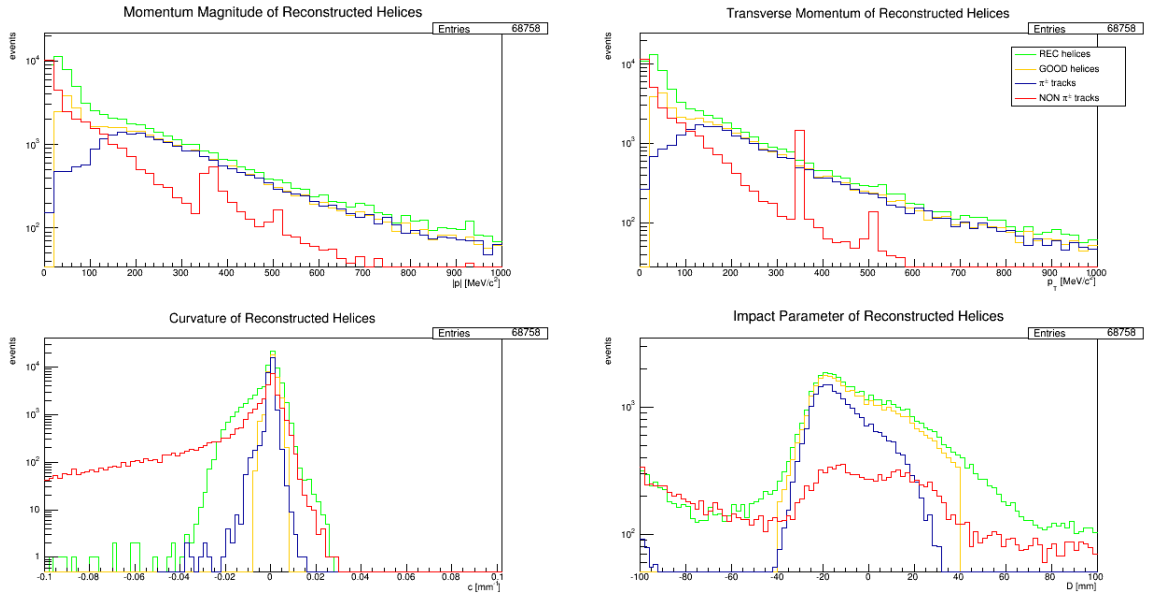


Figure 7.13: Distribution of $|p| = \frac{a}{2c}\sqrt{1 + \lambda^2}$, $p_T = \frac{a}{2c}$, curvature c and impact parameter D for reconstructed helices using the present algorithm, good helices satisfying the cuts in Tab. 7.2, π^\pm tracks and non- π^\pm tracks from MC information combined with the helix reconstruction.

7.2.2.4 Multiple Scattering

Since the charged particles travel through several centimetres of dense material before reaching the detector, a more accurate account of the errors on the reconstructed tracks is desirable. Multiple scattering causes the particle to scatter in the two planes perpendicular and parallel to its path without losing energy. The distribution of each angle is Gaussian with standard deviation [156]

$$\sigma_\theta = \frac{0.0141}{p\beta} \sqrt{\frac{L}{X_R}} = \sqrt{HL}, \quad (7.10)$$

where L is the path length, $X_R \approx 3.21$ cm is the radiation length given by Eq. (4.8), β is the velocity in units of c and $p = \sqrt{p_x^2 + p_y^2 + p_z^2}$ is the magnitude of the linear momentum in GeV/ c given by Eq. (A.6). In order to speed up the evaluation of the multiple scattering errors, L is taken as the line distance between the points where the helix intersects the TPC and the trap wall. Moreover, β is calculated as the ratio of the reconstructed momentum p and the π^\pm mass $m_\pi = 139.566$ MeV/ c^2 .

The final form of the new covariance matrix, proportional to σ_θ^2 given by Eq. (7.10), is added to the one obtained from the track reconstruction; in other words, the errors from the best-fit and the multiple scattering are added in quadrature:

$$\sigma_\gamma^2 = \sigma_{\gamma\text{fit}}^2 + \sigma_{\gamma\text{MS}}^2 \quad \text{with } \gamma = c, \phi_0, D, \lambda, z_0 \quad . \quad (7.11)$$

7.2.3 Vertexing

The vertex reconstruction is achieved through a three step procedure, using the `TMinuit` package provided by the ROOT framework. The procedure is listed below with the detailed calculations for each one of the steps.

Seed finding by minimizing the distance between each pair of helices.

$$\chi_{\text{seed}}^2 = \min_{f', f'' \in \text{good helices}} \sum_{i=1}^3 \frac{[f'_i(s_{\perp}) - f''_i(s_{\perp})]^2}{\sigma_i'^2 + \sigma_i''^2}$$

where

$$\begin{aligned} \sigma_1^2 &= \left(\frac{\partial f_1}{\partial c}\right)^2 \sigma_c^2 + \left(\frac{\partial f_1}{\partial \phi_0}\right)^2 \sigma_{\phi_0}^2 + \left(\frac{\partial f_1}{\partial D}\right)^2 \sigma_D^2 \\ \sigma_2^2 &= \left(\frac{\partial f_2}{\partial c}\right)^2 \sigma_c^2 + \left(\frac{\partial f_2}{\partial \phi_0}\right)^2 \sigma_{\phi_0}^2 + \left(\frac{\partial f_2}{\partial D}\right)^2 \sigma_D^2 \\ \sigma_3^2 &= \left(\frac{\partial f_2}{\partial \lambda}\right)^2 \sigma_{\lambda}^2 + \sigma_{z_0}^2 \end{aligned} \quad (7.12)$$

are calculated from (7.11). The *seed vertex* is taken as the midpoint of the segment joining the best pair of helices at their minimum distance. The calculation of the midpoint takes into account the errors associated with the minimum distance points

$$\mathbf{v}_{\text{seed}} = \frac{\boldsymbol{\sigma}'^2 \cdot \mathbf{f}'^T + \boldsymbol{\sigma}''^2 \cdot \mathbf{f}''^T}{\boldsymbol{\sigma}'^2 + \boldsymbol{\sigma}''^2}.$$

Recalculation of the vertex position by minimizing the distance of the best pair of helices to a common point, the *recalculated vertex* \mathbf{v}

$$\chi_{\text{recalc}}^2 = \sum_{j=1}^2 \sum_{i=1}^3 \frac{[v_i - f_i^j(s_{\perp})]^2}{\sigma_i^{j2}}.$$

Initial values for such a minimization are taken from the previous step.

Improvement of the vertex resolution by minimizing the distance of the best pair of helices and additional helices to a common point. This last step is only possible if the number of reconstructed good helices is greater than two. Every time a new helix is added to the set participating in the minimization to the common point,

$$\chi_{\text{improv}}^2 = \sum_{j=1}^{U(\chi^2)} \sum_{i=1}^3 \frac{[v_i - f_i^j(s_{\perp})]^2}{\sigma_i^{j2}},$$

the newly calculated χ_{improv}^2 is required to be less than a cut-off value,

$$\chi_{\text{improv}}^2 < 3, \quad (7.13)$$

in order to assure improvement in the vertex resolution. Here U denotes the number of *used helices* to determine the final vertex position \mathbf{v} and is a function of χ_{improv}^2 . In case none of the added helices satisfies the χ^2 cut, the final vertex is the recalculated one.

7.2.4 Results

Each simulation consists of the generation of 10 000 \bar{H} annihilations according to Eq. (7.7), propagation of the particles through the detector, production of secondary particles (e.g., ionization electrons and decay products) and creation of the TPC hits.

The input to the analysis software is a ROOT file containing arrays of digitized hit positions. The `AGTPCanalysis` software reconstructs the charged particles trajectories from such space-points and determines the vertex position. The results of the reconstruction are displayed in Figs. 7.14, 7.15 and 7.16, where three fully reconstructed events are shown.

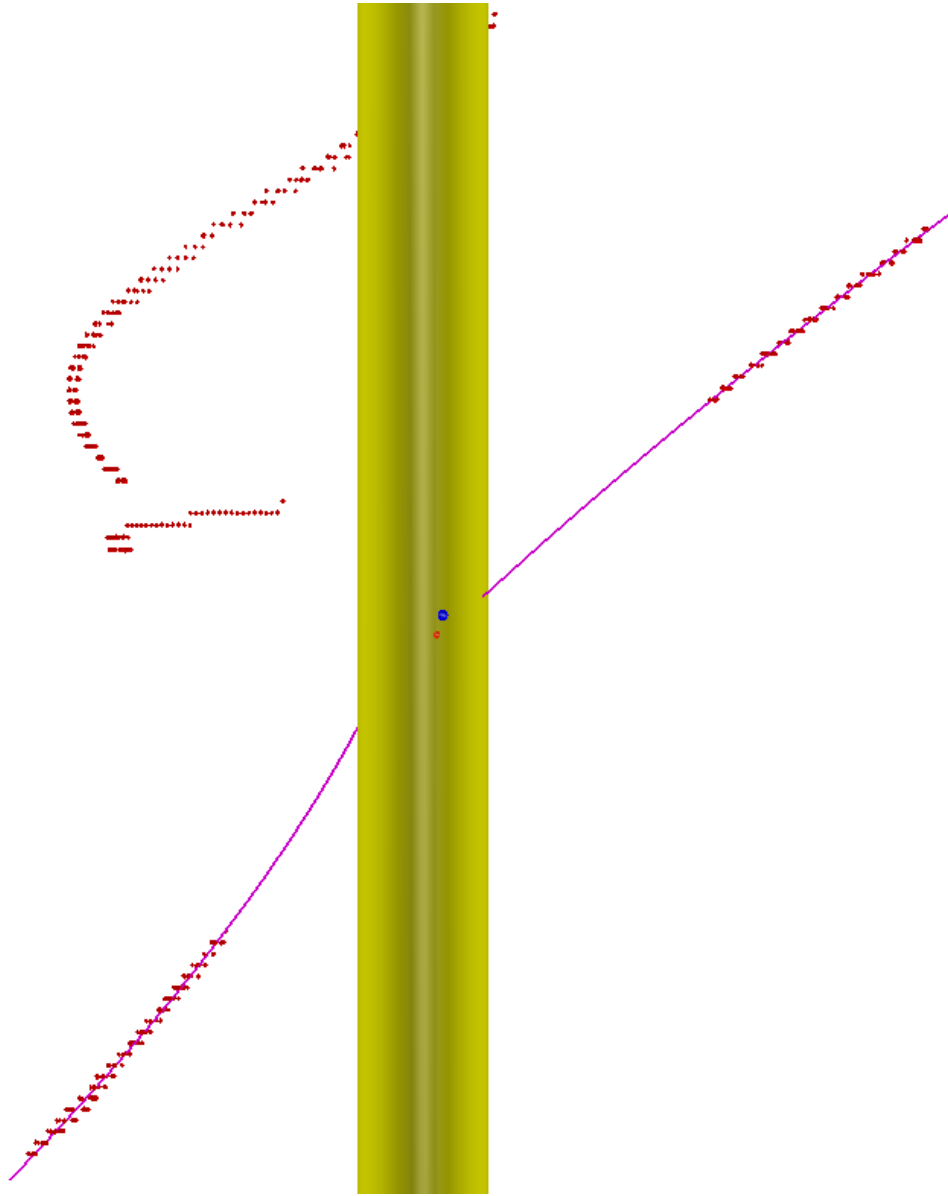


Figure 7.14: Reconstructed event where the reconstructed tracks are drawn together with the TPC hits in red and the yellow tube represents the electrodes stack. Two good helices formed the seed vertex and the final fitted vertex in orange. The “true” MC vertex is the blue point.

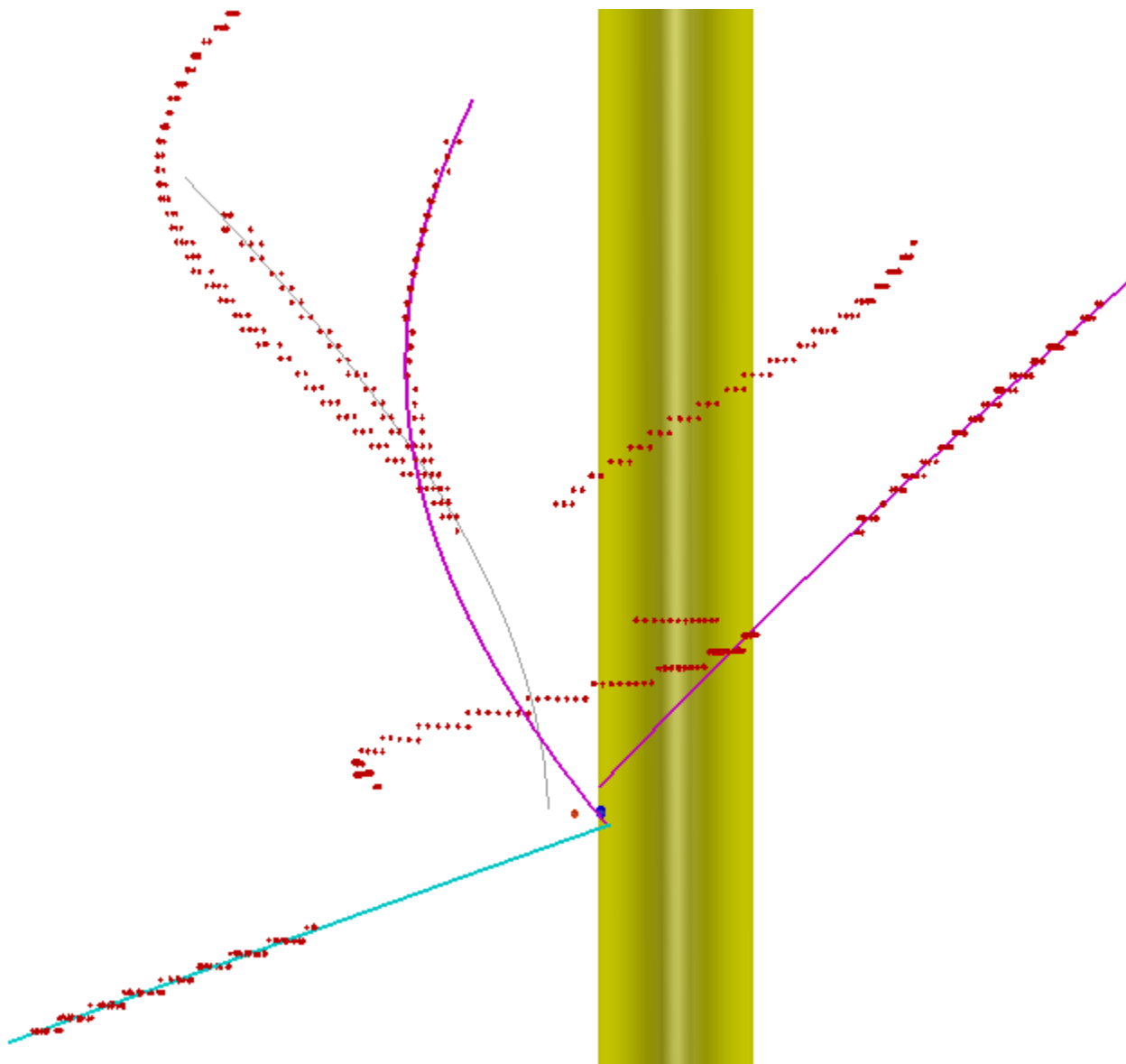


Figure 7.15: Reconstructed event as above. Three good helices: the purple ones give rise to the seed vertex, while the azure one is added to improve the resolution. The grey lines are reconstructed helices that failed the cuts.

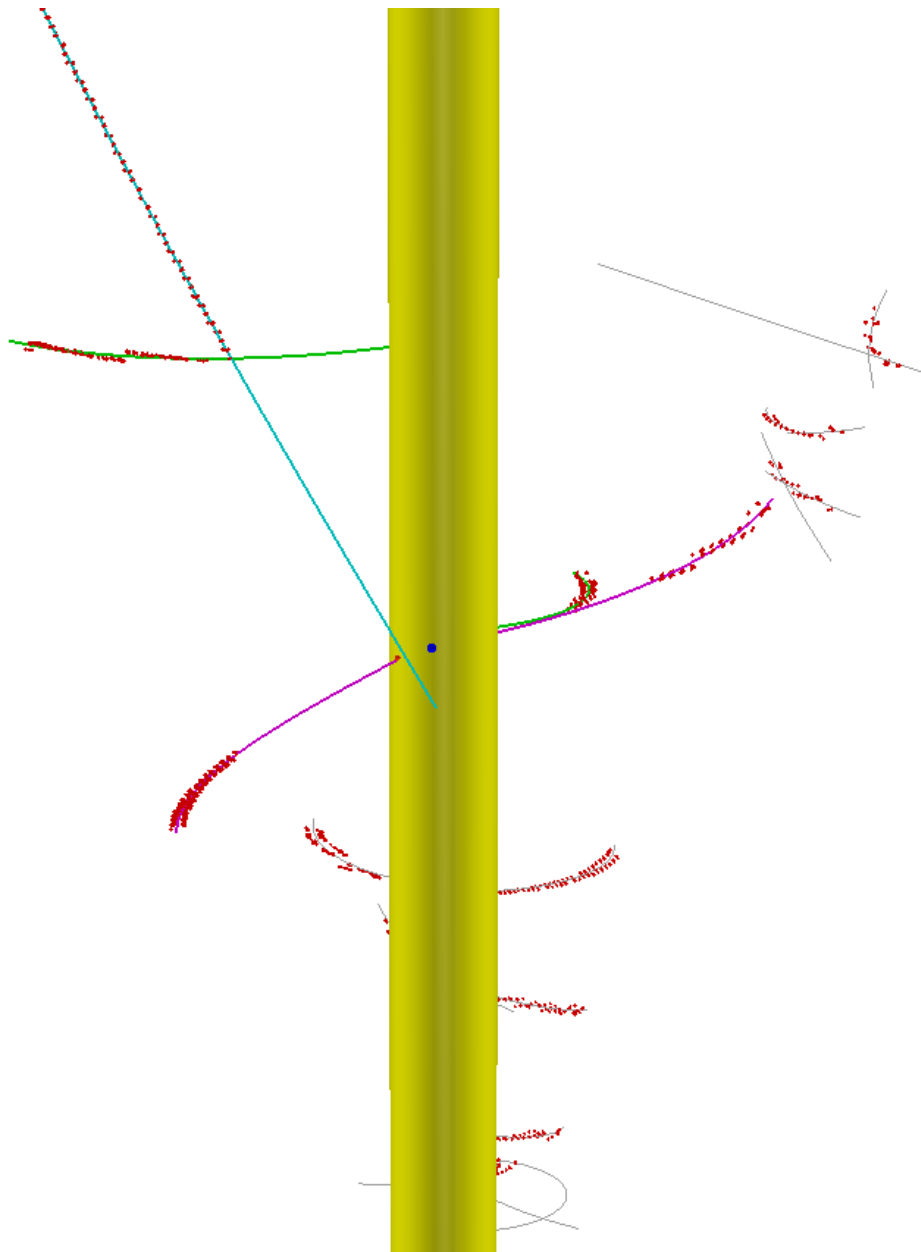


Figure 7.16: Reconstructed event as above. Several reconstructed helices, five good helices passing the cuts, three used for vertexing.

The *vertexing efficiency*, which is the number of events where the vertex is successfully found over the total number of generated events, is

$$\varepsilon = (94.1 \pm 0.2) \%$$

and depends on the optimization of the cuts on the $\chi_{r,z}^2$ and D given by the best-fit to the helices, e.g., inequalities in Tab. 7.2, since the vertex position can be obtained as long as there are at least two reconstructed helices.

The position of the reconstructed vertex (r_v, ϕ_v, z_v) is compared to the actual point of origin of the π^\pm , the so called MC vertex $(r_{\text{MC}} = 22.275 \text{ mm}, \phi_{\text{MC}}, z_{\text{MC}})$. The distributions of

$$\phi_{\text{MC}} - \phi_v, \quad z_{\text{MC}} - z_v \quad \text{and} \quad r_{\text{MC}} - r_v \quad (7.14)$$

are shown in Fig. 7.17 and fitted to a Gaussian in a restricted interval around the centroid and the estimated σ from the fit is taken as detector resolution, along with its error.

The results obtained with the tracking cuts in Tab. 7.2 and the vertex improvement cut, given by Eq. (7.13), are shown in Tab. 7.3.

Vertex Resolution	
r	$(6.0 \pm 0.2) \text{ mm}$
ϕ	$(16.3 \pm 0.4) \text{ deg}$
z	$(3.9 \pm 0.1) \text{ mm}$

Table 7.3: Vertex resolution for ALPHA-g.

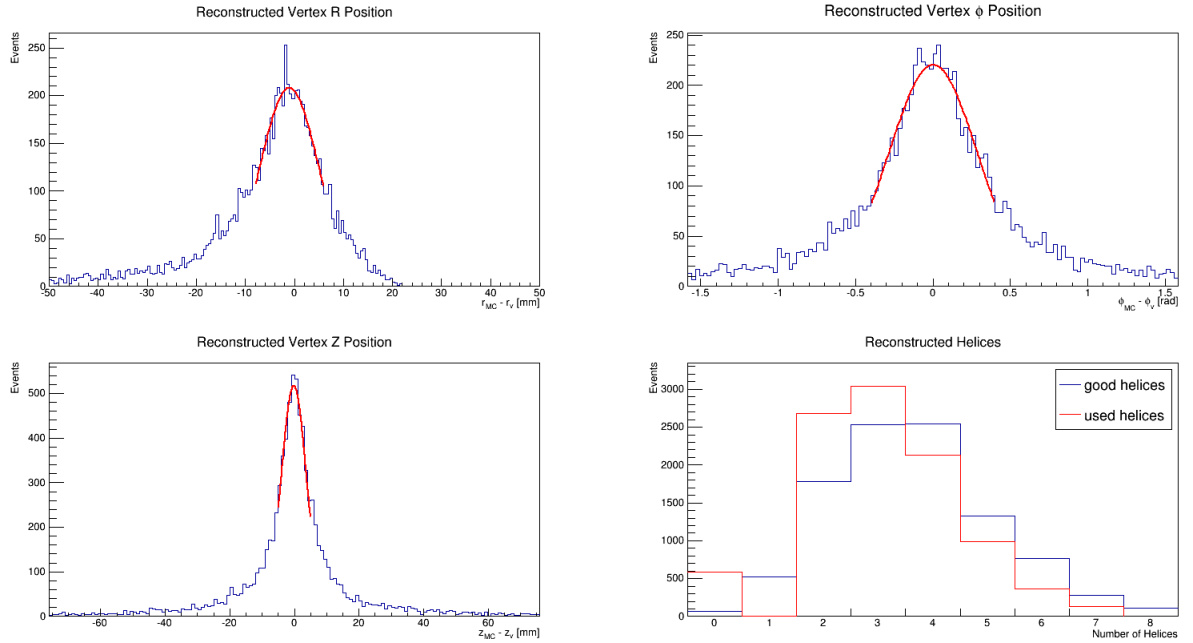


Figure 7.17: Vertex resolution and number of good/used helices.

7.2.5 Conclusion

The first part of the present section describes a realistic (but not complete) simulation of an apparatus, called ALPHA-g, designed to measure the gravitational interaction of \bar{H} . The simulation is focused on the Time Projection Chamber intended to determine the location of the \bar{H} annihilation upon release from the trap or interaction with radiation.

The second part of the present document describes the full reconstruction software for the ALPHA-g TPC. From the signal on pads produced by the primary ionization, the \bar{H} annihilation position is inferred by tracking the annihilation products back to the common origin.

The tracks are determined by finding where the charged particles produced the primary ionization, called space-points, and by identifying the common pattern underlying the space-points envelope of a track. The set of space-points belonging

to a single charged particle are best-fitted with a helix, in order to take into account the solenoidal magnetic field, using the least-squares method. The helices are selected based on the best-fit result and the ones passing the selection criteria are used to calculate the annihilation position, namely the vertex.

The simulation and reconstruction codes, both developed entirely by the author, are ready to be expanded by addressing the following items:

- combining Garfield++ with Geant4 to obtain a realistic simulation of the physics of the drift chambers;
- testing a new readout scheme with pads about 100 times larger in the azimuthal direction in order to reduce the number of channels (the price to pay is that the azimuthal position of the hits must be determined through additional information from the anode wires);
- trying new vertexing algorithms that could reduce, if possible, the “tails” of the resolution distributions.

8 Conclusion

In Chapter 1, the strong motivations to perform high precision experiments on ultra-low energy \bar{H} were presented. These experiments include spectroscopy and measurement of the free fall acceleration. Chapter 2 provided a concise description of the ALPHA apparatus and the methodology employed to produce and confine \bar{H} in a magnetic trap. Chapter 3 provided a technical overview of the Silicon Vertex Detector (SVD) used to identify \bar{H} annihilation. Chapter 4 offered a detailed account of the technique needed to reconstruct the \bar{H} annihilation position from the SVD information. Chapter 5 presented the highest precision experiment performed with \bar{H} - its fractional electric charge has been found to be $(-1.3 \pm 1.1 \pm 0.4) \times 10^{-8}$ at 1σ CL. This analysis also provided a three-fold improvement of the previously measured positron charge anomaly, as well as a test of CPT invariance. Chapter 6 began with the analysis of the commissioning data of the SVD in the upgraded ALPHA apparatus. The procedure to discriminate \bar{H} annihilations from background signals was introduced while describing the analysis of the upgraded ALPHA apparatus commissioning data, where the \bar{H} trapping rate for the new device was established and found to be higher than in the older version. Chapter 6 concluded with an analysis of the new data on the \bar{H} electric charge, by means of a sophisticated machine learning algorithm (MVA). The final Chapter of this dissertation discussed the design of a new experiment, dubbed ALPHA-g, that intends to measure the free fall acceleration of \bar{H} . The first part of the Chapter hinged on the experimental design, while the second part focused on the annihilation detector, a radial Time Projection Chamber (TPC).

At the time of writing ALPHA is taking data. Measurements of the two-photon 1S-2S transition, as well as of the 1S-2P, are underway.

The two-photon spectroscopy occurs in a UV-light enhancement cavity, where the $\bar{\text{H}}$ atom, after the interaction with the laser beams, is ionized by the same laser. Two detection modes are simultaneously adopted, based on counting how many $\bar{\text{H}}$ annihilation signals are detected during the “hold phase”, i.e., when the laser is sent to the $\bar{\text{H}}$ trap, and the “quench phase”, i.e., when the $\bar{\text{H}}$ confinement is removed, of each experiment. The “appearance mode” determines the number of $\bar{\text{H}}$ produced by photo-ionization while the laser is present. The “disappearance mode” determines the deficiency of $\bar{\text{H}}$ after the magnet shutdown. Each experiment with on-resonance laser is followed by one off-resonance, in such a way that the $\bar{\text{H}}$ population in each detection mode is reversed. By using detailed simulations, it has been estimated that $\sim 85\%$ of the original $\bar{\text{H}}$ is ionized for on-resonance interaction (appearance mode), while only $\sim 3\%$ is left in the trap with the same laser frequency (disappearance mode). With off-resonance light only $\sim 1\%$ of $\bar{\text{H}}$ is ionized and $\sim 90\%$ remains trapped.

The Lyman- α spectroscopy, or 1S-2P, employs a single pulsed laser beam that, with some probability, expels $\bar{\text{H}}$ from the trap: the appearance and disappearance detection modes are still employed, interleaved with off-resonance laser experiments. In ten attempts of 500 s of irradiation each, and another ten off-resonance, a clear signal of interaction should be detected.

In addition, positron “spin-flip” measurements with microwave radiation will be performed to improve the previous results obtained by ALPHA and will replace the “magnet shutdown” as the main mechanism to implement the disappearance detection mode.

The gravity experiment with ALPHA-g is proceeding through the design phase.

A Helix Equations

The trajectory of a charged particles, neglecting the multiple scattering and energy loss through the material, in the presence of an uniform magnetic field can be modelled by an helix, whose *canonical* form $(c, \phi_0, D, \lambda, z_0)$ is [157]

$$\begin{aligned}
 f_1 &= -D \sin \phi_0 + \frac{\cos \phi_0}{2c} \sin(2cs_{\perp}) - \frac{\sin \phi_0}{c} [1 - \cos(2cs_{\perp})] \\
 f_2 &= +D \cos \phi_0 + \frac{\sin \phi_0}{2c} \sin(2cs_{\perp}) + \frac{\cos \phi_0}{c} [1 - \cos(2cs_{\perp})] , \\
 f_3 &= z_0 + \lambda s_{\perp}
 \end{aligned} \tag{A.1}$$

where

$$s_{\perp} = \begin{cases} c^{-1} \arcsin \beta & \epsilon = +1 \\ c^{-1}(\pi - \arcsin \beta) & \epsilon = -1 \end{cases} \tag{A.2}$$

is the *arclength parameter* and

$$\beta = c \sqrt{\frac{x^2 + y^2 - D^2}{1 + 2cD}} .$$

Here ϵ indicates whether it is the outgoing or incoming branch of the helix. The curvature parameter c is given by

$$c = \frac{1}{2R_c},$$

where R_c is the radius of curvature.

Alternatively, the helix can be described in terms of β , rather than s_\perp , namely as function of the radius $r = \sqrt{x^2 + y^2}$

$$\begin{aligned} f_1 &= -D \sin \phi_0 + \epsilon \frac{\beta}{c} \sqrt{1 - \beta^2} \cos \phi_0 - \frac{\beta^2}{c} \sin \phi_0 \\ f_2 &= +D \cos \phi_0 + \epsilon \frac{\beta}{c} \sqrt{1 - \beta^2} \sin \phi_0 + \frac{\beta^2}{c} \cos \phi_0, \\ f_3 &= z_0 + \lambda s_\perp \end{aligned} \tag{A.3}$$

where s_\perp stems for the ‘‘complicated’’ β dependence given by Eq. (A.2).

The radial parameters (c, D, ϕ_0) are determined by minimizing

$$\chi_r^2 = \sum_{j=1}^N \sum_{i=1}^2 \frac{[x_{ij} - f_i(r; c, \phi_0, D)]^2}{\sigma_{ij}^2} \tag{A.4}$$

and the axial parameters (λ, z_0) are determined by minimizing

$$\chi_z^2 = \sum_{j=1}^N \frac{[x_{3j} - f_3(r; \lambda, z_0)]^2}{\sigma_{3j}^2}, \tag{A.5}$$

where the index j runs on the number of track measurements (hits) and the j -th hit is located at the position of Cartesian coordinates (x_{1j}, x_{2j}, x_{3j}) . In Eqs. (A.4,A.5), σ_{ij} for $i, j = 1, 2, 3$ are the errors associated with the hit position.

The linear momentum in MeV/ c , under the assumption that the particle does not lose energy along its path, is

$$\begin{aligned} p_x &= \frac{a}{2c} \cos \phi_0 \\ p_y &= \frac{a}{2c} \sin \phi_0 \\ p_z &= \frac{a}{2c} \lambda. \end{aligned} \tag{A.6}$$

Here the parameters are $a = \mp 0.2998$, for a particle with a charge $Q = \pm e$ in a magnetic field of 1 T, and (c, ϕ_0, λ) from the best-fit. Practically, the sign of a is assigned as the one opposite to c .

B Time Evolution of e^+ Spin in Magnetic Field

The magnetic moment of a e^+ in CGS units is given by

$$\boldsymbol{\mu} = \frac{ge}{2mc} \mathbf{S}, \quad (\text{B.1})$$

where g is the gyromagnetic ratio, $e > 0$ is the elementary charge, m is the e^+ mass, c is the speed of light and \mathbf{S} is the spin vector. It is worth noting that the magnetic moment of a e^+ has the opposite sign to that of the e^- .

The potential energy of a particle with magnetic moment $\boldsymbol{\mu}$ in a classical magnetic field \mathbf{B} is given by $-\boldsymbol{\mu} \cdot \mathbf{B}$, hence the Hamiltonian operator is

$$\hat{H} = -\hat{\boldsymbol{\mu}} \cdot \mathbf{B} = -\frac{ge}{2mc} \hat{\mathbf{S}} \cdot \mathbf{B} = -\frac{ge}{2mc} \sum_i \hat{S}_i B_i. \quad (\text{B.2})$$

The Ehrenfest theorem [158] states that the time evolution of a component of the spin operator \hat{S}_i is given by

$$\begin{aligned}
\frac{d\langle\hat{S}_i\rangle}{dt} &= \frac{1}{i\hbar}\langle[\hat{S}_i, \hat{H}]\rangle \\
&= -\frac{ge}{2mc} \frac{1}{i\hbar} \sum_j \langle[\hat{S}_i, \hat{S}_j]\rangle B_j \\
&= -\frac{ge}{2mc} \frac{1}{i\hbar} \sum_j i\hbar\epsilon_{ijk}\langle\hat{S}_k\rangle B_j \\
&= -\frac{ge}{2mc} \sum_j \epsilon_{ijk}\langle\hat{S}_k\rangle B_j, \tag{B.3}
\end{aligned}$$

where $\langle \dots \rangle$ indicates the expectation value of a quantum-mechanical operator.

Therefore, the time evolution of the spin operator $\hat{\mathbf{S}}$ obeys the *torque* equation

$$\frac{d\langle\hat{\mathbf{S}}\rangle}{dt} = \frac{ge}{2mc}\langle\hat{\mathbf{S}}\rangle \times \mathbf{B} = \langle\hat{\boldsymbol{\mu}}\rangle \times \mathbf{B}, \tag{B.4}$$

where $\boldsymbol{\mu} \times \mathbf{B} = \boldsymbol{\tau}$ is the classical torque.

Bibliography

- [1] P. A. M. Dirac, “A Theory of Electrons and Protons”, Proc. Roy. Soc. Lond. **A126**, 360 (1930).
- [2] C. D. Anderson, “The Positive Electron”, Physical Review **43**, 491–494 (1933).
- [3] O. Chamberlain, E. Segrè, C. Wiegand, and T. Ypsilantis, “Observation of antiprotons”, Physical Review **100**, 947 (1955).
- [4] C.-S. Wu, E. Ambler, R. Hayward, D. Hoppes, and R. P. Hudson, “Experimental test of parity conservation in beta decay”, Physical Review **105**, 1413 (1957).
- [5] M. Goldhaber, L. Grodzins, and A. Sunyar, “Helicity of neutrinos”, Physical Review **109**, 1015 (1958).
- [6] J. H. Christenson, J. W. Cronin, V. L. Fitch, and R. Turlay, “Evidence for the 2π Decay of the K_2^0 Meson”, Phys. Rev. Lett. **13**, 138 (1964).
- [7] J. Lees et al., “Observation of time-reversal violation in the B^0 meson system”, Phys. Rev. Lett. **109**, 211801 (2012).
- [8] W. N. Cottingham and D. A. Greenwood, “An introduction to the standard model of particle physics”, in, Second Edition (Cambridge University Press, 2007), pp. 139–144, 176–183.
- [9] O. W. Greenberg, “CPT violation implies violation of Lorentz invariance”, Phys. Rev. Lett. **89**, 231602 (2002).
- [10] G. Lüders, “Proof of the TCP theorem”, Annals Phys. **2**, 1–15 (1957).
- [11] G. Lüders and B. Zumino, “Connection between spin and statistics”, Physical Review **110**, 1450 (1958).
- [12] M. E. Peskin and D. V. Schroeder, “An introduction to quantum field theory”, in (Westview, 1995) Chap. 4, pp. 88–90.
- [13] S. Ulmer et al., “High-precision comparison of the antiproton-to-proton charge-to-mass ratio”, Nature **524**, 196–199 (2015).
- [14] ALICE Collaboration, “Precision measurement of the mass difference between light nuclei and anti-nuclei”, Nature Phys. (2015) 10.1038/nphys3432.

- [15] E. Abouzaid et al., “Precise Measurements of Direct CP Violation, CPT Symmetry, and Other Parameters in the Neutral Kaon System”, *Physical Review D* **83**, 092001 (2011).
- [16] D. Colladay and V. A. Kostelecký, “CPT violation and the standard model”, *Physical Review D* **55**, 6760 (1997).
- [17] D. Colladay and V. A. Kostelecký, “Lorentz-violating extension of the standard model”, *Physical Review D* **58**, 116002 (1998).
- [18] R. Bluhm, V. A. Kostelecký, and N. Russell, “CPT and Lorentz Tests in Hydrogen and Antihydrogen”, *Phys. Rev. Lett.* **82**, 2254–2257 (1999).
- [19] M. Charlton, J. Eades, D. Horváth, R. J. Hughes, and C. Zimmermann, “Antihydrogen physics”, *Phys. Rep.* **241**, 65–117 (1994).
- [20] V. A. Kostelecký and A. J. Vargas, “Lorentz and CPT tests with hydrogen, antihydrogen, and related systems”, arXiv preprint **arXiv:1506.01706** (2015).
- [21] V. A. Kostelecký and M. Mewes, “Fermions with Lorentz-violating operators of arbitrary dimension”, *Physical Review D* **88**, 096006 (2013).
- [22] V. A. Kostelecký and N. Russell, “Data tables for Lorentz and CPT violation”, arXiv preprint **arXiv:0801.0287v8** (2015).
- [23] R. M. Wald, “General Relativity”, in (The University of Chicago Press, 1984), pp. 8–9,22–23.
- [24] C. M. Will, “The confrontation between general relativity and experiment”, *Living Rev. Rel* **17** (2014).
- [25] H. Müller, A. Peters, and S. Chu, “A precision measurement of the gravitational redshift by the interference of matter waves”, *Nature* **463**, 926–929 (2010).
- [26] M. M. Nieto and J. T. Goldman, “The Arguments against ‘antigravity’ and the gravitational acceleration of antimatter”, *Phys. Rep.* **205**, 221–281 (1991).
- [27] V. A. Kostelecký and J. D. Tasson, “Matter-gravity couplings and Lorentz violation”, *Physical Review D* **83**, 016013 (2011).
- [28] T. A. Wagner, J. H. Gundlach, E. G. Adelberger, and S. Schlamminger, “Torsion-balance tests of the weak equivalence principle”, *Class. Quant. Grav.* **29**, 184002–184016 (2012).
- [29] S. Schlamminger, K. Y. Choi, T. A. Wagner, J. H. Gundlach, and E. G. Adelberger, “Test of the Equivalence Principle Using a Rotating Torsion Balance”, *Phys. Rev. Lett.* **100**, 041101 (2008).

- [30] J. G. Williams, S. G. Turyshev, and D. Boggs, “Lunar Laser Ranging Tests of the Equivalence Principle”, *Class. Quant. Grav.* **29**, 184004 (2012).
- [31] A. D. Cronin, J. Schmiedmayer, and D. E. Pritchard, “Optics and interferometry with atoms and molecules”, *Rev. Mod. Phys.* **81**, 1051 (2009).
- [32] S. Dimopoulos, P. W. Graham, J. M. Hogan, and M. Kasevich, “General relativistic effects in atom interferometry”, *Physical Review D* **78**, 042003 (2008).
- [33] S. Herrmann, H. Dittus, and C. Lammerzahl, “Testing the equivalence principle with atomic interferometry”, *Class. Quant. Grav.* **29**, 184003 (2012).
- [34] E. G. Adelberger, B. Heckel, C. Stubbs, and Y Su, “Does antimatter fall with the same acceleration as ordinary matter?”, *Phys. Rev. Lett.* **66**, 850 (1991).
- [35] D. S. Alves, M. Jankowiak, and P. Saraswat, “Experimental constraints on the free fall acceleration of antimatter”, arXiv preprint **arXiv:0907.4110** (2009).
- [36] S. G. Karshenboim, “A constraint on antigravity of antimatter from precision spectroscopy of simple atoms”, *Astronomy letters* **35**, 663–669 (2009).
- [37] R. J. Hughes and M. H. Holzscheiter, “Constraints on the gravitational properties of antiprotons and positrons from cyclotron-frequency measurements”, *Phys. Rev. Lett.* **66**, 854 (1991).
- [38] A Apostolakis et al., “Tests of the equivalence principle with neutral kaons”, *Physics Letters B* **452**, 425–433 (1999).
- [39] S. Menary, “Why We Already Know that Antihydrogen is Almost Certainly NOT Going to Fall” Up”, arXiv preprint **arXiv:1207.7358** (2012).
- [40] G. Chardin, “Motivations for antigravity in General Relativity”, *Hyperfine Interactions* **109**, 83 (1997).
- [41] D. S. Hajdukovic, “Dark energy, antimatter gravity and geometry of the Universe”, *Astrophysics and Space Science* **330**, 1 (2010).
- [42] M. Villata, “CPT symmetry and antimatter gravity in general relativity”, *Europhys. Lett.* **94**, 20001 (2011).
- [43] G. Baur et al., “Production of antihydrogen”, *Physics Letters B* **368**, 251–258 (1996).
- [44] M. H. Holzscheiter, M. Charlton, and M. M. Nieto, “The route to ultra-low energy antihydrogen”, *Phys. Rep.* **402**, 1–2 (2004).

- [45] G. Altarelli and M. W. Gr unewald, “Precision electroweak tests of the standard model”, *Physics Rep.* **403**, 189–201 (2004).
- [46] CMS Collaboration, “Measurement of the ratio of the inclusive 3-jet cross section to the inclusive 2-jet cross section in pp collisions at $\sqrt{s} = 7$ TeV and first determination of the strong coupling constant in the TeV range”, *Eur. Phys. J. C* **73**, 2604 (2013).
- [47] ATLAS Collaboration, *Measurements of the Higgs boson production and decay rates and coupling strengths using pp collision data at $\sqrt{s} = 7$ and 8 TeV in the ATLAS experiment*, July 2015.
- [48] CMS Collaboration, “Precise determination of the mass of the Higgs boson and tests of compatibility of its couplings with the standard model predictions using proton collisions at 7 and 8 TeV”, *Eur. Phys. J. C* **75**, 1–50 (2015).
- [49] Y. Yamazaki and S. Ulmer, “CPT symmetry tests with cold \bar{p} and antihydrogen”, *Annalen Phys.* **525**, 493–504 (2013).
- [50] R. Bluhm, “Lorentz and CPT tests in matter and antimatter”, *Nucl. Instrum. Meth.* **A221**, 6–11 (2004).
- [51] H. A. Bethe and E. E. Salpeter, *Quantum mechanics of one-and two-electron atoms* (Springer, 1977).
- [52] A. Kramida, “A critical compilation of experimental data on spectral lines and energy levels of hydrogen, deuterium, and tritium”, *Atomic Data and Nuclear Data Tables* **96**, 586–644 (2010).
- [53] C. G. Parthey et al., “Improved Measurement of the Hydrogen 1S - 2S Transition Frequency”, *Phys. Rev. Lett.* **107**, 203001 (2011).
- [54] T. W. Darling, F. Rossi, G. I. Opat, and G. F. Moorhead, “The fall of charged particles under gravity: A study of experimental problems”, *Rev. Mod. Phys.* (1992) **10.1103/RevModPhys.64.237**.
- [55] F. C. Witteborn and W. M. Fairbank, “Experimental comparison of the gravitational force on freely falling electrons and metallic electrons”, *Phys. Rev. Lett.* **19**, 1049 (1967).
- [56] F. C. Witteborn and W. M. Fairbank, “Experiments to determine the Force of Gravity on Single Electrons and Positrons”, *Nature* **220**, 10.1038/220436a0, 436–440 (1968).
- [57] P Dyer, J Camp, M. H. Holzscheiter, and S Graessle, “Falling antimatter: An experiment to measure the gravitational acceleration of the antiproton”, *Nucl. Instrum. Meth.* **B40**, 485–488 (1989).

- [58] R. E. Brown, J. B. Camp, and T. W. Darling, “Antimatter gravity experiment”, *Nucl. Instrum. Meth.* **56–57**, **Part 1**, 480–483 (1991).
- [59] D. M. Kaplan, K. Kirch, D. Mancini, J. D. Phillips, T. J. Phillips, T. J. Roberts, and J. Terry, “Measuring Antimatter Gravity with Muonium”, *EPJ Web Conf.* **95**, 05008 (2015).
- [60] M. E. Peskin and D. V. Schroeder, “An introduction to quantum field theory”, in (Westview, 1995) Chap. 20, pp. 705–707.
- [61] M. Hori and J. Walz, “Physics at CERN’s antiproton decelerator”, *Progress in Particle and Nuclear Physics* **72**, 206–253 (2013).
- [62] M. Amoretti et al., “The ATHENA antihydrogen apparatus”, *Nucl. Instrum. Meth.* **518**, 679–711 (2004).
- [63] G. Chardin et al., “Proposal to measure the Gravitational Behaviour of Antihydrogen at Rest”, (2011).
- [64] G. Gabrielse et al., “Trapped antihydrogen in its ground state”, *Phys. Rev. Lett.* **108**, 113002 (2012).
- [65] A. Kellerbauer et al., “Proposed antimatter gravity measurement with an antihydrogen beam”, *Nucl. Instrum. Meth.* **B266**, 351–356 (2008).
- [66] N Kuroda et al., “A source of antihydrogen for in-flight hyperfine spectroscopy”, *Nature Commun.* **5** (2014).
- [67] M. Hori et al., “Two-photon laser spectroscopy of antiprotonic helium and the antiproton-to-electron mass ratio”, *Nature* **475**, 484–488 (2011).
- [68] J. DiSciaccia et al., “One-Particle Measurement of the Antiproton Magnetic Moment”, *Phys. Rev. Lett.* **110**, 130801 (2013).
- [69] C. Amole et al., “The ALPHA antihydrogen trapping apparatus”, *Nucl. Instrum. Meth.* **A735**, 319–340 (2014).
- [70] G. B. Andresen et al., “Trapped antihydrogen”, *Nature* **468**, 673–676 (2010).
- [71] C. Amole et al., “Resonant quantum transitions in trapped antihydrogen atoms”, *Nature* **483**, 439–443 (2012).
- [72] L. S. Brown and G. Gabrielse, “Geonium theory: Physics of a single electron or ion in a Penning trap”, *Rev. Mod. Phys.* **58**, 233 (1986).
- [73] S. Earnshaw, “On the nature of the molecular forces which regulate the constitution of the luminiferous ether”, *Trans. Camb. Phil. Soc* **7**, 97–112 (1842).

- [74] W. T. Scott, “Who Was Earnshaw?”, *American Journal of Physics* **27**, 418–419 (1959).
- [75] F. G. Major, V. N. Gheorghe, and G. Werth, *Charged particle traps: physics and techniques of charged particle field confinement*, Vol. 37 (Springer Science & Business Media, 2006).
- [76] M. H. Holzscheiter, X. Feng, J. T. Goldman, N. King, R. Lewis, et al., “Are anti-protons forever?”, *Phys. Lett.* **A214**, 279 (1996).
- [77] G. B. Andresen et al., “Compression of antiproton clouds for antihydrogen trapping”, *Phys. Rev. Lett.* **100**, 203401 (2008).
- [78] G. B. Andresen et al., “Antiproton, positron, and electron imaging with a microchannel plate/phosphor detector”, *Rev. Sci. Instrum.* **80**, 123701 (2009).
- [79] W. H. Wing, “On neutral particle trapping in quasistatic electromagnetic fields”, *Progress in Quantum Electronics* **8**, 181–199 (1984).
- [80] H. Metcalf and P. van der Straten, “Cooling and trapping of neutral atoms”, *Phys. Rep.* **244**, 203–286 (1994).
- [81] V. Balykin, V. Minogin, and V. Letokhov, “Electromagnetic trapping of cold atoms”, *Rep. Prog. Phys.* **63**, 1429 (2000).
- [82] R. S. Hayano, “Ground-state hyperfine splitting of antihydrogen”, *Hyperfine Interactions* **172**, 53–62 (2006).
- [83] R. Dickson and J. Weil, “Breit-Rabi Zeeman states of atomic hydrogen”, *American Journal of Physics* **59**, 2 (1991).
- [84] E. Majorana, “Atomi orientati in campo magnetico variabile”, *Il Nuovo Cimento* (1924-1942) **9**, 43–50 (1932).
- [85] D. E. Pritchard, “Cooling neutral atoms in a magnetic trap for precision spectroscopy”, *Phys. Rev. Lett.* **51**, 1336 (1983).
- [86] G. B. Andresen et al., “Antimatter Plasmas in a Multipole Trap for Antihydrogen”, *Phys. Rev. Lett.* **98**, 023402 (2007).
- [87] F. Robicheaux, “Atomic processes in antihydrogen experiments: a theoretical and computational perspective”, *Journal of Physics B* **41**, 192001 (2008).
- [88] J. Fajans, N. Madsen, and F. Robicheaux, “Critical loss radius in a Penning trap subject to multipole fields”, *Phys. Plasmas* **15**, 032108 (2008).
- [89] G. B. Andresen et al., “A Novel antiproton radial diagnostic based on octupole induced ballistic loss”, *Phys. Plasmas* **15**, 032107 (2008).

- [90] G. B. Andresen et al., “Evaporative cooling of antiprotons to cryogenic temperatures”, *Phys. Rev. Lett.* **105**, 013003 (2010).
- [91] J. Danielson, D. Dubin, R. Greaves, and C. Surko, “Plasma and trap-based techniques for science with positrons”, *Rev. Mod. Phys.* **87**, 247 (2015).
- [92] T. Murphy and C. Surko, “Positron trapping in an electrostatic well by inelastic collisions with nitrogen molecules”, *Physical Review A* **46**, 5696 (1992).
- [93] M. Amoretti et al., “Production and detection of cold antihydrogen atoms”, *Nature* **419**, 456–459 (2002).
- [94] G. B. Andresen et al., “Autoresonant excitation of antiproton plasmas”, *Phys. Rev. Lett.* **106**, 025002 (2011).
- [95] C. Amole et al., “Experimental and computational study of the injection of antiprotons into a positron plasma for antihydrogen production”, *Phys. Plasmas* **20**, 043510 (2013).
- [96] G. B. Andresen et al., “Search For Trapped Antihydrogen”, *Phys. Lett.* **B695**, 95–104 (2011).
- [97] G. B. Andresen et al., “Antihydrogen formation dynamics in a multipolar neutral anti-atom trap”, *Physics Letters B* **685**, 141 (2010).
- [98] G. Gabrielse, S. Rolston, L. Haarsma, and W. Kells, “Antihydrogen production using trapped plasmas”, *Physics Letters A* **129**, 38–42 (1988).
- [99] W. A. Bertsche et al., “A magnetic trap for antihydrogen confinement”, *Nucl. Instrum. Meth.* **A566**, 746–756 (2006).
- [100] G. Bendiscioli and D. Kharzeev, “Antinucleon-nucleon and antinucleon-nucleus interaction. A review of experimental data”, *La Rivista Del Nuovo Cimento Series 3* **17**, 1–142 (1994).
- [101] C. Amole et al., “Antihydrogen and mirror-trapped antiproton discrimination: Discriminating between antihydrogen and mirror-trapped antiprotons in a minimum-B trap”, *New J. Phys.* (2012).
- [102] G. B. Andresen et al., “Confinement of antihydrogen for 1000 seconds”, *Nature Phys.* **7**, 558–564 (2011).
- [103] J. M. Michan, M. C. Fujiwara, and T. Momose, “Development of a Lyman- α laser system for spectroscopy and laser cooling of antihydrogen”, *Hyperfine Interactions* **228**, 77 (2014).
- [104] P. H. Donnan, M. C. Fujiwara, and F. Robicheaux, “A proposal for laser cooling antihydrogen atoms”, *Journal of Physics B* **46**, 025302 (2013).

- [105] E. Butler, “Antihydrogen formation, dynamics and trapping”, PhD thesis (Swansea U., 2011).
- [106] C. Amole et al., “Description and first application of a new technique to measure the gravitational mass of antihydrogen”, *Nature Commun.* **4**, 1785 (2013).
- [107] C. Amole et al., “An experimental limit on the charge of antihydrogen”, *Nature Commun.* **5**, 3955 (2014).
- [108] C. Amole et al., “Silicon vertex detector upgrade in the ALPHA experiment”, *Nucl. Instrum. Meth.* **A732**, 134–136 (2013).
- [109] M. Saidi and M. Valipour, “Experimental modeling of vortex tube refrigerator”, *Applied thermal engineering* **23**, 1971–1980 (2003).
- [110] F. Hartmann, *Evolution of silicon sensor technology in particle physics* (Springer Science & Business Media, 2009).
- [111] G. B. Andresen et al., “The ALPHA–detector: Module Production and Assembly”, *Journal of Instrumentation* **7**, C01051 (2012).
- [112] *VAITA*, Ideas (2001).
- [113] K. Olchanski, *VME-ALPHA-TTC manual* (2012).
- [114] J. P. Martin and P. A. Amaudruz, “A 48 channel pulse shape digitizer with DSP”, *Nuclear Science, IEEE Transactions on* **53**, 715–719 (2006).
- [115] K. Olchanski, *VME-NIMIO32* (2014).
- [116] *VMIVME-7805*, VMIC GEFanuc (2003).
- [117] *SIS3820 VME Scaler*, SIS GmbH (2009).
- [118] S. Ritt, P. A. Amaudruz, et al., “The MIDAS data acquisition system”, Midas online: <https://midas.psi> (1997).
- [119] R. Brun and F. Rademakers, “ROOT - An object oriented data analysis framework”, *Nucl. Instrum. Meth.* **389**, New Computing Techniques in Physics Research V, 81–86 (1997).
- [120] I. Hrivnacova et al., “The Virtual Monte Carlo”, eConf **C0303241**, THJT006 (2003).
- [121] R. Brun, F. Bruyant, M. Maire, A. McPherson, and P. Zancarini, “GEANT3”, (1987).
- [122] S. Agostinelli et al., “GEANT4: A simulation toolkit”, *Nucl. Instrum. Meth.* **A506**, 250–303 (2003).
- [123] J. Allison et al., “Geant4 developments and applications”, *Nuclear Science, IEEE Transactions on* **53**, 270–278 (2006).

- [124] F. E. James, *Monte Carlo phase space*, tech. rep. (CERN, 1968).
- [125] H. Wind, ed., *1972 CERN computing and data processing school*, Vol. CERN-72-21: *Function Parametrization* (Pertisau, Austria, Sept. 1972).
- [126] K. Olive et al., “Review of Particle Physics”, *Chin. Phys.* **C38**, 090001 (2014).
- [127] R. A. Hydomako, *Detection of trapped antihydrogen* (Springer, 2012).
- [128] M. Baquero-Ruiz, “Studies on the Neutrality of Antihydrogen”, PhD thesis (University of California, Berkeley, 2013).
- [129] C. Amole et al., “In situ electromagnetic field diagnostics with an electron plasma in a Penning-Malmberg trap”, *New J.Phys.* **16**, 013037 (2014).
- [130] G. B. Andresen et al., “Antihydrogen annihilation reconstruction with the ALPHA silicon detector”, *Nucl. Instrum. Meth.* **A684**, 73–81 (2012).
- [131] T. Topçu and F. Robicheaux, “Radiative cascade of highly excited hydrogen atoms in strong magnetic fields”, *Physical Review A* **73**, 043405 (2006).
- [132] B. Bransden and C. Joachain, “Physics of Atoms and Molecules”, in, 1st ed., Pearson Education (Longman, 1983) Chap. 5, pp. 225–227.
- [133] P. T. Greenland, “Antimatter”, *Contemporary Physics* **38**, 181–203 (1997).
- [134] G. Bressi, G. Carugno, F Della Valle, G Galeazzi, G Ruoso, and G. Sartori, “Testing the neutrality of matter by acoustic means in a spherical resonator”, *Physical Review A* **83**, 052101 (2011).
- [135] M. Baquero-Ruiz et al., “Using stochastic acceleration to place experimental limits on the charge of antihydrogen”, *New J.Phys.* **16**, 083013 (2014).
- [136] I. Narsky, “Optimization of signal significance by bagging decision trees”, in *Statistical problems in particle physics, astrophysics and cosmology. Proceedings, Conference, PHYSTAT05, Oxford, UK, September 12-15, 2005* (2005), pp. 143–146.
- [137] I. Narsky, “StatPatternRecognition: A C++ Package for Statistical Analysis of High Energy Physics Data”, arXiv preprint **arXiv:physics/0507143** (2005).
- [138] G. Punzi, “Sensitivity of searches for new signals and its optimization”, arXiv preprint **arXiv:physics/0308063v2** (2003).
- [139] L. Breiman, “Random forests”, *Machine learning* **45**, 5–32 (2001).
- [140] A. K. Jain, “Magnetic field measurements and mapping techniques”, in, CERN, Geneva, 7 - 11 Apr 2003 (CERN, 2003), Streaming video ; transparencies ; 5 DVD video.

- [141] A. I. Zhmoginov, A. E. Charman, J. Fajans, and J. S. Wurtele, “Non-linear dynamics of anti-hydrogen in magnetostatic traps: implications for gravitational measurements”, *Class. Quant. Grav.* **30**, 205014 (2013).
- [142] M. Kasevich and S. Chu, “Atomic interferometry using stimulated Raman transitions”, *Phys. Rev. Lett.* **67**, 181 (1991).
- [143] A. Peters, K.-Y. Chung, and S. Chu, “High-precision gravity measurements using atom interferometry”, *Metrologia* **38**, 25 (2001).
- [144] H. Müller, S.-W. Chiow, S. Herrmann, S. Chu, and K.-Y. Chung, “Atom-interferometry tests of the isotropy of post-Newtonian gravity”, *Phys. Rev. Lett.* **100**, 031101 (2008).
- [145] K.-Y. Chung, S.-W. Chiow, S. Herrmann, S. Chu, and H. Müller, “Atom interferometry tests of local Lorentz invariance in gravity and electrodynamics”, *Physical Review D* **80**, 016002 (2009).
- [146] M. A. Hohensee, S. Chu, A. Peters, and H. Müller, “Equivalence Principle and Gravitational Redshift”, *Phys. Rev. Lett.* **106**, 151102 (2011).
- [147] P. Cladé, E. De Mirandes, M. Cadoret, S. Guellati-Khélifa, C. Schwob, F. Nez, L. Julien, and F. Biraben, “Determination of the fine structure constant based on Bloch oscillations of ultracold atoms in a vertical optical lattice”, *Phys. Rev. Lett.* **96**, 033001 (2006).
- [148] N. Poli, F. Y. Wang, M. G. Tarallo, A. Alberti, M. Prevedelli, and G. M. Tino, “Precision measurement of gravity with cold atoms in an optical lattice and comparison with a classical gravimeter”, *Phys. Rev. Lett.* **106**, 038501 (2011).
- [149] J. B. Fixler, G. Foster, J. McGuirk, and M. Kasevich, “Atom interferometer measurement of the Newtonian constant of gravity”, *Science* **315**, 74–77 (2007).
- [150] P. Hamilton, A. I. Zhmoginov, F. Robicheaux, J. Fajans, J. S. Wurtele, and H. Müller, “Antimatter interferometry for gravity measurements”, *Phys. Rev. Lett.* **112**, 121102 (2014).
- [151] O. Luiten, H. Werij, I. Setija, M. Reynolds, T. Hijmans, and J. Walraven, “Lyman- α spectroscopy of magnetically trapped atomic hydrogen”, *Phys. Rev. Lett.* **70**, 544–544 (1993).
- [152] K. Kleinknecht, *Detectors for particle radiation* (1998).
- [153] J. Apostolakis et al., “An implementation of ionisation energy loss in very thin absorbers for the GEANT4 simulation package”, *Nucl. Instrum. Meth.* **A453**, 597–605 (2000).

- [154] R. Veenhof, “Garfield, a drift chamber simulation program”, Conf.Proc. **C9306149**, 66–71 (1993).
- [155] P. Lu, Private Communication, Nov. 2014.
- [156] P. Avery, “Applied Fitting Theory V: track fitting using the Kalman filter”, CLEO Note CBX92-39 (1992).
- [157] P. Avery, “Applied Fitting Theory IV”, CLEO Note CBX92-39 (1992).
- [158] A. Messiah, “Quantum mechanics”, in, Vol. I (North-Holland Publishing Company, Amsterdam, 1961) Chap. VI, pp. 216–218.